EPFL

Intentional oxygen oscillations on Pd/Al$_2$O$_3$ for enhanced methane removal from the exhaust of natural gas engines

Présentée le 2 décembre 2022

Faculté des sciences de base
Groupe Kröcher
Programme doctoral en chimie et génie chimique

pour l'obtention du grade de Docteur ès Sciences

par

Maneka Claire ROGER

Acceptée sur proposition du jury

Prof. S. Gerber, présidente du jury
Prof. O. Kröcher, Dr D. Ferri, directeurs de thèse
Prof. S. Bensaid, rapporteur
Dr D. Thompsett, rapporteur
Dr P. Dimopoulos, rapporteur

École
polytechnique
fédérale
de Lausanne

2022

"You cannot escape the responsibility of tomorrow by evading it today." ~ Abraham Lincoln

Abstract

Natural gas (NG) is a suitable alternative to gasoline and diesel fuels to decrease the carbon footprint of the mobility and energy sectors. Although NG is considered a fossil fuel, methane (CH_4), its main component, can be produced industrially from power-to-gas processes (syngas) and wet biomass (biogas). Hence, if in the future CH_4 is predominantly produced via these routes, it will become a carbon-neutral fuel. Nonetheless, because CH_4 is a severe greenhouse gas, its emissions will be continuously more stringently regulated by the European emission standards. Therefore, efficient catalytic exhaust after-treatment technologies need to be developed to prevent NG from being ignored in future energy scenarios. NG can be used for many applications, such as fuel for natural gas vehicles (NGVs), electricity generation, domestic heating, or even coupling to endothermic reactions. However, since the transportation sector contributes up to 20 % of the global air emissions, this thesis focuses on the removal of CH_4 from the exhaust of engines fuelled with NG and operated under lean-burn and stoichiometric conditions.

Unburnt CH_4 is typically removed from the exhaust gas using palladium-based catalysts, which suffer from thermal deactivation as well as water and sulphur poisoning. Catalyst deactivation can be countered either by improving the material formulation and properties or by tuning the operating conditions. In the latter case, evidence exists that periodic changes in the reaction conditions can mitigate the deactivation processes and even enhance CH_4 oxidation, thus decreasing the emission levels. For NGV applications, this could be accomplished by periodic variations of the O_2 concentration (lean/rich O_2 pulses) in the reactive feed. This thesis work aims at demonstrating and proposing strategies for the improvement of CH_4 abatement from lean-burn and stoichiometric NG engines through periodic operation while understanding at a fundamental level the behaviour of the active metals (oxidation state and surface structure) using spectroscopic tools.

First, the beneficial effect and structural modifications induced by repeated short reducing pulses (SRP; O_2 cut-off for 3 s every 5 min) were studied on a Pd/Al_2O_3 catalyst for wet lean methane oxidation (cf. lean-burn NG engines; Chapter 3). Under these conditions, we were able to activate the catalyst and bring it to a highly active state compared to static reaction conditions. This strategy also allowed reversing the structural effects

induced by thermal and hydrothermal treatments and therefore recovering the degraded activity of these materials. Under isothermal conditions (435 °C), SRP suppressed the fast deactivation of Pd/Al_2O_3 (fresh and aged) observed under static conditions in the presence of water and allowed to maintain the catalyst active (> 98% CH_4 conversion) over long times. The combination of time-resolved operando X-ray absorption spectroscopy (XAS) data and kinetic models of Pd oxidation showed that under static conditions only moderately active PdO species are present, while during SRP operation an amorphous PdO_x shell around a metallic Pd core is formed repeatedly. We observed that as long as the Pd^0 core is present, high activity could be achieved. However, once the Pd^0 core is fully consumed, PdO_x is believed to densify and crystallize causing a decrease in CH_4 conversion. Such deactivation could be reversed as well by SRP. These findings allowed us to propose a practical range of Pd oxidation degrees (25-65%) to maintain high CH_4 conversion under lean conditions.

The same periodic operation was then applied to the exhaust feed of stoichiometric NG engines (Chapter 4). Because the real exhaust gas composition is more complex (CO, NO, CH_4, H_2O, O_2) than only CH_4, H_2O, and O_2, a step-wise approach was used, wherein the complexity of the reactive mixture was increased progressively starting from lean wet CH_4 oxidation conditions. This allowed resolving the effect of each gas feed component on both the catalytic activity and the dynamics of Pd redox. We observed that CO accelerates Pd bulk oxidation at high O_2 partial pressures while NO limits Pd bulk growth due to blockage of the Pd^0 sites. We also showed that the O_2 partial pressure controls the Pd redox properties and kinetics, while the partial pressure of the reactants influences the collision factor, thus modifying the optimal Pd window to achieve high CH_4 oxidation rates. Finally, the occurrence of CH_4 steam reforming (CH_4-SR) was proven to be essential for the simultaneous removal of NO and CH_4. Indeed, if the Pd species are fully reduced, NO reduction and CH_4-SR occur efficiently, whereas if the Pd species are even slightly oxidized, the system collapses wherein CH_4 oxidation by O_2 takes over and only limited activity towards NO reduction is achieved.

Even if short reducing pulses operation provides essential knowledge on the chemistry of CH_4 oxidation from material and catalytic standpoints, these pulses are not optimal to achieve high conversions of the pollutants over a wide range of conditions (i.e. temperature, O_2 concentrations, gas feed composition), especially when considering the exhaust feed of stoichiometric NG engines. O_2 pulses of smaller amplitudes and higher

frequencies (defined as O_2-dithering) are more efficient to maximize pollutants conversions from the exhaust of stoichiometric NG engines. Nonetheless, it is not yet well understood how the dithering parameters (pulse amplitude and frequency) affect CH_4 conversion, making it difficult to anticipate the impact of such pulses on the catalytic performance. In Chapter 5, we show that the effect of O_2-dithering on the activity of Pd/Al_2O_3 can be reliably assessed as a function of dithering parameters, temperature, and exhaust gas composition. Operando XAS was used to support the conclusions based on considerations of the Pd oxidation state. The approach relies on explicit calculations of the O_2 concentration present in the reactive feed, which is based on the amount of O_2 pulsed to the system and the conversion level of the pollutants. Since NO contributes to the amount of oxygen available during the reaction, its concentration and conversion need to be correctly evaluated. This study shows that the O_2 pulses have a beneficial effect on the activity when CH_4 steam reforming is promoted (O_2-poor conditions, reduced Pd species), whereas an excess of O_2 induces CH_4 oxidation by O_2 and leads to moderate CH_4 conversion and low NO conversion.

A major issue that arises when CH_4-SR is promoted on Pd/Al_2O_3 is the production of NH_3 which is regulated by the European emission standards. Because Rh is efficient for SR reactions and prevents NH_3 formation from NO reduction by H_2, bimetallic Pd-Rh/Al_2O_3 was studied under both static and O_2-dithering conditions (Chapter 6). The results demonstrated that the presence of Rh modifies the redox behaviour of Pd. While the redox dynamics of Pd in Pd/Al_2O_3 are greatly affected by the O_2 concentration present in the reactive environment, the impact is lower on Pd-Rh/Al_2O_3. In the latter case, the metals remain in their reduced state even if O_2 is in excess. Hence, when performing repeated lean/rich O_2 pulses on Pd/Al_2O_3, the activity strongly oscillated with the O_2 concentration, between low and high pollutant conversions, due to the constant oxidation/reduction of the Pd species. On the other hand, on Pd-Rh/Al_2O_3 the activity fluctuated less during the O_2 oscillations, and therefore high conversion levels were achieved over a broader range of dithering parameters (amplitudes and frequencies) compared to Pd/Al_2O_3. The results revealed that the presence of Rh promotes and maintains CH_4-SR, while the resulting H_2 formed from CH_4-SR keeps the Pd species reduced up to higher O_2 concentrations than over Pd/Al_2O_3. Moreover, it is shown that the presence of Pd in the catalyst is crucial to

achieving acceptable conversion rates under oxidizing conditions, while Rh maintains the catalyst reduced and the activity high, under rich conditions.

Finally, to gain insight into the reaction pathways and Pd surface species involved during the reaction, near ambient pressure X-ray photoemission spectroscopic (NAP-XPS) measurements were carried out. Because the exhaust gas composition of stoichiometric NG engines was too complex to draw any reliable conclusion, the gas composition was simplified and periodically switched between CO and O_2 (every 5 min). Furthermore, the time resolution and signal-to-noise (S/N) ratio of synchrotron-based NAP-XPS measurements were too low to follow precisely the evolution of the Pd surface species. Hence, the work described in Chapter 7 focuses on improving the S/N ratio and time resolution of the NAP-XPS experiments on a powder Pd/Al_2O_3 catalyst. To do so two methods were combined, modulation excitation (ME) and phase-sensitive detection (PSD). The ME method allowed for improving the S/N ratio of a photoemission spectrum while restricting the time resolution of the measurement solely to the acquisition time of one spectrum. With PSD, seven Pd species were identified (bulk Pd^0/PdO, surface Pd^0/PdO (2-fold and 4-fold), adsorbed CO on Pd^0 surface, and Pd^{n+} (n > 2)) and their dynamics (consumption/formation) were followed along the gas switches. The kinetic data retrieved from PSD revealed that Pd^{n+} and 2-fold surface PdO species were most active toward CO oxidation. Moreover, our results combined with an in-depth literature review, showed that PdO reduction and Pd oxidation followed a diffusion-controlled reduction and a shrinking core model, respectively.

Keywords

Résumé

Le gaz naturel (GN) est une bonne alternative à l'essence et aux carburants diesel pour réduire l'empreinte carbone des secteurs de la mobilité et de l'énergie. Bien que le GN soit considéré comme un combustible fossile, le méthane (CH_4), son principal composant, peut être produit industriellement à partir de procédés de conversion de l'énergie en gaz (gaz de synthèse) et de la biomasse humide (biogaz). Par conséquent, si à l'avenir le CH_4 est principalement produit par ces voies, il deviendra un combustible neutre en carbone. Néanmoins, le CH_4 étant un gaz à effet de serre important, ses émissions seront de plus en plus réglementées par les normes d'émission européennes. Par conséquent, des technologies efficaces de post-traitement catalytique des gaz d'échappement doivent être développées pour éviter que le GN ne soit pas pris en compte dans les scénarios énergétiques futurs. Le GN peut être utilisé pour de nombreuses applications, comme carburant pour les véhicules au gaz naturel (GNV), pour la production d'électricité, pour le chauffage domestique ou même couplé à des réactions endothermiques. Cependant, étant donné que le secteur des transports contribue jusqu'à 20 % des émissions atmosphériques mondiales, cette thèse se concentre sur l'élimination du CH_4 des moteurs alimentés au GN et fonctionnant dans des conditions de mélange pauvre et stœchiométrique.

Le CH_4 imbrûlé est généralement éliminé des gaz d'échappement à l'aide de catalyseurs à base de palladium, qui souffrent de désactivation thermique ainsi que d'empoisonnement par l'eau et le soufre. La désactivation des catalyseurs peut être combat freinée soit en améliorant la formulation et les propriétés des matériaux, soit en adaptant les conditions de fonctionnement. Dans ce dernier cas, il est prouvé que des modifications périodiques des conditions de réaction peuvent atténuer les processus de désactivation et même améliorer l'oxydation du CH_4, réduisant ainsi les niveaux d'émission. Pour les applications GNV, ceci pourrait être accompli par des variations périodiques de la concentration en O_2 (impulsions de O_2 pauvre/riche) dans mélange réactif. Ce travail de thèse vise à démontrer et à proposer des stratégies pour l'amélioration de l'abattement du CH_4 des moteurs à combustion pauvre et stœchiométrique au GN par des opérations périodiques tout en comprenant à un niveau fondamental le comportement des métaux actifs (état d'oxydation et structure de surface) en utilisant des outils spectroscopiques.

Tout d'abord, l'effet bénéfique et les modifications structurelles induites par de courtes impulsions réductrices répétées (CIR ; coupure de l'O_2 pendant 3 s toutes les 5 min) ont été étudiés sur un catalyseur Pd/Al_2O_3 pour l'oxydation du méthane en milieu humide pauvre (cf. moteurs à GN à combustion pauvre ; chapitre 3). Dans ces conditions, nous avons pu activer le catalyseur et l'amener à un état hautement actif par rapport aux conditions de réaction statiques. Cette stratégie a également permis d'inverser les effets structuraux induits par les traitements thermiques et hydrothermaux et donc de récupérer l'activité dégradée de ces matériaux. Dans des conditions isothermes (435 °C), l'ICR a supprimé la désactivation rapide de Pd/Al_2O_3 (frais et vieilli) observée dans des conditions statiques en présence d'eau et a permis de maintenir le catalyseur actif (> 98% de conversion du CH_4). La combinaison des données de la spectroscopie d'absorption des rayons X (XAS) operando résolue dans le temps et des modèles cinétiques de l'oxydation du Pd a montré que dans des conditions statiques, seules des espèces PdO modérément actives sont présentes, tandis que pendant le fonctionnement du ICP, une coquille amorphe de PdO_x autour d'un noyau métallique de Pd est formé de manière répétée. Nous avons observé que tant que le noyau Pd^0 est présent, une activité élevée peut être atteinte. Cependant, une fois que le noyau Pd^0 est entièrement consommé, on pense que le PdO_x se densifie et se cristallise, entraînant une diminution de la conversion du CH_4. Cette désactivation peut également être inversée par ICP. Ces résultats nous ont permis de proposer une gamme pratique de degrés d'oxydation du Pd (25-65%) pour maintenir une conversion élevée du CH_4 dans des conditions pauvres.

La même opération périodique a été appliquée à l'alimentation en gaz d'échappement de moteurs GN stœchiométriques (chapitre 4). Comme la composition réelle des gaz d'échappement est plus complexe (CO, NO, CH_4, H_2O, O_2) que seulement CH_4, H_2O et O_2, une approche par étapes a été utilisée, dans laquelle la complexité du mélange réactif a été augmentée progressivement en commençant par des conditions d'oxydation pauvres de CH_4 humide. Ceci a permis de résoudre l'effet de chaque composant de l'alimentation en gaz sur l'activité catalytique et la dynamique du redox de Pd. Nous avons observé que le CO accélère l'oxydation du Pd à des pressions partielles d'O_2 élevées tandis que le NO limite la croissance de PdO en raison du blocage des sites Pd^0. Nous avons également montré que la pression partielle de O_2 contrôle les propriétés redox et la cinétique du Pd, tandis que la pression partielle des réactifs influence le facteur de collision, modifiant ainsi la

fenêtre optimale de Pd pour atteindre des taux élevés d'oxydation du CH_4. Enfin, l'occurrence du reformage à la vapeur du CH_4 (CH_4-SR) s'est avérée essentielle pour l'élimination simultanée du NO et du CH_4. En effet, si les espèces de Pd sont complètement réduites, la réduction de NO et le CH_4-SR se produisent efficacement, alors que si les espèces de Pd sont même légèrement oxydées, le système s'effondre, l'oxydation de CH_4 par O_2 prend le dessus et seule une activité limitée vers la réduction de NO est atteinte.

Même si l'utilisation d'impulsions réductrices courtes permet d'acquérir des connaissances essentielles sur la chimie de l'oxydation du CH_4 du point de vue des matériaux et de la catalyse, ces impulsions ne sont pas optimales pour obtenir des conversions élevées des polluants dans une large gamme de conditions (c'est-à-dire la température, les concentrations d'O_2, la composition de l'alimentation en gaz), en particulier si l'on considère l'alimentation en gaz d'échappement des moteurs à GN stœchiométriques. Les impulsions d'O_2 de plus petites amplitudes et de plus hautes fréquences (définies comme des fluctuations d'O_2) sont plus efficaces pour maximiser les conversions de polluants de l'échappement des moteurs à GN stœchiométriques. Néanmoins, on ne comprend pas encore bien comment les paramètres de fluctuation (amplitude et fréquence des impulsions) affectent la conversion du CH_4, ce qui rend difficile l'anticipation de l'impact de ces impulsions sur les performances catalytiques. Dans le chapitre 5, nous montrons que l'effet de la fluctuation l'oxygène sur l'activité de Pd/Al_2O_3 peut être évalué de manière fiable en fonction des paramètres de fluctuation, de la température et de la composition des gaz d'échappement. La spectroscopie d'absorption d'énergie XAS a été utilisée pour étayer les conclusions basées sur des considérations de l'état d'oxydation du Pd. L'approche repose sur des calculs explicites de la concentration de O_2 présente dans l'alimentation réactive, qui est basée sur la quantité de O_2 pulsée vers le système et le niveau de conversion des polluants. Comme le NO contribue à la quantité d'oxygène disponible pendant la réaction, sa concentration et sa conversion doivent être correctement évaluées. Cette étude montre que les impulsions d'O_2 ont un effet bénéfique sur l'activité lorsque le reformage à la vapeur de CH_4 est favorisé (conditions pauvres en O_2, espèces Pd réduites), alors qu'un excès d'O_2 induit l'oxydation de CH_4 par O_2 et conduit à une conversion modérée de CH_4 et à une faible conversion de NO.

Un problème majeur qui se pose lorsque le CH_4-SR est promu sur Pd/Al_2O_3 est la production de NH_3 qui est réglementée par les normes d'émission européennes. Comme Rh est efficace pour les réactions SR et empêche la formation de NH_3 à partir de la réduction de NO par H_2, le bimétallique Pd-Rh/Al_2O_3 a été étudié dans des conditions statiques et dans des conditions de fluctuation de l'O_2 (chapitre 6). Les résultats ont démontré que la présence de Rh modifie le comportement redox de Pd. Alors que la dynamique redox du Pd dans Pd/Al_2O_3 est fortement affectée par la concentration en O_2 présente dans l'environnement réactif, l'impact est moindre sur Pd-Rh/Al_2O_3. Dans ce dernier cas, les métaux restent dans leur état réduit même si l'O_2 est en excès. Ainsi, lors de l'exécution d'impulsions répétées d'O_2 pauvre/riche sur Pd/Al_2O_3, l'activité a fortement oscillé avec la concentration d'O_2, entre des conversions de polluants faibles et élevées, en raison de l'oxydation/réduction constante des espèces de Pd. D'autre part, sur Pd-Rh/Al_2O_3, l'activité a moins fluctué pendant les oscillations de O_2, et donc une activité élevée a été atteinte sur une gamme plus large de paramètres de fluctuation (amplitudes et fréquences) par rapport à Pd/Al_2O_3. Les résultats ont révélé que la présence de Rh favorise et maintient le CH_4-SR, tandis que le H_2 résultant formé à partir du CH_4-SR maintient l'espèce Pd réduite jusqu'à des concentrations d'O_2 plus élevées qu'avec Pd/Al_2O_3. Finalement, il est montré que la présence de Pd dans le catalyseur est cruciale pour atteindre des taux de conversion acceptables dans des conditions oxydantes, alors que Rh maintient le catalyseur réduit et l'activité élevée, dans des conditions riches.

Enfin, pour mieux comprendre les voies de réaction et les espèces de surface Pd impliquées pendant la réaction, des mesures de spectroscopie de photoémission aux rayons X à pression quasi ambiante (NAP-XPS) ont été effectuées. La composition des gaz d'échappement des moteurs à GN stœchiométriques étant trop complexe pour tirer une conclusion fiable, la composition des gaz a été simplifiée et commutée périodiquement entre CO et O_2 (toutes les 5 minutes). En outre, la résolution temporelle et le rapport signal/bruit (S/N) des mesures NAP-XPS basées sur le synchrotron étaient également trop faibles pour suivre précisément l'évolution des espèces de surface Pd. Par conséquent, le travail décrit au chapitre 7 s'est concentré sur l'amélioration du rapport S/B et de la résolution temporelle des expériences NAP-XPS sur un catalyseur Pd/Al_2O_3 en poudre. Pour ce faire, deux méthodes ont été combinées, l'excitation par modulation (ME) et la détection sensible à la

phase (PSD). La méthode ME a permis d'améliorer le rapport S/N d'un spectre de photoémission tout en limitant la résolution temporelle de la mesure au seul temps d'acquisition d'un spectre. Avec la PSD, sept espèces de Pd ont été identifiées (Pd^0/PdO en vrac, Pd^0/PdO en surface (double et quadruple), CO adsorbé sur la surface de Pd^0, et Pd^{n+} ($n > 2$)) et leur dynamique (consommation/formation) a été suivie le long des interrupteurs de gaz. Les données cinétiques extraites du PSD ont révélé que les espèces Pd^{n+} et PdO double en surface étaient les plus actives pour l'oxydation du CO. De plus, nos résultats, combinés à une analyse approfondie de la littérature, ont montré que la réduction et l'oxydation du PdO suivaient respectivement un modèle de réduction contrôlée par diffusion et un modèle de noyau rétrécissant.

Mots-clés

Oxidation du méthane, Moteur au gaz naturel, Pd/Al_2O_3, $Pd-Rh/Al_2O_3$, O_2 oscillations, Spectroscopie d'absorption des rayons X, Spectroscopie photoémission de rayon X

Acknowledgments

First, I would like to thank Prof. Dr. Oliver Kröcher for his supervision as well as for the trust and freedom he has given me during these past four years of doctoral studies. His scientific expertise, availability, and transparency were always very much appreciated.

I would then like to express my deepest gratitude to Dr. Davide Ferri for co-supervising this thesis. Words are not strong enough to tell you how thankful and lucky I feel about having you as a supervisor. You played a major role in the success of this Ph.D. work, through our exhaustive discussions (scientific but not only), your dedication to being as present and attentive as possible but also your passion for detail and perfection that pushed me to try a little harder and to be a little bit better each time. I admire your endless scientific knowledge, but probably, even more, your ability to listen beyond words.

I would also like to thank Dr. Panayotis Dimopoulos Eggenschwiler, Dr. David Thompsett, and Prof. Dr. Samir Bensaid for kindly accepting to be the co-examiners of this thesis, as well as Prof. Dr. Sandrine Gerber for acting as the jury president.

You will often hear people say that the Ph.D. journey is very lonely. To some level it is, but I had the chance to be surrounded by amazing colleagues, friends, and family. So here comes the exhaustive list of people who have made this journey so special.

I would like to start by giving a special thanks to Christophe Baranowski, with whom it all started. You were and still are someone I look up to and admire. I want to thank you for teaching me so much during my master's project. The freedom and the trust you gave me during these four months helped me gain confidence in my abilities as a young scientist. It is thanks to you that I had the confidence to start a Ph.D. With time you also became a real friend, on who I know I can count on. Thank you.

I am deeply grateful to the two post-doctoral ladies I had the opportunity to work with during my Ph.D. First, Tanja Franken, with whom I greatly enjoyed working with. The few months you spent in the ACS group were very insightful to me. Second, Miren Agote-Aran, who was present during the four years of my Ph.D. Thank you for always being so helpful, for the great scientific, and non-scientific office discussions, for motivating me in the low moments of this journey, and also for encouraging me in the high ones. Together we have had enough ideas for the next 20 Ph.D. students. I wish you all the best for the next chapters of your life, as a mum, and as an outstanding scientist. And please never stop paying attention to the constantly moving world.

I would also like to thank the members of the ACS group. A special thanks go to Filippo Buttignol, my favorite Italian, who was always present for me, both, on a professional and personal level. I will miss our morning coffee breaks but what I will miss the most is seeing you daily. Thank you for caring so much, and being so present. I would also like to thank Thibault Fovanna for making me feel at home on the other side of the Röstigraben, especially during my first moments here. I would like to acknowledge Dominik Wierzbicki for constantly putting things in perspective because at the end of the day "it is what it is", Patrik Steiger who taught me a lot during my first months in the laboratory and who made me feel at ease in the group, Rob Nuguid for his kindness and his incredible availability, Ivo Alxneit for the numerous images he did for me despite the lack of cooperation from the instrument, Federico Cambiè for always having a smile on his face (keep the attitude, the group needs your energy!), Martin Elsener for the running adventures (but mainly for the delicious Christmas cookies), Luca Magiulli, Daniel Blanco, and Illia Kochetygov.

I would also like to deeply thank Vilde Jacobsen who did an amazing job during her master's project. It was very insightful and enjoyable to supervise such a talented person. Along the way, you became a friend, and I am extremely grateful for that. You did bring a lot of sun and sparkles into my life. Thank you, thank you, thank you. I would also like to thank Luis Vivas Barreiro who did an internship with us and had to work under the supervision of not one but two women. You did great.

I would like to thank everyone from the Paul Scherrer Institut who collaborated in one way or another on this Ph.D. work. First, Christopher Hunston for greatly contributing to the after-work sessions, Zhara Pourmand Tehrani, for our short (or not) coffee breaks ETH writing sessions, and more importantly for the moral support, Yanting Qian for her positivity and for being an inspiring woman, and Patrick Zimmerman for the XRD adventures. I would also like to thank, Anthony Boucly, Luca Artiglia, Manoj Ghosalya for their great support and help in the X-ray photoemission spectroscopy studies. And finally, I would like to thank the SuperXAS team, Maarten Nachtegaal, Olga Safonova, Adam Clark, Ilia Sadykov, and of course, Urs Vogelsang.

Now, it is time to thank my friends. Léa, 22 years of friendship between France, Switzerland, Singapore, and now the United States, and yet, we continue growing together. Our monthly (sometimes weekly) calls during the last four years were a breath of fresh air and wise advice. Thank you for always being by my side. I am looking forward to many more years of us. I would like to thank my friends from Lausanne, it has been almost a decade since the day we met on the EPFL benches, time flies. Manon (also known as buldozette), what could I possibly say, you have been family since day one. I guess this says it all. I found myself in you. Thank you for caring, thank you for being so present. Diane, thank you for being you. You are my favourite humourist, travel companion (#vanlife), and person. Thank you for being always so positive, peaceful, loving, and most of all, for always correcting my French expressions (I am now on point). Alice, thank you for being so attentive and affectionate. Thank you for being my number one fan. I admire your combativeness, your strength, and your willingness. Everything will fall into place. Emilie, I am grateful to see that we are still caring, loving, and rooting for each other. Thank you for not letting it go, for your love and attention. Hugo, thank you for the energy you put into organising amazing events and holidays, but mainly for caring about us, from far, but we know you are there making sure everything is fine. I would also like to thank Alexandre for his questionable jokes and good energy, Maxime (brun ténébreux, mysterieux) simply for being part of my life, Maëva for being such an amazing friend, especially during my first years in Switzerland, Cécile and Daniel for being so welcoming each time. It feels like the kind of friendship that will never vanish no matter the time

and the distance. I also want to acknowledge, Lukas, Gauthier, Michael, Gabriele, Alice (rockette), Roxane Miller, Pierre, Eric, and Francesco.

To my Zurich friends, thank you. Fanta, I found a bit of home in you, and this is priceless. I would like to thank the running club, Γεώργιος, Annika, Måns, and Vilde, for all the nice evenings and week-ends (sometimes sporty and sometimes less) we spent together. You guys made the end of my Ph.D. so much more enjoyable. I can't express how happy I am to have you in my life. I would also like to thank Astrid and Michael for the times we spent together in Zurich and the memories at PSI (thank you for the nice office). I would also like to thank the two best roommates, who made the lock-down times easier, Victoria and Marc. Justus, thank you for the endless support and confidence you gave me during these years, you were a pillar. I would also like to thank Théotime, who, probably without even knowing, made my writing times more enjoyable and peaceful.

I would like to finish by thanking my family, who were always present no matter the distance. I have learned throughout the years that home is not just about the place, but about the people. Thank you for being here, always, as well as for the endless support, and advice. Je voudrais aussi remercier les papirettes, les chimites de la famille, et mes plus grands supporters. Comme vous le dites si bien, au début vous n'étiez que deux. I love you all.

"Last but not least, I want to thank me, I want to thank me for believing in me, I want to thank me for doing all this hard work, I want to thank me for having no days off, I want to thank me for never quitting, […] I want to thank me for trying to do more right than wrong, I want to thank me for just being me at all times" - Snoop Dogg, 2018.

Baden, le 22 Septembre 2022

Contents

Contents

"If you find a path with no obstacles, it probably doesn't lead anywhere" ~ Frank A. Clark

Chapter 1   Introduction

1.1 Background

Modern society is highly dependent on energy, and more specifically on fossil fuels (petroleum, coal, and natural gas). While the worldwide energy demand keeps increasing due to the growing population, world economy, and urbanization, fossil fuel resources are depleting, and greenhouse gas emissions are rising. Therefore, the transition of the global energy sector from fossil-based to zero-carbon sources is fundamental to reducing energy-related CO_2 emissions and limiting climate change. However, even if significant progress is being made toward the development and use of renewable energies, we will still be relying on fossil fuels in the near future.

Among fossil fuels, natural gas (NG) emerges as a promising sustainable solution to reduce greenhouse gas emissions since it has the highest energy content (CH_4: 55.7 kJ g^{-1}; Coal: 39.3 kJ g^{-1}; Petroleum: 43.6 kJ g^{-1}) and lowest CO_2 emissions (50 % less than coal and 30 % less than petroleum) of all hydrocarbons [1,2]. NG is formed from layers of organic matter (plants and animals) that decompose under anaerobic conditions (absence of O_2) and are subjected to high temperatures and pressures over millions of years. The issue is that the NG reserves are not equally distributed, making their access dependent on geopolitical issues. Nonetheless, the increasing production of synthetic natural gas (SNG) from power-to-gas technologies and biomass makes CH_4, the main component of NG, available at short distances, and regardless of geopolitical issues [3]. Indeed, solid biomass and coal can be converted to SNG using thermochemical processes (ca. 65 % chemical efficiency is achieved from wood) [4,5], while bio-methane can be produced from wet biomass (i.e. manure, crops, sewage sludge) by anaerobic digestion (overall chemical efficiency: 20 to 40 %) [6–8] or hydrothermal gasification processes (supercritical water, T > 375 °C and p > 220 bar) [9–11]. The hydrothermal gasification of wet biomass is currently being studied and developed in several research institutes such as the Paul Scherrer Institut

(Switzerland) [9–11] and the Forschungszentrum Karlsruhe (Germany) [12–14]. It should, however, be mentioned that biomass is limited and can only cover 10 to 20 % of the total energy demand. The gasification steps are followed by a catalysed methanation (CO_2 to CH_4) step and a cleaning step to remove water, and H_2S.

Hence, if in the future CH_4 is predominantly produced from these alternative routes, it will be considered a carbon-neutral fuel, and therefore be a sustainable replacement for other fossil fuels.

Natural gas can be used as a fuel for many applications such as for transportation [15–20], electricity generation using gas turbines or steam generators [21–26], solid oxide fuel cells [27], domestic heating [28–31], and coupling with endothermic reactions [32–37]. However, because CH_4 is a severe greenhouse gas (global warming potential of 21 to 28 based on a 100-year period [38]), and the transportation sector is responsible for about 20 percent of global air emissions [39], special attention needs to be given to the removal of CH_4 from the exhaust of all related applications.

1.2 Emissions of internal combustion engines

Internal combustion engines (ICE) produce significant amounts of pollutants that need to be abated. These include carbon monoxide (CO), unburnt hydrocarbons (UHC; including CH_4), and nitrogen oxides (NO_x; mainly NO and NO_2). The emission of these pollutants depends on the air-to-fuel (A/F) ratio used in the ICE (Figure 1.1) [40–42]. The A/F ratio is the mass ratio of air to a solid, liquid, or gaseous fuel present in a combustion process (Equation 1.1). For example, the A/F ratio of methane is 17.19:1. The A/F ratio determines if the mixture is combustible and gives information on the amount of energy released, and emissions produced during the combustion. However, since the composition of fuels can vary, and many modern vehicles can handle different fuels, it is easier to consider the air-fuel equivalent ratio (λ, lambda), which is the ratio between the dosed A/F ratio and the stoichiometric A/F ratio. Hence, when exactly enough air is fed to the combustion chamber to completely burn all the fuel (i.e. 17.19 kg of air for 1 kg CH_4), the λ ratio is defined as $\lambda = 1$. At λ below 1, the engine operates under rich conditions, leading to high CO and UHC emissions (Figure 1.1). NO_x

emissions instead are higher under slightly lean conditions ($\lambda > 1$) due to higher engine temperatures but are significantly reduced when the engine operates under very lean conditions. At high λ, UHC emissions increase due to misfiring [43].

Air-to-fuel ratio = A/F ratio = air mass for 1 kg of fuel   Equation 1.1
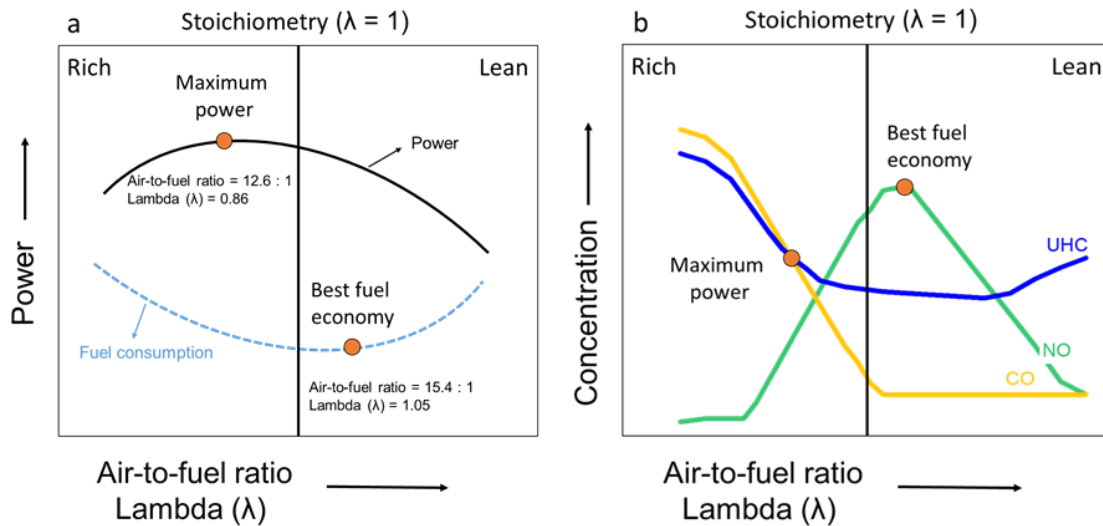
Figure 1.1. Effect of the air-to-fuel ratio on (a) ICE operation (performance and fuel economy) and (b) ICE emissions.

The type of internal combustion engine used depends on the physical and chemical properties of the fuel (flash point, ignition temperature, mixture preparation, etc.). Because the lowest liquid temperature at which diesel gives off vapours in quantities that can form an ignitable vapour/air mixture (cf. flash point) is higher than gasoline (> 52 °C, < - 43 °C, respectively), the ICE is different for diesel and gasoline fuels. In diesel engines (or compression-ignition engines), the ignition of the fuel is caused by mixing the fuel with compressed air of high temperature and pressure. Hence, diesel is injected into the combustion chamber toward the end of the compression stroke. Therefore, the fuel combusts immediately before it has time to spread throughout the available air. The issue is that if the fuel burns with insufficient oxygen, soot is formed during the combustion. Hence, diesel engines are run lean (excess of O_2) to limit soot formation and to achieve high fuel efficiency. Spark ignition engines (or gasoline engines), on the other hand, rely on the low flash point of gasoline and methane, and the ignition is initiated by an electric spark. In gasoline engines, the fuel and air are mixed and

injected before it is ignited. Hence it has time to mix homogeneously. Spark ignition engines require to operate close to stoichiometric or even under slightly rich conditions.

Lambda value definitions

The lambda value can be used either to back-calculate the actual A/F ratio of the engine (A/F ratio = A/F$_{stoich}$ x λ) or to evaluate emissions arising from the combustion process for domestic and international inspection and maintenance programs.

In the former case, it can be determined using exhaust gas oxygen (EGO) sensors, also called lambda sensors. These sensors are placed after the engine and measure the oxygen concentration present in the exhaust gas feed of the engine, and can be used in closed-loop as feedback sensors to help the engine control unit to adjust the air-fuel ratio accurately to achieve stoichiometry (in the case of gasoline engines).

In the latter case, Brettschneider developed an equation to calculate the normalized air-fuel balance of the exhaust treatment systems reliably [44,45]. The method consists in comparing the ratio of oxygen molecules to carbon and hydrogen molecules in the exhaust (Equation 1.2).

$$\lambda = \frac{[CO_2] + \left[\frac{CO}{2}\right] + [O_2] + \left[\frac{NO}{2}\right] + \left(\left(\frac{H_{CV}}{4} \frac{3.5}{3.5 + \frac{[CO]}{[CO_2]}}\right) - \frac{O_{CV}}{2}\right)([CO_2] + [CO])}{\left(1 + \frac{H_{CV}}{4} - \frac{O_{CV}}{2}\right)([CO_2] + [CO] + (n[HC])}$$

Equation 1.2

where H_{CV} is the atomic ratio of hydrogen to carbon in the fuel, O_{CV} is the atomic ratio of oxygen to carbon in the fuel, and n is the number of carbon atoms in a molecule of the selected hydrocarbon.

The initial Brettschneider λ equation contains an empirical estimation for the O atoms in H_2O. With the FTIR and mass spectrometer measurements available, the empirical H_2O considerations can be replaced by the H_2O concentration calculated from H_2 and NH_3 concentrations. The modified λ equation can be rewritten as shown in Equation 1.3.

$$\lambda = \frac{[CO_2] + \left[\frac{CO}{2}\right] + [O_2] + \left[\frac{NO}{2}\right] + (H_{CV} \, ([CO_2] + [CO]) - 3[NH_3] - 2H_2)/4}{\left(1 + \frac{H_{CV}}{4} - \frac{O_{CV}}{2}\right) ([CO_2] + [CO] + (n[HC]))}$$

Equation 1.3

Hence, when discussing the lambda value of TWCs, the definition refers to the Brettschneider definition, whereas when discussing the lambda value of the ICEs, the definition relates to the A/F ratio.

1.3 Emission control strategies

It is only after the establishment of the US Clean Air Act in 1970 which established air quality standards for six major pollutants (hydrocarbons, carbon monoxide, nitrous oxides, particulate matter, sulphur oxides, and photochemical oxidants) [46,47], that measures to reduce emissions were taken. The first catalytic emission control technology was developed by Johnson Matthey in 1971 and consisted of a platinum-rhodium two-way catalyst, which aimed at converting CO and UHC [46,48,49]. In the 1980s, the emission regulations were tightened, leading to further improvement of the catalytic after-treatment systems [40,46,50]. Two different technology paths were developed based on the air-to-fuel ratio used in the engines: stoichiometric or lean-burn conditions [19,51].

For stoichiometric engines, a dual-layer three-way catalyst (TWC) technology consisting of precious metals deposited on ceria and alumina was exploited [40,52]. It comprised a first catalyst layer operated under slightly rich conditions to reduce the NO_x emissions, followed by a second layer operated under slightly lean conditions to oxidize CO and UHC, by using secondary air injected between the beds. The development of precise oxygen sensors (EGO) [53,54], allowed the use of a single-bed TWC operated under stoichiometric conditions (λ = 0.99 – 1.01) and enabled the simultaneous reduction of NO_x and oxidation of CO and UHC [40,55]. However, since hydrocarbons and CO are oxidized mainly under lean conditions (λ > 1) and NO_x reduces to N_2 preferentially under rich conditions (λ < 1), only a narrow operating window around stoichiometry allows for efficient emission control (Figure 1.2a). Nowadays, single-bed TWC technologies are used in stoichiometric gasoline and compressed natural gas (CNG) engines. The commercial TWCs consist of noble metals supported

on alumina and/or ceria-based materials. However, because of the low reactivity of CH_4 [56], the point of optimal CH_4 conversion for the operation of the TWC does not stand at $\lambda = 1$ but needs to be slightly rich to achieve abatement of CH_4, CO, and NO (Figure 1.2b) [57–59].
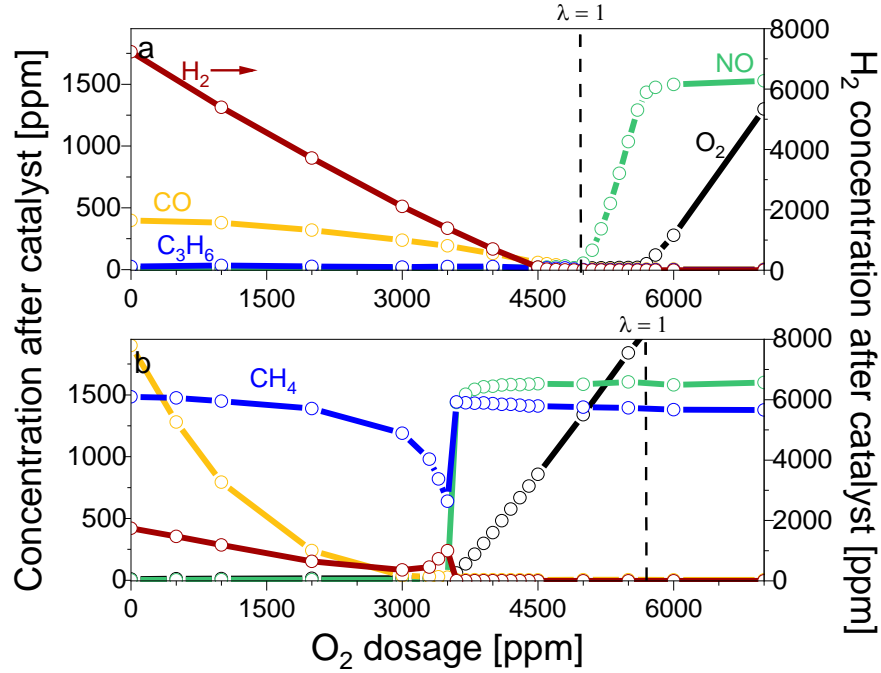
Figure 1.2. Figure adapted from [59]. Concentrations of CO, NO, C_3H_6, CH_4, and O_2 after catalyst at 425 °C in a continuous feed of (a) 7000 ppm CO, 1600 ppm NO, 500 ppm C_3H_6, 5 vol% H_2O and (b) 7000 ppm CO, 1600 ppm NO, 1500 ppm CH_4, 5 vol% H_2O while decreasing the O_2 concentration from 7000 to 0 ppm. The vertical dash lines mark the position for stoichiometry.

Lean-burn engines allow to achieve higher fuel efficiency and lower UHC emissions compared to stoichiometric engines (Figure 1.1) [20]. The issue is that NO_x reduction is difficult when operating under lean conditions [48]. Hence, a multiple-bed catalytic system is required to abate emissions from the lean-burn engine exhaust feed [20]. The technology comprises a methane oxidation catalyst (MOC) and a lean NO_x abatement catalyst. MOCs consist of supported precious metals and operate at lower temperatures (up to 800 °C) than TWCs (up to 1000 °C) since the higher air-to-fuel ratio decreases the combustion temperature. Lean NO_x abatement catalysts consist either of a lean NO_x trap (LNT) or selective catalytic reduction (SCR) by ammonia (NH_3-SCR) [52,60]. LNT catalysts store NO_x on a barium-promoted precious metal catalyst, and the stored

NO_x is then reduced either by a short switch of the engine to rich conditions or by direct fuel injection in the exhaust system [48]. The SCR systems are based on Cu and Fe exchanged zeolite catalysts (i.e. Fe-MFI, Cu-BEA, and Cu-SSZ-13) [61,62] and convert NO_x, using an external reductant (typically NH_3).

TWCs for NGVs applications

The catalytic abatement of CH_4 is more difficult than longer hydrocarbons [63] due to its intrinsic properties (strong hydrogen-carbon bonds, high molecule symmetry, weak adsorption strength [56,63]), the low exhaust temperatures (below 500°C in the case of lean burn engines) [64,65], and the complex reaction pool (Table 1.1). Moreover, CH_4 as well as the other components present in the exhaust feed of NG engines affect the activity toward CH_4 oxidation. Indeed, the presence of CH_4 and CO shifts the optimal lambda value for CH_4 oxidation to net reducing conditions, [15,66] due to the high stability of CH_4 and the competitive oxidation between CO and CH_4 for the same or similar reaction sites [66]. It was also observed that under dry conditions, CH_4 conversion experienced a delay in the presence of CO as a result of the stronger interaction of CO with Pd nanoparticles compared to CH_4, which dominates the surface chemistry [66,67]. The presence of NO was observed to inhibit both CO and CH_4 oxidation under dry conditions due to site blocking effects [67–71]. Finally, CH_4 and NO conversions appear to be correlated under rich conditions [57,59,72], whereas they are not under lean and stoichiometric conditions [57,59], where NO and CO were reported to inhibit CH_4 oxidation [59,66,67].

Table 1.1. Reactions involved during CH_4 abatement from exhaust gas feed of natural gas vehicles

Oxidation reactions	Reforming reactions	NO_x related reactions
$CH_4 + 2O_2 \rightarrow CO_2 + 2H_2O$	$CO + H_2O \rightarrow CO_2 + H_2$	$CO + NO \rightarrow CO_2 + 0.5N_2$
(Equation 1.4)	(Equation 1.7)	(Equation 1.9)
$CO + 0.5O_2 \rightarrow CO_2$	$CH_4 + H_2O \rightarrow CO + 3H_2$	$CO + 2NO \rightarrow CO_2 + N_2O$
(Equation 1.5)	(Equation 1.8)	(Equation 1.10)
$H_2 + 0.5O_2 \rightarrow H_2O$		$N_2O \rightarrow NO + 0.5N_2$
(Equation 1.6)		(Equation 1.11)
		$NO + 2.5H_2 \rightarrow NH_3 + H_2O$
		(Equation 1.12)
		$NO + H_2 \rightarrow H_2O + 0.5N_2$
		(Equation 1.13)
		$NH_3 + 1.5NO \rightarrow 2.5\,N_2 + 1.5\,H_2O$
		(Equation 1.14)
		$CH_4 + 4NO \rightarrow CO_2 + 2N_2 + 2H_2O$
		(Equation 1.15)

1.3.1 Catalyst formulation and development

Commercial TWCs consist of noble metals (i.e. Pd, Pt, Rh) supported on alumina and/or ceria-based materials which are deposited on a ceramic core substrate (usually cordierite monoliths with a honeycomb structure) to provide mechanical strength and increase the surface area and dispersion of the active material. Extensive work has been devoted to the development of non-noble metals TWCs due to the high costs and low availability of noble metals. However, non-noble metals are not efficient for CH_4 abatement and are easily prone to chemical and thermal deactivation.

Among noble metals (platinum group metals, PGMs), ruthenium (Ru) and iridium (Ir) oxides were reported to be volatile at high temperatures, leading to extensive metal loss during operation [73–75]. Platinum (Pt), rhodium (Rh), and palladium (Pd) on the other hand stay in their metallic form in a wide range of operating conditions, and their oxide forms are far less volatile. Nowadays, commercial TWCs are mainly composed of Pd with small amounts of Rh and Pt. Even if both Pd and Pt efficiently oxidize H_2, CH_4, and CO, Pd possesses

higher hydrothermal resistance than Pt and exhibits higher activity toward CH_4 oxidation while Pt is more resistant to sulphur and water poisoning. Rh, on the other hand, promotes NO reduction to N_2 [76] and is more active than Pd for steam reforming (SR) [77,78].

γ-Al_2O_3 is usually used as a support for noble metals due to its high SSA, thermal stability, low chemical activity, mechanical strength, and cost. Because the driving conditions (i.e. acceleration, deceleration, fuel cut, etc.) can lead to broad λ working windows even if lambda sensors are set upstream and downstream of the TWCs to ensure stoichiometric conditions, oxygen storage components (OSC) need to be added to the catalyst formulation to buffer the variations of oxygen concentration from the exhaust feed and therefore narrow the working λ window. Ceria-based materials usually act as OSC components due to the ability of Ceria to store and release oxygen is related to the facile and reversible conversion between Ce^{4+} and Ce^{3+} states and to the creation of replenishable oxygen vacancies (VO) [79,79–83].

Catalyst deactivation

TWCs are prone to thermal aging, water and/or chemical poisoning [84–87]. Chemical poisoning of the catalyst by sulphur will be disregarded in this thesis, since in the future if CH_4 is produced only from syngas or biogas, the sulphur content in the fuel should be negligible.

Thermal-induced deactivation of the catalyst is related to the loss of active surface from structural modifications of the catalyst. The alumina support experiences phase transformation at high temperatures from high surface area γ-Al_2O_3 to lower surface area δ-Al_2O_3 and even α-Al_2O_3 [88]. It is common to add additives such as La_2O_3, BaO, CeO_2 SiO_2, or ZrO_2 to the alumina support to improve its thermal stability [89–91]. Moreover, the thermal stability of CeO_2 is also low, leading to important sintering of the material and subsequent decrease of the OSC. The addition of Zr^{4+} to partly replace Ce^{4+} can improve both the OSC and the thermal stability of the material, but sintering and phase segregation can still occur when the catalyst is exposed to high temperatures for long periods [92–110]. Furthermore, at high temperatures, the active metals are prone to sintering

which decreases the surface-to-volume ratio of the nanoparticles. High temperatures also induce PdO decomposition to Pd^0, which is recognized to be less active for direct CH_4 oxidation by O_2 [111–114] and also facilitates the diffusion of Rh in the Al_2O_3 support [115,116].

The inhibitory effect of water, which is a product of CH_4 combustion is caused by the formation of hydroxylated surface species on the support as well as less active $Pd(OH)_2$ [117–123]. Moreover, oxidation of Pd to PdO is reported to proceed via PdO_x species, which tend to hydroxylate in the presence of water, resulting in improved stability of PdO [118], which has been demonstrated to be less active for high CH_4 oxidation than PdO_x [124–127]. The formation of Pd-OH species can be formed during the oxidation of CH_4, as the mechanism of CH_4 oxidation on coordinatively unsaturated Pd was proposed to occur by adsorption of CH_4 on Pd sites and C-H bond breaking on adjacent Pd-O sites with the formation of Pd-OH species [124]. Recombination of the OH groups is possible and leads to water formation and desorption. Furthermore, since the adsorption of water is disfavoured at high temperatures (> 450 °C) [84], the deactivation of the Pd-based catalysts by water is more pronounced at low temperatures. Finally, the presence of water is also known to inhibit the oxygen exchange between the Pd particles and the reducible supports (i.e. CeO_2) [74,122,128].

Catalyst development for reduced aging effects

Over the years, many research groups have been working towards the development of deactivation-resistant catalysts.

Geometrical barriers can be applied to limit the sintering of the support, and/or active metal. For example, Pd nanoparticles encapsulated in the support show remarkable activity and stability for CH_4 oxidation due to higher metal dispersion provided by the shells [57,73–75]. However, the hierarchical $Pd@CeO_2/Si-Al_2O_3$ catalyst was shown to deactivate reversibly at low temperatures in the presence of water, while at high temperatures (600 °C), irreversible deactivation of the core-shell structure was observed due to hydroxylation of the CeO_2 shell, which hindered the accessibility to the active phase [74]. Hence, the results demonstrated that Pd encapsulation is not beneficial when reducible promoters are used [74]. On the other hand, $Pd@ZrO_2$-based catalysts prepared with the same method showed improved resistance to water while preserving high thermal

stability [73]. This observation was ascribed to the lower affinity of ZrO_2 to water compared to CeO_2, confirming that reducible supports are not beneficial to mitigate the detrimental effect of water on the catalytic activity. Finally, stabilization of the PdO particles against sintering and decomposition to Pd^0 at high temperatures can be achieved by strengthening the interactions between the reducible support and the Pd active sites [129–132]. For example, CeO_2 is known to be very effective for Pd reoxidation, due to the high oxygen mobility in the CeO_2 [133].

The detrimental effect of water on the catalytic activity and stability can be mitigated by using hydrophobic materials such as zeolites with high silicon to aluminium (Si/Al) ratios (i.e. Pd/ZSM-5, Pd/beta) [134–136]. Nonetheless, the high acidity of zeolites enhances the mobility of palladium over the support under reaction conditions [86]. To overcome this issue and improve zeolite stability [86,137], the palladium nanoparticles were confined in the zeolite pores after the complete removal of the acid sites of the zeolites by post-exchange with sodium [138]. Nonetheless, the main limitation of zeolites is their insufficient thermal stability, which limits their applicability for stoichiometric NG vehicles, which operate at higher temperatures than lean-burn NG engines. Therefore, supports with even lower acidity, higher hydrophobicity, and higher hydrothermal stability than zeolites were also studied for the stabilization of palladium nanoparticles under reactive conditions. Pd/SnO_2, showed significantly less $Pd(OH)_2$ formation compared to Pd/Al_2O_3, due to the higher water tolerance of SnO_2 [139]. Indeed, it was demonstrated using simplified bulk thermodynamic analysis that SnO_2 can serve as a sink for hydroxyls extracted from $Pd(OH)_2$, while $Al(OH)_3$ can provide hydroxyls to Pd. Pd supported on an irreducible oxide support, $MgAl_2O_4$, leads to significant improvement of the activity and stability of the catalyst against both hydrothermal aging at elevated temperatures and long-term deactivation in the presence of water vapour [140]. Finally, water inhibition can also be alleviated by adding Pt to Pd-based materials [141–146].

Optimization of the catalyst formulation to mitigate simultaneously thermal ageing and resistance to water poisoning is challenging, as each deactivation process requires different and sometimes contradictory strategies.

1.3.2   Periodic operation

Besides material science developments aimed at optimizing deactivation-resistant catalysts [147–149], it is possible to improve the pollutant abatement rates as well as to mitigate the possible deactivation processes by moving away from static operation (steady-state supply of all the reactants) and working under periodic conditions instead.

What is a periodic operation?

Periodic, cycling, transient operation, or even modulation excitation are similar terminologies that refer to an operation in which one or more of the inputs such as temperature, reactant concentration, and pressure, is periodically varied. In this thesis, we only performed intentional oscillations of the O_2 concentration from the exhaust gas feed.

It can be argued that the term periodic operation should only refer to working conditions that provide catalytic performance that is either difficult or impossible to achieve under static operation [150]. However, we consider that periodic regeneration of the catalytic activity can also be considered a form of transient operation, provided that the pulsing period is not too long (below one day).

Different types of oscillations can be performed depending on the aim of the study. The pulses can be symmetric and applied either at high frequencies to improve the catalytic activity (i.e. three-way catalyst applications [57,59,151]) or at low frequencies to carry out kinetic or mechanistic studies [67,152]. The perturbations can also be asymmetric to periodically regenerate the catalyst [138,153] or can consist of a single pulse, which is also defined as the relaxation time of the system and is usually performed to characterize a system [154,155]. In this thesis, we performed symmetric and asymmetric O_2 oscillations, as well as symmetric modulations between CO and O_2 (low frequency).

It is relevant to question the necessity and applicability of periodic operation as it is often more complicated and expensive to achieve than static operation. Therefore, even if working under transient conditions can improve the catalytic activity, it might, in some cases, be cheaper to change the size of the reactor or the amount of catalyst used. Nonetheless, for catalytic exhaust after-treatment systems used to treat the exhaust of NGVs, the size of the catalytic systems cannot be increased due to space and weight limitations, while the catalyst is too expensive to increase its loading as it contains precious metals. Hence, the use of periodic operation to improve the catalytic activity and mitigate the deactivation processes is relevant for NG engine applications.

Background on periodic operation for TWCs

For automotive applications, the effect of periodic operation was first investigated at engine test rigs when trying to mimic the real conditions experienced by the catalyst while driving [156]. Indeed, to maintain the A/F ratio close to the stoichiometry, a sensing device measures the oxygen partial pressure in the exhaust feed and the signal is used to monitor the control unit which adapts the A/F ratio accordingly. Hence, the instantaneous A/F ratio varies periodically between lean and rich conditions [156]. Studies carried out using the exhaust feed composition of gasoline engines demonstrated that the pollutant conversions achieved during cyclic operation varied greatly with changes in A/F cycling frequency and that important pollutant slips were achieved when too rich conditions were reached (cf. high amplitudes or low frequencies) [157,158]. Therefore, it became clear that to minimize the emissions from TWCs, an in-depth understanding of the dynamic behaviour of the catalysts during the A/F fluctuations was required.

In parallel, periodic operation was tested for CO oxidation on Pt/Al_2O_3 [158–160]. The studies showed that below the light-off temperature of CO oxidation, significant improvement of the catalytic activity was achieved compared to static operation [160], whereas above the light-off temperature of CO oxidation, static operation was preferred [158–160]. When working with more realistic engine exhaust feeds (NO, CO, HC), on Pt/Al_2O_3, similar observations as for CO oxidation were made [159]. It was also mentioned that under transient conditions, the beneficial effect of the pulses was only noticeable at low frequencies (below 1 Hz). This effect was attributed to the fact that at high frequencies, the fluctuations applied in the engine exhaust composition are

diluted and therefore the operating conditions remain very close to the conditions obtained during static operation.

Many studies were then carried out to investigate how modulation of the A/F ratio (amplitude and frequency) affected the performance of TWCs used for gasoline engines [83,161–165]. Schlatter et a1. [166] showed on a Pt-Rh TWC, that CO and NO conversions decreased compared to static operation when modulation of the A/F ratio was performed around stoichiometry but increased when modulation was applied at slightly rich conditions. Moreover, the presence of CeO_2 improved the activity under periodic operation, but not when the A/F ratio was maintained around stoichiometry [166]. Muraki et al. [83] found that periodic changes of the A/F ratio improved NO and HC conversions at frequencies between 0.5 and 0.3 Hz on a Pt-TWC, 1 and 3 Hz on a Pd-TWC, and above 2 Hz on a Rh-TWC. They also stated that increasing the pulsing amplitude had a detrimental effect on the catalytic activity.

1.3.2.1 Periodic lean/rich O_2 pulses

More recently, the beneficial effect of periodic lean/rich O_2 pulses (O_2-dithering) around stoichiometry was proven on commercial TWCs for stoichiometric NG engines [57,72,151,159,167–173]. The amplitude and frequency of the O_2 pulses greatly affected the catalytic activity, as well as the by-product formation (i.e. H_2, N_2O, NH_3) [167,174]. It was also shown that the amplitude of the O_2 pulses was more crucial than their frequency and that the lambda window was significantly broadened at high dithering amplitudes [57,169]. Gong et al. [6] used the O_2 dosage as an effective descriptor of the TWC performance, demonstrating that high dithering amplitudes were required to obtain high CH_4 and NO conversion. The positive effect of O_2-dithering vanished when the O_2 dosage was either too low to be compensated by the oxygen storage capacity (OSC) of the catalyst, inducing both CO slip and NH_3 formation, or in excess, leading to NO and CH_4 slips. The beneficial effect of O_2-dithering on CH_4 conversion was also proven on an engine test rig, thus corroborating the value of this type of operation for improved control of emissions [167].

Pd redox behaviour during periodic operation

The recent studies mentioned above point toward the idea that the activity achieved under periodic operation is strongly related to the catalyst oxidation state. It is known that the activity for CH_4 oxidation is closely related to the Pd oxidation state (Pd^0, PdO, mixed Pd^0/PdO) [167] as well as its surface structures (metallic Pd, chemisorbed O_2 layer around Pd^0, bulk PdO, etc.) [175,176]. Even though studies have shown that Pd^0, PdO, and mixed Pd^0/PdO (PdO_x) species are active for CH_4 oxidation [64,177–182], it is clear that not all species induce the same chemistry and activity. Chin. et al. [182] found that PdO_x species exhibit the lowest activation energy for the C-H bond cleavage, and are therefore the most active species for direct CH_4 oxidation by O_2 despite the strong dependence of the activity on the Pd^0/PdO ratio. Recently, our group demonstrated a remarkable improvement in the activity and long-term stability of a zeolite-supported Pd catalyst using repeated short O_2 cut-offs for wet lean CH_4 oxidation [183] which was related to the repetitive formation of highly active PdO_x species consisting of an amorphous PdO_x layer on small Pd particles. Similar pulses were performed over Al_2O_3 and $Ce_{1-x}Zr_xO_2$ supported Pd-Pt catalysts for wet lean CH_4 oxidation applications, which consisted of periodically adding H_2 to the reaction mixture instead of removing the O_2 present in the feed. Through this approach, the catalyst activity was maintained over long periods by the repeated reducing pulses [153]. However, despite the very similar approach, at first sight, the selected reduction environment influences the properties of metallic Pd. Reduction with H_2 occurs at low temperatures and follows a shrinking core mechanism [175,176] resulting in fewer defective nanoparticle surfaces. On the contrary, reduction with CH_4 occurs at high temperatures while an induction period takes place before the full reduction of Pd. Previous studies show that during this induction period Pd particles segregate from the PdO surface [176] resulting in roughened surfaces [175]; hence, reduction with CH_4 is expected to increase the surface area of the resulting PdO obtained upon re-oxidation.

Hence, to optimize both the working conditions and the material formulation for improved CH_4 oxidation, catalytic and spectroscopic studies need to be performed simultaneously to evaluate the effect of periodic operation not only on the activity but also on the Pd redox behaviour.

1.3.2.2 Modulation excitation and phase-sensitive detection

As mentioned previously, different types of pulses can be applied depending on the aim of the study. While pulses can be applied to improve the catalytic activity, it is also possible to carry out kinetic or mechanistic studies when working under periodic operation. Usually, these pulses do not represent realistic conditions and are of high amplitude and low frequency.

Indeed, a common approach is the modulation excitation (ME) method which consists of applying an external perturbation to the system (i.e. optical, pressure, or chemical modification) to force it away from its equilibrium state. The perturbation is usually chosen such that the species of interest (i.e. catalytically active species) will respond selectively, if not exclusively to the perturbation. Once the perturbation is applied, the system can change either back to its previous equilibrium state (reversible process) or a new equilibrium (non-reversible process). In the case of an irreversible system, the perturbation can be applied once and the response can be followed over time (relaxation technique [154,155]) while if the system is reversible, the stimulation can be performed repeatedly in a periodic manner (ME technique [184–187]). The dynamic changes during perturbation can be followed using any time-resolved technique (i.e. Infrared spectroscopy [187–191], X-ray diffraction spectroscopy [67], X-ray absorption spectroscopy [186,192–194], X-ray photoelectron spectroscopy [195–201]).

In the case of a reversible system, the perturbation can be applied repeatedly in a periodic manner, and the spectra can be averaged into one period (A(t)) [195]. Usually, the system evolves over the first cycles before reaching a so-called quasi steady-state, which requires the initial cycles to be discarded from the analysis. By averaging the data into one period, the size of the dataset decreases, and the S/N ratio is improved by the square root of the number of averaged cycles ($\sqrt{N}$, Poisson statistics) [202].

The averaged spectra obtained from ME experiments are a result of the sum of three components, A(t) = B(t) + C(t) + D(t), where B(t) is the active species response, C(t) is the spectator species response (or background species), and D(t) is the noise. Since the spectral lines of all three components contribute to the time domain spectra, it is difficult to distinguish between the features arising from the active and spectator species.

Moreover, the spectral features arising from the active species are usually small and therefore difficult to distinguish. Hence, to improve the sensitivity toward the active species, a mathematical treatment can be applied to the averaged spectra (A(t)). This method is called phase-sensitive detection (PSD) or demodulation (Equation 1.16) [202,203].

PSD converts the time domain response A(t) to a phase domain response $A(\varphi^{PSD})$ wherein the signal from the active species affected by the perturbation remains, whereas the signal from the spectator species and the noise (unaffected by the perturbation) is suppressed. Hence, PSD allows for significant improvement of the S/N ratio of the active species response. Moreover, the dynamics (rate of consumption and formation) of the active species can be determined more accurately from the phase domain than from the time domain, therefore allowing to perform kinetic analysis of the system.

$$A_k^{\phi^{PSD}}(e) = \frac{2}{T}\int_0^T A(e,t)\, \sin(k\omega t\, +\, \phi_k^{PSD})\, dt \qquad\qquad \text{Equation 1.16}$$

where $A_k^{\phi^{PSD}}$ is the signal in the phase domain, T is the modulation period, k is the demodulation index, ω is the stimulation frequency, and ϕ_k^{PSD} is the phase angle.

MES and PSD have already been used to gain knowledge on the chemistry of CH_4 oxidation. The inhibition effect of CO on CH_4 oxidation under dry conditions was demonstrated on a Pd/Al_2O_3 by performing operando time-resolved XRD, XAS, and IR [67], and was attributed to the strong interaction between the CO molecules and the Pd nanoparticles which block the surface Pd sites for CH_4 oxidation to proceed. The experiments consisted of O_2 pulses of 60 s added to a constant CH_4 or CH_4/CO feed. Hence, even if these periodic pulses do not reflect realistic working conditions, they revealed that Pd reoxidation upon O_2 introduction in the feed occurred in two steps, formation of a fast amorphous Pd oxide phase on the surface, followed by slower reordering of the PdO phase. On the other hand, Pd reduction was observed to be very fast but slower than the first reoxidation step. Moreover, the effect of the O_2 concentration on CH_4 oxidation was investigated by performing periodic lean/rich cycles of 360 s while measuring XAS spectra [114,204]. The experiments demonstrated that over a Pd/Al_2O_3, reduced Pd sites or mixed Pd/PdO sites display the highest activity for methane oxidation.

It was also shown that when the lean periods are operated close to stoichiometry, the reoxidation of the Pd species is limited due to the formation of a chemisorbed oxygen layer or surface oxides on the Pd surface, leading to lower CH_4 conversion levels. When leaner conditions are applied, the Pd species oxidize to a higher extent leading to higher conversions. Over Pd/CeO_2, the Pd species reoxidized faster after the rich periods allowing to mitigate the detrimental effect of the surface oxide species formed during reoxidation (10 min modulation cycles) [204].

1.4 Scope of the thesis

This thesis work aimed at gaining knowledge on the catalytic structure/activity relationship of Pd-based catalysts to enhance CH_4 removal from the exhaust feed of natural gas engines.

The catalytic removal of CH_4 can be improved through material development and/or optimization of the operating conditions. Nonetheless, these two approaches are complementary since not all catalytic properties and requirements (i.e. redox behavior/dynamics, selectivity, reaction pathways, by-products, etc.) can be fulfilled using only one of the two strategies.

We decided to start by proposing an optimal pulsing protocol based on the operating conditions (i.e. temperature, reactant concentration, lambda value, etc.), for a simple Pd/Al_2O_3 catalyst. The development of a reliable pulsing protocol can only be achieved through an in-depth understanding of the catalytic structure/activity relationship. The results obtained then served to modify the catalyst formulation to improve specific properties that could not be modified through periodic O_2 pulses.

In order to fine-tune the operating conditions and the material composition, it is crucial to gain extensive knowledge of the Pd species responsible for improved catalytic activity and stability under relevant working conditions. This is achieved by performing operando spectroscopic measurements (i.e. X-ray absorption spectroscopy, X-ray photoemission spectroscopy, Infrared spectroscopy, etc.). However, these techniques need to have a high signal-to-noise (S/N) ratio and time resolution, to follow the evolution of the active species whose concentrations are often small and lifetime limited. Surface-sensitive techniques, such as ambient pressure X-

ray photoemission spectroscopy (NAP-XPS), are essential in heterogeneous catalysis since the reactions take place at the interface between the gas phase and the surface of the nanoparticles. Nonetheless, the time resolution and S/N ratio of NAP-XPS measurements are low, especially when working under realistic conditions (i.e. low metal loading, diluted gas compositions, etc.). Hence, we aimed at mitigating both shortcomings by combining NAP-XPS measurements with modulation excitation and phase-sensitive detection methods.

Chapter 2 Experimental

2.1 Catalyst synthesis

Various catalysts were used in this project, which were either synthesized in the laboratory or commercial samples. Therefore, the synthesis methods as well as post-synthesis treatments are described in the corresponding chapters.

2.2 Catalytic tests

The catalytic tests were performed in a quartz plug-flow reactor (ID = 6 mm) loaded with the sieved catalyst (50 mg; 150 - 200 µm) mixed with sieved cordierite (100 - 150 µm) in a 1:3 ratio. The sample temperature was measured by placing a thermocouple in the middle of the catalyst bed. Since the catalytic bed is small (1.5 cm), we are measuring the actual temperature of the catalyst and the effect of the exothermic and endothermic reactions are already considered. The gas mixing setup was identical to that used for the operando XAS measurements. The outlet stream composition was analysed using an FTIR spectrometer (Alpha II, Bruker) and a mass spectrometer (MS; InProcess GAM400). The time resolution of the MS and FTIR instruments were 0.5 ms and 30 s, respectively.

Prior to the catalytic tests, the catalyst was exposed to a flow of 1500 ppm CH_4 and 3000 ppm O_2 (balance Ar) at a weight hourly space velocity (WHSV) of 240 $Lh^{-1}g^{-1}$ to ensure comparable measurements with an identical initial state of the catalyst. The temperature was increased from 200 to 600 °C (10 °Cmin^{-1}) and kept at this temperature for 30 min before cooling to the desired temperature and changing to the desired feed. This pre-treatment is referred to as oxidative pre-treatment in Chapter 6. If a reductive pre-treatment was applied, the flow was changed at 600 °C from 1500 ppm CH_4 and 3000 ppm O_2 (balance Ar, WHSV = 240 $Lh^{-1}g^{-1}$) to

2000 ppm H_2 in Ar (WHSV = 240 $Lh^{-1}g^{-1}$) and maintained for 5 min before cooling to the desired temperature and changing the gas flow. The temperature ramps were recorded using a heating/cooling ramp of 5 $°Cmin^{-1}$. The temperature ramps were recorded using a heating/cooling rate of 5 $°Cmin^{-1}$. The short reducing pulses (SRP) experiments were performed by cutting off O_2 for 3 s every 5 min, thus pulses occurred every ca. 25 °C during the temperature ramps (Figure 2.1).
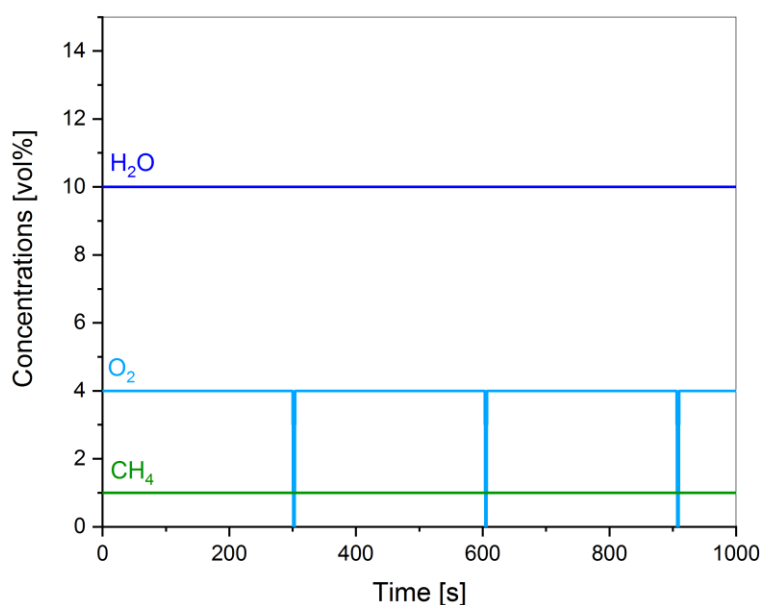
Figure 2.1. Pulse sequence conducted for operation under short reduction pulse (SRP) mode.

The oxygen balance of the reactive mixture was calculated using Equation 2.1, while the lambda value was calculated using the empirical definition which was modified to reflect the absence of H_2 and NH_3 in the feed [44] (Equation 2.2).

$$\text{oxygen balance} = 0.5[CO] + 2[CH_4] - 0.5[NO] \qquad\qquad \text{Equation 2.1}$$

$$\lambda = \frac{[O_{2air}]}{2} \cdot \frac{4[CH_4] + 3[CO] - 2[O_2] - [NO] - 4}{([CO] - 2)[O_{2air}] + 2[O_2] + [NO] - [CO] - 4[CH_4]} \qquad\qquad \text{Equation 2.2}$$

O_2-dithering

The dithering efficiency (η_d, Equation 2.3), reflecting the actual amount of O_2 pulsed during O_2-dithering operation, was determined in the same quartz plug-flow reactor used for the catalytic tests but loaded with sieved cordierite (200 mg) under alternate pulses of O_2 and Ar of the desired amplitude and frequency.

$$\text{dithering efficiency} = \eta_d = 100 \cdot \frac{[O_2]_{real}}{[O_2]_{expected}}$$
Equation 2.3

where $[O_2]_{expected}$ is the desired O_2 concentration dosed to the system in the O_2 pulses and $[O_2]_{real}$ is the calibrated O_2 concentration determined by mass spectrometry at the reactor outlet when dosing $[O_2]_{expected}$.

Additional O_2 values are needed for the calculations used in Chapter 5. The O_2 concentration dosed continuously to the system is defined as $[O_2]_{initial}$ under static operation and $[O_2]_{baseline}$ under dithering operation. The $[O_2]_{baseline}$ is defined as the lowest O_2 concentration seen by the catalyst in the rich phase of the O_2 pulses (Figure 2.2). $[O_2]_{th}$ corresponds to the recalculated O_2 concentration present in the reactive environment based on $[O_2]_{initial}$ (Equation 2.4, static conditions) or $[O_2]_{baseline}$ (Equation 2.5, dithering conditions), η_d as well as pollutants concentration and conversion. Under dithering conditions, $[O_2]_{th}$ needs to be calculated separately for the rich and lean pulses as η_d is different.
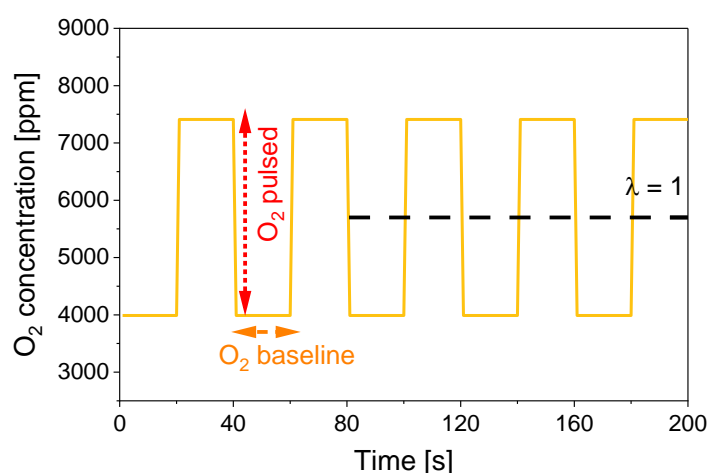

Figure 2.2. Scheme of the alternate symmetric pulses around stoichiometry at an amplitude of 3420 ppm O_2, and a frequency of 0.05 Hz. The horizontal black dashed line indicates the value of 5700 ppm O_2, corresponding to $\lambda = 1.000$.

$$[O_2]_{th} = [O_2]_{initial} - 0.5[CO]_i \cdot X_{CO} - 2[CH_4]_i \cdot X_{CH4} + 0.5[NO]_i \cdot X_{NO}$$ Equation 2.4

$$[O_2]_{th} = [O_2]_{baseline} + [O_2]_{expected} \cdot \eta_d - 0.5[CO]_i \cdot X_{CO} - 2[CH_4]_i \cdot X_{CH4} + 0.5[NO]_i \cdot X_{NO}$$ Equation 2.5

Finally, the steps used for the calculations performed in Chapter 5 are as follow. First, static temperature ramps were performed under lean, stoichiometric, and rich conditions (including conditions wherein CH_4 steam reforming, CH_4-SR, is the only possible reaction pathway for CH_4 oxidation). This step allows obtaining knowledge on the catalytic system (kinetic regimes, reaction rates, and key O_2 concentrations to consider) and information on the conversion values of CH_4, CO, and NO as a function of temperature. The dithering efficiency, η_d, also needs to be determined at the amplitudes and frequencies of interest. With all these inputs, the calculation of $[O_2]_{th}$ for different dithering amplitudes and frequencies can be achieved using Equations 2.4 and 2.5. Finally, by comparing $[O_2]_{th}$ with the O_2 concentration value known to induce high conversion (defined from the static experiments), the calculations identify which dithering parameters will induce high conversion under given conditions (temperature, exhaust gas composition). Therefore, the most challenging part is to correctly define the O_2 concentration value where CH_4-SR is promoted.

2.3 Activation energy calculation

Water decreases significantly the activity of palladium catalysts towards CH_4 oxidation [65,84,121]. Hence, when considering the reaction rate, water has to be taken into account, as described by the methane oxidation kinetic rate (Equation 2.6). The rate of reaction is inversely proportional to the concentration of water, whether it is fed to the system or produced during the reaction [205–207].

$$r = k[CH_4]^{0.7}[O_2]^{0.2}[H_2O]^{-0.9}$$ Equation 2.6

The apparent reaction rate constant was determined by deriving the reaction rate with respect to CH_4 with n = 0.7 from the rate law:

$$-\frac{d[CH_4]}{dt} = k_{app}[CH_4]^n \qquad \text{Equation 2.7}$$

$$k_{app} = \left(\frac{1}{[CH_4]^{n-1}} - \frac{1}{[CH_{4,0}]^{n-1}}\right) / (n-1) \cdot t \qquad \text{Equation 2.8}$$

where, $k_{app} = k \cdot [O_2]^{0.2}[H_2O]^{0.9}$, n is the reaction order, [i] is the concentration of gas i, and t is the residence time in the reactor.

Finally, the apparent activation energy was extracted from the slope of the linearized Arrhenius equation (Equation 2.10). In order to exclude the impact of mass transfer limitation and to ensure the kinetic regime data below 20 % conversion were utilized. Hence, in Chapter 3, the $E_{A,app}$ was evaluated between 300 and 395 °C and between 300 and 350 °C under static and SRP conditions, respectively. Moreover, no external or internal mass transfer limitations are taking place within this evaluated conversion range.

$$k = Ae^{\frac{-E_{A,app}}{RT}} \qquad \text{Equation 2.9}$$

$$\ln k = \ln(A) - \frac{E_{A,app}}{RT} \qquad \text{Equation 2.10}$$

2.4 Kinetic models

Under isothermal conditions and reaction rates, the rate of a solid-state reaction can be defined as:

$$\frac{d\alpha}{dt} = Ae^{-\left(\frac{E_{A,app}}{RT}\right)}f(\alpha) \qquad \text{Equation 2.11}$$

where A is the pre-exponential (frequency) factor, $E_{A,app}$ is the apparent activation energy, T is the absolute temperature, R is the gas constant, $f(\alpha)$ corresponds to the reaction model and α refers to the oxidation degree.

The integral reaction model $g(\alpha)$ is described, for isothermal rate laws, as:

$$g(\alpha)=Ae^{-(\frac{E_{A,app}}{RT})}t$$

Equation 2.12

Table 2.1. Solid state integral expressions of the different models [208,209] used in Chapter 3 (Figure 3.8 and Figure A21).

Model	Integral form $g(\alpha) = kt$
Power law	$\alpha^{1/2}$
Avrami-Erofeyev (A2)	$[-\ln(1-\alpha)]^{1/2}$
Avrami-Erofeyev (A3)	$[-\ln(1-\alpha)]^{2/3}$
Avrami-Erofeyev (A4)	$[-\ln(1-\alpha)]^{3/4}$
1d diffusion	α^2
3d diffusion	$((1-\alpha)\ln(1-\alpha)) + \alpha$
Mott-Fehlner*	$(e^{(r_0/\alpha A)}-1)/B$
Cabrera-Mott*	$e^{((A-1/(\alpha r_0)/B)}$
Contracting volume	$1-(1-\alpha)^{1/3}$

* r_0 is the particle radius of reduced Pd (calculated from EXAFS at the end of a pulse)

2.5 Characterization techniques

2.5.1 Inductively coupled plasma optical emission spectrometry

The elemental analysis was performed using inductively coupled plasma-optical emission spectroscopy (ICP-OES) after digestion with a solution of HNO_3, HCl, HF, and H_2SO_4.

2.5.2   X-ray diffraction

X-ray diffraction (XRD) was measured to characterize and analyse the structure of the crystalline materials. The diffraction patterns were collected using a D8 Advance Bruker instrument equipped with a 1D-LynxEye detector at a step size of 0.01° and an acquisition time of 2 s.

In situ XRD diffractograms were collected using an XRK 900 chamber. The sieved samples (150 - 200 µm) were first exposed to 2000 ppm H_2 in N_2 (50 mLmin^{-1}) from 60 to 600 °C (diffractograms were acquired at 60, 170, 300, 450, and 600 °C), and the gas mixture was changed to 2000 ppm O_2 in N_2 (50 mLmin^{-1}) at 600 °C (patterns were measured every 25 °C from 600-300 °C). The samples were left at the desired temperature for 5 min before acquisition of the diffractogram was initiated.

2.5.3 N_2 physisorption

The specific surface area of the samples (Brunauer-Emmet-Teller, BET) was measured by N_2 physisorption at liquid nitrogen temperature (-196 °C) and p/p_0 values in the 0.05 - 0.3 range using a Quantachrome Autosorb I instrument. Prior to analysis, the sample was outgassed at 250 °C for 6 h.

2.5.4 H_2 temperature programmed reduction

H_2 temperature-programmed reduction (H_2-TPR) experiments were carried out in a TPDRO 1100, ThermoScientific equipped with a thermal conductivity detector to study the reducibility of the materials. H_2-TPR profiles were collected in the temperature range of 30 to 800 °C at a heating rate of 5 °Cmin^{-1} in a gas flow of 10 vol% H_2 in Ar (20 mLmin^{-1}). Before measurement, a pre-treatment from 50 to 350 °C in He (20 mLmin^{-1}) was applied to desorb water and possible impurities.

2.5.5 Electron microscopy

Transmission electron microscopy images were obtained using a JEOL 2010 microscope equipped with a LaB_6 cathode and operated at 200 keV. The images were recorded using a slow-scan CCD camera (4008 x 2672 pixels, Orius Gaten Inc.). A sufficient number of particles was counted to obtain the average particle size and the Pd dispersion [210].

Energy-dispersive X-ray (EDX) spectroscopy was measured at the Interdisciplinary Center for Electron Microscopy (CIME) at École Polytechnique Fédérale de Lausanne (EPFL). The measurements were performed with an FEI Titan Themis microscope operated at 200 kV for chemical characterization of the materials. It is equipped with a high-brightness field emission gun (X-FEG), a probe aberration corrector (CEOS D-COR), windowless silicon drift detectors with a large X-ray collection angle (Bruker Super-X), and a Fischione HAADF detector. EDX spectrum images were acquired using a multi-frame strategy with 100 µs dwell time, 0.8 nA beam current, and 20 mrad convergence angle. The elemental net count maps were processed with Velox software.

2.5.6 X-ray absorption spectroscopy

The local geometry and electronic structure of the metals present in the materials used were evaluated by X-ray absorption spectroscopy (XAS). Operando Pd K-edge X-ray absorption near edge structure (XANES) spectra were measured at the SuperXAS beamline of the Swiss Light Source (SLS, Paul Scherrer Institute). The incident X-ray beam was collimated using a Pt coated mirror at 2.9 mrad prior to monochromatization using a channel cut Si(111) crystal. The monochromatic beam was then focused using a Pt coated toroidal mirror. The monochromator was oscillated at 5 Hz frequency yielding a time resolution of 0.2 s per spectrum. Energy calibration and linear combination fitting was performed with the ProXAS [211] software and cali-brated by simultaneously measured Pd reference foil. Linear combination fitting of the XANES region was performed using reference states of the catalyst after in situ reduction and oxidation of the material. EXAFS fitting was conducted with FEFF included in the Artemis [212] software. Extraction of the Pd-metal particle

size was obtained by previously fitting the Pd-Pd scattering path of the Pd-foil and fixing the CN at 12 to calibrate the amplification factor for all fits. The Pd particle size was calculated according to Jentys [213] assuming spherical particles from the obtained coordination number of the samples. The oxidation degree obtained from LCF-analysis was used for fitting the different oxidation mechanisms by minimizing the square root of the error. The equation of the investigated oxidation models can be found elsewhere [208,209].

The sample (20 mg, 150-200 µm) was loaded in a quartz glass capillary (ID = 3 mm; Hilgenberg) between two quartz wool plugs. Heating was achieved using two infrared heaters (80 W, Elstein). The outlet of the capillary reactor was analysed using a mass spectrometer (MS; Pfeiffer Omnistar). The sample temperature was monitored using a thermocouple inserted in the middle of the catalyst bed. The capillary reactor was attached to a gas mixing setup composed of mass flowmeters and two solenoid valves (Series 9, Parker) enabling fast changes in gas phase composition. The same experimental conditions of the catalytic tests described below were used for the XAS measurement.

Chapter 3 Effect of short reducing pulses on the dynamic structure, activity, and stability of Pd/Al$_2$O$_3$ for wet lean methane oxidation

3.1 Introduction

Pd-based materials, typically Pd supported on Al$_2$O$_3$, CeO$_2$, and ZrO$_2$ [124,214–216] are the most efficient catalysts for lean CH$_4$ oxidation but suffer from deactivation induced by steam, SO$_2$, and high temperatures [84,179]. These deactivation processes can be mitigated either by improving the material formulation and properties [147–149,217] or by modifying the working conditions [59,65,151,153,169,218].

In this study, we decided to use a simple catalyst, Pd supported on Al$_2$O$_3$, while performing periodic short reducing pulses (SRP) consisting of cutting off the O$_2$ from the reactive feed for 3 s every 5 min. This strategy allowed to suppress the inhibition effect of steam on the activity as well as to improve the long-term stability of the catalyst. The degraded activity of the thermally aged catalysts was also reverted by applying the SRP approach through structural changes of the catalyst. Furthermore, fit of time-resolved operando XAS data using kinetic models of oxidation revealed that only moderately active PdO exists under static operation, while during SRP operation highly active PdO$_x$ species are formed and maintained by the presence of metallic Pd. Based on the combined spectroscopic and kinetic data, we propose a practical range of Pd oxidation degrees (25−65% Pd content) to preserve high CH$_4$ conversion.

3.2 Materials and methods

3.2.1   Material synthesis

The 2 wt% Pd/Al_2O_3 catalyst was prepared by wet impregnation of aluminum oxide (γ-Al_2O_3, Puralox; Sasol) with a solution of palladium (II) nitrate (Alfa Aesar, 4 – 5 wt% solution) at 80 °C for 6 h, followed by drying at 120 °C for 24 h and by calcination in a muffle oven at 500 °C (ramping 5 °Cmin^{-1}) for 2 h. The thermally aged sample was obtained by a second calcination at 800 °C (ramping 5 °Cmin^{-1}) in air for 60 h. The hydrothermally aged sample was obtained by a second calcination at 600 °C for 24 h in an atmosphere of 10 vol% H_2O and 4 vol% O_2 (balance Ar; 100 mLmin^{-1}).

3.2.2   Material characterization

The structure of the samples was studied by scanning transmission electron microscopy (STEM) at the Scientific Center for Optical and Electron Microscopy (ScopeM) of ETH Zurich, on aberration-corrected HD-2700CS (Hitachi; cold-field emitter), operated at an acceleration potential of 200 kV. A probe corrector (CEOS) was incorporated in the microscope column between the condenser system and the probe-forming objective lens providing high-resolution capability (beam diameter ca. 0.1 nm). Images (1024 x 1024 pixels) were recorded with a high-angle annular dark-field (HAADF) detector (frame times of ca 15 s) which provides atomic number (Z) contrast.

3.3 Results and discussion

3.3.1   Catalytic activity of calcined and aged Pd/Al_2O_3

The favourable effect of short reducing pulses (SRP) on CH_4 oxidation was proven on a calcined 2 wt% Pd/Al_2O_3 catalyst (Table A1) by assessing its catalytic activity in static (steady supply of all reactants) and

SRP mode (repeated O_2 cut-off from the reaction feed for 3 s every 5 min – Figure 2.1) in the presence of 10 vol% H_2O (Figure 3.1a). To evaluate the water inhibition, the sample was also tested under static dry conditions. The poisoning effect of water on this catalyst is demonstrated by the increase in the temperature at half CH_4 conversion ($T_{50\%}$ - Table 3.1) by ca. 85 °C in the heating segment under static conditions in wet feed compared to dry conditions (Figure 3.1a). Comparison between static and SRP operation of the calcined catalyst under wet conditions shows that $T_{50\%}$ shifted from 428 °C (static mode) to 370 °C (SRP mode 2nd cycle), while full conversion was reached at 480 °C and 420 °C, respectively (Figure 3.1a). This significant shift of $T_{50\%}$ under wet conditions in SRP mode to close to the value obtained under dry static conditions demonstrates that SRP counteracts inhibition by water.
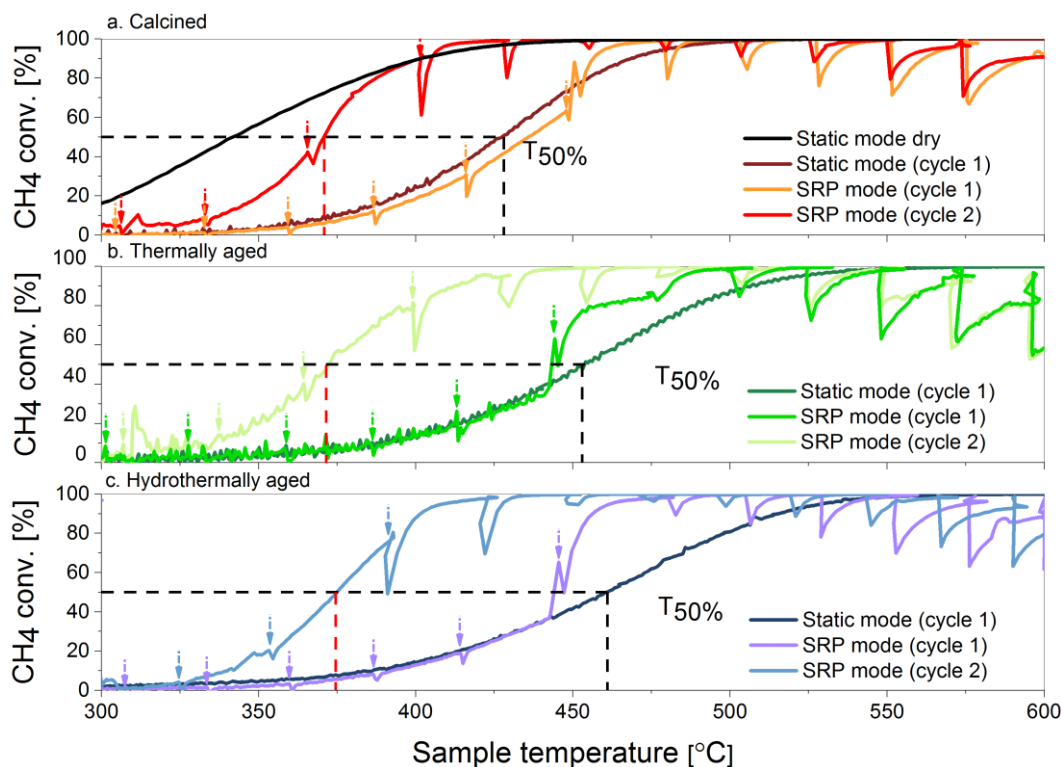
Figure 3.1. CH_4 conversion obtained from ascending linear temperature ramps under static and SRP wet lean conditions over 2 wt% Pd/Al_2O_3. (a) Calcined, (b) thermally aged, and (c) hydrothermally aged. The dashed lines represent $T_{50\%}$ in static (black) and SRP (red) mode. The arrows ($\rightarrow$) indicate the occurrence of a pulse. Dry conditions: 1 vol% CH_4, 4 vol% O_2; wet conditions: 1 vol% CH_4, 4 vol% O_2, 10 vol% H_2O; WHSV = 120 $Lh^{-1}g^{-1}$. Panel a. includes the data collected under static dry conditions.

Closer inspection of Figure 3.1a reveals that catalyst activation by pulses occurs above 430 °C in the first heating ramp under SRP conditions. Indeed, while O_2 cut-offs below 430 °C did not produce appreciable changes in CH_4 conversion compared to the static mode, the pulse at ca. 430 °C triggered an increase in CH_4 conversion. Temperature programmed reduction with CH_4 under similar conditions as during the CH_4-pulses (CH_4-TPR, Figure A1) shows that PdO reduction by CH_4 took place above 300 °C in this material, suggesting that such reduction leads to catalyst activation during pulsing. Once the activation had been induced, the conversion remained significantly higher throughout the subsequent cooling segment (Figure 3.1; Figure A2) compared to static operation and generated a wide hysteresis in CH_4 conversion that was absent in the heating/cooling ramps under static feed. This hysteresis vanished in the following heating/cooling segments in SRP mode, showing that the catalyst had reached a new equilibrium. It should be noted that due to the O_2 cut-offs, CH_4 slip occurred in each of the 3 s rich pulses due to O_2 deficiency as indicated by the transient drop in CH_4 conversion. Under SRP conditions the conversion was higher than in static mode below 475 °C, even in a reducing pulse (i.e. at 430 °C, conversion dropped to 79 % during a pulse in the 2nd heating ramp, while it reached 53 % under static conditions).

While the O_2 cut-off produced very narrow pulses below 525 °C, suggesting rapid regain of activity, above 525 °C the recovery of CH_4 conversion after each rich pulse was slower, implying increased CH_4 slip. This effect vanished completely when the temperature was decreased again below 525 °C, demonstrating that a reversible process is at the origin of this behaviour (Figure 3.1).

The same catalyst was thermally (800 °C, 60 h; Figure 3.1b) and hydrothermally aged (600 °C, 10 vol% H_2O, 24 h; Figure 3.1c) before the measurement of CH_4 conversion under identical conditions. These treatments lead to slightly lower BET-specific surface areas and an increase in PdO particle size (Table A1) but did not modify the phase composition significantly (Figure A3). Transmission electron micrographs showed that the PdO particles of the calcined catalyst were round, while those of the aged samples exhibited on average more defined edges (Figure A4-6). Both aging treatments caused a further increase in $T_{50\%}$ under wet static conditions compared to the situation obtained with the calcined catalyst (Table 3.1), suggesting a permanent deactivation. Conversely, under SRP conditions the $T_{50\%}$ decreased to values comparable to calcined Pd/Al_2O_3

($\Delta T_{50\%} = 5$ °C) and was maintained in the next heating/cooling segments (Table 3.1). The deactivation induced by thermal and hydrothermal treatments was clearly suppressed by the SRP mode. Also, the increased CH_4 slip at high temperatures occurred to the same extent in the aged samples.

Table 3.1. Apparent activation energy ($E_{A,app}$) and first order rate constants (k_{app}) in static and SRP modes of calcined, thermally, and hydrothermally aged 2 wt% Pd/Al_2O_3. Conditions: 1 vol% CH_4, 4 vol% O_2, ±10 vol% H_2O; WHSV = 120 $Lh^{-1}g^{-1}$.

		$T_{50\%}$ [°C]	$E_{A,app}$ [$kJmol^{-1}$]	k_{app} [10^{-5} s^{-1}]
Static mode (1st heating/cooling)	Calcined (dry conditions)	342	29.3 ± 0.2	18.8
	Calcined	428 / 430	65.3 ± 0.7	2.44
	Thermally aged	455 / 470	77.8 ± 1.1	2.06
	Hydrothermally aged	461 / 473	75.7 ± 1.1	2.01
SRP mode (1st heating)	Calcined	436	61.2 ± 0.9	2.43
	Thermally aged	444	74.1 ± 1.2	2.07
	Hydrothermally aged	447	72.3 ± 1.4	2.04
SRP mode (2nd heating)	Calcined	370	45.8 ± 1.1	15.3
	Thermally aged	373	45.8 ± 1.4	15.1
	Hydrothermally aged	375	45.9 ± 0.6	15.0

All catalysts exhibited comparable first-order apparent activation energy ($E_{A,app}$) values between 65 and 78 $kJmol^{-1}$ under static feed (Table 3.1) consistent with previously reported values [182,207,219]. In the first heating segment, a comparable $E_{A,app}$ was obtained under SRP and static conditions. However, after activation above 430 °C under SRP conditions, $E_{A,app}$ decreased to ca. 46 $kJmol^{-1}$, while the apparent rate constant increased from $2·10^{-5}$ s^{-1} to ca. $15·10^{-5}$ s^{-1}, regardless of thermal or hydrothermal treatments. The remarkable decrease of $E_{A,app}$ confirms that the severe deactivation observed under static conditions was suppressed by the

repeated O_2 cut-offs. We consider that the very similar $E_{A,app}$ values obtained indicate that SRP induces structural changes, which lead to the same highly active state.
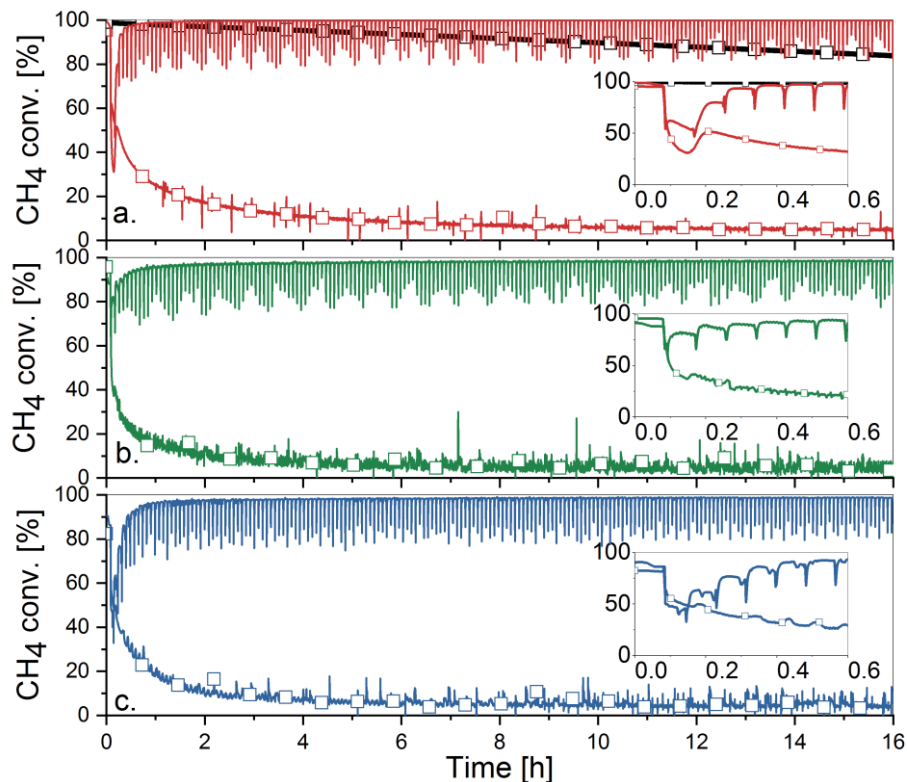

Figure 3.2. CH_4 conversion over Pd/Al_2O_3 under static (-□-) and SRP (-) lean conditions at 435 °C. (a) Calcined, (b) thermally aged, and (c) hydrothermally aged Pd/Al_2O_3. Conditions: 1 vol % CH_4, 4 vol % O_2, 10 vol % H_2O; WHSV = 120 Lh^{-1}g^{-1}. Panel a. includes data collected for the calcined sample in dry static conditions (black).

Figure 3.2a shows that under isothermal conditions at 435 °C, CH_4 oxidation decreased rapidly below 10 % in wet static feed (in the presence of 10 vol% H_2O) over the calcined catalyst. Under dry feed conditions, the activity decreased to a lower extent (from 98 to 80 % within 16 h), attesting again the detrimental effect of water on lean CH_4 oxidation under static operation. The average CH_4 conversion under wet conditions was markedly enhanced by starting the SRP mode [138]. Upon changing to wet conditions, CH_4 conversion dropped initially to 60 %, in agreement with the inhibition effect of water on catalytic activity (inset of Figure 3.2a). However, the average conversion increased continuously from 60 to over 99 % within the first four pulses (ca. 25 min) and remained at this level for the next 15 h. Thermally (Figure 3.2b) and hydrothermally

aged (Figure 3.2c) samples exhibited the same extent of activation under SRP operation as well as high stability over time but required a higher number of reducing pulses to reach a similar conversion level of the calcined catalyst (inset of Figure 3.2).

Experiments repeated at lower temperatures in order to reduce the conversion rate (Figure A7) confirmed that activation by CH_4 through O_2 cut-off does not take place below 420 °C, as noted above (Figure 3.1). At ca. 420 °C, the catalyst temperature raised to 435 °C in response to the repeated rich/lean pulses, most likely due to the exothermicity of the lean reaction (see Figure A7-8 where the temperature and thus the conversion decrease within a reducing pulse). Furthermore, the stepwise increase in space velocity from 120 to 360 $Lh^{-1}g^{-1}$ (Figure A9) at 435 °C only slightly affected CH_4 conversion, which remained at a high level of 93 %. Hence, these isothermal tests demonstrate that SRP not only activates but also maintains high activity as well as high water resistance of Pd/Al_2O_3. Characterization by powder X-ray diffraction (XRD) (Figure A10-12) showed that irrespective of the catalyst, the fraction of reduced Pd increased at the expense of PdO after the isothermal test under SRP mode. Scanning electron microscopy (STEM) images of the thermally treated catalyst indicated that the cuboid shape of the particles (Figure A4-6) changed to round particles after the pulsed operation (Figure A13-15). In contrast, XRD patterns after stability tests under static conditions show only the presence of PdO and resemble the ones of the unused catalysts (Figure A10-12). Hence, SRP reverses the structural effects of thermal and hydrothermal aging and transfers the catalysts into the same highly activated state regardless of thermal or hydrothermal treatment.

3.3.2   Operando XAS

The activation behaviour of calcined Pd/Al_2O_3 under SRP mode was observed in time-resolved operando XAS analysis in presence of 10 vol% H_2O at 435 °C (Figure 3.3a). While the sample is not perfectly homogeneous it displays a narrow Pd particle size distribution (Figure A16-17) suggesting that all Pd particles respond to the gas changes in a similar manner and exhibit comparable oxidation and reduction kinetics. Linear combination fit (LCF) analysis of the Pd K-edge X-ray absorption near edge (XANES) region reveals that the

catalyst was in a fully oxidized state after calcination and pre-treatment. Upon applying rich pulses by repeat-edly cutting off O_2 for 3 s, followed by wet lean CH_4 oxidation for 5 min, CH_4 conversion increased with each pulse incrementally from 10 to 80 %. At the beginning of the experiment the PdO content decreased in each consecutive pulse until it reached a level of quasi-equilibrium (ca. 80 %) while during each pulse, the PdO content dropped to 10 %. In the lean phases, reoxidation proceeded in two stages [175,176,220], a very fast process directly after the switch followed by a slower reoxidation. Fitting the extended X-ray absorption fine structure (EXAFS) spectra taken 3 min after each rich pulse (Figure 3.4a) revealed an increase in coordination number of the Pd-Pd first shell of metallic Pd that was mirrored by the simultaneous decrease of the first Pd-O coordination shell in line with LCF analysis.
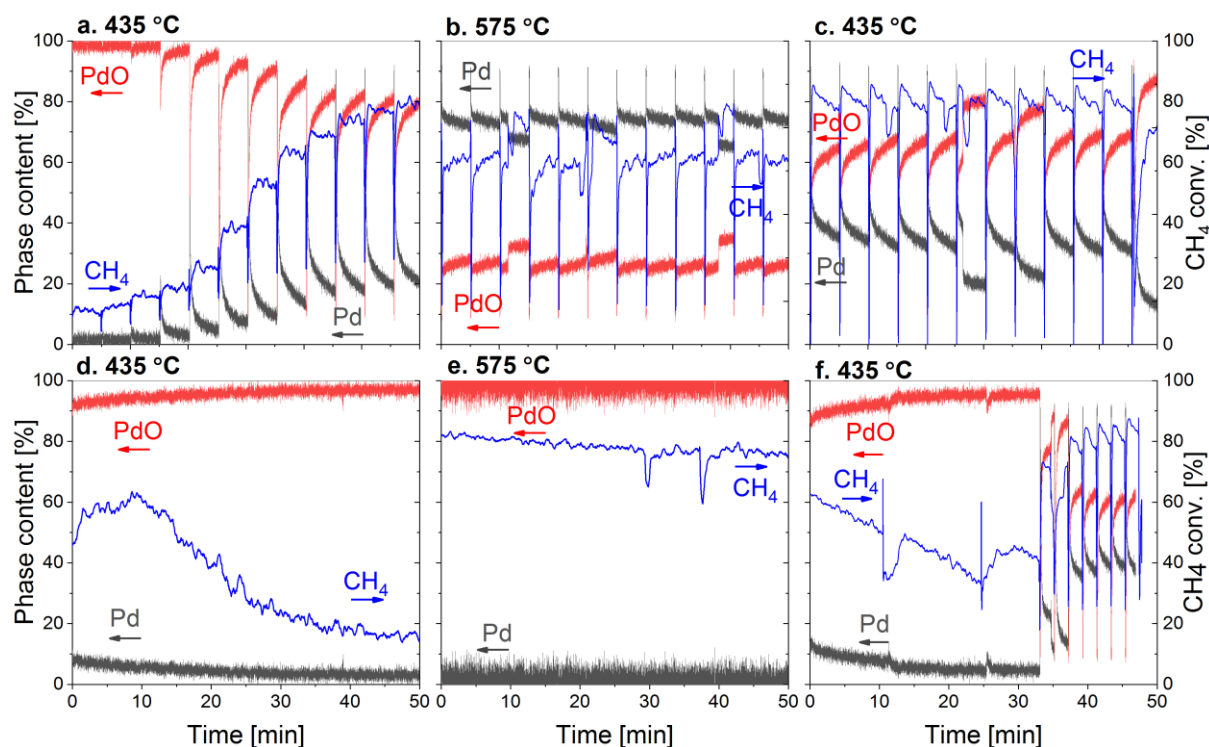
Figure 3.3. CH_4 conversion (blue) and Pd phase content (PdO (red) / Pd (black)) of calcined Pd/Al_2O_3 in (a-c) SRP and (d-f) static lean operation at 435 °C, 575 °C and a second time at 435 °C. Reactivation through SRP after deactivation in static mode is shown in (f) (> 33 min). Conditions: 1 vol% CH_4, 4 vol% O_2, 10 vol% H_2O; WHSV = 360 Lh^{-1}g^{-1}.

The EXAFS analysis of the data collected in the static lean period after SRP at 435 °C confirms that the activity decreased as soon as metallic Pd was consumed (Figure 3.4b; Figure 3.3d). During the first 10 min of

the experiment, signals from metallic Pd-Pd scattering at 2.43 Å can still be extracted and during this time, CH_4 conversion is at 60 %. After 10 min, no Pd-Pd scattering path can be fitted and LCF revealed more than 95 % PdO. Accordingly, CH_4 conversion decreased from 60 to 15 % in the next 30 min concomitant with the intensity increase in the FT-EXAFS peak at 2.94 Å corresponding to the Pd(-O-)Pd scattering path (Figure A18). Such an increase suggests an increased order and hence crystallization of the oxide that limits CH_4 oxidation under static operation.
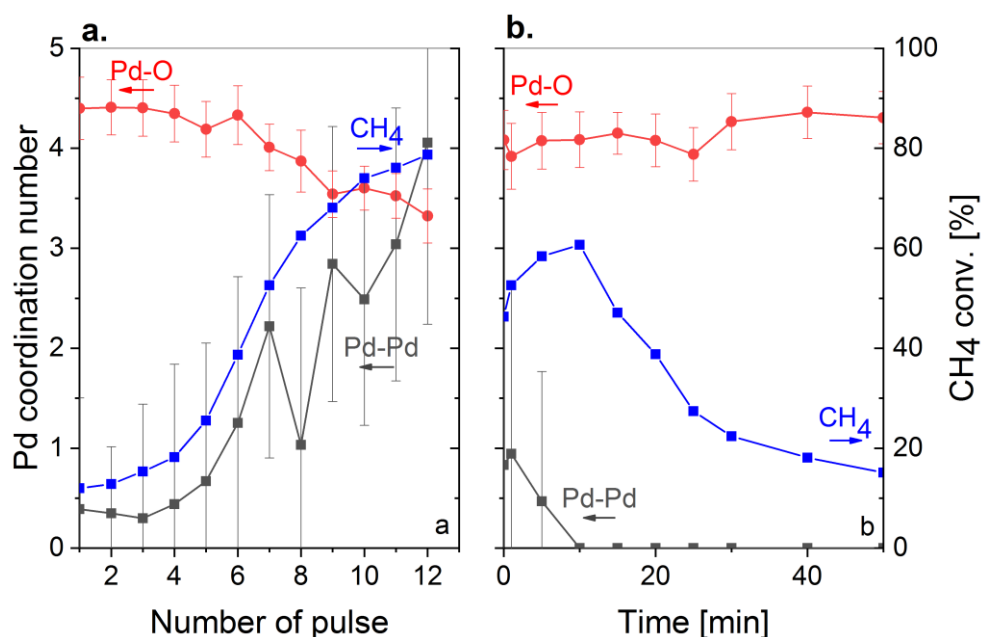
Figure 3.4. CH_4 conversion (blue) and Pd coordination number (Pd-O (red) / Pd-Pd (black)) of calcined Pd/Al_2O_3 in (a) SRP and (b) static lean operation at 435 °C. Conditions: 1 vol% CH_4, 4 vol% O_2, 10 vol% H_2O; WHSV = 360 $Lh^{-1}g^{-1}$.

Under pulsed conditions, (Figure 3.3a-c), CH_4 conversion decreased by at least 20 % at 575 °C and returned to its initial value after cooling back to 435 °C. The same behaviour was observed in the laboratory experiments (Figure A8). The XANES spectra at 435 °C (Figure 3.5) reveal the presence of 90 % metallic Pd in the reductive pulses and 20 % in the lean phase, which is accompanied by fast reoxidation (inset Figure A8; Figure 3.3a). However, at 575 °C, reoxidation of Pd was slower and the PdO formation within the lean phases after each pulse was ca. 27 %. CH_4 conversion decreased accordingly to 62 % at 575 °C (Figure 3.3b). Since no thermodynamic limitation is expected, the data evidence that the presence of a higher fraction of reduced Pd

limits CH_4 conversion. The subsequent pulsed operation at 435 °C leads to, on average, a higher fraction of PdO accompanied by higher CH_4 conversion values (Figure 3.3c).

After this sequence at 435 °C, SRP was switched off leaving the catalyst under static lean conditions (Figure 3.3d-e). The PdO content increased to 99 % and concurrently CH_4 conversion decreased over time. The temperature increase to 575 °C under static operation induced the usual Arrhenius behaviour of higher conversion at elevated temperature up to 81 %; nonetheless, the conversion decreased gradually to 75 % in the next 50 min. Cooling to 435 °C maintained Pd fully oxidized but decreased CH_4 conversion. Hence, in marked contrast to SRP, only PdO is present under static lean operation at all temperatures and is less active than the surface species created by SRP (at 435 °C). However, a too high fraction of reduced Pd also limits the activity under SRP conditions. These results support the general agreement that highly deficient PdO_x or Pd-PdO species are active for CH_4 oxidation under lean conditions [151,221]. SRP mode allows to periodically replenish this highly active metastable transient PdO_x species and thus maintains high activity over long periods of time.
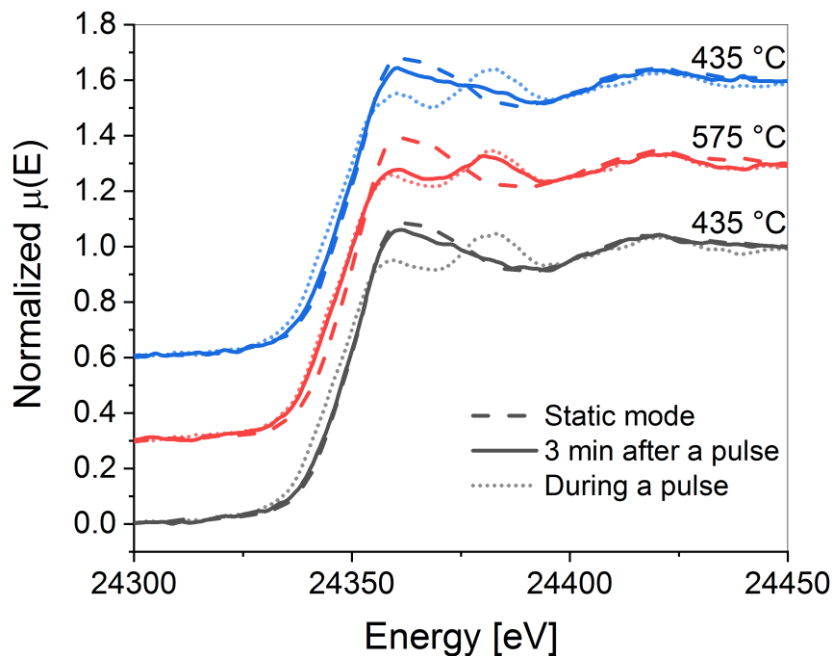

Figure 3.5. Transmission operando Pd K-edge XAS spectra of calcined Pd/Al$_2$O$_3$ recorded in the following sequence 435 °C (black), 575 °C (red), and 435 °C (blue) under (- -) static operation, (—) 3 min after a pulse and (⋯) during a pulse. Conditions: 1 vol% CH_4, 4 vol% O_2, 10 vol% H_2O; WHSV = 360 Lh^{-1}g^{-1}.

Conversely, switching SRP on after exposure to static lean conditions at 435 °C (40 % CH$_4$ conversion) induced an increase in CH$_4$ conversion as well as a decrease in the PdO content (Figure 3.3f). Catalyst reactivation occurred in the first pulses and the catalyst behaved as in the initial activation (Figure 3.3a) causing an increase of CH$_4$ conversion to 80 %. Hence, the observed continuous deactivation under static lean operation can be reversed by applying SRP as shown in Figure 3.2.

The conversion values obtained in the operando XAS measurements correlated with the degree of Pd reduction from LCF analysis allowed the identification of an optimal window of reduced Pd content. Figure 3.6 shows that an increased fraction of reduced Pd from 0 to 25 % enhances CH$_4$ conversion, which remains above 80 % up to 65% of reduced Pd. Higher Pd reduction degrees (up to 75 %) inhibit CH$_4$ oxidation. This behaviour underlines the relevance of the presence of a Pd/PdO (PdO$_x$) mixed phase to obtain high CH$_4$ conversion levels.
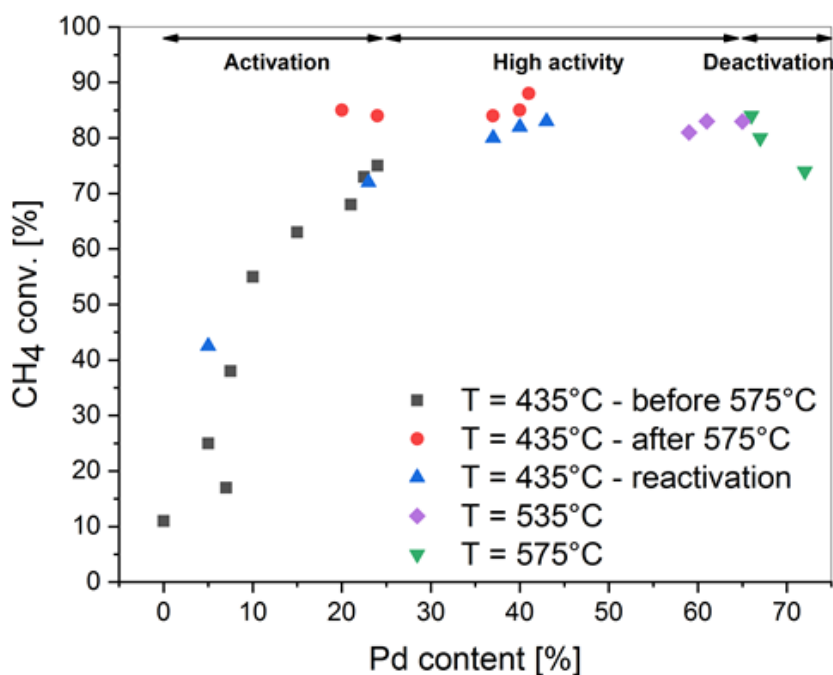
Figure 3.6. CH$_4$ conversion of calcined Pd/Al$_2$O$_3$ as a function of the content of reduced Pd extracted from the operando XAS data collected in SRP mode. Conditions: 1 vol% CH$_4$, 4 vol% O$_2$, 10 vol% H$_2$O; WHSV = 360 Lh^{-1}g^{-1}.

Experiments performed with different partial pressures of water and at different temperatures demonstrate the importance of placing the degree of Pd oxidation in the optimal range. At 435 °C, the change at 26.5 min

from 10 to ca. 25 vol% H_2O caused a decrease of CH_4 conversion by 10 % but also increased instantaneously the PdO content from 60 to 80% (Figure 3.7a). This drop in conversion was fully reversible and the initial conversion was regained once the water concentration in the feed was decreased back to 10 vol%. Nonetheless, the elevated PdO content remained at 80 % when returning to lower water concentrations. As both values, 60 and 80 % PdO, are within the optimal range for CH_4 oxidation activity, the conversions obtained under different H_2O content at 435 °C can be explained in terms of water inhibition effects solely (i.e. reversible formation of hydroxylated surface species and blockage of active sites by adsorbed water) [65].
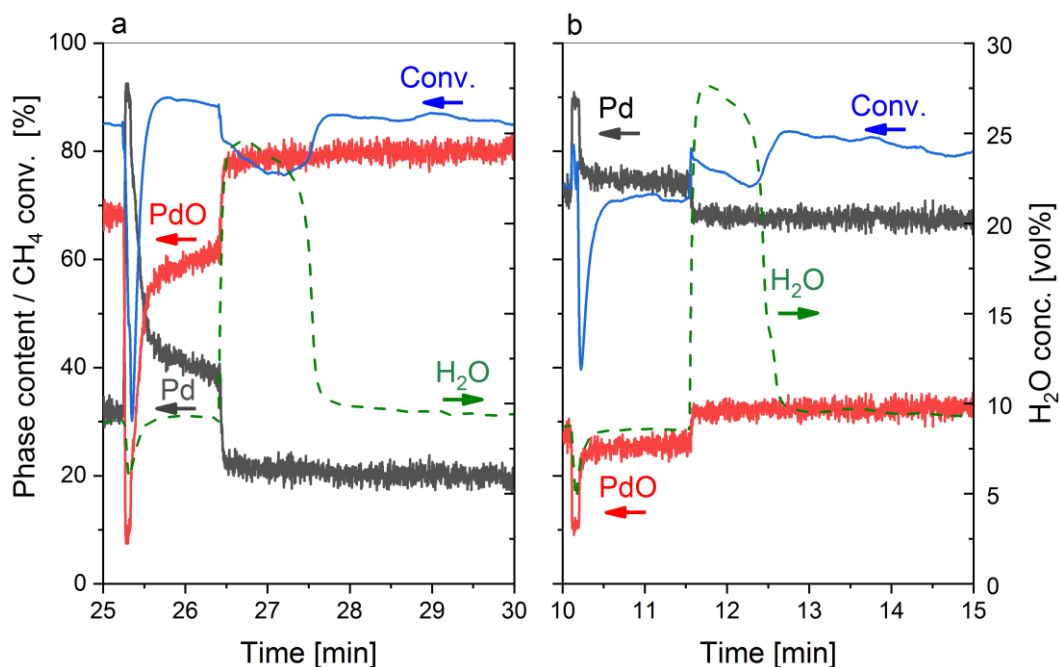
Figure 3.7. Effect of water concentration on CH_4 conversion (blue), H_2O content (green) and Pd phase (PdO (red) / Pd (black)) of calcined Pd/Al_2O_3 under lean SRP conditions at (a) 435 °C and (b) 575 °C. Conditions: 1 vol% CH_4, 4 vol% O_2, 10-25 vol% H_2O; WHSV = 360 $Lh^{-1}g^{-1}$.

At 575 °C, the effect of higher water partial pressure on CH_4 conversion inverts (Figure 3.7b). The oxidation degree of Pd increased instantaneously from 25 to 32 % with the increase in water concentration at 11.5 min. Since the catalyst was in a highly reduced state, the water-assisted oxidation shifted the system towards the optimal Pd/PdO content (Figure 3.6), which increased the conversion by 5 %. Nevertheless, the higher water

concentration leads to the reversible inhibition by water as described above. In line, lowering the water concentration from 20 to 10 vol% increased the CH_4 conversion even further by 8 % without affecting the oxidation degree. Finally, over fully oxidized PdO, only CH_4 concentration was affected as the water concentration was increased, this effect vanishing when the water content was restored to 10 vol% (Figure A19).

3.3.3   Kinetics of Pd oxidation

Kinetic analysis of the fast change of oxidation state obtained from LCF as well as the EXAFS data after a reductive CH_4 pulse was conducted to understand the behaviour of the Pd/PdO pair under working conditions. The fit of the oxidation degree obtained experimentally from LCF with different solid-state kinetic oxidation models [208] showed that the Cabrera-Mott (CM) model [209] and the 3D diffusion model were able to approximate the experimental data (Figure A20, Figure 3.8). Although the 3D diffusion model displayed high correlation, it showed a systematic underestimation in the initial oxidation phase. On the contrary, the CM model exhibited a correlation above 98 % and thus describes better our experimental data over the fitted range. This model is valid only for the oxidation of small metal particles (below 10 nm) [222]. The average metal particle size derived from the first Pd-Pd coordination shell of the calcined Pd/Al_2O_3 sample is 9 nm (Table A1) after 3 s of reduction, confirming the applicability of the CM model to the operando XAS data. According to this model, a thin oxide film forms upon oxidation, across which electrons tunnel from the metallic core to ionize adsorbed oxygen. The resulting charge separation induces an electric field that is the driving force for ion transport and growth of the oxide layer. Electron tunnelling is reported to take place through an oxide layer as thick as 3 nm [209]. Beyond this critical layer thickness, the further slow oxide growth follows the 3D diffusion model. Oxidation of Pd according to the CM model was previously reported to take place in O_2 [176] and we confirm that it also proceeds under lean CH_4 oxidation conditions. According to both the CM model and the 3D diffusion model, the oxide layer formed around the metallic core is amorphous and highly defective due to ion diffusion from the core to the surface [209]. Therefore, the CM model suggests that PdO is present in a highly defective and amorphous phase when SRP operation is applied as long as metallic Pd is present. The presence of this amorphous PdO_x phase explains the observed improved CH_4 oxidation activity under SRP

mode. The CM model encourages to think that the Pd-PdO pair involved in the experiments shown above is a core-shell structure, of which however we have only sporadic hints from electron microscopy.

It is widely accepted that coordinatively unsaturated Pd species in the form of PdO_x or Pd-PdO are responsible for high CH_4 oxidation activity [124–127]. Oxidation of Pd to PdO is reported to proceed via PdO_x species. In the presence of water, PdO_x is preferentially hydroxylated, which results in improved stability of PdO at high temperatures [118]. The mechanism of CH_4 oxidation on coordinatively unsaturated Pd was proposed to occur by adsorption of CH_4 on Pd sites and C-H bond breaking on adjacent Pd-O sites with the formation of Pd-OH species [124]. Combination of OH groups leads to water formation and desorption.
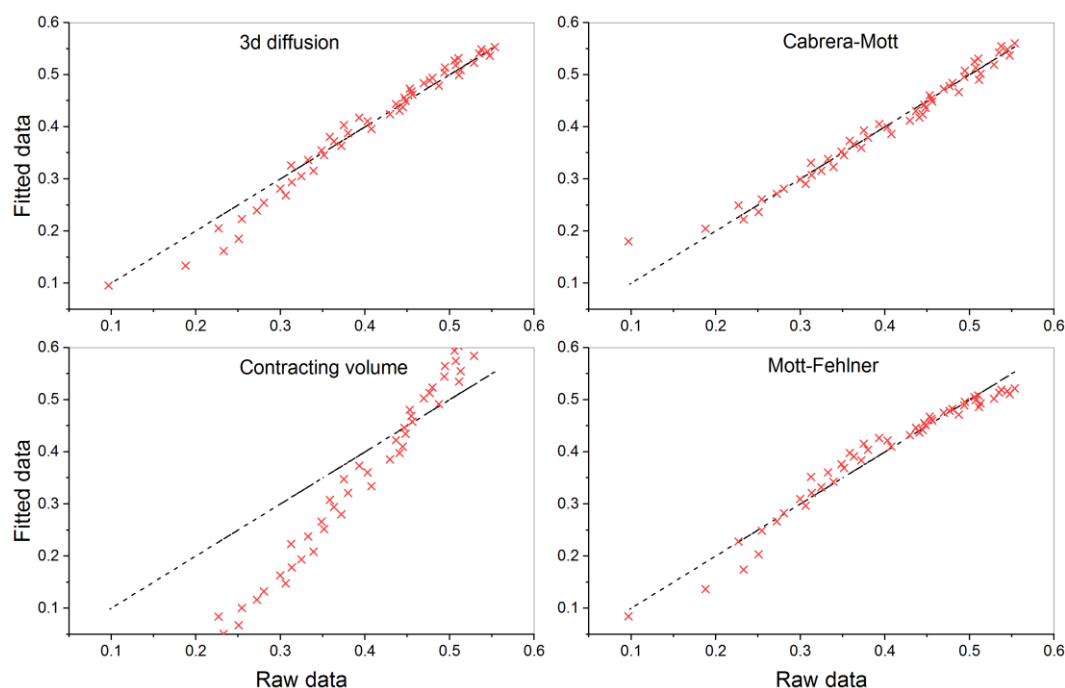
Figure 3.8. Parity plots of the four most suited oxidation mechanisms of Pd to PdO proposed in literature [208,209].

Based on these observations, we propose a model that rationalizes the improvements obtained in SRP mode over the static lean operation (Scheme 3.1). For simplicity, we represent a core-shell structure for Pd and PdO phases, although other structural arrangements could be considered as well. Initially, crystalline PdO is the main species after calcination. By repeatedly applying CH_4 pulses, PdO reduces partly. The increase in surface roughness induced by reduction of PdO by CH_4 causes structural changes that facilitate the reducibility of the

reoxidized PdO [175]. The partial and proceeding reduction of PdO needs to overcome a temperature threshold dependent on the applied reaction conditions. During each rich pulse, up to 90 % of PdO is reduced to metallic Pd leading to an increase in CH_4 conversion. During the lean phase, after each pulse, a thin layer of highly defective PdO_x forms (as indicated by the CM model) whose thickness increases first very fast and then more slowly by diffusion of O atoms to the Pd core. The defective character of this PdO_x layer is maintained by diffusion of Pd towards the surface according to the CM theory. Therefore, the presence of reduced Pd acts as a reservoir to maintain the highly active PdO_x phase. Amorphous PdO_x starts to densify and crystallizes as soon as the metallic core is consumed. Due to the very fast reduction of PdO to Pd, adoption of the SRP mode reverses the growth of the PdO layer and increases the metallic Pd core. Hence, on the time scale of the reducing pulses with CH_4, the Pd core was never fully consumed in the subsequent lean operation periods. The presence of the highly active PdO_x phase maintains and sustains the high isothermal activity and stability. If SRP mode is switched to static operation, the catalyst maintains high activity until the metallic core is fully consumed. The following densification and crystallization of amorphous PdO_x to crystalline PdO leads to isothermal deactivation and a significant decrease in CH_4 conversion due to the loss of coordinatively unsaturated Pd species in PdO_x, which is in line with the decreased performance of the hydrothermally and thermally aged catalysts. The formation of the crystalline and less active PdO state can be reversed by applying SRP with CH_4 at any state of deactivation leading to the recovery of performance. The creation and maintenance of transient states of reduction and oxidation in combination with the formation of the highly active PdO_x phase during SRP operation justify that even hydrothermally and thermally deactivated catalysts of comparable particle size can be reactivated upon creation of the same active sites as evidenced by the similar apparent activation energies.
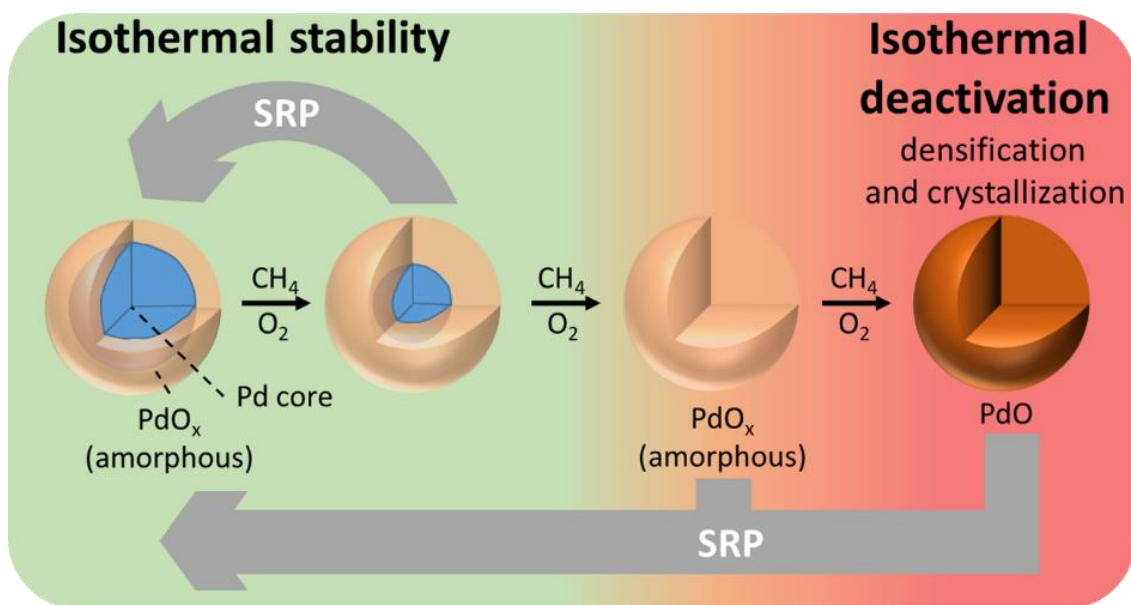
Scheme 3.1. Schematic representation of the elementary steps promoting isothermal stability under SRP mode or causing isothermal deactivation under static mode at T > 430 °C.

3.4 Conclusions

Water is known to severely but reversibly deactivate Pd/Al_2O_3 catalysts for CH_4 oxidation under static reaction conditions. In this work, we show that short reductive pulses (SRP) activate a 2 wt% Pd/Al_2O_3 catalyst and maintain it in a highly active state under continuous feed of water. The structural changes induced by activation through repeated SRP overcome also the deactivating effects of thermal and hydrothermal aging at comparable Pd particle size. In-depth operando XAS analysis revealed that under static lean CH_4 oxidation mode Pd is fully oxidized. In contrast, SRP preserves the catalyst in a partially reduced state. An optimal window of reduced Pd content between 25 and 65 % was determined from LCF analysis of the XANES data. Based on time-resolved LCF and EXAFS analysis as well as available kinetic models, we see that PdO reoxidation after each reducing pulse under wet lean CH_4 oxidation conditions follows the Cabrera-Mott mechanism. The high CH_4 oxidation activity and stability in SRP mode rely on creating and maintaining amorphous PdO_x in contact or around metallic Pd. As long as metallic Pd is present, it acts as a reservoir for defects that

maintain the amorphous character of the PdO_x phase. If it is fully consumed, PdO_x densifies and crystallizes leading to the loss of activity in wet feed. Deactivation induced by crystallization and densification can be reversed by SRP. We believe that these findings bear practical relevance for the control of unburnt CH_4 emissions as SRP operation can be applied in modern gas engines by means of the engine control unit similar to the O_2-dithering operation of three-way catalysts.

Chapter 4 CH_4 steam reforming: efficient route for methane abatement over Pd/Al_2O_3 using short reducing pulses

4.1 Introduction

The beneficial effect of short reducing pulses was established for wet lean CH_4 oxidation conditions (Chapter 3). By periodically regenerating the Pd active sites for CH_4 oxidation (PdO_x), high isothermal stability of the catalyst was achieved, while the detrimental effect of water and thermal ageing on the catalytic activity was suppressed. Pairing such periodic operation with operando X-ray absorption spectroscopic measurements provided significant knowledge on the chemistry of CH_4 oxidation, and especially on the relation between Pd oxidation state and activity for CH_4 oxidation.

In this Chapter, the same material (Pd/Al_2O_3) and operating conditions (SRP; O_2 cut-off for 3 s every 5 min) were used while the complexity of the gas feed composition was increased step-wise from lean wet CH_4 oxidation to the exhaust feed of stoichiometric NG engines. This strategy allowed evaluation of the effect of each pollutant, as well as O_2 concentration, and temperature on both, the catalytic activity and the Pd redox response to periodic operation. The results demonstrated that both, Pd^0 and PdO_x species are active for CH_4 oxidation but through different reaction routes. The presence of PdO species allows CH_4 oxidation by O_2 (but limited NO reduction), whereas the ubiquity of Pd^0 species promotes CH_4 steam reforming (CH_4-SR) and thus simultaneous high conversion of all pollutants, including NO. The effect of each pollutant (CH_4, CO, NO) on the Pd redox dynamics when performing short reducing pulses, was also reported in this Chapter. The presence of CO in the exhaust feed, under lean conditions, leads to the rapid release of vacant Pd sites for the dissociation of O_2 which, in turn, allows for fast and complete reoxidation of the Pd nanoparticles. In contrast, the presence

of NO inhibits PdO growth due to the blockage/poisoning of the Pd^0 surface sites, which consequently limits the O_2 adsorption and dissociation on the Pd surface. Finally, the partial pressure of O_2 and the pollutants were shown to significantly influence the catalyst redox properties as well as the collision factor.

4.2 Materials and methods

4.2.1   Material synthesis

The catalyst, 1.6 wt% Pd/γ-Al_2O_3 doped with lanthanum (4 wt%), was kindly provided by Umicore in powder form.

4.2.2   Catalytic study

Tables 4.1 and 4.2 present the different gas mixtures and corresponding O_2 concentrations used in this Chapter.

Table 4.1. Reactant concentrations used in the different experiments.

	CH_4 conc. [vol%]	CO conc. [vol%]	NO conc. [vol%]	H_2O conc. [vol%]
Concentrated conditions	1	4.6	1	5
Diluted conditions	0.15	0.7	0.16	5

Table 4.2. O_2 concentration used in the different experiments.

			CH_4	CH_4-CO	CH_4-NO	CH_4-CO-NO
O_2 conc. [vol%]	Lean conditions	Concentrated conditions	4	8.6	3	7.6
		Diluted conditions	0.6	1.3	0.44	1.14
	Stoichiometric conditions	Concentrated conditions	2	4.3	1.5	3.6
		Diluted conditions	0.3	0.65	0.22	0.57

4.3 Results and discussion

4.3.1 Lean CH_4 oxidation

Catalytic results

The beneficial effect of short reducing pulses (SRP) for wet lean CH_4 oxidation was confirmed over this 1.6 wt% Pd/Al_2O_3 catalyst (154.3 m^2g^{-1}; Figure B1-2) in the presence of 5 vol% H_2O (Figure 4.1a). It should be mentioned that lower H_2O concentrations were used in this study, compared to Chapter 3 (5 vs 10 vol%). Indeed, this work aimed to progressively switch from lean wet CH_4 oxidation conditions (1 vol% CH_4, 4 vol% O_2, 10 vol% H_2O) to the exhaust feed composition of stoichiometric NG engines (0.15 vol% CH_4, 0.16 vol% NO, 0.7 vol% CO, 0.57 vol% O_2, 5 vol% H_2O). Hence, the first step was to decrease the water concentration. As observed in Chapter 3, the temperature of 50 % CH_4 conversion ($T_{50\%}$) shifted from 370 °C in static operation, to 347 °C under SRP operation (2nd heating ramp; Figure B3). Under SRP conditions, an activation pulse above 430 °C was necessary to raise CH_4 conversion to higher levels compared to the static mode. H_2 formation, which was triggered concomitantly to this activation pulse (Figure B3) mirrored the start of catalyst reduction (thus activation) by CH_4. CH_4 conversion remained significantly higher throughout the subsequent

cooling segment compared to static operation and displayed a wide positive hysteresis (Figure 4.1a). The activity remained high in the subsequent heating/cooling cycle as the catalyst had already been activated (Figure B3).
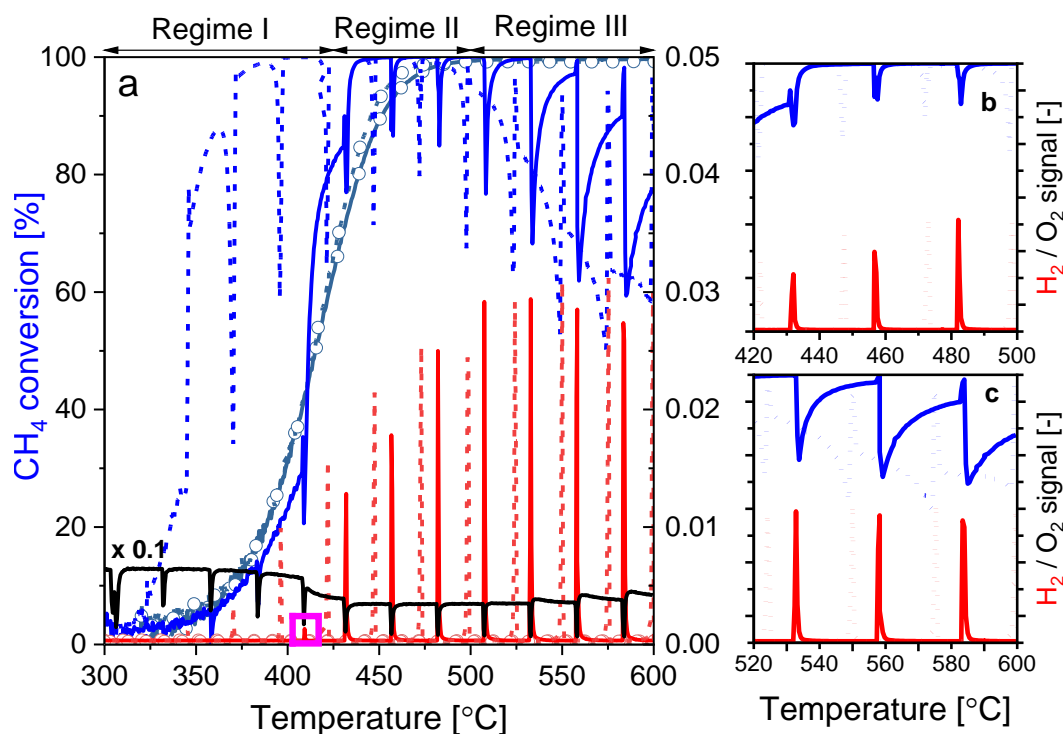
Figure 4.1. (a) CH_4 conversion, as well as H_2 (red) and O_2 (black) MS signals during heating (—) and cooling (---) ramps, under static (-o-) and SRP (—) wet lean concentrated conditions. (b) Inset between 420 and 500 °C. (c) Inset between 520 and 600 °C. The first H_2 appearance during the heating ramp is at 410 °C. The pink rectangles highlight the first H_2 appearance during the heating ramp. Conditions: 1 vol% CH_4, 4 vol% O_2, 5 vol% H_2O; WHSV = 240 $Lh^{-1}g^{-1}$.

The response of CH_4 oxidation upon a reducing pulse varied with temperature. To facilitate the interpretation, the temperature range was divided into three windows: 300 - 425 °C (regime I), 425-500 °C (regime II), and 500-600 °C (regime III). In the first two temperature regimes (Figure 4.1b), the decrease in conversion upon a reducing pulse was short, attesting for a rapid regain in activity, while the recovery after each reducing pulse was slower and incomplete in regime III (Figure 4.1c), causing overall lower activity levels. Towards the end of regime III (> 575 °C; Figure 4.1c), a sharp increase in CH_4 conversion to ca. 95 % was induced for

ca. 20 s upon the O_2 cut-off but was followed by a dip in conversion (51 %). This phenomenon was emphasized in the cooling ramp and maintained up to 480 °C.

Closer inspection of the MS signals demonstrated that between 380 and 500 °C (temperature regimes I-II; Figure 4.2a) the CH_4 signal increased during a reducing pulse, while those of CO_2 and H_2O decreased. This observation evidences that under these conditions CH_4 oxidation by O_2 was the prevailing reaction pathway. In temperature regime III (> 500 °C; Figure 4.2b), in a reducing pulse, the decrease in the CH_4 signal was accompanied by an increase in both CO_2 and CO signals and a decrease in the H_2O signal. If direct CH_4 oxidation by O_2 was taking place, the H_2O production should have occurred, however, the decrease in the H_2O signal is taken as evidence that the CH_4 steam reforming (CH_4-SR) and the water gas shift (WGS) reaction occurred at high temperatures during the O_2 cut-offs.
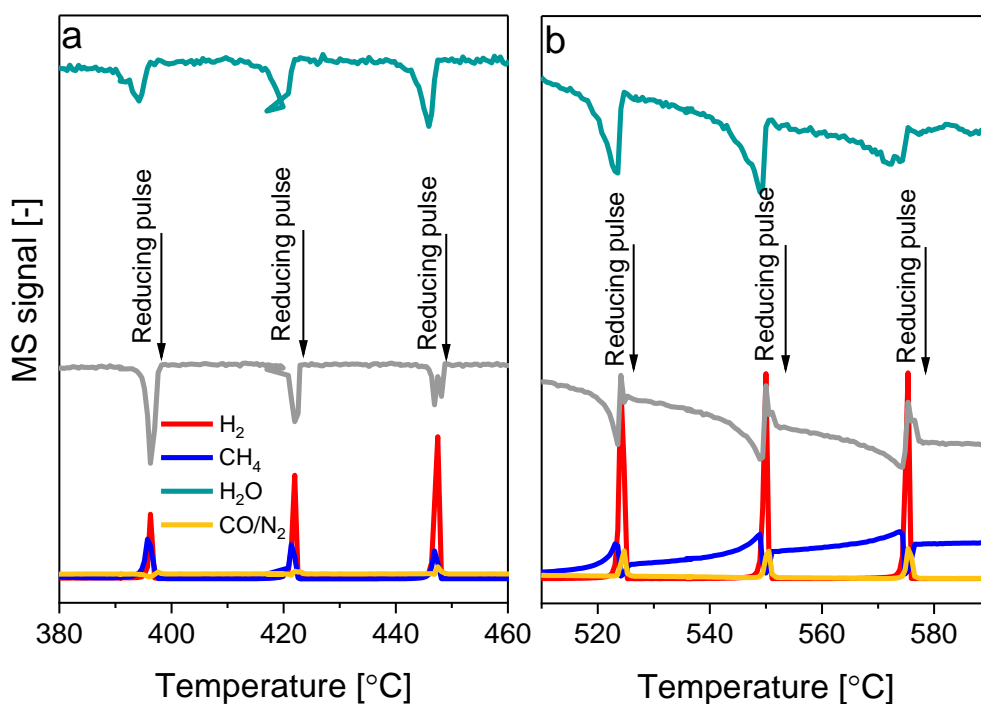

Figure 4.2. MS signals of H_2, CH_4, H_2O, CO/N_2, and CO_2 in the first cooling ramp under SRP wet lean concentrated conditions in the presence of CH_4/H_2O, between (a) 380 and 460 °C, and (b) 510 and 590 °C. Conditions: 1 vol% CH_4, 4 vol% O_2, 5 vol% H_2O; WHSV = 240 Lh^{-1}g^{-1}.

Spectroscopic results

The linear combination fit (LCF) analysis of the X-ray absorption near edge spectroscopic (XANES) region measured at the Pd K-edge at 435 °C (temperature regime II; Figure 4.3a-b), revealed that the PdO content reached very low values (2 %) in a reducing pulse and increased up to 80 % in the subsequent lean phase. Hence, decreasing the water concentration allowed accessing higher Pd^0 contents (cf. Figure 3.3 in Chapter 3). Moreover, under these conditions, reoxidation occurred in two steps. First fast surface oxidation followed by a slower reoxidation of the Pd bulk [67,114]. The fits of the Fourier Transform extended X-ray fine structure (FT-EXAFS; Figure 4.4a) demonstrated that at 435 °C, the contribution from the Pd-O scattering path (2.018 Å) in a reducing pulse was small but present. Despite the loss of conversion upon the O_2 cut-off, the activity started to recover as soon as the PdO content was above 35 % (Figure 4.3a-b), in agreement with the optimal interval of PdO content for wet lean CH_4 oxidation (35-75 %) (cf. Chapter 3). Furthermore, in the isothermal experiments at 575 °C (temperature regime III; Figure 4.3c-d), only Pd^0 was present in the reducing pulse, which correlates with the increase in CH_4 conversion (Figure 4.1a, c). Fitting of the EXAFS region confirmed that at 575 °C no contribution from the Pd-O scattering path was present (Figure 4.4a). In the lean phase of the pulses, reoxidation of the catalyst also took place in two steps, but the second oxidation step was slow and limited to a maximum PdO content of 15 % (Figure 4.3c-d). This behaviour was likely caused by the formation of strongly bonded oxygen atoms at the Pd^0 surface, which greatly suppress nucleation and growth of the active species of bulk PdO [223,224]. The presence of such a strongly chemisorbed oxygen layer is typical when metal Pd particles are generated at high temperatures [223]. These surface oxide species were not formed at 435 °C because of the easier reoxidation of small metallic Pd domains generated from incomplete reduction (Figure 4.3a-b) [223]. Furthermore, in the lean phase, CH_4 conversion was higher at 435 °C (100 %) than at 575 °C (85 %; Figure 4.3) because CH_4 oxidation is more efficient when the Pd nanoparticles are bulk oxidized than when they are covered with chemisorbed oxygen. Indeed, when a dense chemisorbed oxygen layer surrounds Pd^0 clusters, there are no surface Pd^0 sites for the concerted C-H bond activation by Pd^0 and PdO which was proposed to produce a four-center transition state $(H_3C \cdots Pd_{ox} \cdots H \cdots O_{ox})^{\ddagger}$ [182].
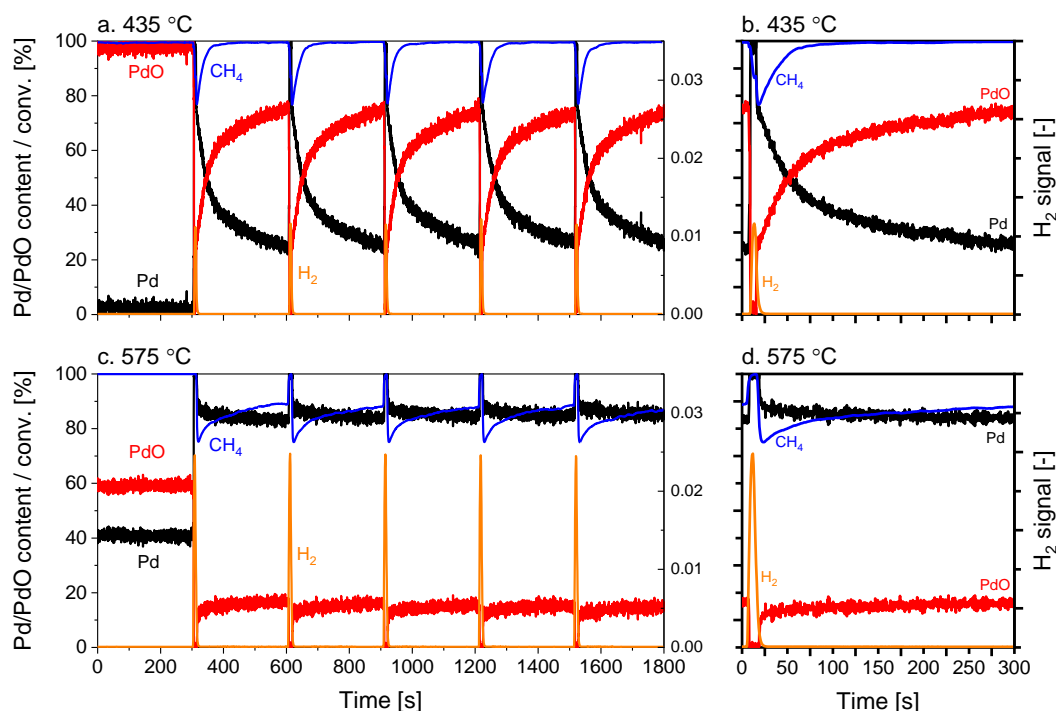
Figure 4.3. CH_4 conversion, Pd phase content (PdO / Pd), and H_2 MS signal at (a-b) 435 °C (c-d) 575 °C under SRP wet lean concentrated conditions, in the presence of CH_4/H_2O. Conditions: 1 vol% CH_4, 4 vol% O_2, 5 vol% H_2O; WHSV = 240 $Lh^{-1}g^{-1}$.

Finally, the catalytic results from operando XAS measurements showed that at 575 °C, CH_4-SR persisted for ca. 9 s (Figure 4.3c-d). The R-space plots obtained at different times after a reducing pulse (Figure 4.4b) demonstrated that the Pd-O scattering path was negligible up to 6 s after the O_2 cut-off. However, after 9 s, when CH_4-SR vanished, the Pd-O scattering intensity was comparable to that at 435 °C, at t = 0 s. These results show that as long as the Pd-O scattering path is present, only CH_4 oxidation by O_2 occurs (i.e. 435 °C; Table B1), whereas if only the Pd-Pd scattering path is present CH_4-SR is promoted. Hence, it is clear that at 435 °C the Pd-O contribution in a reducing pulse was too high to induce CH_4-SR, while the PdO content was too low (2 %) to achieve high CH_4 conversion levels following oxidation by O_2. The lack of fit of the LCF analysis is shown in Figure B4.

The results show that both, Pd^0 and mixed Pd^0/PdO (PdO_x) species are active toward CH_4 oxidation but through different reaction routes. The results obtained in Chapter 3, revealed that the presence of PdO species (in PdO_x) permits CH_4 oxidation by O_2 to take place, which is enhanced as the Pd^0 content increases from 0 to

25 % and is then maintained high up to 65 % (Figure 3.6). The results of this study show higher CH_4 conversions for the same Pd^0 content due to the lower inhibition effect of H_2O (lower H_2O concentration compared to Chapter 3). However, because the H_2O content was lower, higher Pd^0 contents were reached compared to our previous work (Chapter 3). Hence, in this work, CH_4 oxidation by O_2 was seen to be inhibited when the Pd^0 content is between 80 and 98 %, which we assign to the presence of a dense chemisorbed oxygen layer around the Pd^0 core (Figure 4.5). It should be mentioned that this dense surface oxide layer, and therefore Pd^0 content between 80 and 98 %, is only formed if the Pd species are fully reduced before reoxidation of the catalyst. Finally, when the Pd species are fully reduced, CH_4-SR is promoted, leading to high CH_4 conversion levels (Figure 4.5).
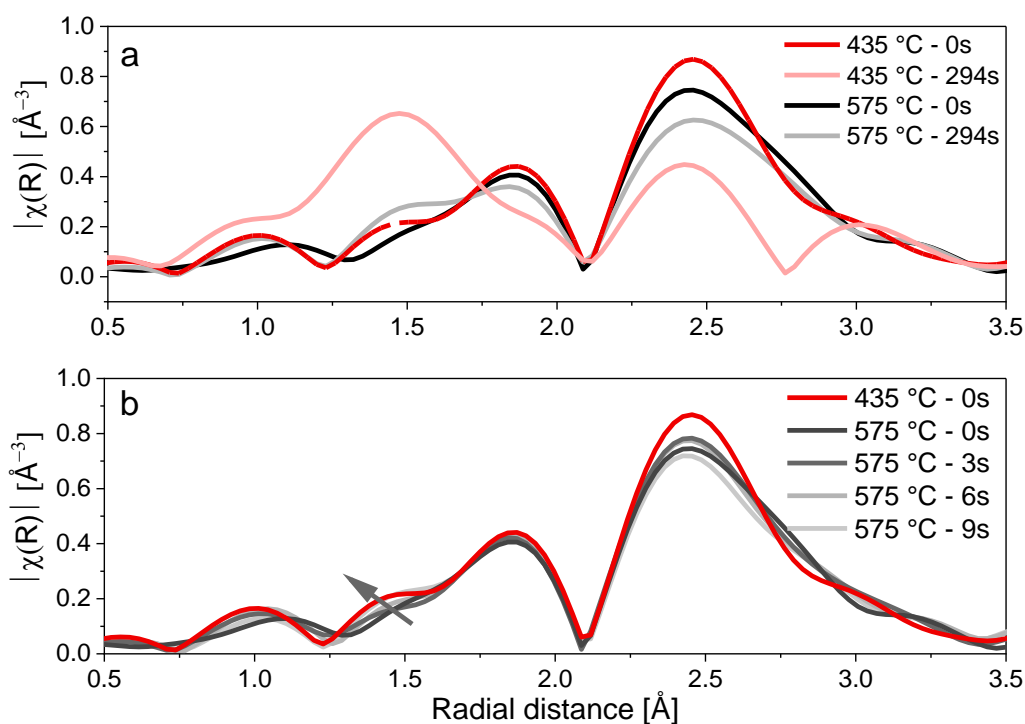
Figure 4.4. Pd K-edge FT-XAFS (not phase corrected) illustrating the change in intensities of Pd-Pd (from Pd) and Pd-O (from PdO) scattering paths (a) at 0 s and 294 s after a reducing pulse at 435 °C and 575 °C and (b) as a function of time at 575 °C as well as during a pulse at 435 °C under SRP wet lean concentrated conditions, in the presence of CH_4/H_2O. Conditions: 1 vol% CH_4, 4 vol% O_2, 5 vol% H_2O; WHSV = 240 $Lh^{-1}g^{-1}$.
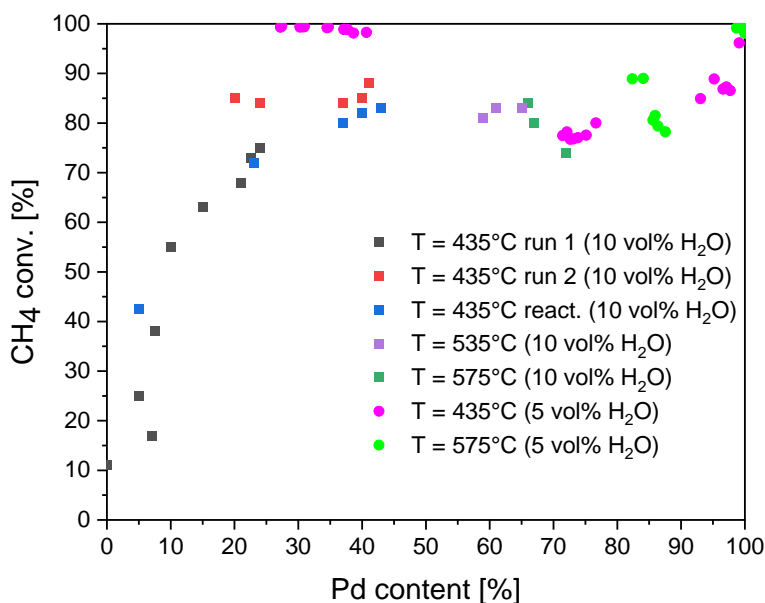
Figure 4.5. Updated version of Figure 3.6, based on the results achieved in this Chapter.

4.3.2 Lean CH_4 oxidation: effect of CO and NO

Since SRP operation is beneficial for wet lean CH_4 oxidation, the same approach was applied to the full exhaust gas composition (CH_4, CO, NO, H_2O) under lean conditions. For this purpose, the CO and NO concentrations were proportional to that of CH_4 and thus much higher than required when working with simulated exhaust feed of stoichiometric NG engines (Table 4.1).

Catalytic results

When CO was co-fed to CH_4 and H_2O (Figure 4.6a), the $T_{50\%}$ value for CH_4 conversion was significantly lower under SRP conditions (317 °C) compared to static operation (407 °C). Similar behaviour was observed in the presence of all pollutants, wherein CH_4 conversion reached 50 % at 321 and 368 °C in SRP and static operation, respectively (Figure 4.7a). Furthermore, unlike with CH_4 only, in the presence of CO, the reducing pulses did not induce any significant increase in reaction rate in the temperature range evaluated (Figure 4.6a, and Figure 4.7a), suggesting that either no activation pulse was needed or the activation pulse occurred below 300 °C. These results indicate that CO activates (and thus reduces) the catalyst at lower temperatures than CH_4.

The partial reduction of the catalyst at 300 °C in the presence of CO, was inferred from the H_2 spikes in the reducing pulses (Figure 4.6a, Figure 4.7a), contrary to the appearance of H_2 only after the 5th pulse for CH_4/H_2O and $CH_4/NO/H_2O$ (430 and 395 °C, respectively; Figure 4.1a, Figure 4.8a).

Figure 4.6. (a) CH_4 conversion, as well as H_2 (red) and O_2 (black) MS signals during heating (—) and cooling (---), under static (-o-) and SRP (—) wet lean concentrated conditions in the presence of $CH_4/CO/H_2O$. (b) Inset between 420 and 500 °C. (c) Inset between 520 and 600 °C. The orange line in insets b and c represents CH_4 conversion under lean concentrated conditions during the heating ramp in the presence of CH_4/H_2O. Conditions: 1 vol% CH_4, 4.6 vol% CO, 8.6 vol% O_2, 5 vol% H_2O; WHSV = 240 $Lh^{-1}g^{-1}$.

In the temperature regime I and/or II and in the presence of all pollutants (Figure 4.7c), the recovery in activity after a reducing pulse was longer than with CH_4 alone (Figure 4.1b). While in the presence of CO, CH_4, and H_2O, the reducing pulses were as narrow as with CH_4 only (Figure 4.6b), in the presence of NO, CH_4, and H_2O, the recovery after each pulse was slow and the extent limited (Figure 4.8c). Hence, the presence of NO appears to inhibit the activity recovery after each O_2 cut-off. In temperature regime III, the recovery after a reducing pulse was moderate for all the gas compositions evaluated (Figure 4.6c, Figure 4.7d, and Figure 4.8d).

Interestingly, for all gas mixtures, CH_4 conversion increased shortly when the O_2 was cut-off before dropping to ca. 50 % and recovering slowly in the lean phase.

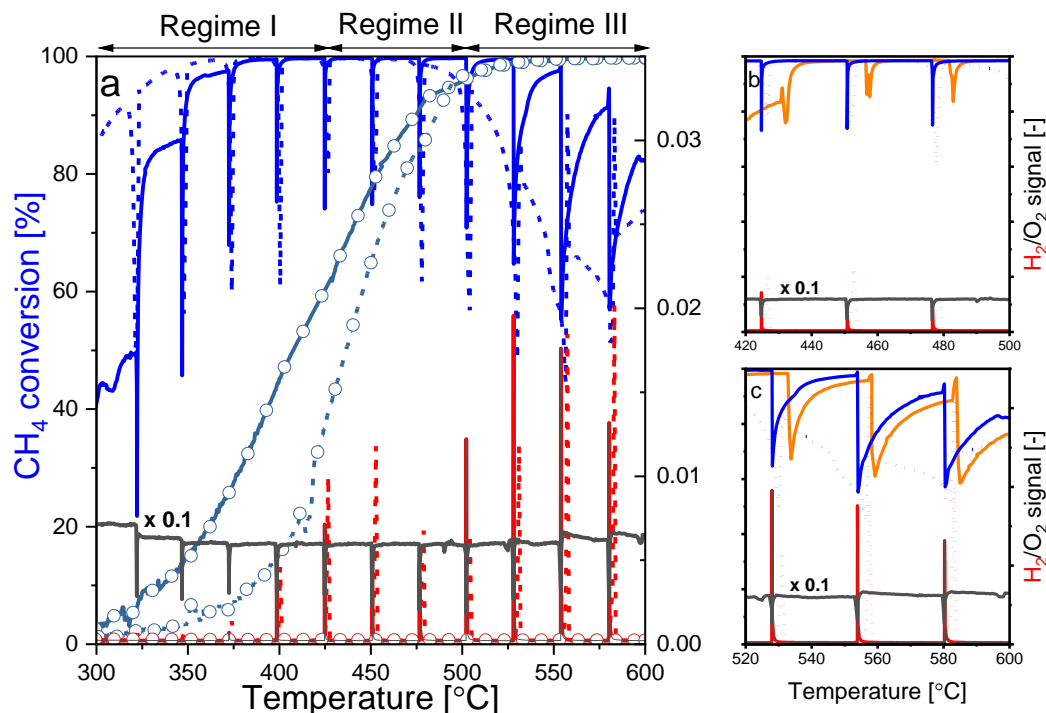Figure 4.7. (a) CH_4 and (b) NO conversions, as well as H_2 (red) and O_2 (black) MS signals during heating (—) and cooling (---), under static (-o-) and SRP (—) wet lean concentrated conditions in the presence of $CH_4/CO/NO/H_2O$. (c) Inset between 420 and 500 °C. (d) Inset between 520 and 600 °C. The orange line in insets c and d represents CH_4 conversion under SRP lean concentrated conditions during the heating ramp in the presence of CH_4/H_2O. Conditions: 1 vol% CH_4, 1 vol% NO, 4.6 vol% CO, 7.6 vol% O_2, 5 vol% H_2O; WHSV = 240 $Lh^{-1}g^{-1}$.

Furthermore, a positive hysteresis is visible in the cooling segment in the $CO/CH_4/H_2O$ feed, wherein CH_4 conversion reached 82 % at 300 °C (40 % higher compared to the heating segment; Figure 4.6a). On the contrary, the presence of NO induced a negative hysteresis, during which the activity was never fully recovered (ca. 90 % maximum CH_4 conversion; Figure 4.7a, Figure 4.8a), confirming the inhibiting effect of NO on CH_4 oxidation.

Moreover, CO was always fully converted during the catalytic tests but CO slips were observed during the O_2 cut-offs (Figure B5), which are due to either unreacted CO or partial CH_4-SR. Interestingly, when CO was detected in the reducing pulses, CH_4 conversion increased only after the disappearance of CO (insets of Figure B5), suggesting that CO inhibits CH_4 oxidation.

Finally, in the presence of NO, a sharp increase in NO conversion up to ca. 60-70 % was observed in the reducing pulses (Figure 4.7b, Figure 4.8b).
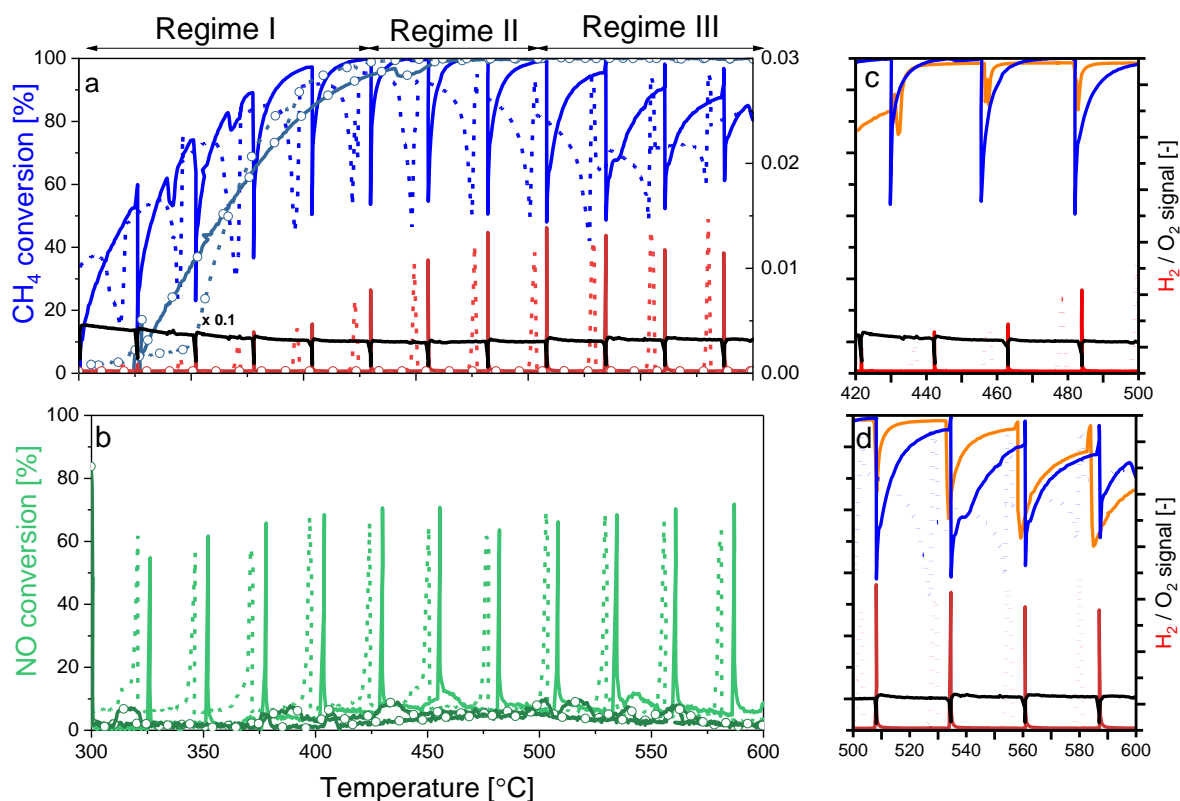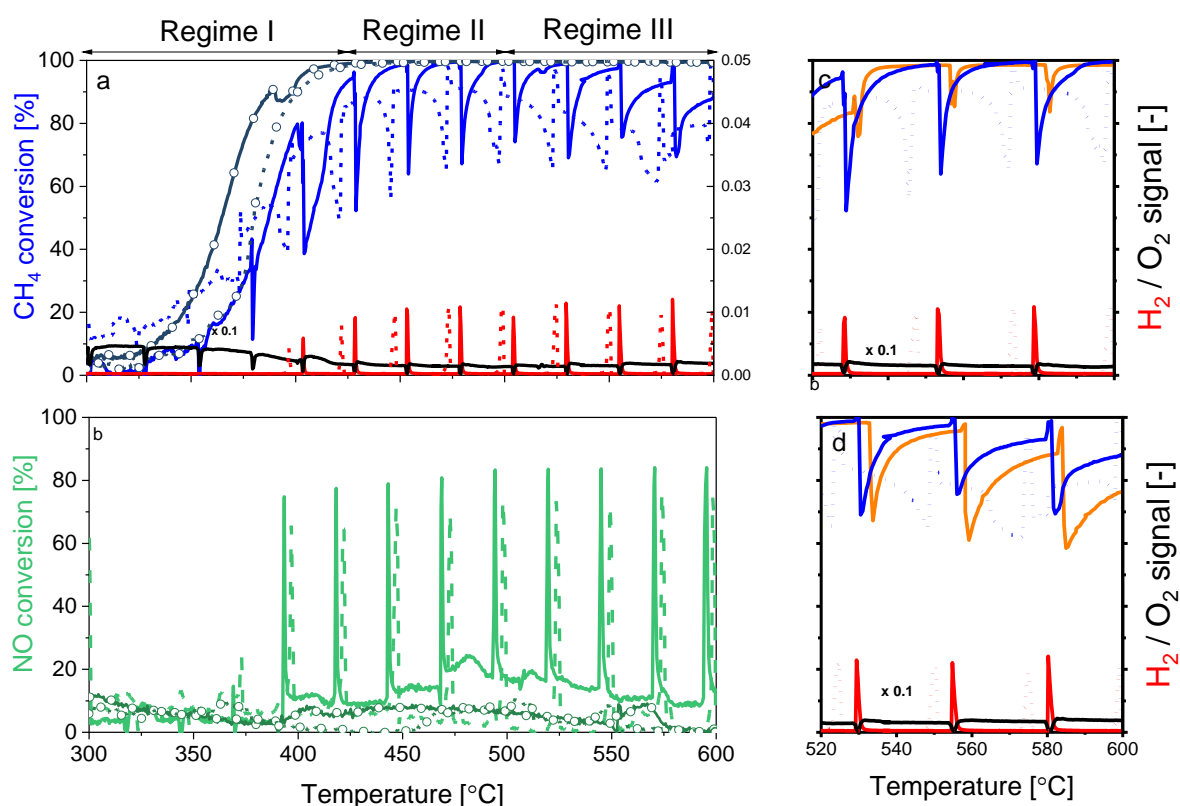

Figure 4.8. (a) CH_4 and (b) NO conversions, as well as H_2 (red) and O_2 (black) MS signals during heating (—) and cooling (---), under static (-o-) and SRP (—) wet lean concentrated conditions in the presence of $CH_4/CO/NO/H_2O$. (c) Inset between 420 and 500 °C. (d) Inset between 520 and 600 °C. The orange line in insets c and d represents CH_4 conversion under lean concentrated conditions during the heating ramp. Conditions: 1 vol% CH_4, 1 vol% NO, 3 vol% O_2, 5 vol% H_2O; WHSV = 240 $Lh^{-1}g^{-1}$.

Spectroscopy results

Figure 4.9a-b shows the operando XAS results achieved at 435 °C in the different gas feeds. While Pd reduction and surface oxidation rates were not affected by the composition of the gas mixture, the bulk oxidation rate was significantly influenced by it.

The presence of CO considerably accelerates the rate of PdO bulk growth compared to the CH_4 feed (Figure 4.9a). We ascribe this observation to the fast CO oxidation rate over the Pd particles in lean conditions, leading to rapid CO desorption from the surface and thus to the rapid release of Pd sites for O_2 dissociation and diffusion into the bulk [225,226]. The Pd species were completely oxidized by the end of the lean phase in the presence of CO (Figure 4.9a). On the other hand, NO appears to inhibit Pd bulk reoxidation since the PdO content only reached 65 % by the end of the lean phase, in marked contrast with the values achieved in CH_4/H_2O (75 %) and $CH_4/CO/H_2O$ (100 %) feeds (Figure 4.9a). This is believed to originate from the high surface coverage of NO over the Pd^0 sites formed in the reducing pulses, whose desorption is inhibited by the presence of O_2 and the subsequent formation of PdO (in the lean phases). Indeed, NO dissociation requires two adjacent Pd^0 sites, therefore when O_2 is reintroduced in the feed after a reducing pulse, the amount of neighbouring Pd^0 sites decreases, and NO is blocked on the Pd surface sites [69–71]. The poisoning of the surface Pd sites by the NO molecules limits the number of available Pd sites for O_2 to adsorb and dissociate on, which in turn slows down the PdO bulk growth. In the CH_4 feed, Pd bulk oxidation was slower than in the presence of CO but faster than with NO. Hence, CH_4 limits Pd bulk oxidation due to its slower reaction rate compared to CO. In $CH_4/CO/NO/H_2O$ feed, the kinetics of bulk oxidation was predominantly ruled by the presence of CO, likely due to both, the high CO concentration compared to the other pollutants, the fast CO oxidation rate, and the possible release of NO on the Pd^0 surface via reaction with CO [235-236]. Oxidation was however slower than in the $CH_4/CO/H_2O$ feed due to the discussed inhibitory effect of NO.

The conversions of CH_4 achieved during the operando XAS measurements performed at 425 °C in the different gas feeds (Figure B6) show that the activity after a reducing pulse was fully recovered only once the PdO content was above 35 % which, according to the optimal window of Pd^0 content presented in Figure 4.5,

corresponds to the minimum PdO content necessary to achieve high CH_4 conversions. Because Pd bulk oxidation was faster in the presence of CO, the optimal PdO content (> 35 %) was reached earlier than in the presence of NO, and therefore the recovery of activity after an O_2 cut-off was faster.

Finally, the catalyst remained reduced longer in $NO/CH_4/H_2O$ compared to the other gas compositions (Figure 4.9b), demonstrating that the presence of NO maintains the Pd species in their reduced state longer.
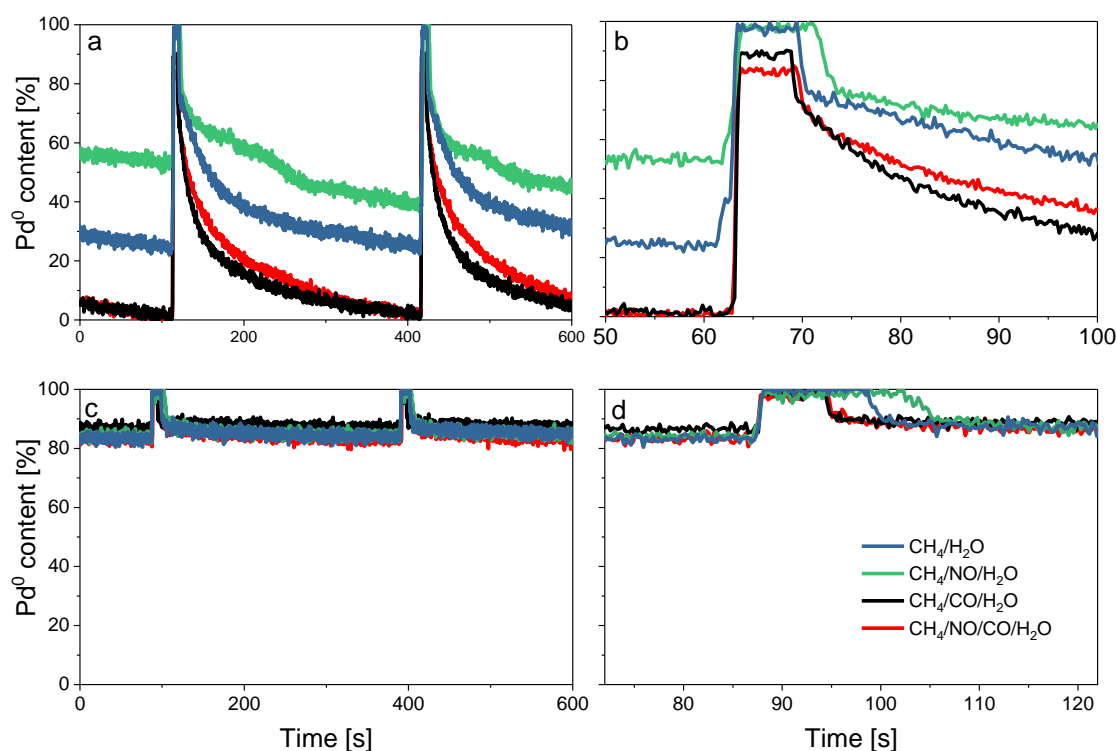
Figure 4.9. Pd^0 content measured at (a-b) 435 °C and (c-d) 575 °C in the presence of (blue) CH_4/H_2O, (green) $CH_4/NO/H_2O$, (black) $CH_4/CO/H_2O$, and (red) $CH_4/NO/CO/H_2O$ under SRP wet lean concentrated conditions (a) over three cycles, (b) inset of one cycle. Conditions: (blue) 1 vol% CH_4, 4 vol% O_2, 5 vol% H_2O; (green) 1 vol% CH_4, 1 vol% NO, 3 vol% O_2, 5 vol% H_2O; (black) 1 vol% CH_4, 4.6 vol% CO, 8.6 vol% O_2, 5 vol% H_2O; (red) 1 vol% CH_4, 1 vol% NO, 4.6 vol% CO, 7.6 vol% O_2, 5 vol% H_2O; WHSV = 240 $Lh^{-1}g^{-1}$.

At 575 °C, the LCF analysis revealed that the kinetics of surface and bulk oxidation were similar for all gas feed compositions (Figure 4.9c-d). In the reducing pulse, only metallic Pd was present which promoted CH_4-SR and high conversion of all pollutants simultaneously (Figure 4.9c-d, Figure B7). In the lean phase, only 17

% PdO formed, suggesting that only the Pd surface species oxidized. The presence of a dense chemisorbed oxygen layer around the Pd^0 core in the lean phase leads to limited activity recovery after a reducing pulse is applied (Figure B7). These results demonstrate that the limited reoxidation of the Pd species at high temperatures is an intrinsic property of the material rather than related to the composition of the feed. Moreover, at this temperature, the inhibition effect of NO on the reoxidation of Pd^0 was even more evident from the delayed reoxidation observed after a reducing pulse.

In summary, CO appeared to considerably improve CH_4 abatement in SRP mode since it allowed activating the catalyst at a lower temperature than CH_4. Therefore, high CH_4 conversion levels were obtained already at 300 °C. The operando XAS results showed that the fast CO reaction rate over Pd induced the formation of vacant Pd sites for dissociative O_2 adsorption, leading to rapid and complete reoxidation of the Pd particles within the 5 min lean phase of SRP. The presence of NO, however, limited the PdO growth due to blockage of the Pd^0 sites by the NO adsorbed on the surface in the rich pulses. At high temperatures (> 550°C), the catalytic behaviour and the Pd redox dynamics under SRP operation were similar for all gas feed compositions. In a reducing pulse, full reduction to Pd^0 promoted both, CH_4-SR and NO reduction, whereas in the lean phase a surface oxide layer systematically formed around the Pd^0 particles, thus inhibiting both Pd bulk oxidation and CH_4 oxidation by O_2.

4.3.3 Effect of oxygen and pollutants partial pressures

4.3.3.1 O_2 partial pressure

The effect of the oxygen partial pressure on CH_4 abatement was evaluated under stoichiometric conditions ($\lambda = 1$) at the same pollutant concentrations used above (Table 4.1 and 4.2).

Figure B8a, c show that under static conditions an important negative hysteresis was observed with all gas feeds. In CH_4/H_2O and $CH_4/CO/H_2O$ feeds, the activity dropped abruptly as soon as the temperature was decreased, and was followed by partial activity recovery below ca. 500 °C. This behaviour is typically associated

with the decomposition of PdO species at high temperatures [64,224,227,228], which leads to the fast formation of a stable but less active saturated layer of chemisorbed oxygen around a Pd^0 core when the temperature is decreased [224]. Under such conditions, further oxidation of the Pd particles occurs only at lower temperatures (T = 500 °C in this case), where PdO is thermodynamically favoured over Pd^0 at this O_2 partial pressure [224,229]. As a result, CH_4 conversion increases. Such phenomenon was not observed under lean conditions because the temperature at which PdO decomposes depends on the O_2 partial pressure and requires higher temperatures than 600 °C [227]. In presence of NO (Figure B8b, d) CH_4 conversion decreased monotonously with decreasing temperature in line with the above results, implying that Pd^0 does not oxidize at low temperature with NO and that NO inhibits bulk oxidation of Pd.
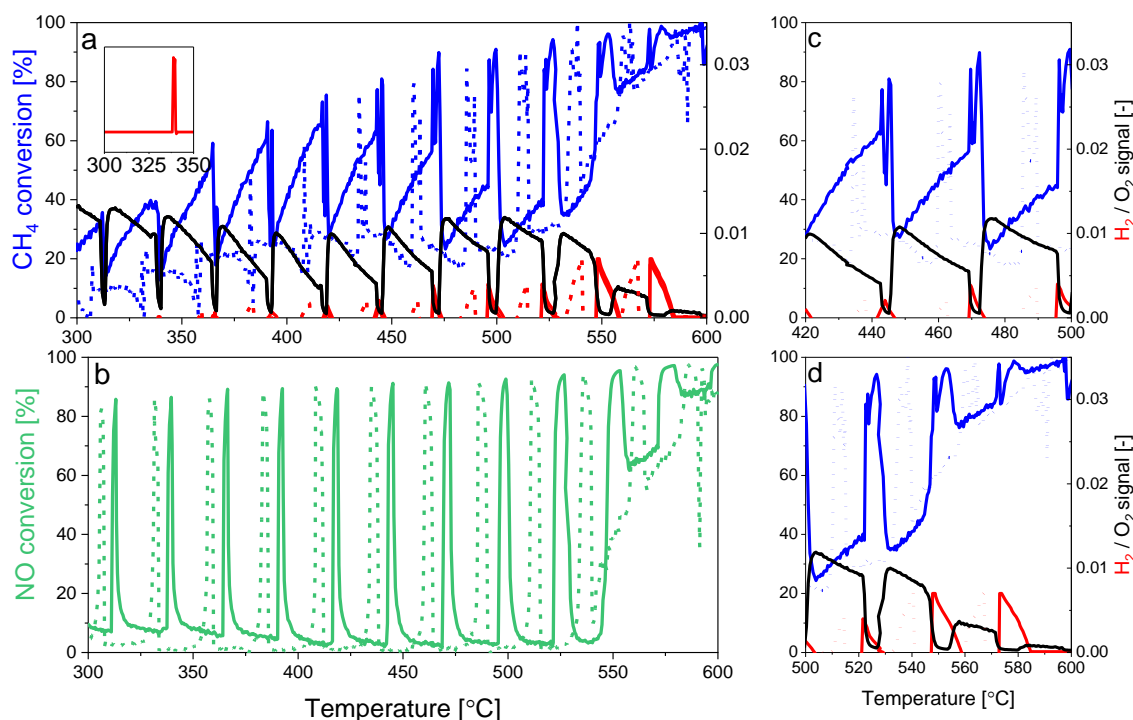
Figure 4.10. (a) CH_4 and (b) NO conversions, as well as H_2 (red) and O_2 (black) MS signals during heating (—) and cooling (- - -) ramps, under SRP wet stoichiometric concentrated conditions, in the presence of CH_4 /NO/CO/H_2O/O_2. (c) Inset between 420 and 500 °C. (d) Inset between 520 and 600 °C. The orange line in insets c and d represents CH_4 conversion under lean concentrated conditions during the heating ramp. Conditions: 1 vol% CH_4, 1 vol% NO, 4.6 vol% CO, 3.8 vol% O_2, 5 vol% H_2O; WHSV = 240 $Lh^{-1}g^{-1}$.

Under SRP conditions in the full gas feed (Figure 4.10), CH_4 conversion reached 20 % at 300 °C, which from the discussion above and Figure B9 was attributed to the presence of CO. On the other hand, long and limited activity recovery was observed after each reducing pulse for all gas mixtures compared to lean conditions (Figure B9-10), regardless of the temperature. The phenomenon was exacerbated in the presence of NO. Hence, it can be concluded that under stoichiometric conditions, the slow activity recovery after each O_2 cut-off was related to the low O_2 partial pressure, while the presence of NO further inhibited the activity recovery process (cf. Pd oxidation). Due to the lower O_2 concentration flown to the system, the Pd species reduced at lower temperatures compared to lean conditions, as confirmed by XAS measured at 435 °C (Figure 4.11a vs Figure 4.9) as well as by the breakthrough of H_2 at ca 338 °C (Figure 4.10a). In turn, this promoted spikes in conversions of both, CH_4 and NO as the pulses were performed. However, when complete Pd reduction is achieved, only limited PdO bulk growth was obtained in the lean phases, which consequently led to a rapid decrease in CH_4 conversion (Figure 4.11). Hence, under these conditions, because Pd reduction is induced at ca 338 °C, moderate CH_4 oxidation by O_2 is observed in the lean phase above this temperature.

In the full gas feed, the Pd^0 content only reached 70 % by the end of the lean phase at 435 °C compared to full re-oxidation under lean conditions. This suggests that under stoichiometric conditions the presence of CO did not increase the rate of bulk oxidation of Pd (Figure 4.11a). According to Engel et al. [225] when the $CO:O_2$ ratio is higher than 0.33, each oxygen ad-atom immediately reacts making the oxygen adsorption rate limiting. On the contrary, when the $CO:O_2$ ratio is lower than 0.33, the oxygen coverage increases and the reaction rate becomes independent of the O_2 partial pressure. Under the present conditions, $CO:O_2 > 0.33$ (3.8 vol% O_2, 4.6 vol% CO) which therefore supports the results reported by Engel et al. [225]. On the other hand, it appears that Pd bulk oxidation was faster in the CH_4 feed than in $CH_4/CO/H_2O$ (Figure B11) most probably due to the slower reaction rate of CH_4 oxidation compared to CO oxidation leading to longer O_2 residence time on the catalyst surface, and a thus higher probability for O_2 to diffuse into the particle.

At high temperatures (> 550 °C), the overall conversion increased with temperature and both, CH_4 and NO conversions reached almost 100 % at 600 °C (Figure 4.10). However, the high activity vanished as soon as the

temperature was decreased, and remained low in the lean phases during the entire cooling segment. Nonetheless, NO reduction still increased in each pulse and remained high for longer as long as the catalyst was in its reduced state.
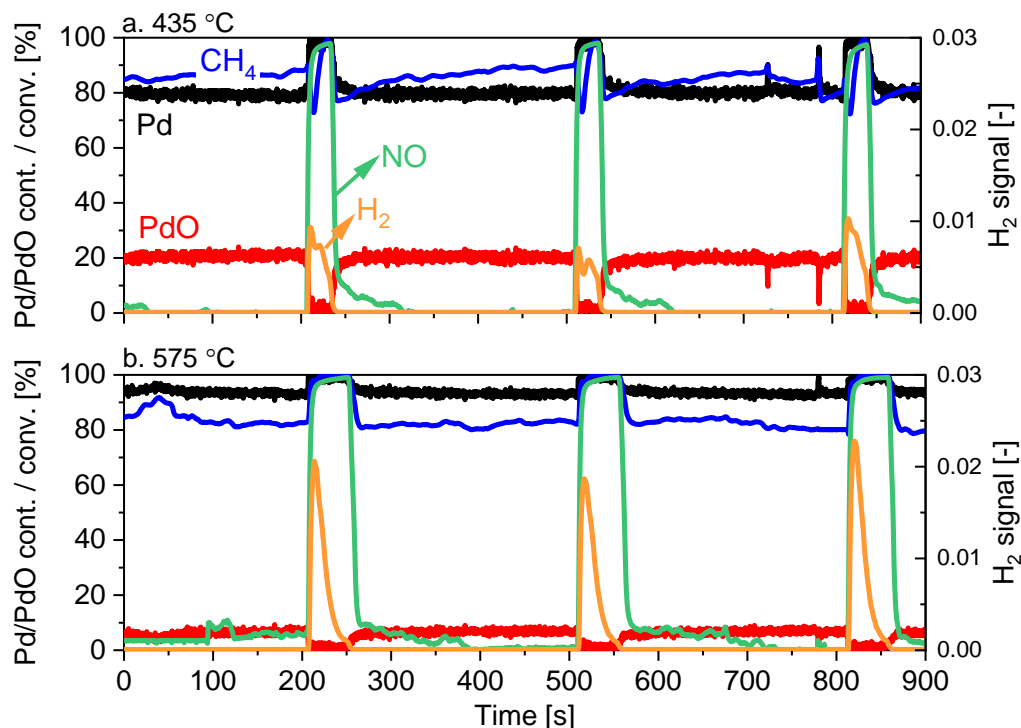
Figure 4.11. CH_4 and NO conversions, Pd phase content (PdO / Pd), and H_2 MS signals at (a) 435 °C (b) 575 °C under SRP wet stoichiometric concentrated conditions in the presence of $CH_4/CO/NO/H_2O$. Conditions: 1vol% CH_4, 1 vol% NO, 4.6 vol% CO, 3.8 vol% O_2, 5 vol% H_2O; WHSV = 240 $Lh^{-1}g^{-1}$.

These findings show that under such stoichiometric conditions, complete Pd reduction can be triggered at lower temperatures than under lean concentrated conditions. As a consequence, high NO and CH_4 conversions could be achieved at lower temperatures as NO reduction and CH_4-SR are efficient over Pd^0 species. However, this also inevitably leads to limited abatement rates in the lean phase due to the formation of Pd surface oxide species (see comparative graph in Figure B10). Overall, under stoichiometric conditions, SRP operation has a detrimental effect on the activity.

4.3.3.2 Reactant partial pressure

A lower O_2 partial pressure was further evaluated under lean conditions ($\lambda = 2$) by decreasing the pollutants concentrations (diluted conditions; see Table 4.1-2).

Under SRP operation (Figure 4.12), CH_4-SR was promoted in the reducing pulses already in the temperature regime I leading to improved conversion rates, but limited activity in the lean phases. Hence, despite the lean conditions, full catalyst reduction was achieved already at low temperatures and maintained for long times as confirmed by the operando XAS experiments at 435 °C (Figure 4.13). Hence, under these conditions, the catalytic behaviour seemed to be guided by the low O_2 partial pressure rather than the lean conditions (Figure 4.12; Figure B12).
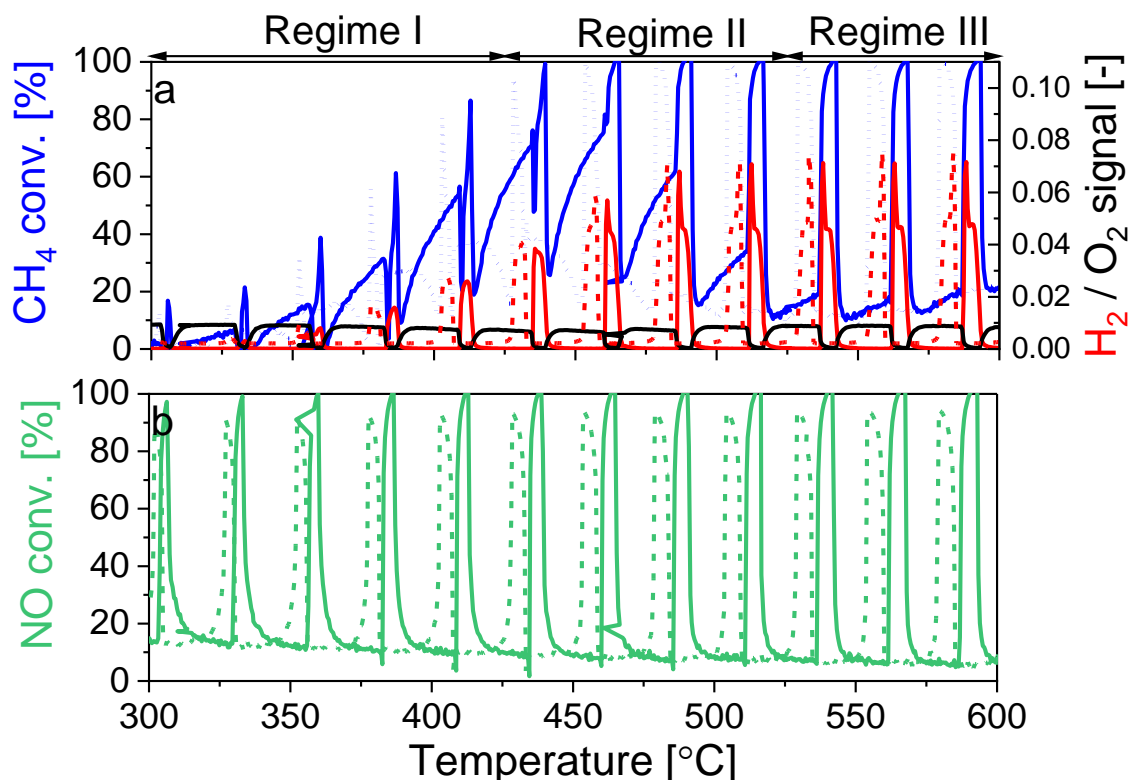

Figure 4.12. (a) CH_4 and (b) NO conversions as well as H_2 (red) and O_2 (black) MS signals under SRP wet lean diluted conditions in the presence of $CH_4/CO/NO/H_2O$. Conditions: 0.15 vol% CH_4, 0.16 vol% NO, 0.7 vol% CO, 1.14 vol% O_2, 5 vol% H_2O; WHSV = 240 $Lh^{-1}g^{-1}$.

The LCF analysis of the experiment performed at 435 °C demonstrated that the catalyst fully reduced in a reducing pulse and remained in this state longer than under lean concentrated conditions but shorter than under stoichiometric concentrated conditions (Figure B13). In the lean phase, Pd oxidation occurred faster and to a higher extent compared to stoichiometric concentrated conditions (Figure B13). CH_4 conversion achieved under lean diluted conditions and stoichiometric concentrated conditions were similar (ca. 80 %) though the Pd species were more oxidized in the former case. These results show that Pd reoxidation was influenced by the relative O_2 concentration (cf. λ value), whereas the activity was ruled by the total O_2 partial pressure. It is also clear that when working with diluted concentrations the optimal PdO window to achieve high CH_4 activity is shifted towards higher PdO content. This is especially apparent when overlapping the Pd content, and CH_4 conversion obtained when feeding only CH_4, under the different conditions evaluated (Figure B14). The Pd reoxidation kinetics under stoichiometric concentrated and lean diluted conditions were similar but the conversion values under lean diluted conditions were always 20 % lower. Moreover, in the presence of all pollutants, when the PdO content was around 45 %, conversion reached 70 % under lean diluted conditions, 80 % under stoichiometric concentrated conditions, and 95 % under lean concentrated conditions.

Calculations of the apparent activation energy ($E_{A,app}$) and the collision factor (A) were performed using the results obtained in SRP conditions with only CH_4 (Table 4.3) while $E_{A, app}$ increased with decreasing pollutant partial pressures. The frequency factor decreased considerably with the partial pressure of O_2 and pollutants due to the likeliness for collisions to occur. Hence, as the activity is strongly dependent on the frequency factor, which in turn depends on the reactants' partial pressures the efficiency of CH_4 oxidation by O_2 will decrease as the concentration of the reactant in the feed decreases.

Table 4.3. Apparent Activation Energy ($E_{A,app}$) and collision factor (A) under SRP mode calculated from the 1st heating ramp in the presence of CH_4/ H_2O. Conditions: see Table 4.1-2, WHSV = 240 $Lh^{-1}g^{-1}$.

		Concentrated conditions		Diluted conditions	
		Lean cond.	Stoich. cond.	Lean cond.	Stoich. cond.
$E_{A,app}$ [kJ mol^{-1}]	SRP op.	70 ± 4.0	108.8 ± 6.1	117.3 ± 0.9	125.2 ± 1.0
A [-]	SRP op.	1018 ± 0.01	0.01 ± 0.01	0.003 ± 0.02	0.0005 ± 0.02

Finally, a comparison of the temperatures at which CH_4-SR started over metallic Pd species under SRP operation (Table 4.4), reveals that CH_4-SR occurred at lower temperatures under lean diluted conditions, in the presence of CH_4/H_2O than under stoichiometric concentrated conditions since the O_2 partial pressure was lower despite the excess O_2, and the pollutants concentrations were lower. Therefore, the temperature at which Pd reduces was strictly related to the O_2 partial pressure rather than the lambda value considered.
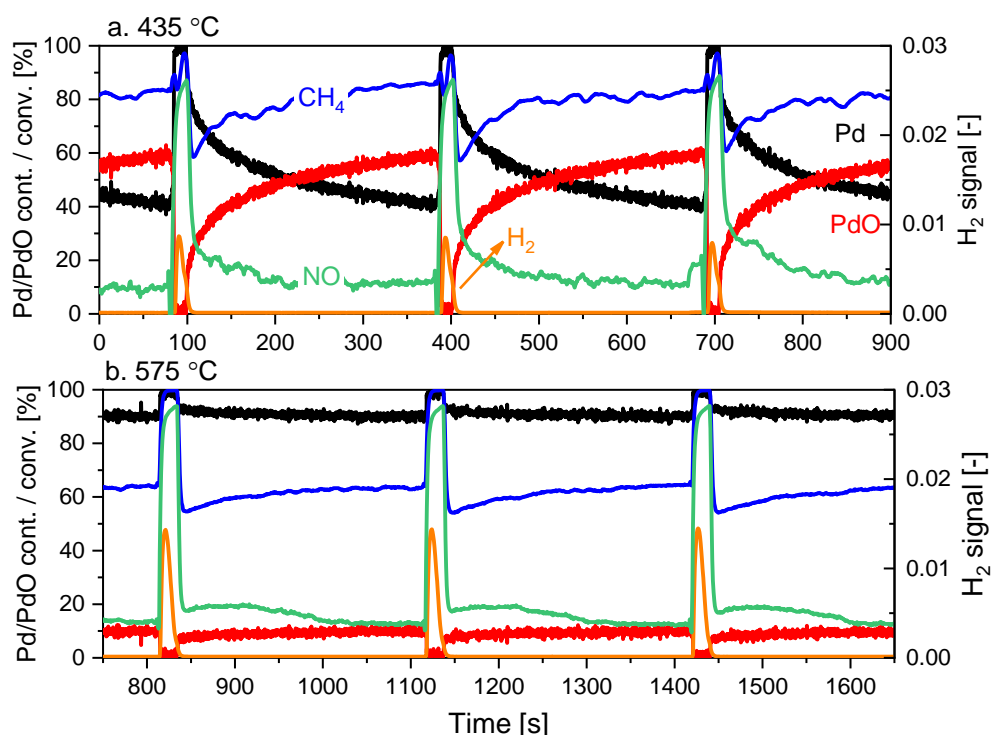
Figure 4.13. CH_4 and NO conversions, Pd phase content (PdO / Pd), and H_2 MS signals at (a) 435 °C (b) 575 °C under SRP wet lean diluted conditions in the presence of $CH_4/CO/NO/H_2O$. Conditions: 0.15 vol% CH_4, 0.16 vol% NO, 0.7 vol% CO, 1.14 vol% O_2, 5 vol% H_2O; WHSV = 240 $Lh^{-1}g^{-1}$.

These results demonstrate the importance of considering the effect of the partial pressure of the reactants (including O_2) and not only the lambda values when discussing the Pd species in action for CH_4 abatement. Indeed, while the lambda value and O_2 partial pressure affect the extent of Pd oxidation, the partial pressure of the reactants (excluding O_2) influences the collision factor, and thus modifies the optimal Pd window to achieve high CH_4 oxidation rates by O_2. Therefore, new optimal Pd windows need to be established when the CH_4 concentration is modified.

Table 4.4. Temperature at which CH_4-SR is promoted by a reducing pulse under SRP wet conditions in the presence of CH_4/H_2O and $CH_4/CO/NO/H_2O$. Conditions: see Table 4.1-2, WHSV = 240 $Lh^{-1}g^{-1}$.

	Start of CH_4-SR [°C]	
	CH_4/H_2O	$CH_4/CO/NO/H_2O$
Lean concentrated cond.	557	560
Stoichiometric concentrated cond.	501	442
Lean diluted cond.	380	325
Stoichiometric diluted cond.	327	325

4.3.4 Simulated exhaust feed of NG engines operated under stoichiometric conditions

Finally, SRP operation was applied to the exhaust feed of stoichiometric NG engines (diluted concentrations and $\lambda = 1$; Figure 4.14). The activity was similar to that achieved under lean diluted and stoichiometric concentrated conditions up to 475 °C but when a reducing pulse was performed, the conversions remained high longer. Above 475 °C, CH_4 and NO conversions remained high and did not oscillate as a result of the O_2 cut-offs. The constant H_2 formation proved that CH_4-SR occurred in this conversion regime. LCF analysis obtained from operando XAS experiments at 435 °C, showed that the catalyst was fully reduced by a rich pulse, and re-oxidation reached only 20 % PdO by the end of the lean phase (Figure B15a). At 575 °C the catalyst was fully reduced over the entire O_2 cut-off cycle (Figure B15b). This behaviour was common to all gas compositions evaluated in this work (Figure B16-17).
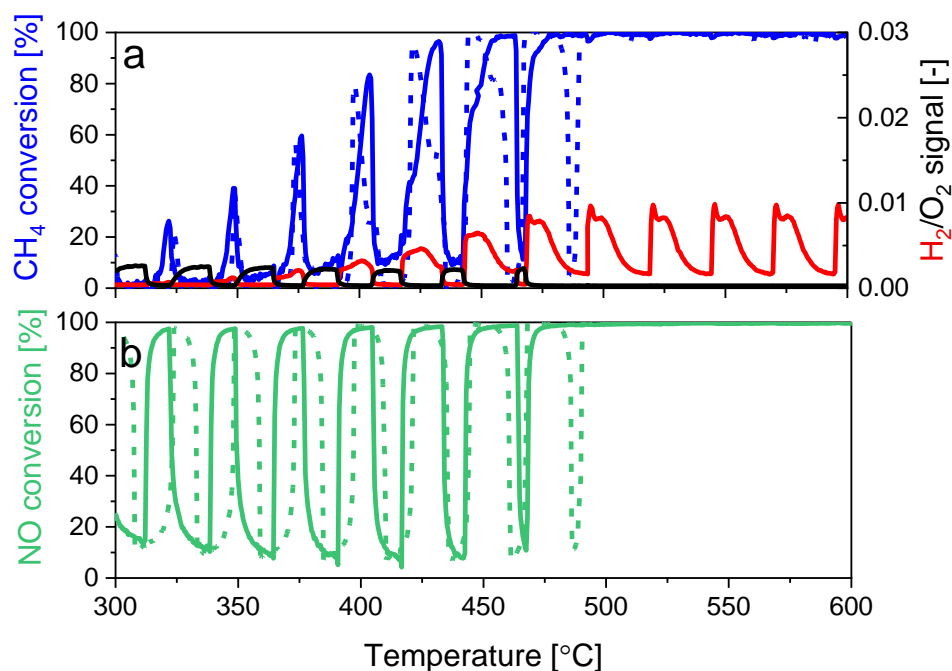
Figure 4.14. (a) CH_4 and (b) NO conversions, as well as H_2 (a; red) and O_2 (a; black) MS signals during heating (—) and cooling (- - -) ramps, under SRP wet stoichiometric diluted conditions, in the presence of $CH_4/CO/NO/H_2O$. Conditions: 0.15 vol% CH_4, 0.16 vol% NO, 0.7 vol% CO, 0.57 vol% O_2, 5 vol% H_2O; WHSV = 240 $Lh^{-1}g^{-1}$.

4.4 Conclusion

In this work, repeated short reducing pulses (SRP; O_2 cut-off 3 s every 5 min) were performed on a Pd/Al_2O_3 catalyst, to gain insight into the effect of each pollutant present in the exhaust feed of stoichiometric NG engines, on CH_4 oxidation and the Pd redox dynamics. We demonstrated, that both Pd^0 and PdO_x species are active for CH_4 oxidation but through different oxidation pathways. While a PdO content between 0 and 80 % allows for CH_4 oxidation by O_2 to take place (but with limited NO reduction), the ubiquity of Pd^0 promotes CH_4 steam reforming as well as complete NO reduction. However, when the catalyst undergoes full reduction, a dense oxide layer forms around the Pd^0 core corresponding to a Pd^0 content between 80 and 98 % that greatly inhibits both, CH_4 oxidation by O_2 and Pd bulk reoxidation. The extent of Pd reoxidation depends on both, the

lambda value and the O_2 partial pressure while the rate of Pd oxidation is only affected by the O_2 partial pressure. On the other hand, the partial pressure of the pollutants influences the collision factor, and thus modifies the optimal Pd window to achieve high CH_4 oxidation rates by O_2. The optimal Pd content shifts to increased PdO content with decreasing pollutants partial pressures regardless of the lambda ratio used.

The presence of CO in the reactive mixture, under lean conditions, permits rapid release of vacant Pd sites for O_2 to dissociatively adsorb on, leading to fast and complete reoxidation of the Pd particles within the lean phase. Nonetheless, since the O_2 partial pressure plays a crucial role in the Pd reoxidation kinetics if it is lower than that of CO (i.e. stoichiometric conditions), the reoxidation of Pd is limited when O_2 is re-introduced in the feed. On the other hand, NO inhibits PdO growth due to site blockage of the Pd^0 surface species generated during the O_2 cut-offs, which consequently inhibits O_2 adsorption and dissociation on Pd.

SRP operation was only beneficial for lean CH_4 oxidation at temperatures below 525 °C. When the O_2 partial pressure in the reactive feed was decreased compared to lean CH_4 oxidation conditions (cf. 4 vol%), the overall activity achieved in SRP mode decreased. Indeed, lower O_2 concentrations induce full reduction of the Pd species in the O_2 cut-offs, which promotes high conversion levels but leads to low activity as soon as the O_2 is replenished in the lean phases of the pulses, due to the formation of a dense chemisorbed oxygen layer around the Pd^0 core. Since the lean phases of the pulses are significantly longer than the O_2 cut-offs (5 min compared to 3 s), the overall catalytic activity achieved is low when the O_2 partial pressure in the feed is decreased to reach stoichiometric conditions.

Therefore, the results demonstrate the importance of designing pulsing protocols that are adapted to the working conditions (i.e. temperature, O_2 concentrations, pollutant concentrations, catalysts) as well as to the intended effect of the pulses. In the case of stoichiometric NG engines, the aim would be to apply pulsing conditions that can maintain the presence of Pd^0 while limiting the formation of less active PdO surface species. For that shorter lean/rich O_2 pulses of smaller amplitudes and higher frequencies are necessary.

Chapter 5   Assessing the effect of O_2-dithering on CH_4 oxidation on Pd/Al$_2$O$_3$

5.1 Introduction

The results obtained up to now provided important information on the chemistry of CH_4 removal from material and catalytic standpoints, but the pulses applied (short reducing pulses) were not optimal to achieve high pollutant conversions over a broad range of conditions (i.e. temperature, gas feed composition, λ value). Periodic lean/rich O_2 pulses of smaller amplitude and higher frequency (also referred to as O_2-dithering) are more suited to optimize the activity of Pd-based TWCs for CH_4 oxidation [57,59,72,151,162,168].

In this Chapter, we show that we can estimate and anticipate the effect of O_2-dithering on CH_4 oxidation pathways (by O_2 or by H_2O) as well as the overall catalytic activity on an OSC-free TWC, Pd/Al$_2$O$_3$, by taking into account the O_2 concentration present in the reactive environment at a given point in time (i.e. exhaust gas composition, temperature, dithering amplitude, and frequency). This is crucial to realize a close-loop control strategy for emission control [230,231]. The O_2 concentration was calculated based on the conversion levels of CO, NO, and CH_4, which were related to the temperature, as well as to the real O_2 concentration present in the lean and rich phases of the pulses. In turn, the real O_2 concentration in the pulses depends on the setup geometry and the dithering parameters (amplitude and frequency), which need to be evaluated beforehand. Our calculations were assessed and validated under various feed conditions and were proven to be reliable and applicable to a broad range of working conditions. The novelty of this work lies in the proof that an OSC-free TWC as simple as Pd/Al$_2$O$_3$ can be efficient towards CH_4 abatement under appropriate O_2-dithering conditions and that the resulting catalytic activity can be readily understood and anticipated.

5.2 Materials

The catalyst, 1.6 wt% Pd/γ-Al$_2$O$_3$ doped with lanthanum (4 wt%), was kindly provided by Umicore in powder form.

The amount of O$_2$ provided by the Pd redox for the 50 mg of sample loaded in the reactor, is 2 umolO$_2$ (600 ppm) at 450 °C, hence the contribution of O$_2$ from the Pd^0/PdO redox is neglected in this work, and the catalyst is considered as OSC-free material.

5.3 Results and discussion

5.3.1 Static operation

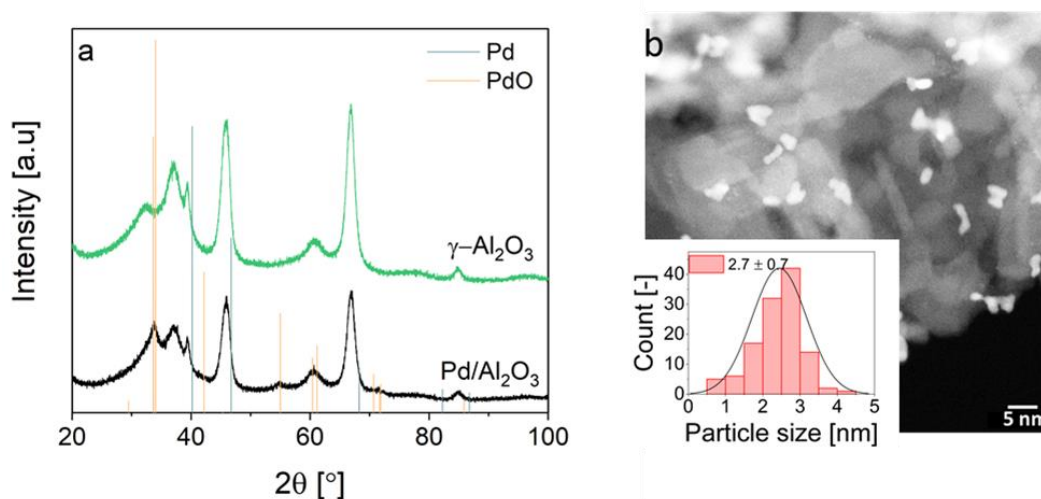Figure 5.1. (a) Powder X-ray diffraction of calcined Pd/Al$_2$O$_3$ and γ-Al$_2$O$_3$. (b) Dark-field HAADF-STEM image and particle size distribution of Pd/Al$_2$O$_3$.

The Pd/Al$_2$O$_3$ catalyst consisted of PdO nanoparticles with a diameter of ca. 2.7 nm (d = 41 %) dispersed on γ-Al$_2$O$_3$ and exhibited a specific surface area of 150 m^{2}g^{-1} (Figure 5.1). After exposure to 1500 ppm CH$_4$

and 3000 ppm O_2 at 600 °C for 30 min and cooling to the desired temperature, the linear combination fit of the XANES spectra indicated that the catalyst was fully oxidized (Figure C1). When exposed to the stoichiometric feed, 60-70 % of the catalyst was reduced to metallic Pd.

Static experiments performed under slightly lean conditions (5980 ppm O_2, $\lambda = 1.001$) induced full CH_4 conversion at 600 °C (Figure 5.2a). CH_4 conversion increased at a rate of 10.2 $umol_{CH_4}/mol_{Pd}/s$ up to 465 °C, followed by 1.9 $umol_{CH_4}/mol_{Pd}/s$ until 600 °C. The change in reaction rate at 465 °C coincided with the full consumption of O_2 (Figure 5.2b). Under these conditions, the feed contained enough O_2 to allow for full CO and 82 % CH_4 conversion at 465 °C. Above this point, the remaining CH_4 needed to be oxidized by the oxygen carried by NO. The linear combination fit (LCF) analysis of the operando Pd K-edge XAS measurements showed that under these conditions NO conversion began only when the catalyst started reducing to a higher extent than its initial state (Figure 5.3a-b). From the lab-scale catalytic activity results, this situation corresponded to nearly full consumption of O_2 fed to the catalyst (450 °C, Figure 5.2b). Finally, NO conversion reached a maximum of 84 % at 600 °C (Figure 5.2b). CO was never detected while the CO_2 concentration increased with increasing CH_4 conversion (Figure C2).

Under stoichiometric conditions (5700 ppm O_2, $\lambda = 1.000$), three different conversion regimes were observed (Figure 5.2). The first two conversion regimes (referred to as low conversion regimes) were related to CH_4 oxidation by O_2, wherein the reaction rate was 10.2 $umol_{CH_4}/mol_{Pd}/s$ up to 446 °C and 1.9 $umol_{CH_4}/mol_{Pd}/s$ until 500 °C due to O_2 depletion from the reactive environment. The amount of O_2 in the feed allowed converting 73 % CH_4, which was consistent with the decrease in reaction rate (446 °C). The third conversion regime (> 475 °C; high conversion regime) was characterized by rapid and complete NO and CH_4 conversion as well as by H_2 formation, attesting to the occurrence of methane steam reforming (CH_4-SR) and water gas shift (WGS). CO formation was not observed even in this third conversion regime (Figure C3). This regime coincided with the fast and complete reduction of the Pd species, as confirmed by the operando XAS measurements performed under slightly rich conditions (5415 ppm O_2, $\lambda = 0.998$; Figure 5.3c-d). After a slow increase of the fraction of PdO, the third kinetic regime started at ca. 375 °C and was accompanied by the rapid

complete reduction of the catalyst (Figure 5.3c-d) [59]. In coincidence to the start of the third conversion regime, the rate of CH_4 conversion (Figure 5.3d) and the rate of PdO reduction (Figure 5.3c) were 32.48 and 32.82 %/min between 370 and 383 °C, respectively, demonstrating the close relationship between the two processes. In these experiments, CH_4 conversion also displayed a very similar kinetic behaviour to that observed in the catalytic reactor (Figure 5.2), even though, the temperatures at which the different regimes occur differ because the reactor configuration, catalyst mass, gas flow, heaters, and temperature controllers were different.
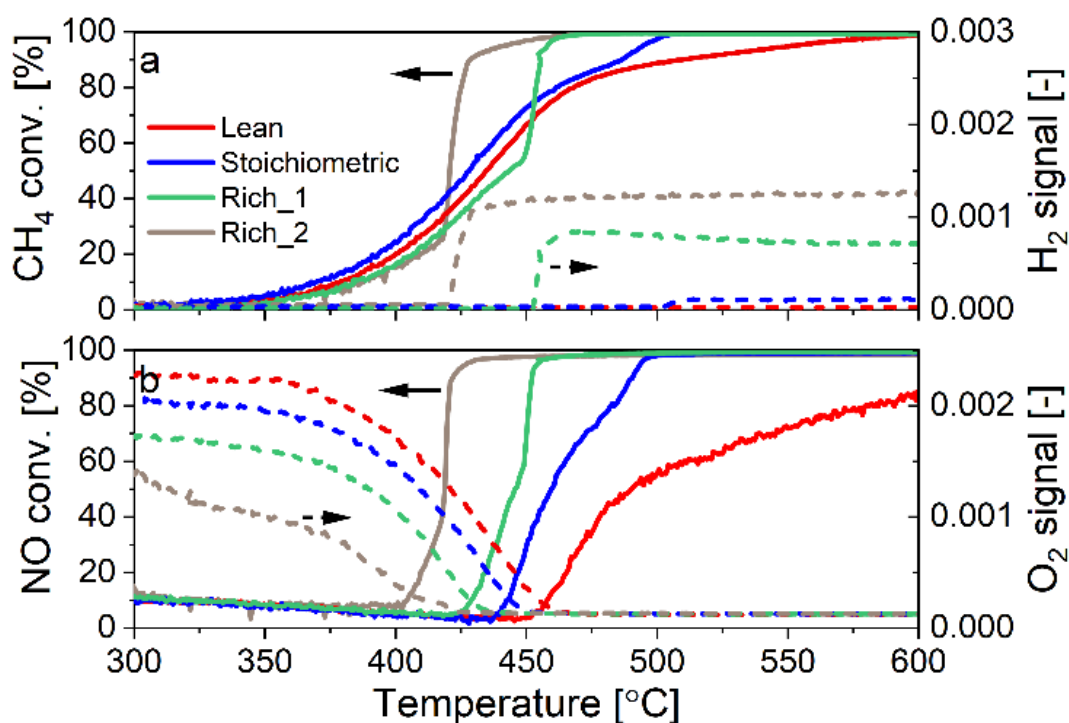
Figure 5.2. (a) CH_4 and (b) NO conversion as well as MS signals of (a) H_2 and (b) O_2 during heating ramps under static lean (5980 ppm O_2; $\lambda = 1.001$), stoichiometric (5700 ppm O_2; $\lambda = 1.0$), rich_1 (4845 ppm O_2; $\lambda = 0.996$) and rich_2 (4275 ppm O_2; $\lambda = 0.993$) conditions. Conditions: 1500 ppm CH_4, 1600 ppm NO, 7000 ppm CO, variable O_2, 5 vol% H_2O; WHSV = 240 $Lh^{-1}g^{-1}$.

The same kinetic behaviours were observed when the O_2 concentration was further decreased (Rich_1, Rich_2; Figure 5.2). However, the richer the conditions, the more the kinetic regimes shifted to low temperatures. This behaviour was emphasized by shifting the conversion curves of CH_4, and thus NO, to approximately

the same light-off temperature (Figure C4). The result shows that the profiles perfectly overlap in the low conversion regime and the changes in the kinetic regimes occurred at different temperatures depending on the O_2 concentration in the feed. This demonstrates that the system is predictable. Under rich conditions, CO breakthrough (up to 250 ppm at 600 °C) occurred concurrently with the decrease in CO_2. The CO slip arises from either, incomplete CH_4-SR, lower efficiency of the water gas shift, or oxidation reactions [57,151,169].

If NO conversion is plotted as in Figure 5.2b but against the actual O_2 concentration present in the feed ($[O_2]_{real}$, Figure C5a), it becomes clear that NO reduction starts at the same O_2 level (184 ppm) irrespective of the initial O_2 concentration ($[O_2]_{initial}$). The theoretical O_2 concentration present in the feed ($[O_2]_{th}$), calculated from $[O_2]_{initial}$ as well as the pollutants concentrations and conversions (Equation 2.4) and plotted together with NO conversion (Figure C5b), demonstrates that CH_4-SR started always at the same O_2 level (84 ppm).
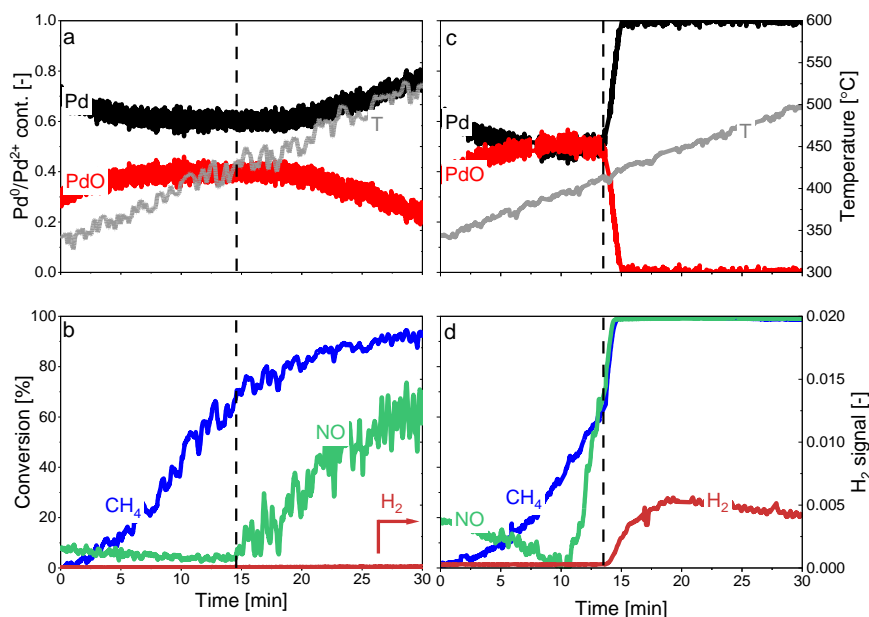
Figure 5.3. Temporal evolution of (a, c) Pd phase content (PdO / Pd) and temperature as well as (b, d) CH_4 and NO conversion under (a-b) static lean conditions (5980 ppm O_2; λ = 1.001) and (c-d) static rich conditions (5415 ppm O_2, λ = 0.998). The MS signal of H_2 is shown in (b) and (d). Conditions: 1500 ppm CH_4, 1600 ppm NO, 7000 ppm CO, 5 vol% H_2O; λ = 1 ± 0.018; WHSV = 240 $Lh^{-1}g^{-1}$.

$[O_2]_{th}$ provides additional information about the ongoing chemistry compared to $[O_2]_{real}$ measured at the outlet of the reactor. For example, under slightly lean conditions, $[O_2]_{th}$ was always higher than necessary to achieve high CH_4 conversion (> 84 ppm, Figure C5b), justifying the low NO conversion measured at 600 °C. In contrast, $[O_2]_{real}$ only showed that the O_2 was fully consumed above 465 °C (Figure C5a). Furthermore, the constant level of $[O_2]_{th.}$ observed for all conditions once all $[O_2]_{initial}$ was consumed (Figure C5b) indicates that despite the increase in CH_4 and NO conversion with increasing temperature, the amount of O_2 involved in the process is constant. Therefore, as soon as an oxygen atom is released by NO, it is consumed by CH_4, demonstrating that once all the O_2 initially present was consumed, CH_4 relied on NO to convert. This result proves that CH_4 and NO conversions are correlated, once $[O_2]_{initial}$ is fully consumed [57,59,72], and that from this moment on, NO reduction is the limiting step for CH_4 oxidation. This is emphasized by flowing various gas compositions over the catalyst, with and without NO, under stoichiometric conditions (Figure C6). Indeed, CH_4 oxidation by O_2 was only slowed down in the presence of NO, as soon as O_2 was depleted. Furthermore, the transition from PdO to Pd^0 was shown to be smoother in the presence of NO, indicating that NO slows down the transition from the first/second, and third kinetic regime [59].

5.3.2 O_2-dithering operation

Since the catalytic behaviour of Pd/Al_2O_3 towards CH_4 oxidation appears to be predictable, the knowledge gained from static conditions was applied to the O_2-dithering operation. In this study, symmetric O_2 pulses were performed around stoichiometry using different pulsing amplitudes and frequencies.

The amplitude changes were performed by adding a precise amount of O_2 ($[O_2]_{pulsed}$) periodically to a constant O_2 feed ($[O_2]_{baseline}$; Figure 5.4a) to reach an average concentration of 5700 ppm O_2, corresponding to $\lambda = 1.000$. Therefore, higher amplitude resulted in a lower $[O_2]_{baseline}$ (Figure 5.4b). The rich phase of the pulses refers to the phase where only the $[O_2]_{baseline}$ is seen by the catalyst, whereas the lean phases consist of the combination of both $[O_2]_{baseline}$ and $[O_2]_{pulsed}$ to reach an average of 5700 ppm O_2 (Figure 5.4). Figure 5.5, depicts the O_2 concentration expected in the rich phases ($[O_2]_{baseline}$) and in the lean phases ($[O_2]_{baseline}$ + $[O_2]_{pulsed}$) of the pulses. It is clear that as the pulsing amplitude increases, the O_2 concentration decreases in the

rich phases of the pulses and increases in the lean phases of the pulses. Nonetheless, the average O_2 concentration remains the same regardless of the pulsing amplitude used. Moreover, the dithering frequency defines the length of the O_2 pulses but not the amount of O_2 available in the rich and lean phases of the pulses. Therefore, the O_2 concentration available in the system should be independent of the frequency used.
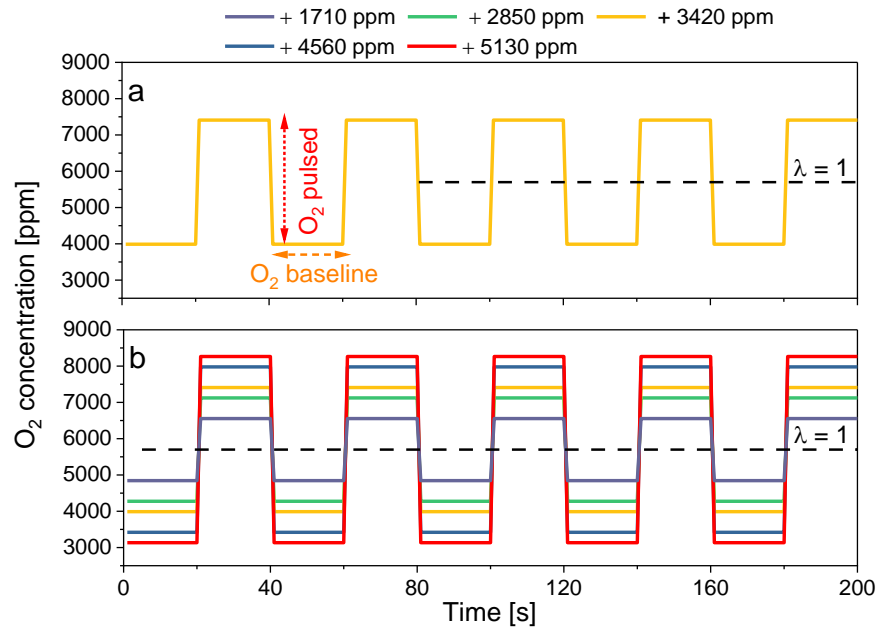

Figure 5.4. Scheme of the alternate symmetric pulses taking as example various amplitudes around stoichiometry at a frequency of 0.05 Hz. The horizontal black dashed line indicates the value of 5700 ppm O_2, corresponding to $\lambda = 1.000$.
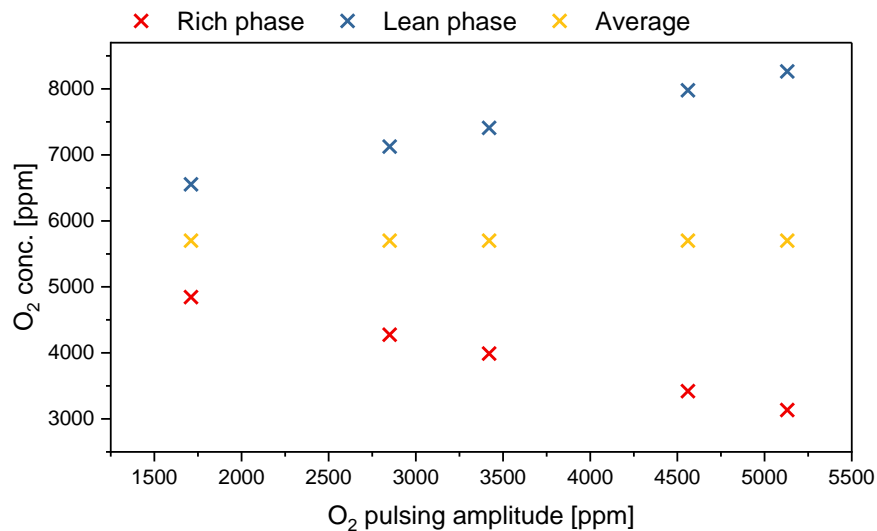

Figure 5.5. O_2 concentration expected in the rich and lean phases of the pulses, as well as on average.

If the pulses were fully efficient (i.e. 100 % of the desired O_2 is pulsed in the lean phase and 0 % in the rich phase), the average O_2 concentration throughout the pulsing sequence would be the same for all dithering parameters (amplitude and frequency; 5700 ppm O_2; Figure 5.5). In reality, this is never the case, as the amplitude and frequency do affect the O_2 concentration pulsed to the system due to the setup geometry. Blank experiments were performed at room temperature in the reactor filled with cordierite to evaluate the real O_2 concentration experienced by the catalyst, and thus the dithering efficiency, η_d (Equation 2.3). The results (Table C1, Figure 5.6) show that η_d was always less than 100 % in the lean phases and more than 0 % in the rich phases, proving that the pulses were not fully efficient. The η_d decreased with decreasing amplitude due to decreasing O_2 concentration pulsed and with increasing frequency due to the increasingly shorter opening time of the pulsing valves. It can be further explained by the fact that the pulse sequences appear as half-sinusoidal waves rather than ideal square waves because of the setup geometry (Figure 5.6). Hence, $[O_2]_{real}$ was lower than the aimed concentration ($[O_2]_{expected}$) in the lean phases and higher in the rich phases (Figure 5.7; Table C2). As our calculations rely on the O_2 concentration present in the feed, it is crucial to precisely evaluate the amount of O_2 present in the lean and rich pulses, to implement the correct η_d value (Equation 2.5).

An example is given in Figure 5.7. The results are shown for two frequencies, 0.05 and 0.1 Hz, and various amplitudes, 5130, 4560, 3990, 2850, and 1710 ppm O_2. It is seen that the $[O_2]_{expected}$, was always lower than $[O_2]_{real}$ in the lean phases of the pulses and higher than $[O_2]_{real}$ in the rich phases of the pulses. Moreover, the average $[O_2]_{real}$ was systematically lower than the average $[O_2]_{expected}$ (5700 ppm). These observations are emphasized with increasing frequency.
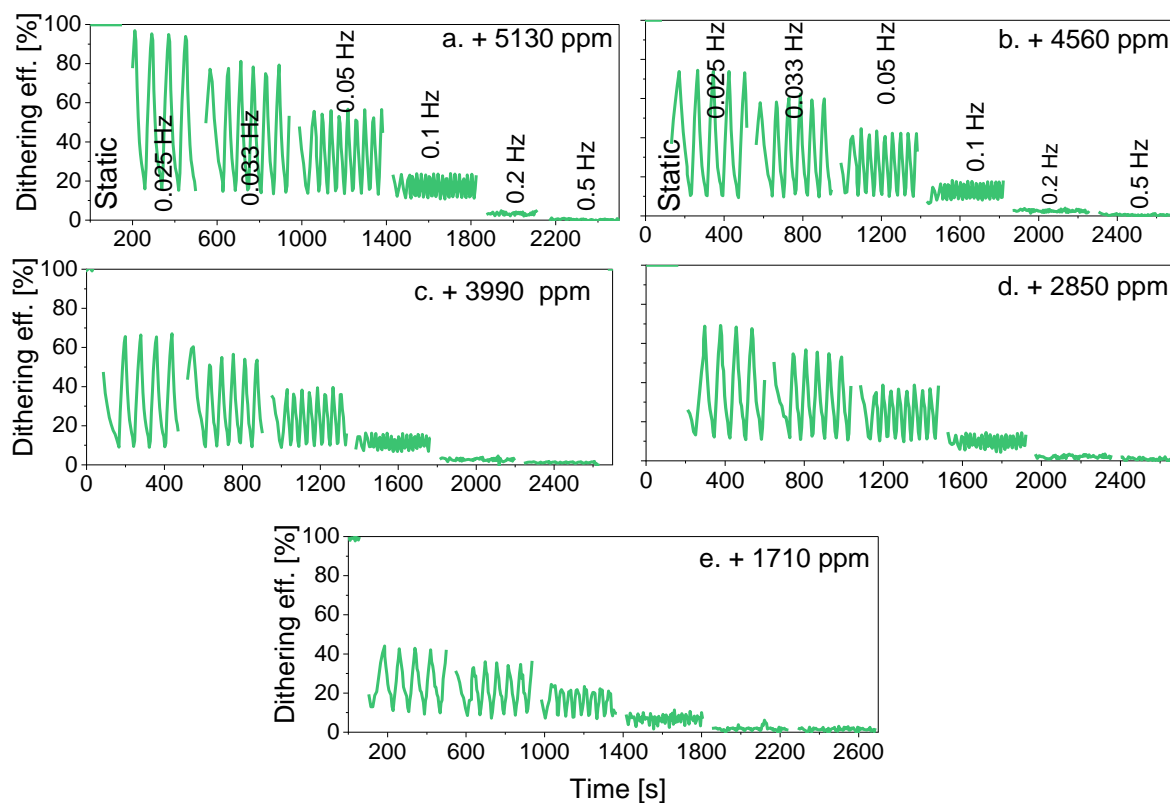
Figure 5.6. Dithering efficiency, η_d, obtained when pulsing 1000 ppm O_2/Ar in Ar (WHSV = 240 $Lh^{-1}g^{-1}$) at room temperature at different amplitudes and frequencies. The pulsing flows correspond to the flows needed to reach amplitudes of (a) + 5130, (b) + 4560, (c) + 3990, (d) + 2850, and (e) + 1710 ppm O_2 around stoichiometry (1500 ppm CH_4, 1600 ppm NO, 7000 ppm CO, 5 vol% H_2O). For each amplitude, frequencies of 0.025, 0.033, 0.05, 0.1, 0.2 and 0.5 Hz were used.
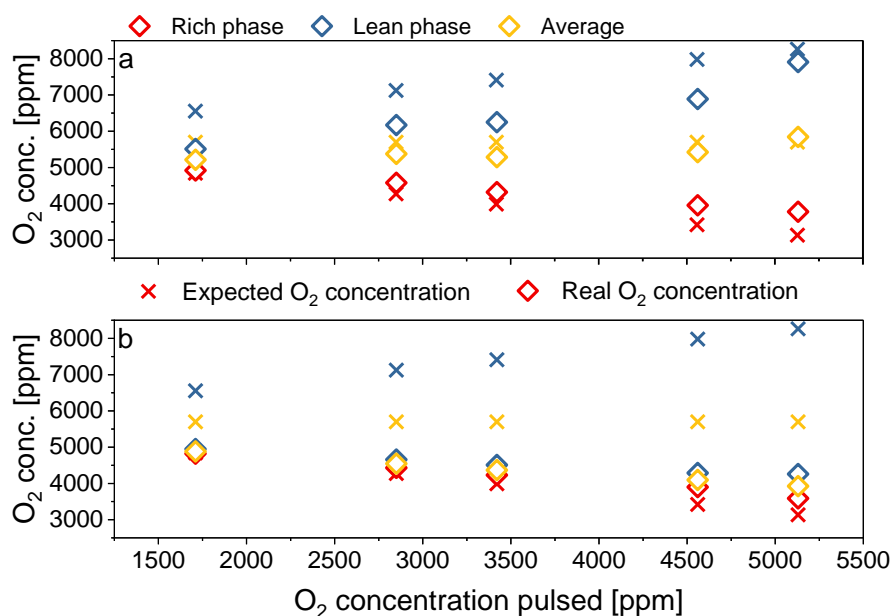
Figure 5.7. $[O_2]_{expected}$ and $[O_2]_{real}$ present in the rich (red), lean (blue) phases of the pulses, as well as on average (yellow), as function of the pulsing amplitude for frequencies of (a) 0.05 Hz, and (b) 0.1 Hz.

5.3.2.1 Effect of temperature

Symmetric pulses were applied at dithering conditions of $3990 + 3420$ ppm O_2 ($\lambda = 1 \pm 0.018$) and 0.05 Hz, while the temperature was increased from 400 to 440 °C in 5 °C steps. As CH_4 and NO conversions contribute to $[O_2]_{th}$ (Equation 2.5), it is important to be aware of the catalytic activity of these pollutants at each temperature. Therefore, CH_4 (12 %) and NO (10.5 %) conversions were retrieved from a static isothermal experiment performed at 400 °C. Then, CH_4 conversion was recalculated as a function of temperature by applying the reaction rate determined from the stoichiometric temperature ramp (10.2 $umol_{CH_4}/mol_{Pd}/s$; Figure 5.2a, Table 5.1), which as mentioned above is valid up to 465 °C when working under stoichiometric conditions. Since NO conversion remained at ca. 10.5 % until all the O_2 was consumed, this conversion value was kept constant throughout the calculations for all temperatures considered.

Table 5.1. CH_4 and NO conversions in the low conversion regime (oxidation by O_2) and corresponding theoretical O_2 concentration in the rich and lean pulses, and the average of both, when performing O_2-dithering (3990 + 3420 ppm O_2 and 0.05 Hz). The initial CH_4 and NO conversion values were retrieved from the static isothermal experiment at 400 °C; then CH_4 conversion was calculated based on the reaction rate (10.2 $umol_{CH_4}/mol_{Pd}/s$). Conditions: 1500 ppm CH_4, 1600 ppm NO, 7000 ppm CO, 5 vol% H_2O; λ = 1 ± 0.018; WHSV = 240 $Lh^{-1}g^{-1}$. The start of the high NO reduction is indicated in bold ($[O_2]_{th}$ < 184 ppm) while the high conversion regime is shown in red ($[O_2]_{th}$ < 84 ppm).

Temperature [°C]	CH_4 conversion [%]	NO conversion [%]	$[O_2]_{th\_lean}$ [a,b] [ppm]	$[O_2]_{th\_rich}$ [a,b] [ppm]	$[O_2]_{th\_average}$ [a,b] [ppm]
400	12	10.5	1467	560	1014
405	15.95	10.5	1349	442	895
410	19.9	10.5	1112	323	718
415	23.85	10.5	1112	205	658
420	27.8	10.5	993	**86**	540
425	31.75	10.5	875	**-32**	421
430	35.7	10.5	756	**-151**	303
435	39.65	10.5	638	**-269**	184
440	43.6	10.5	519	**-388**	**66**

[a] Considering NO conversion.

[b] Adapting the O_2 concentration seen by the catalyst based on the η_d (Table C1).

Before describing the results, the procedure used in this part of the work should be explained. First, the $[O_2]$ available in the system ($[O_2]_{real}$) in the rich and lean phases of the pulses, as well as on average was calculated (Figure 5.8a). The $[O_2]_{expected}$ (○, in Figure 5.8a) was calculated according to Equation 5.1 while $[O_2]_{real}$ (□, in Figure 5.8a) was calculated according to Equation 5.2. Equations 5.1 and 5.2 can be derived for the lean and rich phases of the pulses.

$$[O_2]_{real\_lean/rich} = [O_2]_{baseline} + [O_2]_{expected}$$
Equation 5.1

$$[O_2]_{real\_lean/rich} = [O_2]_{baseline} + [O_2]_{expected} \cdot \eta_{d\_lean/rich}$$
Equation 5.2

Since the same dithering conditions (3990 + 3420 ppm O_2; and 0.05 Hz) were used for all temperatures, the $[O_2]_{real}$ was the same throughout the experiment (Figure 5.8a; shown only for 400, 410, 420, 430, and 440 °C). Then, the amount of O_2 consumed by CO and CH_4 oxidation and given by NO reduction was calculated by considering the pollutants conversions at the different temperatures evaluated (using Table 5.1; Figure 5.8b). In this case, the amount of O_2 consumed was dependent on the temperature (Arrhenius law). It should be mentioned that in Figure 5.8b the $[O_2]$ consumed and released by the reactants only depend on the temperature and not on the $[O_2]$ present in the feed. Therefore, the values obtained for the rich and lean phases of the pulses (and on average) overlap as the same amount of O_2 is consumed and released. Then, the amount of O_2 consumed and released by the reactants was substracted to the $[O_2]_{real}$ for each temperature (Equation 5.3; Figure 5.8c). The O_2 concentration calculated at this step corresponds in this study to the theoretical O_2 concentration ($[O_2]_{th.}$). Finally, the $[O_2]_{th.}$ values at which NO reduction and CH_4-SR start were determined from the static temperature ramp experiments described in section 5.3.1 (184 and 84 ppm, respectively; green and blue horizontal lines).

$$[O_2]_{th\_lean/rich} = [O_2]_{baseline} + [O_2]_{expected} \cdot \eta_{d\_lean/rich} - 0.5[CO]_i \cdot X_{CO} - 2[CH_4]_i \cdot X_{CH4} + 0.5[NO]_i \cdot X_{NO} \qquad \text{Equation 5.3}$$

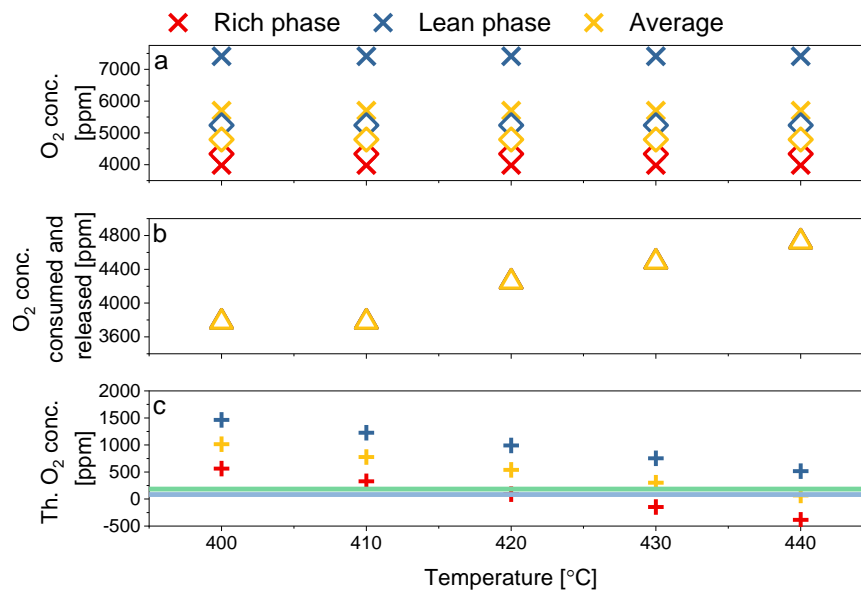Figure 5.8. (a) $[O_2]_{expected}$ (○) and $[O_2]_{real}$ (□), (b) $[O_2]$ consumed and released by the pollutants, (c) $[O_2]_{th.}$, in the rich (red), lean (blue) phases of the pulses, as well as on average (yellow), as a function of the temperature.

The green and blue horizontal lines represent the start of NO reduction and CH_4-SR, respectively. Conditions: 1500 ppm CH_4, 1600 ppm NO, 7000 ppm CO, 5 vol% H_2O; $\lambda = 1 \pm 0.018$; WHSV = 240 $Lh^{-1}g^{-1}$.

Figure 5.9a shows that up to 415 °C, CH_4 and NO conversions did not deviate significantly from the static values suggesting that the pulses did not affect the activity. Until this temperature, the O_2 concentration calculated ($[O_2]_{th}$) from CH_4 and NO conversions at the different temperatures (Figure 5.9c) was always higher than the value necessary to trigger NO conversion (184 ppm, Table 5.1), in both the lean and rich phases of the pulses. At 420 °C, the $[O_2]_{baseline}$ in the rich phases was low enough to initiate NO reduction ($[O_2]_{th\_rich} < 184$ ppm; Table 5.1; Figure 5.9). Hence, high oscillations of NO conversion were induced between the rich and the lean phases (± 80 %; Figure 5.9). However, $[O_2]_{th\_rich}$ was too high to induce CH_4-SR ($[O_2]_{th\_rich} > 84$ ppm). At 425 °C and up to 435 °C, the appearance of H_2 revealed that CH_4-SR occurred in the rich phases, which was also expected from the $[O_2]_{th\_rich}$ value ($[O_2]_{th\_rich} < 84$ ppm in the rich pulses; Table 5.1). However, the average O_2 concentration over the rich and lean pulses, $[O_2]_{th\_average}$, was much above 84 ppm, justifying the absence of CH_4-SR throughout the entire dithering cycle (Table 5.1). At 440 °C, the pulses caused full NO reduction and ca. 90 % CH_4 conversion. At this temperature, $[O_2]_{th\_average}$ (66 ppm) was low enough to maintain CH_4-SR over the entire dithering cycle despite the high O_2 concentration in the lean periods ($[O_2]_{th\_lean} = 519$ ppm; Table 5.1, Figure 5.9).

It is important to mention that when CH_4-SR was active in the high conversion regime, NO was fully reduced and thus released more oxygen on the catalyst surface than in the low conversion regime (100 % vs 10.5 % conversion, respectively). This can alter our calculations and their robustness because they rely on the amount of available oxygen. For this reason, it is important to determine the theoretical O_2 concentration also when NO conversion is 100 % instead of 10.5 %. Nonetheless, complete NO reduction implies that CH_4-SR takes place as observed from the static experiments performed under various O_2 concentrations (Figure 5.2). While the reaction sequence and detailed mechanisms are still unclear, it is accepted that when O_2 is depleted in the reactive feed, CH_4 and NO conversions are correlated [57,59,72]. Static experiments performed under stoichiometric conditions ($[O_2]_{initial} = 5700$ ppm) and under conditions that force CH_4-SR to be the only reaction pathway for CH_4 oxidation ($[O_2]_{initial} = 2700$ ppm, O_2 fed only for CO oxidation while considering the presence

of NO) demonstrated, that CH_4 conversion differs at low temperatures if CH_4 is oxidized by O_2 or by H_2O (Figure C7). Hence, CH_4 conversion needs to be adapted accordingly in the calculations for the high conversion regime (Table C3). The same approach as for CH_4 oxidation by O_2 was applied, but the main difference is that the input NO conversion for the calculations was 100 %, while the initial CH_4 conversion at 400 °C (37.6 %) and the reaction rate (12 $umol_{CH_4}/mol_{Pd}/s$) were different. The results were similar to the calculations performed in the low conversion regime (Table 5.1 and Table C3). Since under these conditions 100 % NO conversion is considered, the $[O_2]_{th}$ needed to activate CH_4-SR is 0 ppm.
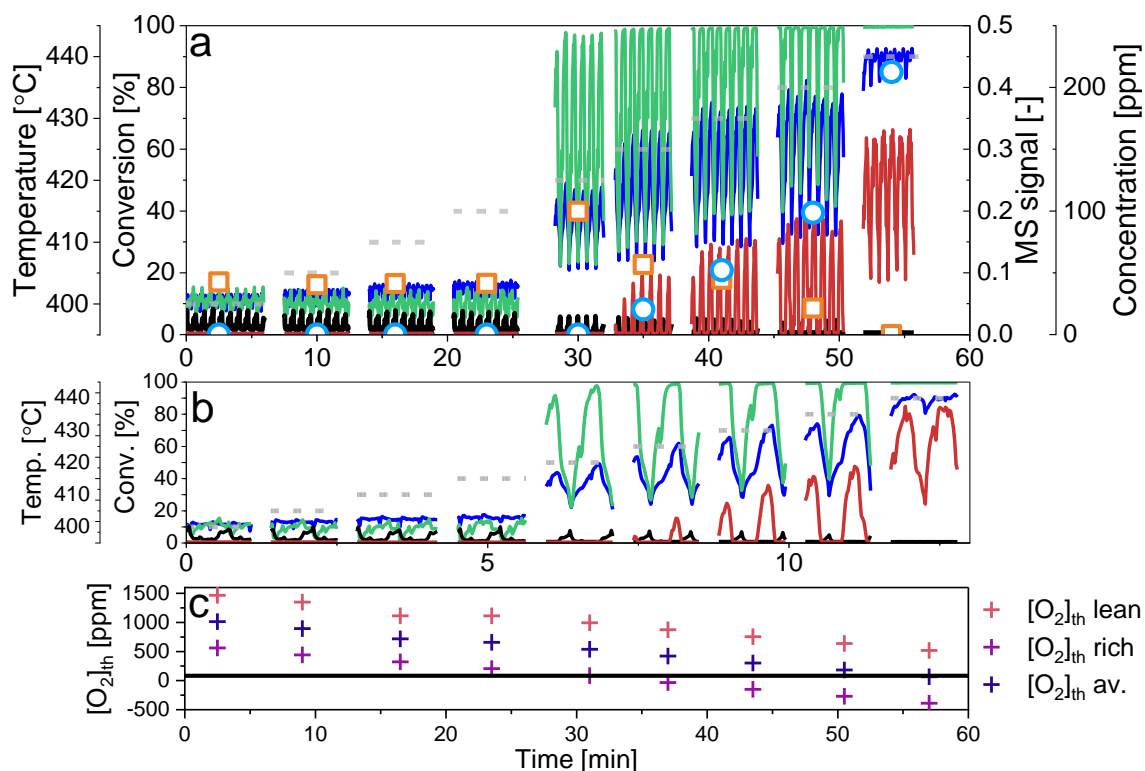
Figure 5.9. (a) CH_4 (blue) and NO (green) conversion, MS signals of H_2 (red) and O_2 (black), and concentration of N_2O (orange; □) and NH_3 (light blue; ○) at different temperatures (dashed grey) under O_2-dithering conditions (3990 + 3420 ppm O_2 and 0.05 Hz). (b) Magnification of (a) to help visualize the O_2 pulses. (c) $[O_2]_{th}$ calculated from the low conversion regime, in the lean and rich phases of the pulses, and the average between the lean and rich phases. The black horizontal line represents the 84 ppm $[O_2]_{th}$. Conditions: 1500 ppm CH_4, 1600 ppm NO, 7000 ppm CO, 5 vol% H_2O; $\lambda = 1 \pm 0.018$; WHSV = 240 $Lh^{-1}g^{-1}$.

The LCF of the operando XAS spectra obtained under the same dithering conditions while increasing the temperature showed that the high conversion achieved in each rich phase of the pulses (Figure 5.10b-b') coincided with a full reduction of the catalyst ($Pd^0/(Pd^0+Pd^{2+}) = 1$; Figure 5.10a-a') and with H_2 evolution. However, partial Pd reoxidation in the lean phase of the pulses was concomitant to a drop in CH_4-SR activity, monitored by the H_2 signal (Figure 5.10b-b'). These results confirm that reduced Pd was involved in the high conversion regime ($[O_2]_{th} < 84$ ppm), whereas as soon as the Pd species reoxidized, even partially, lower conversion was achieved. It is however difficult to comment further on the link between CH_4-SR, Pd oxidation state, and surface composition with the data set we have.
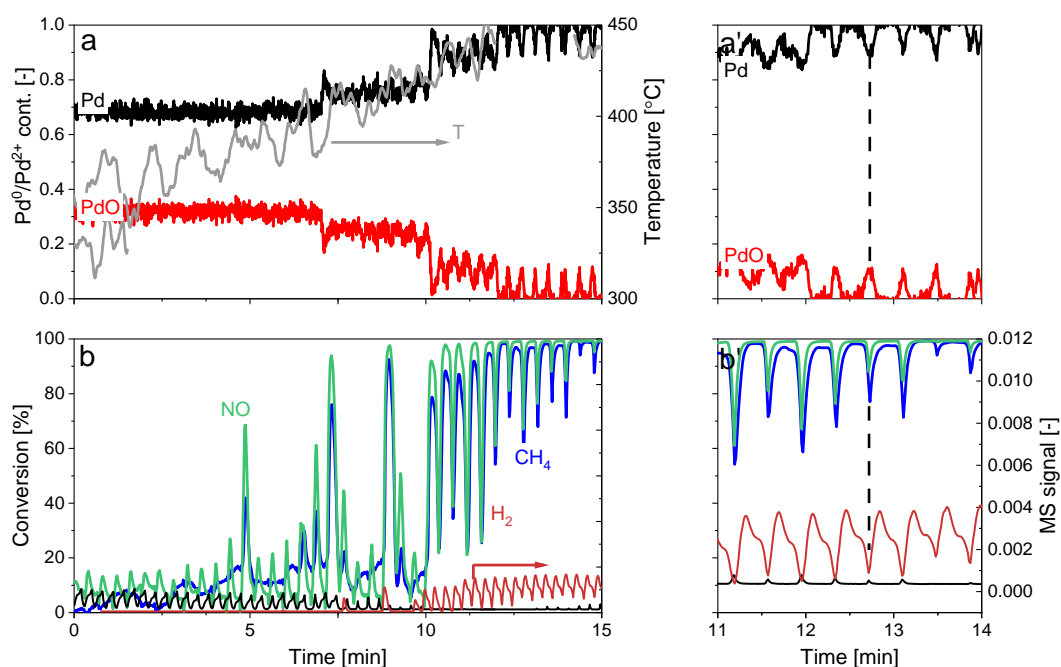
Figure 5.10. Temporal evolution of (a) Pd phase content (PdO / Pd) and temperature (grey) as well as (b) CH_4 (blue) and NO (green) conversion under O_2-dithering conditions (3990 + 3420 ppm O_2 and 0.05 Hz). (c, d) Magnification of (a, b) to help visualize the pulses. The MS signal of H_2 is shown in (b) and (d). Conditions: 1500 ppm CH_4, 1600 ppm NO, 7000 ppm CO, 5 vol% H_2O; $\lambda = 1 \pm 0.018$; WHSV = 240 $Lh^{-1}g^{-1}$.

Finally, a note on by-products. Figure 5.9 shows that N_2O was detected in the online FTIR spectrometer when CH_4 oxidation by O_2 proceeded and NO conversion was low (≤ 415 °C). N_2O is known to be formed under oxidizing conditions from NO and CO via the surface isocyanate intermediate [232,233]. Under the

conditions in which H_2 formed and was detected by MS, N_2O was replaced by NH_3 arising from the reaction

between NO and H_2 [59,233]. When CH_4-SR was promoted only in the rich phase of the pulses, both N_2O and

NH_3 were observed, because of the low time resolution of the FTIR measurement (30 s/spectrum), which did

not allow to follow the concentration of the two products in a full rich or lean pulse. We thus conclude that for

this situation N_2O was formed in the lean phases and NH_3 in the rich phases [174]. Furthermore, CO slips were

observed from 430 °C in the rich phases of the O_2 pulses and at 440 °C ca. 270 ppm CO were detected over

the full O_2 dithering cycle (Figure C8). Hence, our results demonstrate that high conversion of both CH_4 and

NO occurs simultaneously to full Pd reduction, but at the expense of NH_3 and CO slips. On the contrary, the

loss of conversion in a lean environment is accompanied by a selectivity in favour of N_2O and complete CO

oxidation.

5.3.2.2 Effect of amplitude and frequency at different temperatures

O_2-dithering was then performed at different pulse amplitudes and frequencies at 410 and 435 °C. It is

important to recall that if η_d was 100 % in the lean pulses and 0 % in the rich pulses, the results would be the

same for all amplitudes and frequencies. Since this is not the case (Figure 5.6), the effect of the pulses varied

with the dithering parameters used but in a predictable way.

At 410 °C, CH_4 and NO conversions used for the calculations were 19.9 and 10.5 % in the low conversion

regime (Table 5.1), and 46.5 and 100 % in the high conversion regime (Table C3). Figure 5.11a shows that the

pulses did not affect appreciably CH_4 or NO conversion at an amplitude of 4725 + 2850 ppm O_2. The beneficial

effect of the pulses on the activity appeared and increased with increasing amplitude since the overall O_2 con-

centration ($[O_2]_{real}$) experienced by the catalyst decreased with increasing amplitudes (Table C2, Figure 5.11).

Hence, with increasing amplitude, the pulses were more efficient to trigger CH_4-SR. At an amplitude of 3990

+ 3420 ppm O_2, high conversion was maintained during the full dithering cycle at frequencies of 0.5 and 0.2

Hz (Figure 5.11b). At amplitudes of 3420 + 4560 ppm O_2 and 3135 + 5130 ppm O_2, this was also achieved at

0.1 Hz (Figure 5.11c-d). At these amplitudes, CH_4-SR occurred only in the rich pulses at frequencies of 0.025,

0.033, and 0.05 Hz (Figure 5.11c-d and Figure C9a-b). These results show that η_d induced different catalytic

responses for the same amplitude. All the results presented in Figure 5.11 were fully predicted by our calculations (Table C4 and C5) based on the definitions of $[O_2]_{real}$, $[O_2]_{baseline}$, and $[O_2]_{th}$.

It is important to mention that if η_d was not considered in the calculations, the calculations would have been erroneous. For example, if the efficiency of the pulse was considered to be 100 % in the lean pulses and 0 % in the rich pulses, CH_4-SR would not have been predicted to be maintained throughout the entire dithering cycle at any amplitude or frequency and the effect of the O_2 pulses would be expected to be the same at each amplitude regardless of the frequency used (Table C6).

Figure 5.11. (a - d) CH_4 (blue) and NO (green) conversion, MS signals of H_2 (red) and O_2 (black) and concentration of N_2O (orange; □) and NH_3 (light blue; ○) under O_2-dithering conditions at 410 °C at 0.025, 0.033, 0.05, 0.1, 0.2 and 0.5 Hz and given amplitude of (a, 1) 4275 + 2850 ppm O_2, (b, 2) 3990 + 3420 ppm O_2, (c, 3) 3420 + 4560 ppm O_2, (d, 4) 3135 + 5130 ppm O_2. $[O_2]_{th}$ calculated from the low conversion regime in the lean and rich phases of the pulses and the average between the lean and rich phases are shown on top of each panel (1-4). The black horizontal line represents

the 84 ppm $[O_2]_{th}$. Conditions: 1500 ppm CH_4, 1600 ppm NO, 7000 ppm CO, 5 vol% H_2O; (a) $\lambda = 1 \pm 0.015$, (b) $\lambda = 1 \pm 0.018$, (c) $\lambda = 1 \pm 0.024$ and (d) $\lambda = 1 \pm 0.027$; WHSV = 240 $Lh^{-1}g^{-1}$.

Figure 5.12 shows that the effect of the pulses was slightly different at 435 °C because of the higher CH_4 conversion (39.65 and 68.75 % when oxidized by O_2 and H_2O, respectively). Hence, high conversion was already achieved at the amplitude 4725 + 2850 ppm O_2 due to earlier O_2 depletion (Figure 5.12b). Thus, a lower amplitude was tested at this temperature (4845 + 1710 ppm O_2, Figure 5.12a). The experimental results and our calculations (Table C7) showed that at this amplitude the average CH_4 conversion did not change as a result of changes in frequency. As the amplitude was increased (Figure 5.12b-e), CH_4-SR was promoted and maintained over the entire dithering cycle (4275 + 2850, 3990 + 3420, 3420 + 4560, and 3135 + 5130 ppm O_2) at 0.5, 0.2, and 0.1 Hz because the overall O_2 concentration ($[O_2]_{th}$) was always below 84 ppm (Table C7). The calculations were also able to estimate the effect in the rich phase of a pulse, anticipating the occurrence of CH_4-SR at all frequencies for amplitudes above 3420 ppm O_2 (Table C7; Figure 5.12b-e, Figure C10). Finally, at amplitude 3135 + 5130 ppm O_2, high conversion was also promoted over the entire dithering cycle at a frequency of 0.05 Hz (Figure 5.12e). The calculations were as accurate when considering CH_4 oxidation either by O_2 (low conversion regime, Table C7) or H_2O (high conversion regime, Table C8).
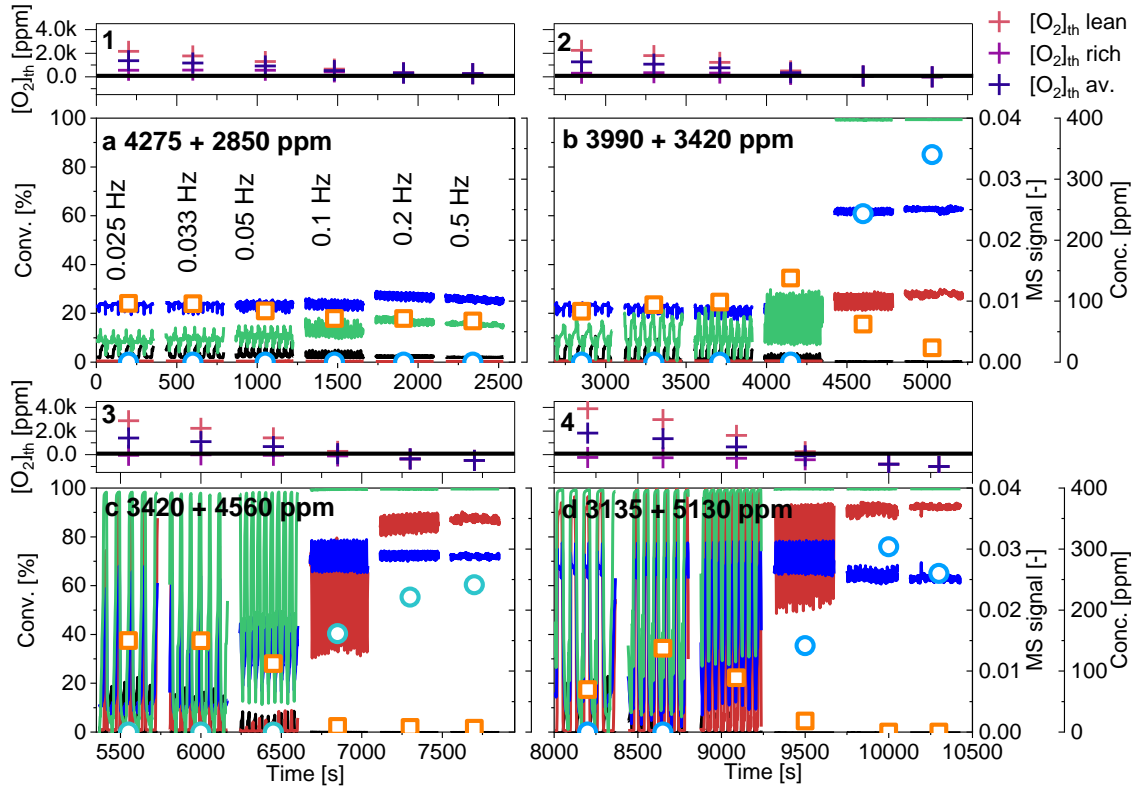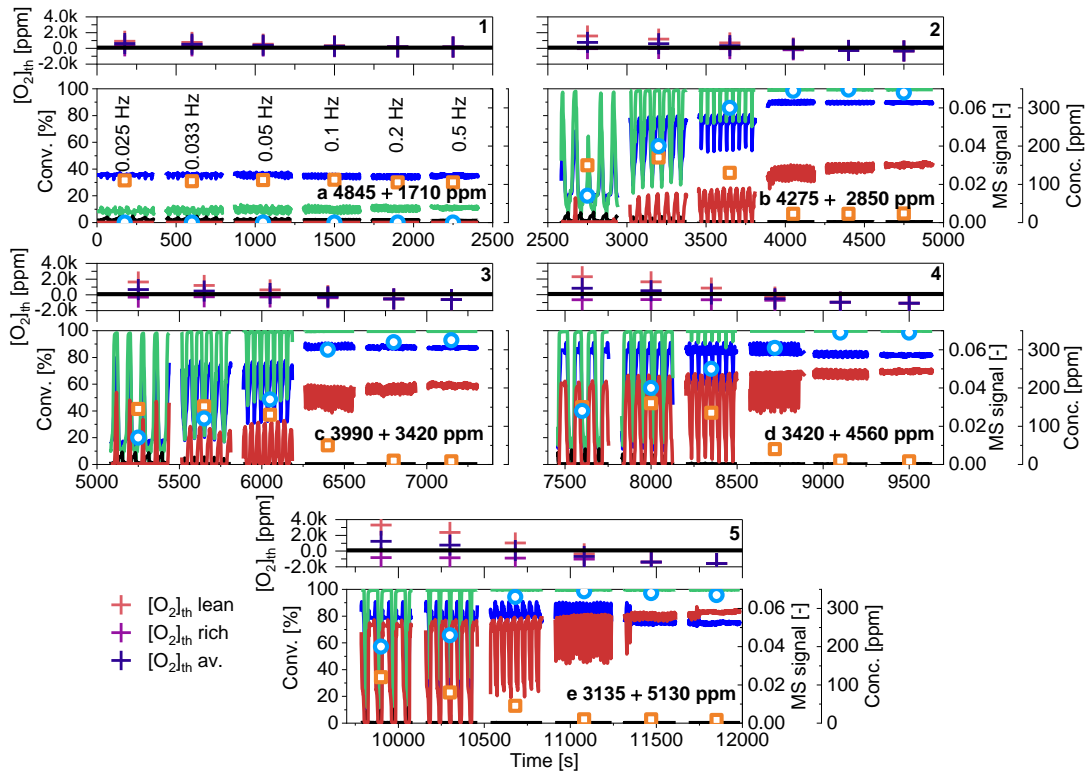
Figure 5.12. (a - e) CH_4 (blue) and NO (green) conversion as well as H_2 (red) and O_2 (black) and concentration of N_2O (orange; □) and NH_3 (light blue; ○) under O_2-dithering conditions at 435 °C at 0.025, 0.033, 0.05, 0.1, 0.2 and 0.5 Hz and given amplitude of (a, 1) 4845 + 1710 ppm O_2, (b, 2) 4275 + 2850 ppm O_2, (c, 3) 3990 + 3420 ppm O_2, (d, 4) 3420 + 4560 ppm O_2, (e, 5) 3135 + 5130 ppm O_2. $[O_2]_{th}$ calculated from the low conversion regime in the lean and rich phases of the pulses and the average between the lean and rich phases are shown on top of each panel (1-5). The black horizontal line represents the 84 ppm $[O_2]_{th}$. Conditions: 1500 ppm CH_4, 1600 ppm NO, 7000 ppm CO, 5 vol% H_2O; (a) $\lambda = 1 \pm 0.009$, (b) $\lambda = 1 \pm 0.015$, (c) $\lambda = 1 \pm 0.018$, (d) $\lambda = 1 \pm 0.024$ and (e) $\lambda = 1 \pm 0.027$; WHSV = 240 $Lh^{-1}g^{-1}$.

5.3.2.3 Effect of exhaust composition

The gas composition is an important factor to consider in real engine exhaust because it can vary rapidly with driving conditions. Hence, the effect of pollutants concentration in the feed was tested under O_2-dithering conditions (3990 + 3420 ppm O_2 and 0.05 Hz) at 435 °C.

Figure 5.13. CH₄ (blue) and NO (green) conversion, MS signals of H_2 (red) and O_2 (black), and concentration of N_2O (orange; □) and NH_3 (light blue; ○) at 435 °C under O_2-dithering conditions (3990 + 3420 ppm O_2 and 0.05 Hz) while varying [CH₄] from 0 to 1800 ppm. [O_2]$_{th}$ in the lean and rich phases of the pulses and the average between the lean and rich phases are shown on top of each panel. LCR, low conversion regime; HCR, high conversion regime. The black horizontal line represents the 84 ppm [O_2]$_{th}$. Conditions: variable CH₄, 1600 ppm NO, 7000 ppm CO, 5 vol% H_2O; $\lambda = 1 \pm 0.018$; WHSV = 240 Lh^{-1}g^{-1}.

CH₄ concentration was varied from 0 to 1800 ppm at constant NO (1600 ppm) and CO (7000 ppm) concentrations and the results are displayed in Figure 5.13. As indicated above (Table 5.1), ca. 595 ppm of the initial 1500 ppm CH₄ reacted at 435 °C in static conditions (ca. 40 % conversion). Therefore, CH₄ conversion needed to be adapted based on this value. When less than 595 ppm CH₄ was used, 100 % conversion was considered in the calculations, while the conversion was decreased accordingly above this concentration (Table C9). The calculations predicted that CH₄-SR could be maintained over the entire dithering cycle from 0 ppm up to 1400 ppm CH₄ irrespective of the conversion regime considered (Table C9). Above this concentration, CH₄ and NO conversions were expected to decrease in the lean phase of the pulses because the calculated O_2 value over the full pulsing cycle was higher than 84 ppm, but CH₄-SR could still be promoted in the rich phases

up to 1700 ppm CH_4. Finally, for 1800 ppm CH_4, low conversion was expected over the entire dithering sequence. All the calculations were verified and confirmed experimentally (Figure 5.134), demonstrating the need to use a variable value of CH_4 conversion rather than the constant value obtained under static conditions. This is emphasized for 1800 ppm CH_4, where if CH_4 conversion was kept at 40 % (static conditions) rather than 33 %, a high conversion would have been expected in the rich phases (Figure 5.13, Table C10). Furthermore, CO slips were detected in the rich phases of the pulses, and increased with CH_4 concentration, as long as the high conversion regime was promoted (Figure C11a).

NO concentration was varied from 0 to 4400 ppm at constant CH_4 (1500 ppm) and CO (7000 ppm) concentration, as depicted in Figure 5.14. From the low conversion regime (40 % CH_4 conversion and 10.5 % NO conversion), our calculations pointed to high conversion in the rich phases of the pulses for NO concentration above 400 ppm (Table C11). Moreover, CH_4-SR should be maintained during the entire dithering cycle for more than 1600 ppm NO. However, the experimental results of Figure 5.14 show that CH_4-SR was promoted in the rich phases already in the absence of NO, while CH_4-SR was never maintained during the entire cycle. This mismatch between the experiment and the calculations is due to the fact that much more oxygen was available to the catalyst in the rich phases at full NO conversion than considered in the calculations (10.5 % NO conversion). This was especially true for high NO concentrations of 4400 ppm that can release a correspondingly higher amount of oxygen on the catalyst surface. Therefore, it is important to consider also the calculations obtained in the high conversion regime (68.65 % CH_4, 100 % NO). These calculations indicated that CH_4-SR was never expected over the entire dithering cycle but was active only in the rich phases of the pulses (Table C11). Hence, under these conditions, the control calculations between low and high conversion regimes were essential to compensate for the fraction of oxygen released by NO and exploited to react CH_4. Moreover, unreacted CO was present in the rich phases of the pulses, but its concentration was not affected by the NO concentration used in the feed (Figure C11b).
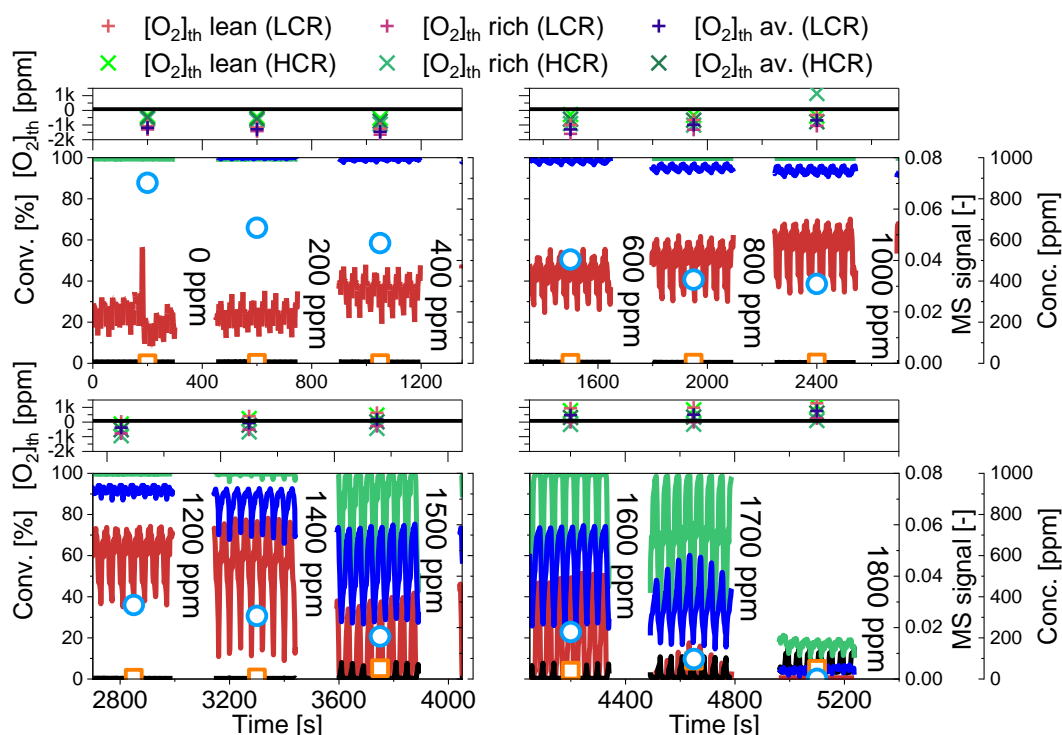
Figure 5.14. CH_4 (blue) and NO (green) conversions, MS signals of H_2 (red) and O_2 (black), and concentration of N_2O (orange; □) and NH_3 (light blue; ○) at 435 °C under O_2-dithering conditions (3990 + 3420 ppm O_2 and 0.05 Hz) while varying [NO] from 0 to 4400 ppm. $[O_2]_{th}$ in the lean and rich phases of the pulses and the average between the lean and rich phases are shown on top of each panel. LCR, low conversion regime; HCR, high conversion regime. The black horizontal line represents the 84 ppm $[O_2]_{th}$. Conditions: 1500 ppm CH_4, variable NO, 7000 ppm CO, 5 vol% H_2O; $\lambda = 1 \pm 0.018$; WHSV = 240 $Lh^{-1}g^{-1}$.

In the case of the variation of CO concentration from 0 to 11000 ppm at constant CH_4 (1500 ppm) and NO (1600 ppm), the experimental data were always correctly predicted by the calculations (Figure 5.15, Table C12). For this set of experiments since NO concentration was constant, both calculations from CH_4 oxidation by O_2 and by H_2O provided the same result. The model estimated that CH_4-SR would never be triggered up to 5000 ppm of CO in the feed; above this concentration, it would be promoted in the rich pulses. Under these conditions, the CO slips, observed in the high conversion regime increased with the CO concentration used (Figure C11c).
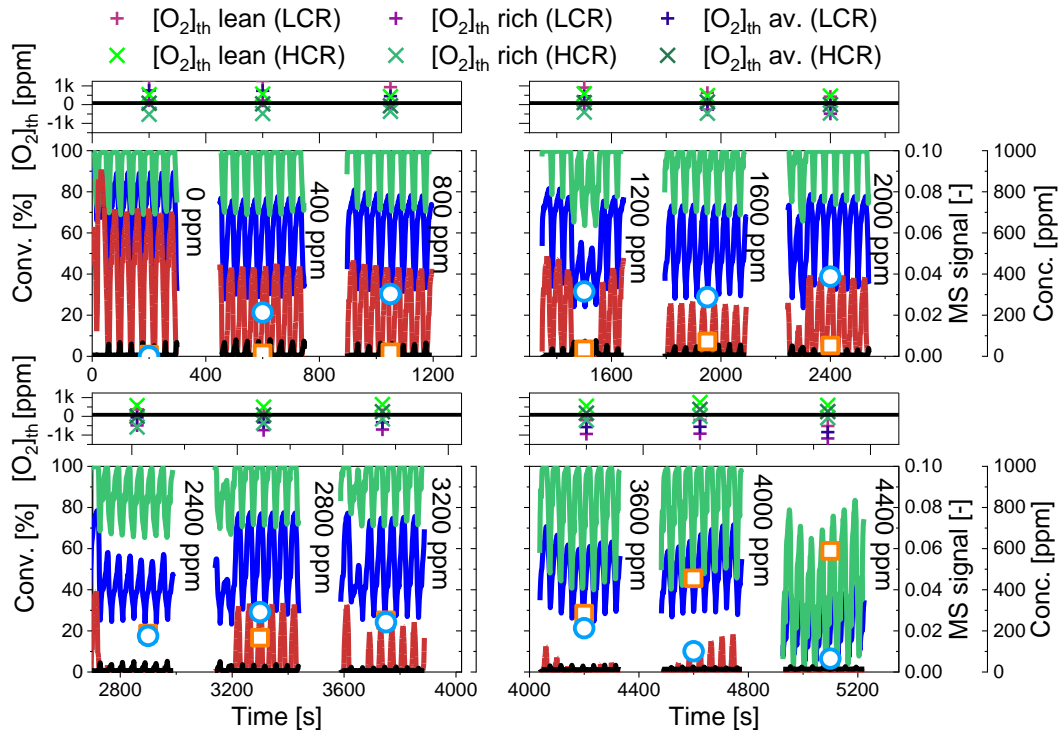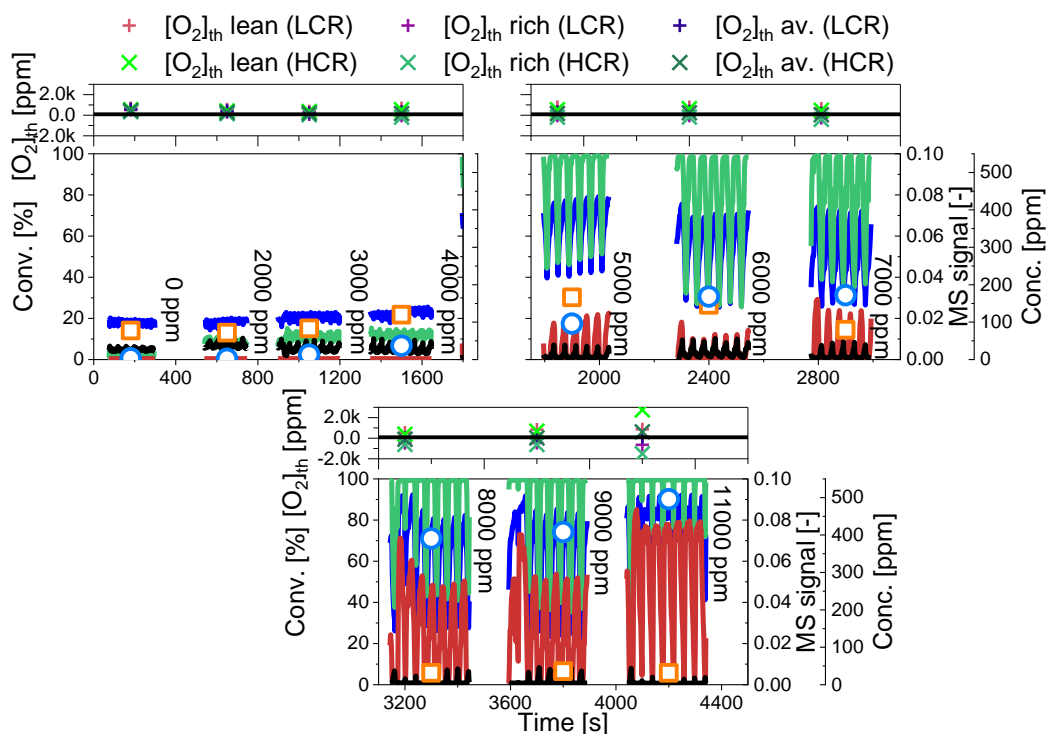
Figure 5.15. CH_4 (blue) and NO (green) conversion as well as MS signals of H_2 (red) and O_2 (black) and concentration of N_2O (orange; □) and NH_3 (light blue; ○) at 435 °C during O_2-dithering (3990 + 3420 ppm O_2 and 0.05 Hz) while varying CO from 0 to 11000 ppm. The top part of each panel shows the $[O_2]_{th}$ in the lean and rich phases of the pulses, and the average between the lean and rich phases, LCR, low conversion regime; HCR, high conversion regime. The black horizontal line represents the 84 ppm $[O_2]_{th}$. Conditions: 1500 ppm CH_4, 1600 ppm NO, variable CO, 5 vol% H_2O; $\lambda = 1 \pm 0.018$; WHSV = 240 $Lh^{-1}g^{-1}$.

5.4 Conclusions

In this study, we demonstrated on a model Pd/Al_2O_3 three-way catalyst without oxygen storage component that CH_4 conversion is fully predictable under both static and O_2-dithering operation. Catalytic activity and CH_4 oxidation pathways (oxidation by O_2 and by H_2O) are correlated to the O_2 concentration present in the reactive feed. The O_2 concentration is the main parameter influencing the Pd oxidation state, which in turn controls CH_4 oxidation pathways. Therefore, by precisely knowing the amount of O_2 available at any point in

time, it is possible to anticipate the effect of the O_2 pulses on the activity. Hence, we have used explicit calculations that determine the O_2 concentration present in the feed at all times. The calculations consider the temperature, pollutants concentrations, conversions, and the dithering efficiency, which is affected by the dithering conditions used (amplitude and frequency). While in theory, the average O_2 concentration fed to the catalyst is the same for all dithering conditions used, in reality, it decreases with increasing amplitude and decreasing frequency. It is, therefore, crucial to evaluate the dithering efficiency as a function of the pulsing conditions to precisely determine the O_2 concentration delivered to the catalyst in the lean and rich phases of the O_2 pulses. The predictions were evaluated at different temperatures, dithering conditions, and pollutant concentrations and consistently agreed with the experimental results.

Overall, the results show that the O_2 pulses had a beneficial effect on the activity when CH_4 steam reforming was promoted (O_2-poor conditions, reduced Pd species), whereas an excess of O_2 induced CH_4 oxidation by O_2 and led to moderate CH_4 conversion and low NO conversion. Because of the evident benefits of O_2-dithering found here for Pd/Al_2O_3, we believe that the addition of an OSC component will result in a similar behaviour but not necessarily under identical conditions that are optimal for Pd/Al_2O_3.

Chapter 6 Effect of Rh on Pd/Al$_2$O$_3$ in exhaust natural gas vehicles conditions under static and O$_2$-dithering operation

6.1 Introduction

Repeated lean/rich O$_2$ pulses can significantly improve pollutant removal if the pulsing parameters (amplitude and frequency) applied are chosen correctly according to the conditions (i.e. temperature, gas feed composition, λ value, etc.). It was shown that when simultaneous high removal of all pollutants is achieved, CH$_4$ steam reforming is involved. Nonetheless, the hydrogen formed from SR reactions can react with NO to form NH$_3$, which emissions are strongly regulated by the European emissions standards. Therefore, the material formulation should be tailored with the aim of enhancing SR and minimizing NH$_3$ emissions during periodic operation.

The combination of two or more metals to form alloys, core-shell or complex heterometallic structures has gained interest over the past decades. Many bimetallic systems exhibit superior properties than their monometallic counterparts [234–236] since they present the properties of each metal as well as new properties that result from the synergy between the two metals. This synergy can arise from electronic coupling effects (also defined as ligand effect) between the two metals (i.e. changes in the Fermi level, or work functions), unique structural/geometric arrangements of atoms (ensemble effect) or/and complementary contributions from each metal that improve the overall material properties (bifunctional effect) [237–240,240,241]. Hence, the chemical and physical properties of the catalysts can be tuned by varying the composition, atomic ordering as well as size of the bimetallic particles.

While many combinations of metals have been investigated for TWC applications [242–250], Rh is the most interesting metal to alloy with Pd, as it is efficient for NO$_x$ reduction and SR reactions [99,251,252], and

significantly reduces the NH_3 emissions [248]. Indeed, Maillet et al. examined the role of Rh in C_3H_8 oxidation and SR reactions over a $Pd-Rh/Al_2O_3$ catalyst and found that the improved SR activity was mainly attributed to the presence of Rh while C_3H_8 oxidation was not affected by the increase of the Rh loading due to the high oxidation activity of Pd compared to Rh [253]. The poor activity of Rh toward oxidation reactions is ascribed to the formation of well-ordered surface rhodium oxide [116] and the fast diffusion of Rh^{3+} into the support, where these ions initiate compaction or even phase transformations of the latter [116,254,255].

In this Chapter, Pd/Al_2O_3, Rh/Al_2O_3, and $Pd-Rh/Al_2O_3$ were synthesized to investigate the effect of Rh on the catalytic properties of a Pd-based catalyst under both static and periodic operation. Under static operation and oxidative conditions, the presence of PdO/PdO_x species appeared essential for CH_4 oxidation by O_2 (but limited NO reduction) whereas the presence of (oxidized) Rh did not improve the catalytic activity. Once all the O_2 present in the reactive environment had been consumed for CH_4 oxidation, the metals reduced, and CH_4-SR was promoted while complete NO reduction was achieved. From Chapter 5, it is clear that the Pd oxidation state (cf. redox dynamics) is greatly affected by the O_2 concentration present in the reactive environment, and controls the pollutant removal efficiency: low activity in the presence of oxidic Pd and high activity when Pd is reduced. Hence, when performing repeated lean/rich O_2 pulses on Pd/Al_2O_3, the activity oscillated with the O_2 concentration between low and high conversion rates due to the constant oxidation/reduction of the catalyst. On the other hand, the redox dynamics of Rh are significantly less affected by the O_2 concentration, and once reduced, the Rh species remain predominantly in that state. Moreover, when Pd and Rh are in close contact ($Pd-Rh/Al_2O_3$) the ability of Rh to remain in its reduced state over a broad range of O_2 concentrations is transferred to the Pd species. Hence, when O_2-dithering is performed on the Rh-based samples, high activity was achieved over a much broader range of dithering parameters (amplitudes and frequencies) than Pd/Al_2O_3. This work reveals that Pd is crucial to achieving acceptable conversion rates under oxidizing conditions, while Rh maintains the catalyst reduced and the activity high under rich conditions. Hence, when Pd and Rh are in close contact, the lean/rich O_2 pulses can be applied over a wide range of dithering parameters.

6.2 Materials and methods

6.2.1   Material synthesis

A commercial aluminum oxide (γ-Al_2O_3, Puralox; Sasol) was used as support. Pd and/or Rh were added by incipient wetness impregnation of palladium (II) nitrate (Alfa Aesar, 4-5 wt% solution) and rhodium (III) nitrate (Alfa Aesar, 32 % Rh assay) solutions. The bimetallic sample was prepared using a mixed solution of the two metal precursors and stirred at room temperature for 2 h. Then, the powders were dried at 120 °C for 12 h and calcined in air at 550 °C for 3 h (5 °Cmin^{-1}). The total metal content was kept to ca. 1.6 wt% in Pd-Rh/Al_2O_3 and a Pd:Rh ratio equal to 3:2 was used, as it is reported to be the most active Pd:Rh ratio for TWC application [256]. The Rh content in Rh/Al_2O_3 was aimed to be equal to the one in Pd-Rh/Al_2O_3.

6.2.2   X-ray absorption spectroscopy

Table 6.1. Summary of the samples measured by ex situ X-ray absorption spectroscopy

Material	Name	Pre-treatment	Quenched in temp. ramp at 425 °C
Pd/Al_2O_3	Pd/Al_2O_3 - aft. calcination	-	-
	Pd/Al_2O_3 - aft. H_2 PT	Reductive	-
	Pd/Al_2O_3 - act. aft. H_2 PT	Reductive	Yes
	Pd/Al_2O_3 - act. aft. O_2 PT	Oxidative	Yes
Rh/Al_2O_3	Rh/Al_2O_3 - aft. calcination	-	-
	Rh/Al_2O_3 - aft. O_2 PT	Oxidative	-
	Rh/Al_2O_3 - aft. H_2 PT	Reductive	-
	Rh/Al_2O_3 – act. aft. O_2 PT	Oxidative	Yes
	Rh/Al_2O_3 – act. aft. H_2 PT	Reductive	Yes
Pd-Rh/Al_2O_3	Pd-Rh/Al_2O_3 - aft. calcination	-	-
	Pd-Rh/Al_2O_3 - aft. H_2 PT	Reductive	-
	Pd-Rh/Al_2O_3 – act. aft. O_2 PT	Oxidative	Yes
	Pd-Rh/Al_2O_3 – act. aft. H_2 PT	Reductive	Yes

The ex situ X-ray absorption spectroscopic spectra of the pelletized samples were acquired for 5 min. The samples were either measured in their fresh state (after calcination in air), after an oxidative or reductive pre-treatment, or retrieved during the temperature ramp measurements. In the latter case, the calcined samples were pre-treated (oxidative or reductive pre-treatment) before performing a temperature ramp. The samples were then quenched in argon at 425 °C in the descending ramp and cooled down to room temperature in argon to ensure that the catalysts retained their oxidation state.

6.3 Results and discussion

6.3.1 Material characterization

The Pd and Rh concentrations in the sample were obtained by ICP-OES and the specific surface area was calculated using the BET method (Table 6.2).

Table 6.2. ICP-OES of the samples.

	Pd/Al_2O_3	Rh/Al_2O_3	Pd-Rh/Al_2O_3
Pd [wt %]	1.64	-	1.05
Rh [wt%]	-	0.71	0.82
Specific surface area [m^2g^{-1}]	147.2	150.6	147

The XRD patterns of the samples confirmed that impregnation and calcination of the material did not affect the alumina phase (Figure 6.1a). The Pd-based samples only displayed reflections of PdO. Rh, however, was not detected in the Rh-containing samples since it was present in low amounts and was highly dispersed on and in the Al_2O_3 support after calcination in air at 500 °C for 3 h [116,255,257]. The XANES spectra and FT-XAFS confirmed that all three samples were fully oxidized after calcination (Figure 6.2).
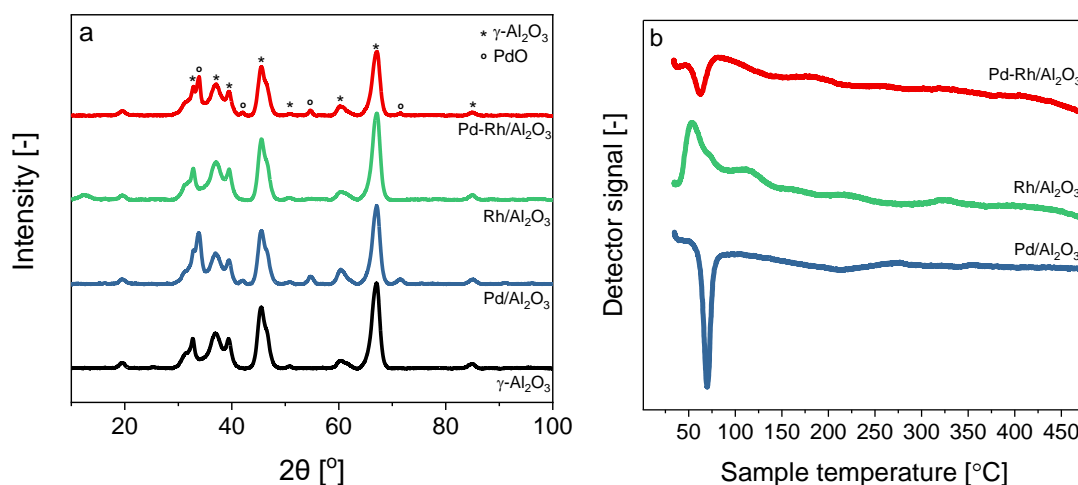
Figure 6.1. (a) X-ray diffraction patterns of γ-Al_2O_3, Rh/Al_2O_3, Pd/Al_2O_3, and Pd-Rh/Al_2O_3 after calcination in air and (b) H_2-TPR of Pd/Al_2O_3, $RhAl_2O_3$ and Pd-Rh/Al_2O_3.

TEM imaging evidenced that all three samples consist of small Pd and/or Rh particles of about 6.6 nm width and narrow size distribution (FWHM of the distribution is about 4.9 nm; Figure D1). EDX maps of Pd-Rh/Al_2O_3 after calcination (Figure 6.3a) show that Pd and Rh agglomerate in the same particles, supporting that the two metals are in close contact (atomic ratio Pd/Rh in the particles below 0.4). After reductive pre-treatment, three types of particles are observed: enriched Pd particles (atomic Pd/Rh ratio above 1), enriched Rh particles, and particles wherein Pd and Rh are in close contact (Figure 6.3b). Moreover, according to the surface energy of Pd and Rh (reduced and oxidized state), the two metals are not miscible, and can therefore not be alloyed [250,258–261]. Hence, our bimetallic system forms a core-shell and/or complex heterometallic structure.

The H_2-TPR profiles of Pd/Al_2O_3 and Pd-Rh/Al_2O_3 present a negative peak arising from PdH_x decomposition at 70 and 63 °C, respectively (Figure 6.1c-d) [262,263]. The peak is shifted to lower temperatures in Pd-Rh/Al_2O_3, suggesting that when Pd and Rh are in close enough contact, the presence of Rh alters the reactivity of Pd. Moreover, the results show that Rh^{3+} reduction occurs at higher temperatures (52 °C) than PdO reduction (< 25 °C) [264,265].
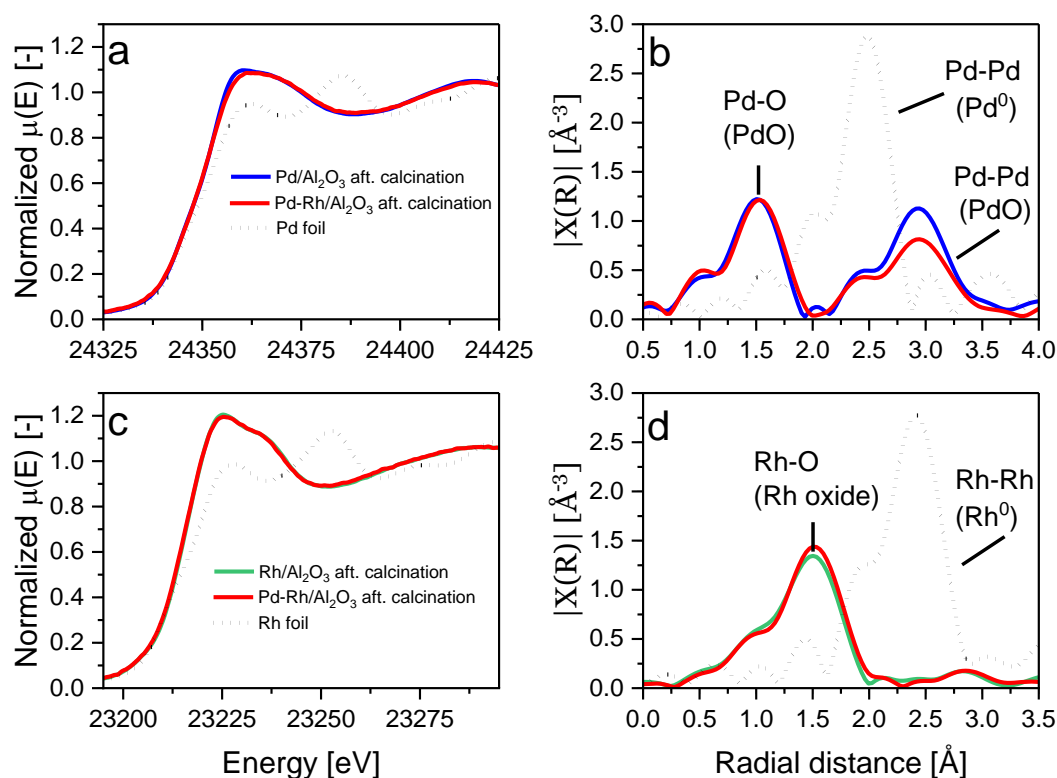
Figure 6.2. Ex-situ XAS of Pd/Al$_2$O$_3$, Pd-Rh/Al$_2$O$_3$, and Rh/Al$_2$O$_3$ were acquired at the (a-b) Pd K-edge and (c-d) Rh K-edge after calcination. (a, c) Spectra of the XANES region, and (b, d) FT-XAFS (not phase corrected).

In situ XRD measurements were carried out on Pd/Al$_2$O$_3$ and Pd-Rh/Al$_2$O$_3$, and consisted in heating the samples from 60 to 600 °C in H$_2$, and then cooling them to 60 °C in O$_2$ (Figure 6.4). The diffractograms were acquired at 60, 170, 300, 450, and 600 °C during heating and every 25 °C from 600 to 300 °C during cooling (more details in section 2.6.2). The results demonstrated that under reducing conditions, Pd-Rh/Al$_2$O$_3$ reduced below 60 °C (absence of the PdO reflection, and presence of Pd^0 peak) while Pd/Al$_2$O$_3$ reduction occurred between 60 and 170 °C (Figure 6.4), which is consistent with the H$_2$-TPR data. Therefore the Pd species reduce at lower temperatures in H$_2$ when in close contact with Rh. Then, when switching to an oxidative environment at 600 °C, the Pd species reoxidized at 500 and 475 °C in Pd-Rh/Al$_2$O$_3$ and Pd/Al$_2$O$_3$, respectively. The results demonstrate that the redox properties of Pd are affected by the presence of Rh.

Figure 6.3. High-angle annular dark-field STEM image of Pd-Rh/Al$_2$O$_3$ and EDX net count maps from 3 different Pd-Rh particles of the STEM image (square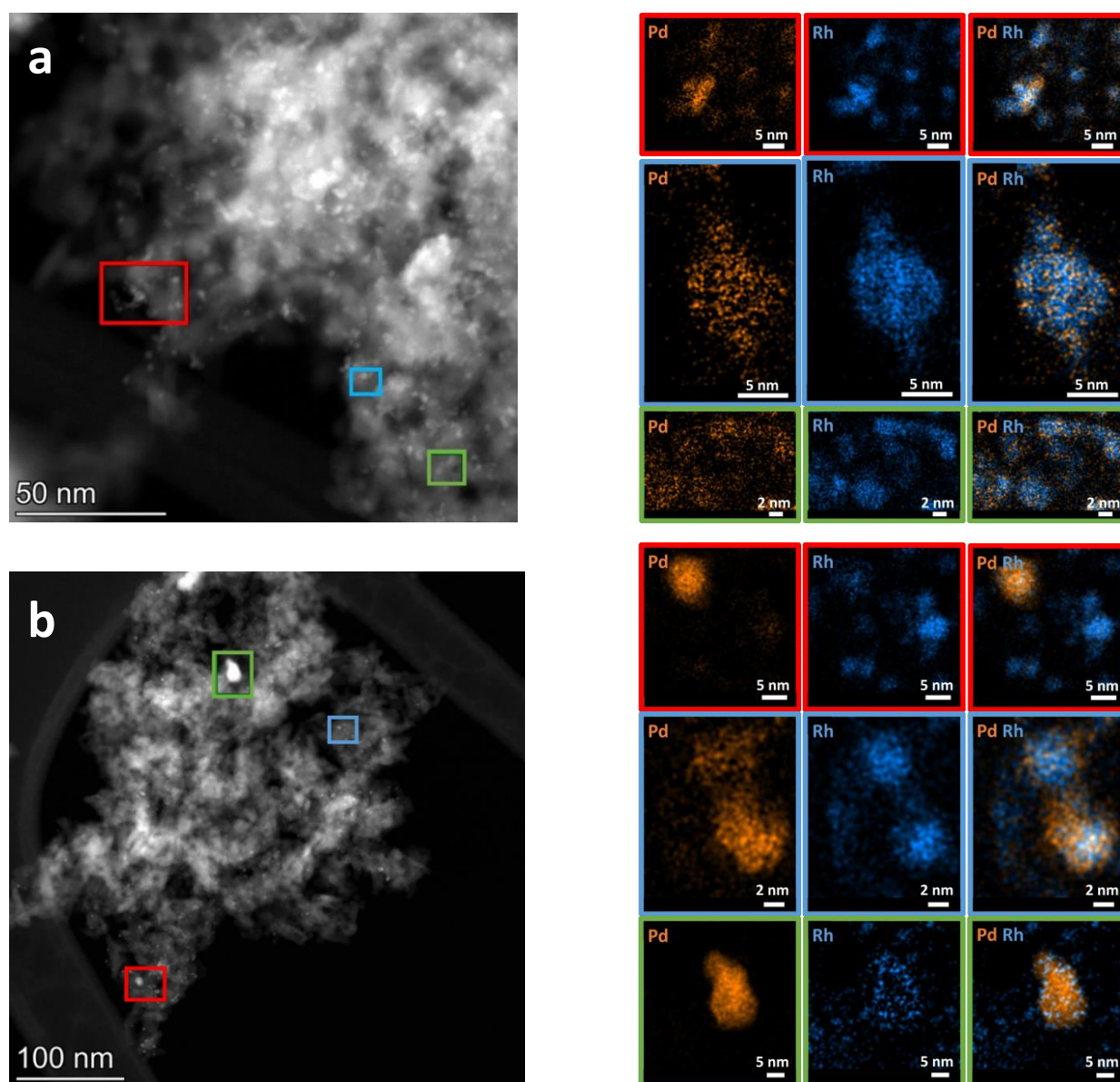d in red, blue, and green) after (a) calcination and (b) reducing pre-treatment. Quantification of the atomic Pd/Rh ratio in the six different maps of particles (a, red) 0.35, (a, blue) 0.17, (a, green) 0.30, (b, red) 1.51, (b, blue) 1.07 and (b, green) 57.8.
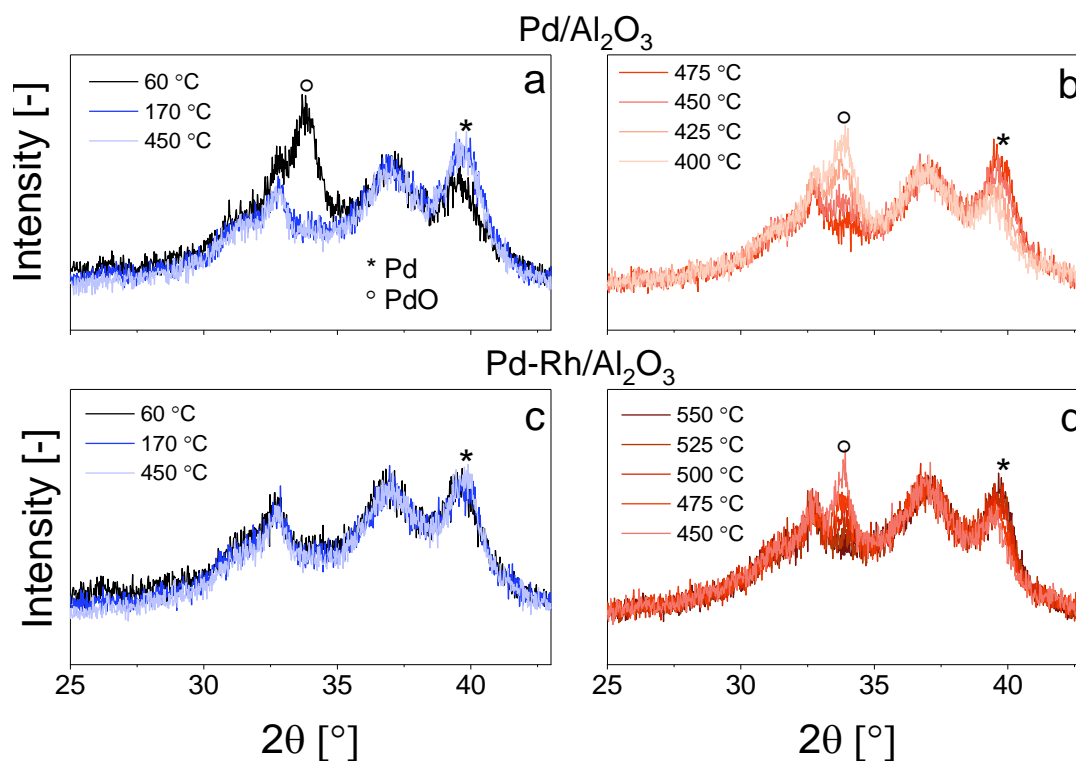
Figure 6.4. In situ XRD patterns of (a-b) Pd/Al$_2$O$_3$ and (c-d) Pd-Rh/Al$_2$O$_3$ measured (a, c) in 2000 ppm H$_2$ (50 mLmin^{-1}; rest N$_2$) from 60 to 600 °C, and (b, d) in 2000 ppm O$_2$ (50 mLmin^{-1}; rest N$_2$) from 600 to 60 °C.

6.3.2 Catalytic study

Static operation

The catalytic activity of Pd/Al$_2$O$_3$ was evaluated first under static stoichiometric conditions after an oxidative pre-treatment (Figure 6.5a-b). Two conversion regimes were observed. First, CH$_4$ oxidation by O$_2$ proceeded up to 438 °C, together with limited NO conversion (5 % at 420 °C; low conversion regime). Above 438 °C, rapid and complete NO and CH$_4$ conversions were obtained and were accompanied by H$_2$ formation, attesting to the occurrence of methane steam reforming (high conversion regime). The high conversion regime occurred only once all the O$_2$ fed to the catalyst was consumed (Figure D2). In Chapters 3 to 5, we showed that when only CH$_4$ oxidation by O$_2$ occurs, the Pd species are oxidized (fully or partially), whereas if CH$_4$-

SR is promoted, the Pd species are fully reduced (cf. Chapter 4-5). Therefore, we consider that the Pd species are partially oxidized up to 438 °C and fully reduced above this temperature. Furthermore, upon cooling, CH_4 and NO conversions dropped abruptly to 20 % at 480 °C, resulting in a negative hysteresis between the heating and cooling segment. This is due to the formation of a dense chemisorbed oxygen layer around the Pd^0 particles as the oxidation process of Pd^0 follows a shrinking core mechanism [223,224], which is considerably less active toward CH_4 oxidation than bulk PdO, PdO_x, and Pd^0. Ex-situ XAS measured at the Pd K-edge on the sample retrieved in the cooling segment, at 425 °C, after the loss of activity (Pd/Al_2O_3 - act. aft. O_2 PT; Table 6.1), confirmed that the Pd species were partially oxidized when the activity dropped in the descending ramp. Indeed, the XANES spectra (Figure 6.6a) showed that the Pd species were less oxidized than after calcination (Pd/Al_2O_3 - aft. calcination) and less reduced than after an H_2 pre-treatment (Pd/Al_2O_3 - aft. H_2 PT), while the FT-XAFS (Figure 6.6b) displayed features of both PdO and Pd^0. Moreover, at low temperatures, NO reduction showed about 50 % selectivity towards N_2O (Figure 6.5b), which forms under oxidizing conditions from the reaction between NO and CO, through surface isocyanate intermediates [232,233]. The N_2O concentration increased with temperature, reaching a maximum of ca. 141 ppm at 438 °C before dropping to zero when CH_4 oxidation started, suggesting a displacement of the intermediate isocyanate species. On the other hand, in the high conversion regime, only NH_3 was formed (and N_2; Figure 6.5b) from the reaction between NO and the H_2 formed from CH_4-SR [59,233].

Lambda sweep experiments were performed at 420 °C (Figure 6.7a-b) from lean (6840 ppm O_2; $\lambda = 1.006$) to rich conditions (0 ppm O_2; $\lambda = 0.971$) and back to lean conditions. Under lean conditions, CH_4 and NO concentrations were constant (1020 ppm and 1560 ppm, respectively; Figure 6.7a). Below stoichiometry (5415 ppm O_2, $\lambda = 0.998$), NO concentration decreased to ca. 1380 ppm, accompanied by N_2O formation (ca. 90 ppm). The NO−CH_4 crossover point was reached at 5130 ppm O_2 ($\lambda = 0.997$), resulting in complete NO reduction and higher CH_4 conversion (+ 44 %). This point coincided with the start of H_2 formation due to the promotion of CH_4-SR and therefore resulted in NH_3 production (ca. 270 ppm). The NH_3 concentration increased with decreasing O_2 concentration, reaching 1350 ppm in an O_2-free environment. When proceeding to rich conditions, significant amounts of CO were observed, up to ca. 3030 ppm (7000 ppm CO were fed) at λ

= 0.971, while CH_4 concentration reached 1445 ppm (4 % conversion). In the absence of O_2, H_2 was still detected, and CO was partly converted, indicating that the water gas shift reaction (WGS) was occurring. In the rich-to-lean sweep (Figure 6.7b), the opposite trend was observed. However, the $NO-CH_4$ crossover point occurred at richer conditions (4560 ppm O_2, λ = 0.994) compared to the lean-to-rich sweep. This negative hysteresis observed between the lean-to-rich and rich-to-lean sweeps indicates that Pd reoxidation is very sensitive to the O_2 concentration present in the feed, and the surface oxide layer species form at lower O_2 concentrations than required to reduce the oxidic Pd species.
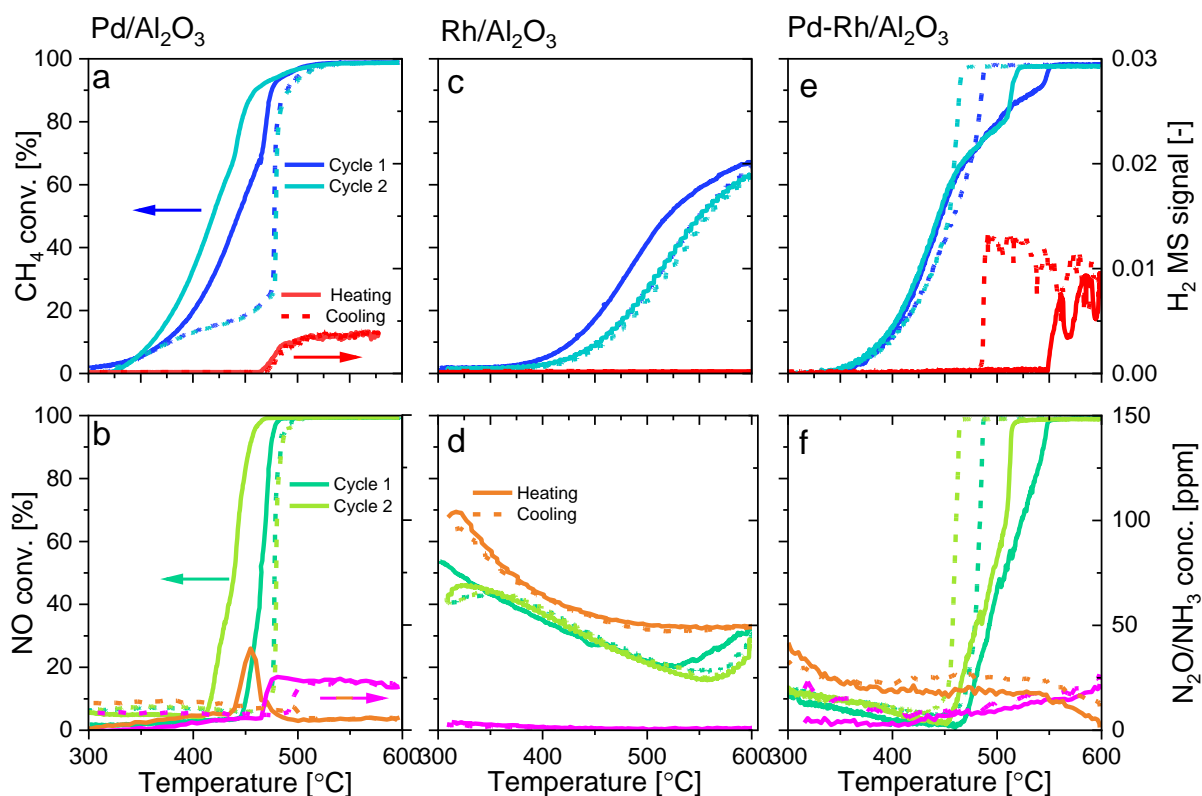
Figure 6.5. CH_4 (a, c, e) and NO (b, d, f) conversion as well as H_2 (red; a, c, e) MS signal and N_2O (orange; b, d, f) and NH_3 (pink; b, d, f) concentrations during heating (—) and cooling (---) segments performed under static stoichiometric (5700 ppm O_2; λ = 1.0) conditions over (a-b) Pd/Al_2O_3, (c-d) Rh/Al_2O_3 and (e-f) $Pd-Rh/Al_2O_3$. CH_4 and NO conversions are shown for two consecutive cycles. The catalytic measurements were performed after an oxidative pre-treatment. Conditions: 1500 ppm CH_4, 1600 ppm NO, 7000 ppm CO, 5700 ppm O_2, 5 vol% H_2O; WHSV = 240 $Lh^{-1}g^{-1}$.

Figure 6.6. Ex-situ XAS acquired at the Pd K-edge of Pd/Al$_2$O$_3$ after calcination and retrieved in the cooling performed O$_2$ PT, as well as the Pd foil. (a) Spectra of the XANES region, and (b) FT-XAFS (not phase corrected).

For Rh/Al$_2$O$_3$, only CH$_4$ oxidation by O$_2$ was observed (low conversion regime) in the static stoichiometric temperature ramp experiments (Figure 6.5c-d). The activity for CH$_4$ oxidation was limited: the temperature at half CH$_4$ conversion (T$_{50\%}$) shifted by 130 °C to higher temperature compared to Pd/Al$_2$O$_3$ and the maximum conversion (65 %) was only reached at 600 °C (Figure 6.5c). NO conversion was also low and led to significant amounts of N$_2$O, which followed the trend of NO conversion. NH$_3$ was not observed because H$_2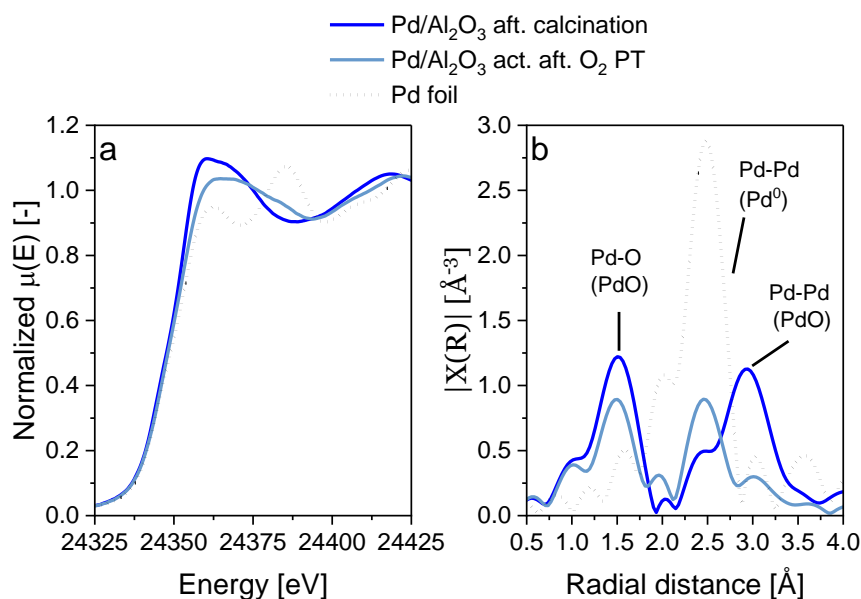$ was not formed. The low activity achieved in the temperature ramps is attributed to the presence of highly stable and inactive Rh^{3+} species formed during the calcination step which was followed by an oxidative pre-treatment (Figure 6.2) [97,116,255,266–271]. Indeed, Burch et al. [267] showed that when Rh/Al$_2$O$_3$ is heated above 500 °C under an oxidizing atmosphere, Rh coordinates to Al (Rh–O–Al), evidencing that Rh^{3+} incorporates into the surface layer of the Al$_2$O$_3$ support. The formation of highly stable and inactive Rh^{3+} species in the Al$_2$O$_3$ support inhibits the reduction of Rh oxide to active Rh^0 [97,255,266–272]. The λ sweep experiments (Figure 6.7c-d) revealed that in the lean-to-rich sweep, a richer environment (3420 ppm O$_2$, λ = 0.988) was necessary to reach the NO−CH$_4$ crossover point compared to Pd/Al$_2$O$_3$ (Figure 6.7c), demonstrating that the Rh oxide species formed were more difficult to reduce than Pd in the exhaust feed of stoichiometric NG engines. Indeed,

the reduction of Rh oxides requires harsh conditions, as shown by Machida et al. [266] on Rh/Al$_2$O$_3$, wherein temperatures above 1100 °C (in a feed of 20 % H$_2$/He) were necessary to reduce and disperse the Rh nanoparticles. Furthermore, above 3420 ppm O$_2$, CH$_4$ conversion was low while NO conversion increased gradually as the feed became richer. Below 3420 ppm O$_2$, NO was fully converted and CH$_4$ concentration increased with decreasing O$_2$ concentration. In an O$_2$-free environment ($\lambda = 0.971$), CH$_4$ and CO concentrations were lower for Rh/Al$_2$O$_3$ compared to Pd/Al$_2$O$_3$, demonstrating that reduced Rh species are more efficient towards CH$_4$-SR and WGS than Pd [253]. In rich-to-lean sweeps (Figure 6.7d), the NO−CH$_4$ crossover point was shifted to 5415 ppm O$_2$ ($\lambda = 0.998$), indicative of a positive hysteresis between the two λ sweep directions. Hence, once reduced in the lean-to-rich sweep, Rh remained active and reduced up to higher O$_2$ concentrations when sweeping back from rich to lean conditions.
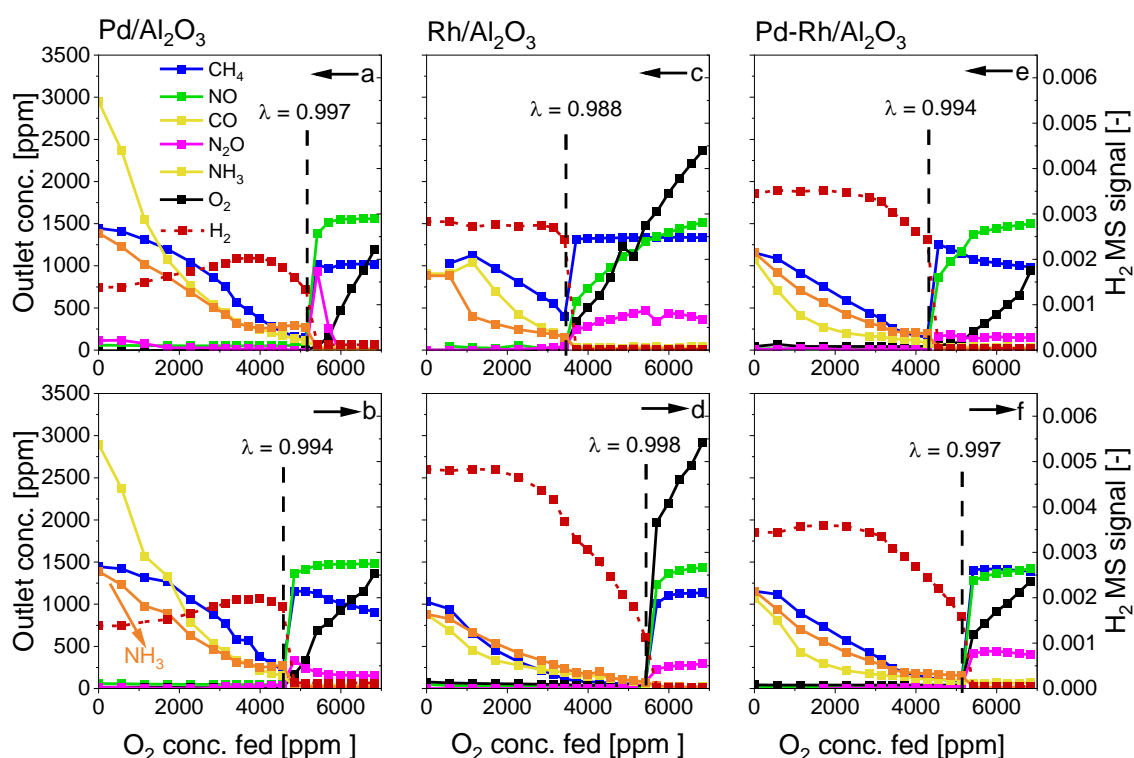
Figure 6.7. Lambda sweep experiments at 420 °C for (a-b) Pd/Al$_2$O$_3$, (c-d) Rh/Al$_2$O$_3$ and (e-f) Pd-Rh/Al$_2$O$_3$. Lean-to-rich λ sweep (a, c, e) and rich-to-lean λ sweep (b, d, f). The measurements were performed after an oxidative pre-treatment. Conditions: 1500 ppm CH$_4$, 1600 ppm NO, 7000 ppm CO, varied O$_2$, 5 vol% H$_2$O; WHSV = 240 Lh^{-1}g^{-1}.

For Pd-Rh/Al_2O_3, the CH_4 and NO conversion profiles obtained from the static stoichiometric temperature ramps were similar to Pd/Al_2O_3 (Figure 6.5e-f). First CH_4 oxidation by O_2 proceeded (up to 510 °C), followed by oxidation by H_2O, leading to complete CH_4 and NO removal. The main difference with Pd/Al_2O_3 was the shift of the conversion curves to higher temperatures ($\Delta T = 72$ °C, 2nd temperature cycle). Ex situ XAS measurements demonstrated that the active metals (Pd and Rh) were fully oxidized after calcination (Figure 6.2), and most probably after the oxidative pre-treatment as well. Hence, these results suggest that in the low temperature regime, the PdO species were the main responsible for the activity as Rh oxide is not very active for CH_4/CO oxidation (Figure 6.5 c-d) [97,116,255,266–271]. Therefore, the shift of the conversion curves to higher temperatures in Pd-Rh/Al_2O_3 compared to Pd/Al_2O_3 was attributed to the lower Pd content. Above 510 °C (Figure 6.5e-f), the occurrence of the high conversion regime led to the reduction of both metals, as seen from the ex situ XAS results acquired at the Pd and Rh K-edge (Figure 6.8). Indeed, in the FT-XAFS (Figure 6.8b) features from metallic Pd-Pd and Rh-Rh scattering paths at 2.43 and 2.78 Å, respectively, were present in the sample retrieved in the cooling segment, at 425 °C, in the high conversion regime (Pd-Rh/Al_2O_3 - act. aft. O_2 PT; Table 6.1). Comparison of the XANES spectra between the foils, catalyst after calcination (Pd-Rh/Al_2O_3 - aft. calcination), and Pd-Rh/Al_2O_3 - act. aft. O_2 PT (Figure 6.8a), reveals that the Pd species in the hysteresis loop are fully reduced, while only partial reduction of the Rh species is achieved. Furthermore, unlike for Pd/Al_2O_3, a positive hysteresis between the heating and cooling segment was observed, indicating that the catalyst remained active towards SR until lower temperatures in the presence of Rh. Indeed, since Rh^0 is more effective for SR reactions than Pd [77,78], once Rh is reduced (even partially) by the H_2 formed from CH_4-SR, it can sustain the high conversion regime longer than Pd/Al_2O_3. This, in turn, prolongs the presence of H_2 in the feed, which keeps the catalyst in its reduced state. This statement was also confirmed with the λ sweep experiments performed on Pd-Rh/Al_2O_3 (Figure 6.7e-f). Indeed, the NO−CH_4 crossover point was observed at 4275 ppm O_2 ($\lambda = 0.993$) in the lean-to-rich sweep but was shifted to 5130 ppm O_2 ($\lambda = 0.997$) on the rich-to-lean sweep. This positive hysteresis confirms that the presence of Rh delays the switch between the high and low conversion regimes, and therefore affects the redox behaviour of the catalyst.
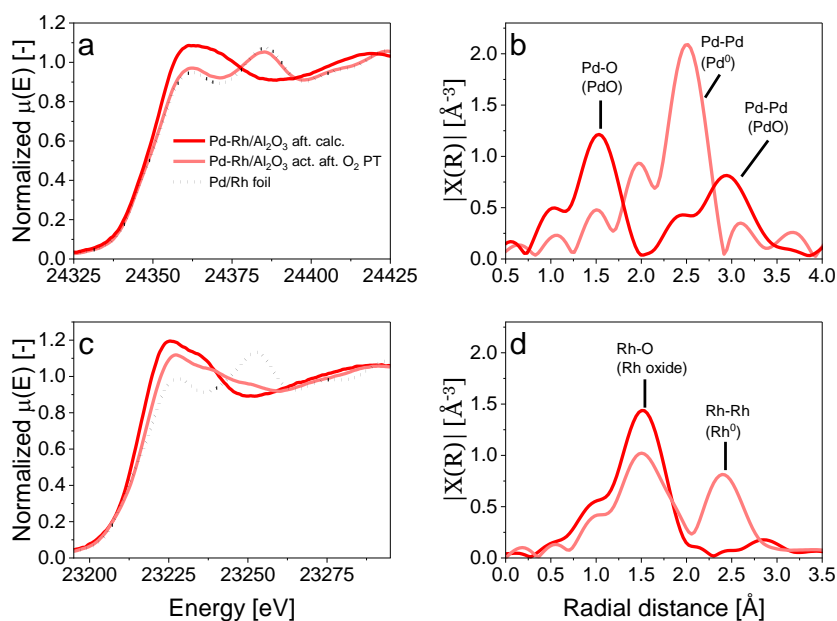
Figure 6.8. Ex-situ XAS acquired at the (a-b) Pd K-edge, and (c-d) Rh K-edge, of Pd/Al$_2$O$_3$ after calcination, and retrieved in the cooling ramp performed after an O$_2$ PT, as well as the Pd and Rh foils. (a, c) Spectra of the XANES region, and (b, d) FT-XAFS (not phase corrected).

The results show that after calcination in air and an oxidative pre-treatment, both Pd and Rh are oxidized. While oxidized Pd is active for CH$_4$ oxidation by O$_2$, oxidized Rh is only moderately active. However, if CH$_4$ oxidation by O$_2$ does not proceed to completion (full consumption of the O$_2$ fed), the second conversion regime (complete NO reduction and CH$_4$-SR) cannot take place. In this case, the metals remain oxidized, leading to low abatement rates as observed over Rh/Al$_2$O$_3$. Thus, in the temperature range evaluated, if an oxidative pre-treatment is applied after calcination in air, the high conversion regime can only be promoted in the presence of Pd. Under oxidizing conditions, the activity is therefore proportional to the Pd content. Since, up to this point, the Pd species are the main species involved in the reaction scheme, they reduce before Rh, due to the promotion of CH$_4$-SR. The H$_2$ evolution in the reactive environment, produced from CH$_4$-SR promotes the (partial) reduction of Rh. The presence of reduced Rh can then maintain CH$_4$-SR longer than Pd/Al$_2$O$_3$ since Rh is more active for SR reactions. Therefore, H$_2$ evolution is preserved, which delays the reoxidation of the catalyst. Furthermore, the in situ XRD experiments (section 6.3.1; Figure 6.3) showed that Pd-Rh/Al$_2$O$_3$ reduces before Pd/Al$_2$O$_3$, in the presence of H$_2$, indicating that reduction of Pd-Rh/Al$_2$O$_3$ is more easily achieved

and maintained than with Pd/Al_2O_3. This explains why under reactive conditions $Pd-Rh/Al_2O_3$ remains reduced until higher λ values in the rich-to-lean sweeps and lower temperatures in the static ramps compared to Pd/Al_2O_3.

Reductive pre-treatment

The beneficial effect of Rh on Pd/Al_2O_3 was observed only once Rh had been reduced. Therefore, a reductive pre-treatment was applied to emphasize the effect of Rh from the beginning of the activity tests. Ex-situ XAS of the samples after the reductive pre-treatment confirmed that Pd and Rh were reduced during this procedure (Figure 6.9). However, Rh was only partially reduced, due to the formation of Rh^{3+} coordinated with Al during the calcination step, whose reduction requires harsher conditions (i.e. high temperatures and dwell times [97,255,266–272]). The activities of all three samples remained similar over several consecutive reaction cycles, indicating that the effects discussed are intrinsic to the materials and not just temporary.
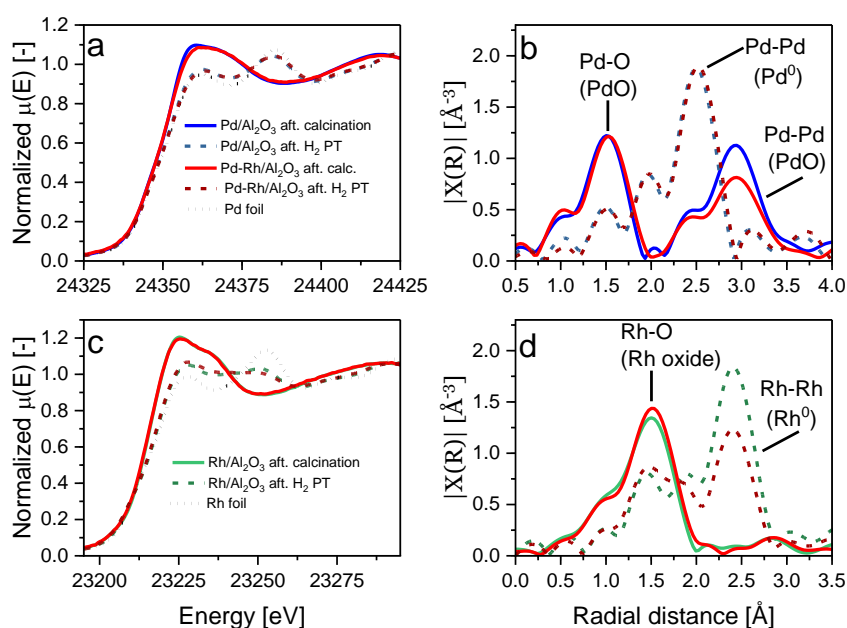

Figure 6.9. Ex-situ XAS acquired at the (a-b) Pd K-edge, and (c-d) Rh K-edge, of Pd/Al_2O_3, $Pd-Rh/Al_2O_3$, and Rh/Al_2O_3 after calcination, and after a reductive pre-treatment, as well as the Pd and Rh foils. (a, c) Spectra of the XANES region, and (b, d) FT-XAFS (not phase corrected).

First, the $T_{50\%}$ values observed when raising the temperature increased with decreasing Pd content from Pd/Al$_2$O$_3$ (397 °C) to Pd-Rh/Al$_2$O$_3$ (446 °C) and Rh/Al$_2$O$_3$ (519 °C; Figure 6.10). This indicates that regardless of the pre-treatment, the presence of Pd is essential in the low conversion regime. The reductive pre-treatment was beneficial to Rh/Al$_2$O$_3$ as full conversion of CH$_4$ and NO was observed at 568 °C, demonstrating that pre-reduced Rh can promote higher conversions. Furthermore, while a negative hysteresis was still observed for Pd/Al$_2$O$_3$, a wide positive hysteresis was found for both Rh-based catalysts. In the case of Pd-Rh/Al$_2$O$_3$, the width of the hysteresis loop increased from 50°C to 90 °C compared to when an oxidative pre-treatment was applied (compared with Figure 6.5).
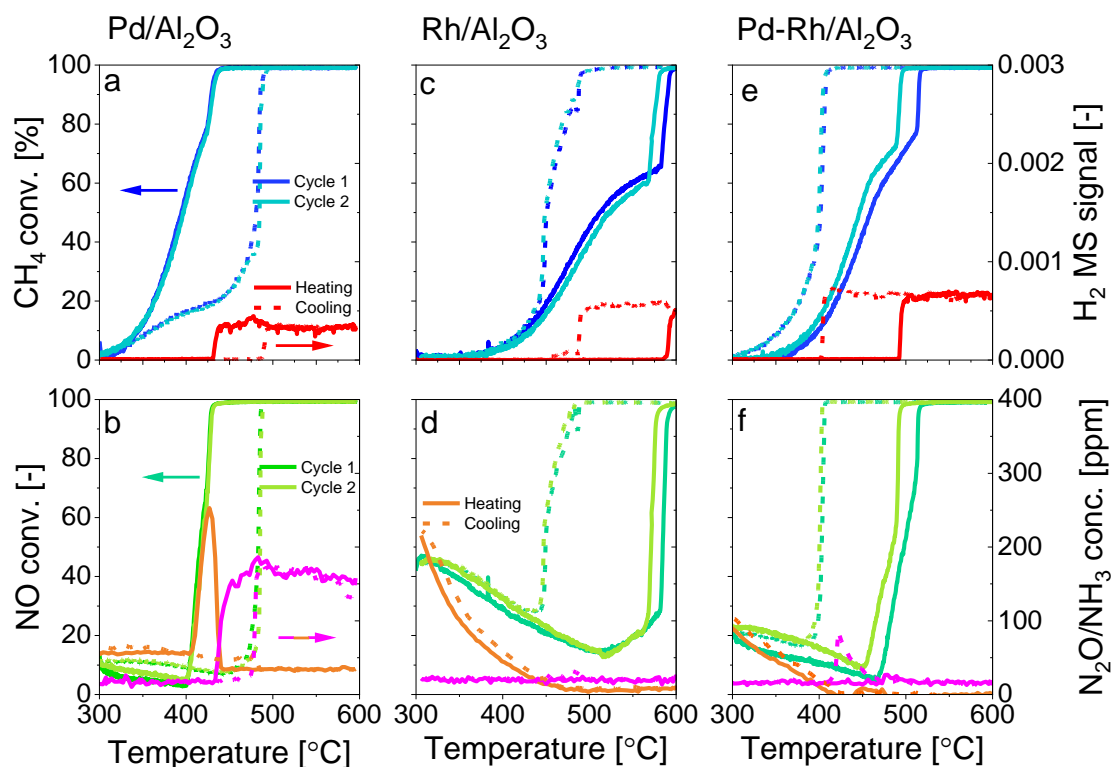
Figure 6.10. CH$_4$ (a, c, e) and NO (b, d, f) conversion as well as H$_2$ (red; a, c, e) MS signal and N$_2$O (orange; b, d, f) and NH$_3$ (pink; b, d, f) concentrations during heating (—) and cooling (---) during heating (—) and cooling (---) segments performed under static stoichiometric (5700 ppm O$_2$; λ = 1.0) conditions over (a-b) Pd/Al$_2$O$_3$, (c-d) Rh/Al$_2$O$_3$ and (e-f) Pd-Rh/Al$_2$O$_3$. CH$_4$ and NO conversions are shown for two consecutive cycles. The catalytic measurements were performed after a reductive pre-treatment. Conditions: 1500 ppm CH$_4$, 1600 ppm NO, 7000 ppm CO, 5700 ppm O$_2$, 5 vol% H$_2$O; WHSV = 240 Lh^{-1}g^{-1}.

Ex-situ XAS spectra of Pd-Rh/Al$_2$O$_3$ retrieved at 425 °C in the descending ramp, performed after either an oxidative or reductive pre-treatment (Pd-Rh/Al$_2$O$_3$ - act. aft. O$_2$ PT, and Pd-Rh/Al$_2$O$_3$ - act. aft. H$_2$ PT) are shown in Figure 6.11. At this temperature, both samples were taken in the hysteresis loop, when high conversions of CH$_4$ and NO were achieved. The results show that for both samples, the Pd species were fully reduced, while the Rh species were reduced to a higher extent after a reductive pre-treatment compared to an oxidative pre-treatment. Hence, the width of the positive hysteresis loop, during the temperature ramps, appears to be related to the extent of Rh reduction. Finally, only 100 ppm NH$_3$ were detected between 450 and 600 °C on Pd-Rh/Al$_2$O$_3$ (Figure 6.10), whereas 570 ppm NH$_3$ slipped when only Pd was present in the catalyst. Hence, the presence of Rh also significantly mitigates the NH$_3$ emissions, which is essential.
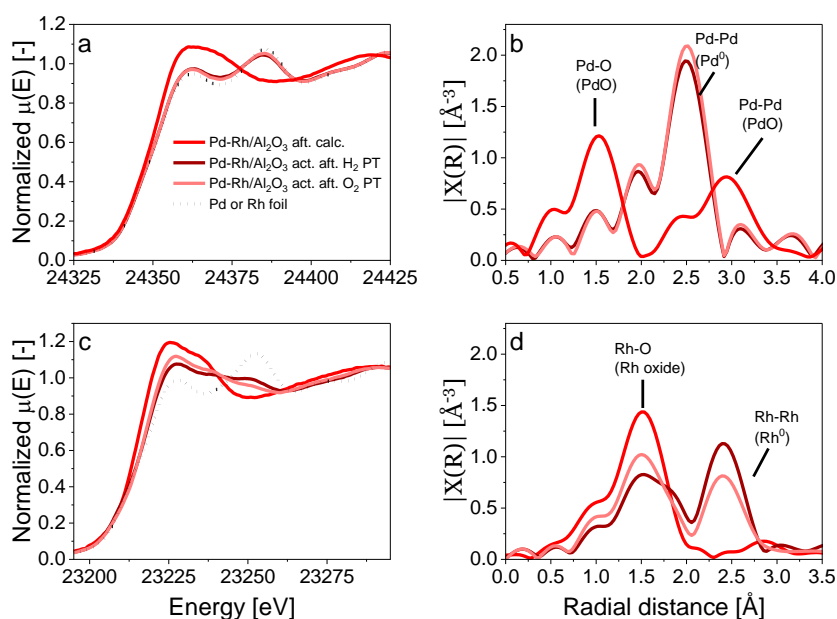

Figure 6.11. Ex-situ XAS acquired at the (a-b) Pd K-edge, and (c-d) Rh K-edge $_2$O$_3$, of Pd-Rh/Al$_2$O$_3$ after calcination, and retrieved in the descending ramp in the hysteresis loop after oxidative and reductive pre-treatment, as well as the Pd and Rh foils. (a, c) Spectra of the XANES region, and (b, d) FT-XAFS (not phase corrected).

6.3.3   O$_2$-dithering operation

Isothermal conditions

The activity of Pd-based catalysts improves significantly by continuously alternating between lean/rich O$_2$ pulses (O$_2$-dithering) compared to static operation (cf. Chapter 5) [57,59,151,153]. Under such conditions, the activity is directly affected by the redox properties and oxidation state of the catalyst [57,72,169]. This aspect is particularly interesting to study with catalysts possessing different redox dynamics such as the ones described in this Chapter.

The catalytic performance of the three catalysts was evaluated at 420 °C by applying symmetric O$_2$ pulses around stoichiometry ($\lambda = 1$) while using different dithering parameters (frequency and amplitude). The O$_2$ pulse sequences were performed successively and were started at the lowest amplitude. At each amplitude, different dithering frequencies were applied as shown in Figure D3. It should be recalled that the O$_2$ concentration experienced by the catalyst during the lean/rich pulses was always lower than 100 % of the O$_2$ pulsed in the lean phases and more than 0 % in the rich phases (cf. Chapter 5).

From the λ sweeps experiments performed at the same temperature as the O$_2$-dithering tests (section 6.3.2.1), high activity is expected to take place below $\lambda = 1$ (5700 ppm O$_2$) once all the O$_2$ present in the feed is consumed. The exact O$_2$ concentration leading to high conversions at 420 °C was calculated for each catalyst from the results of the λ sweeps measurements (Figure 6.7), using Equation 6.1, which defines the amount of O$_2$ consumed at $\lambda = 1$. Hence, at 420 °C, Pd/Al$_2$O$_3$, Rh/Al$_2$O$_3$, and Pd-Rh/Al$_2$O$_3$ were active toward CH$_4$-SR when the O$_2$ concentration was below 4540, 3705, and 4350 ppm O$_2$, respectively.

$$[O_2]_{high\,act.} = 5700 - 2([CH_4]_i - [CH_4]_{\lambda=1}) - 0.5([CO]_i - [CO]_{\lambda=1}) + 0.5([NO]_i - [NO]_{\lambda=1}) \qquad \text{Equation 6.1}$$

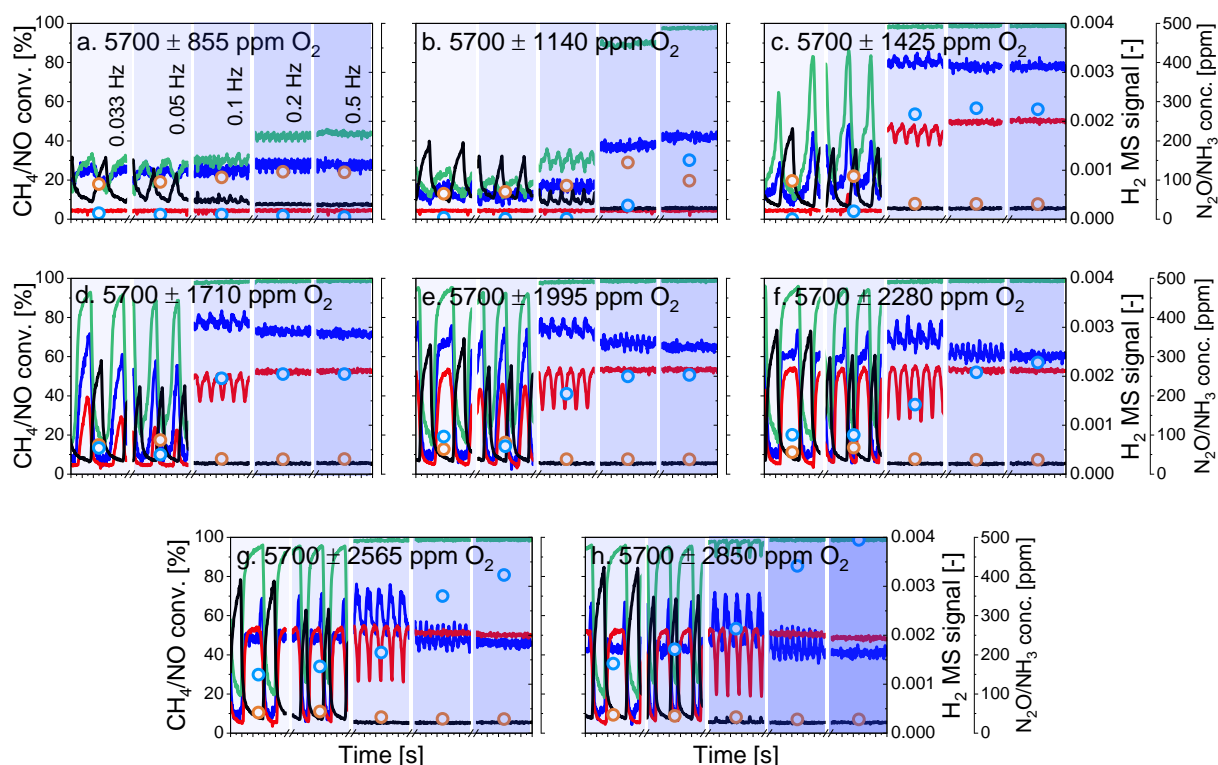Figure 6.12. CH$_4$ (blue) and NO (green) conversions as well as H$_2$ (red) and O$_2$ (black) MS signal and N$_2$O (orange; ○) and NH$_3$ (light blue; ○) concentrations under O$_2$-dithering conditions at 420 °C over Pd/Al$_2$O$_3$ at 0.025, 0.033, 0.05, 0.1, 0.2 and 0.5 Hz and amplitude of (a) 5700 ± 855 ppm O$_2$, (b) 5700 ± 1140 ppm O$_2$, (c) 5700 ± 1425 ppm O$_2$, (d) 5700 ± 1710 ppm O$_2$, (e) 5700 ± 1995 ppm O$_2$, (f) 5700 ± 2280 ppm O$_2$, (g) 5700 ± 2565 ppm O$_2$, and (h) 5700 ± 2850 ppm O$_2$. Conditions: 1500 ppm CH$_4$, 1600 ppm NO, 7000 ppm CO, 5 vol% H$_2$O; (a) $\lambda = 1 ± 0.004$, (b) $\lambda = 1 ± 0.006$, (c) $\lambda = 1 ± 0.007$, (d) $\lambda = 1 ± 0.009$ and (e) $\lambda = 1 ± 0.01$, (f) $\lambda = 1 ± 0.012$, (g) $\lambda = 1 ± 0.013$ and (h) $\lambda = 1 ± 0.015$; WHSV = 240 Lh^{-1}g^{-1}.

For Pd/Al$_2$O$_3$ (Figure 6.12), at an amplitude of 5700 ± 855 ppm O$_2$, CH$_4$, and NO conversions were not altered by the pulses because the O$_2$ concentration in the lean and the rich phases of the pulses were above 4540 ppm regardless of the frequency applied (Table D1). At an amplitude of 5700 ± 1140 ppm O$_2$, full NO conversion and an increase in CH$_4$ conversion by ca. 21 % were achieved at frequencies 0.2 and 0.5 Hz, even though the O$_2$ concentration was above 4540 ppm O$_2$. According to the results of Chapter 5, high NO conversion and a moderate increase in CH$_4$ conversion should be observed below 4640 ppm O$_2$, as this value lies 100 ppm O$_2$ above the O$_2$ value required for CH$_4$-SR to occur (4540 ppm O$_2$). At 5700 ± 1425 ppm O$_2$, the average

O_2 concentration during a full lean/rich cycle was always below 4540 ppm O_2 at frequencies 0.5, 0.2, and 0.1 Hz, justifying the high conversions maintained throughout the entire dithering cycle. However, at frequencies of 0.033 and 0.05 Hz, the O_2 concentration in the rich and lean phases of the pulses was too high to induce CH_4-SR. In the rich phases, the O_2 concentration was below 4640 ppm O_2 and therefore caused high NO conversion but no CH_4-SR (absence of H_2). At higher amplitudes, the average O_2 concentration was always below 4540 ppm O_2 at frequencies of 0.1, 0.2, and 0.5 Hz, which generated high conversions. At lower frequencies (0.033 and 0.05 Hz) high activity was achieved in the rich phases of the pulses but dropped in the lean phases.

The fast changes in the conversion values during the lean/rich O_2 pulses demonstrate that the activity of Pd/Al_2O_3 was very responsive to the O_2 concentration present in the feed, which also significantly affects the oxidation state of the Pd species. Indeed, if the O_2 concentration is too high, rapid formation of a dense chemisorbed O_2 layer around the Pd^0 core occurs which induces a collapse of the activity. However, since the reduction of oxidic Pd is fast, the high activity is restored as soon as the O_2 concentration is low enough [114,224,273]. The results show that O_2-dithering improved conversion only under very specific dithering conditions.

For Rh/Al_2O_3 (Figure 6.13), the O_2 concentration was above 3702 ppm at amplitudes below 5700 ± 1995 ppm O_2 (all frequencies; Table D1), thus the pulses had no significant effect on the activity. It is clear that in the absence of Pd, higher amplitudes (cf. richer conditions) were necessary to obtain good performance due to the lower reducibility of the oxidic Rh species formed after calcination in air. At amplitude 5700 ± 1995 ppm O_2, the average O_2 concentration was below 3702 ppm O_2 at 0.5 Hz, leading to full CH_4 and NO conversions over the entire dithering period (Table D1). At higher amplitudes, high conversions were always induced at frequencies of 0.2 and 0.5 Hz. At amplitudes equal to or higher than 5700 ± 2280 ppm O_2, high conversions were promoted during the entire dithering cycle at a frequency of 0.1 Hz. Since the pulses were performed consecutively (Figure D3), and unlike Pd^0, Rh^0 oxidation is only mildly affected by the O_2 concentration present in the feed, once reduced at 5700 ± 1995 ppm O_2 and 0.5 Hz, the catalyst remained in that state during the following pulsing conditions applied. Hence, high conversions were maintained, even if the O_2 concentration

was higher than 3702 ppm (i.e. 5700 ± 2280 ppm O_2, 0.1 Hz). Nonetheless, the activity still dropped in the lean phases especially when the O_2 concentration was high and the frequency was low (i.e. 3420 ± 4560 ppm O_2, at 0.033 Hz). However, because the presence of Rh tends to retain the catalyst in its reduced form, the decrease in conversion in the lean phases of the pulses is delayed, and therefore the pollutants slips are minimized compared to Pd/Al$_2$O$_3$.

Figure 6.13. CH$_4$ (blue) and NO (green) conversions as well as H$_2$ (red) and O$_2$ (black) MS signal and N$_2$O (orange; ○) and NH$_3$ (light blue; ○) concentrations under O$_2$-dithering conditions at 420 °C over Rh/Al$_2$O$_3$ at 0.025, 0.033, 0.05, 0.1, 0.2 and 0.5 Hz and amplitude of (a) 5700 ± 855 ppm O_2, (b) 5700 ± 1140 ppm O_2, (c) 5700 ± 1425 ppm O_2, (d) 5700 ± 1710 ppm O_2, (e) 5700 ± 1995 ppm O_2, (f) 5700 ± 2280 ppm O_2, (g) 5700 ± 2565 ppm O_2, and (h) 5700 ± 2850 ppm O_2. Conditions: 1500 ppm CH$_4$, 1600 ppm NO, 7000 ppm CO, 5 vol% H$_2$O; (a) $\lambda = 1 \pm 0.004$, (b) $\lambda = 1 \pm 0.006$, (c) $\lambda = 1 \pm 0.007$, (d) $\lambda = 1 \pm 0.009$ and (e) $\lambda = 1 \pm 0.01$, (f) $\lambda = 1 \pm 0.012$, (g) $\lambda = 1 \pm 0.013$ and (h) $\lambda = 1 \pm 0.015$; WHSV = 240 Lh^{-1}g^{-1}.

For Pd-Rh/Al$_2$O$_3$ (Figure 6.14), the O_2 concentration was always higher than 4350 ppm in the lean and rich phases of the pulses, at amplitudes of 5700 ± 855 and 5700 ± 1140 ppm O_2 (all frequencies; Table D1). At

5700 ± 1425 ppm O_2, the average O_2 concentration was below 4350 ppm at 0.5 and 0.2 Hz, leading to full CH_4 and NO conversions. At higher amplitudes, high activity was achieved at all frequencies even though the O_2 concentration was above the defined O_2 value needed to induce CH_4-SR. Hence, the presence of Rh allowed the catalyst to remain reduced up to a higher O_2 concentration than needed for the reduction of the catalyst, and therefore to maintain high activity over a broader range of dithering conditions than Pd/Al_2O_3. As for Rh/Al_2O_3, the conversion dropped in the lean phases of the pulses only under a few conditions (i.e. 5700 ± 2280 ppm O_2, 0.03 Hz), and the pollutants slips were relatively narrow.
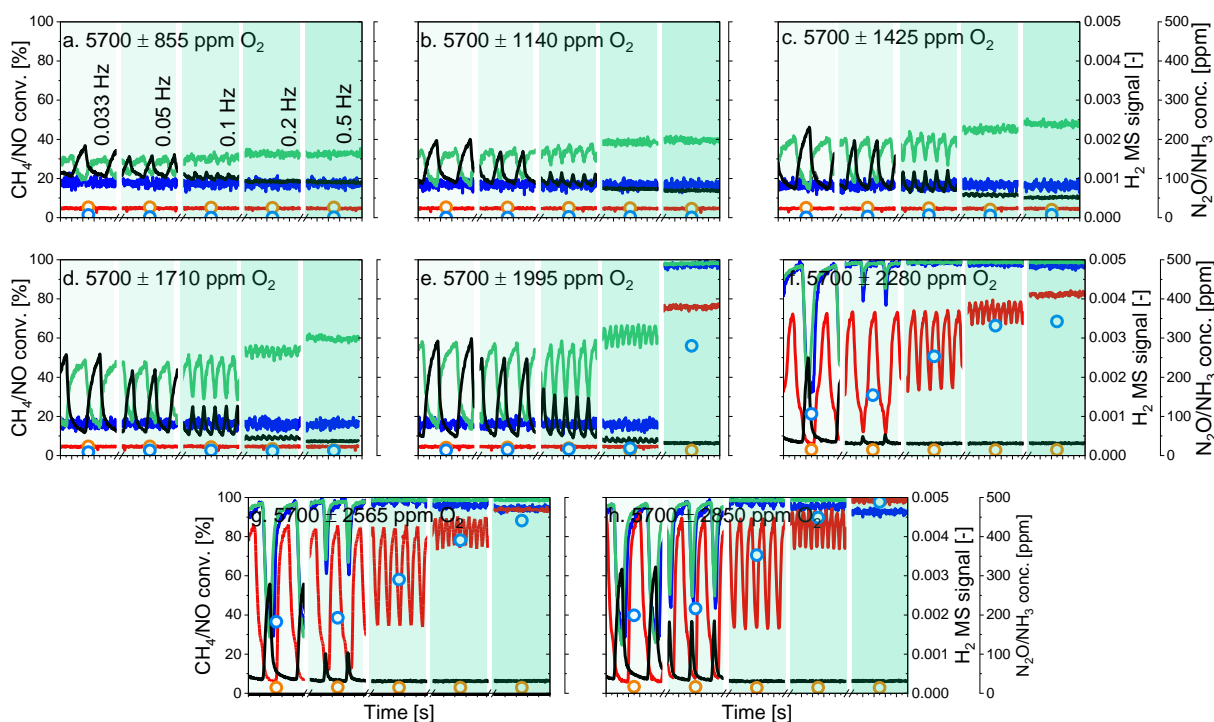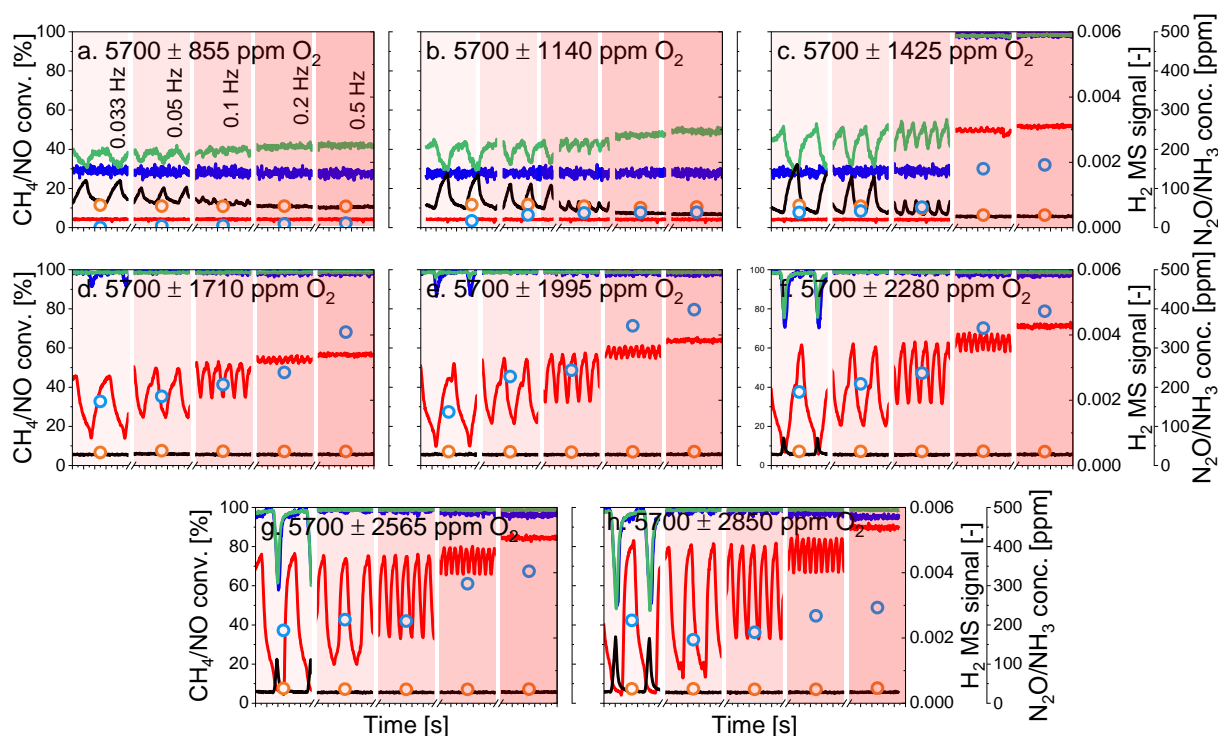

Figure 6.14. CH_4 (blue) and NO (green) conversions as well as H_2 (red) and O_2 (black) MS signal and N_2O (orange; ○) and NH_3 (light blue; ○) concentrations under O_2-dithering conditions at 420 °C over Pd-Rh/Al_2O_3 at 0.025, 0.033, 0.05, 0.1, 0.2 and 0.5 Hz and amplitude of (a) 5700 ± 855 ppm O_2, (b) 5700 ± 1140 ppm O_2, (c) 5700 ± 1425 ppm O_2, (d) 5700 ± 1710 ppm O_2, (e) 5700 ± 1995 ppm O_2, (f) 5700 ± 2280 ppm O_2, (g) 5700 ± 2565 ppm O_2, and (h) 5700 ± 2850 ppm O_2. Conditions: 1500 ppm CH_4, 1600 ppm NO, 7000 ppm CO, 5 vol% H_2O; (a) $\lambda = 1 \pm 0.004$, (b) $\lambda = 1 \pm 0.006$, (c) $\lambda = 1 \pm 0.007$, (d) $\lambda = 1 \pm 0.009$ and (e) $\lambda = 1 \pm 0.01$, (f) $\lambda = 1 \pm 0.012$, (g) $\lambda = 1 \pm 0.013$ and (h) $\lambda = 1 \pm 0.015$; WHSV = 240 $Lh^{-1}g^{-1}$.

In summary, O_2-dithering has a beneficial effect on the activity only once the available O_2 concentration is low enough to induce the reduction of the catalyst and thus high conversions. Since Pd is more efficient for CH_4 oxidation by O_2 than Rh, the O_2 amplitude needed to induce high pollutants conversions decreased with increasing Pd content. Indeed, the average O_2 concentration available in the lean/rich O_2 pulses, decreases with increasing amplitude (for a given frequency), while under oxidizing conditions, the O_2 consumption increases with the Pd content (due to better conversion of CH_4). Furthermore, because the Pd redox dynamics are dictated by the O_2 concentration present in the reactive environment, important oscillations in conversions, over Pd/Al_2O_3, can be observed between the lean and rich phases of the O_2 pulses, which follow the changes in the Pd oxidation state. In the presence of oxidic Pd, low activity is achieved, and when Pd is reduced, high activity is obtained. On the other hand, the redox dynamics of Rh are less affected by the O_2 concentration present in the feed, and once reduced, the Rh species tend to remain in that highly active state for SR reactions. Hence once Rh^0 is formed, high activity is achieved over a wide range of dithering conditions, and in turn, the Pd species are kept reduced by the H_2 formed from the promotion of CH_4-SR.

Temperature ramps

Temperature ramps were also performed under O_2-dithering conditions (Figure 6.15). The dithering conditions were chosen from the results obtained in the experiments described above, in order to maximize CH_4 and NO conversions while minimizing the amounts of NH_3 and N_2O produced. The dithering parameters were 5700 ± 1425 ppm O_2 at 0.2 Hz for Pd/Al_2O_3 (Figure D4), 5700 ± 2280 ppm O_2 at 0.05 Hz for Rh/Al_2O_3 (Figure D5), and 5700 ± 1425 ppm O_2 at 0.2 Hz for $Pd-Rh/Al_2O_3$ (Figure D6).

Figure 6.15 shows that high conversion was achieved at the same temperature, for all three samples (420 °C). This temperature corresponds to the temperature from which the optimal dithering parameters were selected. Interestingly, at 420 °C, complete CH_4 and NO conversions were achieved over the Rh-based catalysts, whereas, over Pd/Al_2O_3, the conversion reached ca. 80 %. This observation demonstrates that Rh^0 is more active toward SR reactions. Furthermore, a positive hysteresis was observed for all samples, demonstrating that the redox dynamics of Pd can be modified by working under lean/rich O_2 conditions. The most notable

improvements were observed for Rh/Al$_2$O$_3$. Its activity resembled that of the two Pd-based catalysts, and under these conditions, Rh reduction was induced without the need for a reductive pre-treatment (as indicated by the promotion of CH$_4$-SR). Finally, over Pd/Al$_2$O$_3$ the NH$_3$ formation was significant (1100 ppm at 600 °C), whereas, for the Rh-based samples, the amount of NH$_3$ detected was much smaller and decreased with temperature, being negligible above 600 °C (Figure 6.15e).
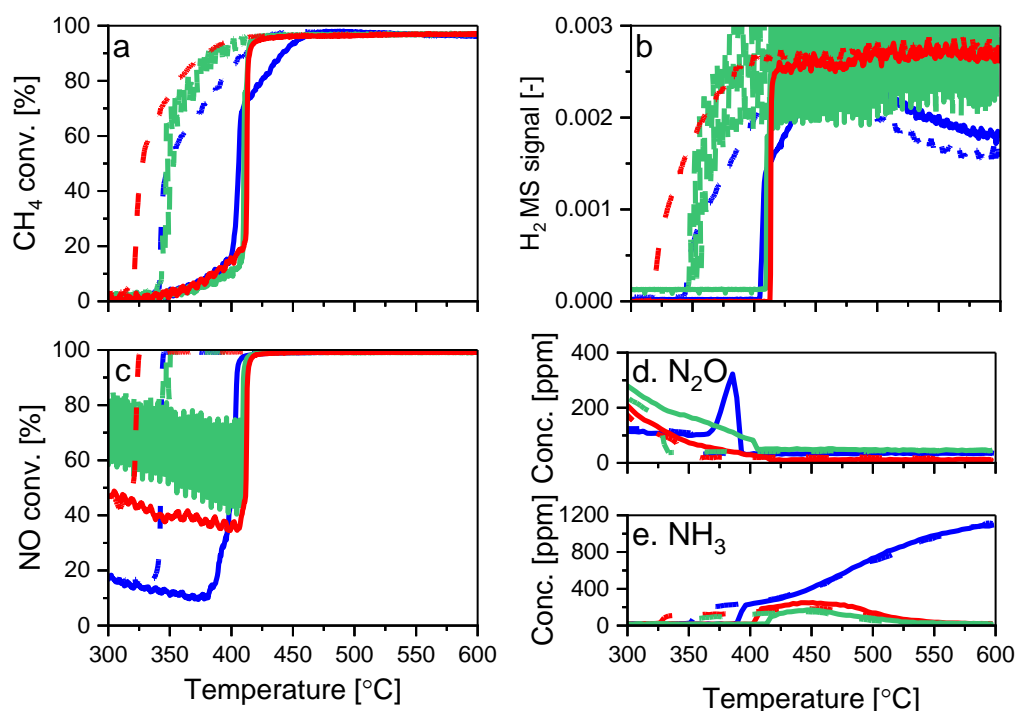
Figure 6.15. (a) CH$_4$, (c) NO conversions, and (b) H$_2$ MS signal as well as (d) N$_2$O and (e) NH$_3$ concentrations during heating (—) and cooling (- - -) ramps under O$_2$-dithering conditions over (blue) Pd/Al$_2$O$_3$, (green) Rh/Al$_2$O$_3$ and (red) Pd-Rh/Al$_2$O$_3$. The catalytic measurements were performed after an oxidative pre-treatment. The dithering conditions were 5700 ± 1425 ppm O$_2$, and 0.2 Hz for Pd/Al$_2$O$_3$, 5700 ± 2280 ppm O$_2$, 0.05 Hz for Rh/Al$_2$O$_3$, and 5700 ± 1425 ppm O$_2$, 0.2 Hz for Pd-Rh/Al$_2$O$_3$. Conditions: 1500 ppm CH$_4$, 1600 ppm NO, 7000 ppm CO, 5700 ppm O$_2$ (average), 5 vol% H$_2$O; WHSV = 240 Lh^{-1}g^{-1}.

Hence, under O$_2$-dithering conditions, the activity of all catalysts was significantly improved compared to static operation, and interestingly, all catalysts performed similarly. However, even if a high activity was obtained over Pd/Al$_2$O$_3$ it came with the drawback of high NH$_3$ production that was strongly suppressed in Rh-

containing catalysts. Therefore, Rh appears to be essential not only to improve the reducibility of Pd, which allows working under a wider range of dithering conditions but also to mitigate the NH_3 emissions during periodic operation.

6.4 Conclusion

In this Chapter, we shed light on the effect of Rh on the redox properties of Pd by studying three catalysts: Pd/Al_2O_3, Rh/Al_2O_3, and $Pd\text{-}Rh/Al_2O_3$. Two main conversion regimes occur when working under simulated stoichiometric NG engine exhaust conditions: CH_4 oxidation by O_2 leading to limited NO conversions due to the presence of unreacted O_2 in the reactive environment (low conversion regime) and CH_4 oxidation by H_2O (CH_4-SR) which takes place once all the O_2 has reacted, and induces full NO reduction and H_2 formation (high conversion regime). In the low conversion regime, Pd and Rh are predominantly in the oxidized form, whereas they are in the reduced state in the high conversion regime. However, all the O_2 present in the reactive environment needs to be fully consumed by the oxidation reactions (of CO and CH_4) for the high conversion regime to proceed.

While Pd oxide is efficient for CH_4 oxidation by O_2, Rh oxide is only moderately active. Hence, under oxidizing conditions, the activity is proportional to the Pd content. The transition between the low and high conversion regime requires the catalyst to reduce. While Pd reduction is easy to achieve under stoichiometric conditions, Rh reduction requires either richer conditions or a harsh reducing pre-treatment. Nonetheless, once reduced, the Rh species are very active toward SR, and while being only mildly affected by the O_2 concentration present in the feed, unlike Pd/Al_2O_3 which re-oxidizes more easily. Hence, when the high conversion regime is promoted over Rh-based catalysts, the activity remains high until lower temperatures (in temperature ramp experiments) and higher O_2 concentrations (λ sweep experiments) than Pd/Al_2O_3.

Therefore, since Pd redox dynamics are strongly affected by the variation of O_2 concentration in the feed important oscillations of the activity between the low and high conversion regimes are observed in the lean/rich O_2 pulses on Pd/Al_2O_3, which narrows the number of optimal operating conditions (cf. pulsing conditions). On

the other hand, once reduced, the Rh-based samples can maintain high activity over a broad range of dithering conditions. Since the presence of metallic Rh maintains CH_4-SR, the hydrogen produced from this reaction can maintain the Pd species reduced.

This work reveals that Pd is crucial to achieving acceptable conversion values under oxidizing conditions, while Rh maintains the catalyst reduced and the activity high, under rich conditions. Hence, the addition of Rh to a Pd/Al_2O_3 catalyst modifies the redox behaviour of Pd during periodic operation and therefore widens the range of dithering parameters that can be exploited to enhance pollutants removal from the exhaust of stoichiometric NG engines. .

Chapter 7 Phase-sensitive detection applied to near ambient pressure X-ray photoelectron spectroscopy of powder catalysts: methodology and proof of concept

7.1 Introduction

X-ray photoemission spectroscopy (XPS) is a core-level, surface-sensitive spectroscopic technique [274,275]. Due to the localization of the core level, this technique is element-specific and therefore well suited for studying chemical composition, and local bonding. The method can be applied to follow structures and site-specific dynamics in solid, liquid, and gas phases as well as the interfaces formed between them [276–278]. Until recently, the main drawback of X-ray photoemission spectroscopy was the necessity to work in high vacuum due to the low kinetic energy of the photoelectrons emitted from the first layers of the condensed material which can easily be inelastically scattered in the gas phase. Significant scientific and technological improvements have been made in the past decades to bridge the gap between atmospheric pressure and ultra-high vacuum conditions, which is an essential step toward the study of realistic catalysts (i.e. materials such as supported nanoparticles, low metal loadings) [279–283]. Efforts are still needed to further improve near ambient pressure X-ray photoelectron spectroscopy (NAP-XPS), among which are: increasing the signal-to-noise (S/N) ratio of a photoemission spectrum collected on real catalysts and improving the time resolution of photoemission measurements [278]. In the former case, the S/N ratio of the collected spectra can be improved by increasing the metal loadings used or by averaging the signal over long acquisition times [278]. However, high metal loadings may not represent realistic conditions and by averaging the spectra, the time resolution of the measurement is considerably decreased. Yet, improving the time resolution becomes especially important when the purpose is to detect active sites whose concentrations are small and lifetime limited. Indeed, the elemental steps of a catalytic process occur within the picosecond range while milliseconds to seconds are

needed to follow structural surface changes of the catalyst (i.e. phase transitions, surface roughening, segregation) [284].

The data quality of any spectroscopic measurement can be improved by employing the modulation excitation spectroscopy (MES) method (c.f. section 1.3.2.2). By averaging the data into one period, the size of the dataset decreases, the S/N ratio is improved by the square root of the number of averaged cycles ($\sqrt{N}$, Poisson statistics) [202], and the time resolution is only restricted by the acquisition time of one spectrum. For accurate data alignment and averaging, this method requires performing fast and reproducible perturbations without delay between the perturbation event and the time at which the sample experiences it. Knudsen et al. [195] carried out repeated gas switches over a Pd(100) crystal while measuring in situ NAP-XPS and were able to achieve a time resolution of 60 ms. However, due to the delay between the gas switch and the substitution of the gas composition in the experimental cell as well as pulse irregularities, they were not able to align the cycles based on the time of the perturbation. Hence, they identified a lock-in signal within the data that would indicate a structural change caused by the gas switches and used it to average the data. Such an approach requires a sufficient initial S/N ratio to find a lock-in signal with the image recognition algorithm, as well as a fully reversible process, which are both difficult to achieve with real materials. Then, phase-sensitive detection (PSD) or demodulation (Equation 1.13) [203], in order to enhance the signal from the active species affected by the perturbation, and supress the signal from the spectator species and the noise (unaffected by the perturbation).

In this Chapter, in situ near ambient pressure X-ray photoemission measurements were performed on a 5 wt% Pd/Al$_2$O$_3$ catalyst. The photoemission signal of Pd 3d was followed while switching between oxidative (O$_2$) and reducing (CO) environments every 5 min over a period of 6 h. By averaging all the cycles into one period, the S/N ratio of a spectrum was significantly improved (c.f. modulation excitation method). The cycle averaging was done based on the gas switching event since the exchange of the gas composition in the experimental cell was fast compared to the acquisition time of a spectrum. Then, phase-sensitive detection was performed to discriminate the active species affected by the change in gas composition from the noise and spectator species. The improved signal and time resolution allowed identifying seven Pd species and their

dynamics. The species consist of three reduced Pd species (bulk and surface Pd^0, and adsorbed CO on surface Pd^0), and four oxidized species (bulk and surface PdO (2 and 4-fold surface), as well as Pd^{n+} (n > 2). The highly oxidized and 2-fold surface oxide Pd species were the most active toward CO oxidation. We also demonstrated that PdO reduction and Pd^0 oxidation followed a diffusion-controlled reduction model and a shrinking core oxidation model, respectively.

It should be mentioned that in this Chapter the reactive conditions were simplified compared to the composition of the exhaust feed from stoichiometric NG engines since the system would have been too complex, making the interpretation of the results unreliable. Indeed, the more gas components are fed to the system, the more surface species are generated, which are then difficult to assign in a trustworthy manner.

7.2 Materials and methods

7.2.1 Material

The 5 wt% Pd/γ-Al$_2$O$_3$ catalyst was purchased in powder and reduced form from Johnson Matthey. The presence of Pd^0 species was observed at a 2 theta angle of 40.1 ° in the X-ray diffraction pattern (Figure 7.1a). The catalyst displayed a narrow particle size distribution (4.4 ± 1.1 nm; Figure 7.1b-c).

7.2.2 X-ray photoelectron spectroscopy study

The experiments were carried out at the In Situ Spectroscopy beamline (X07DB) at the Swiss Light Source synchrotron. The solid-gas interface endstation was connected to a differentially pumped Scienta R4000 HiPP-2 electron analyser to allow the manipulation of solid samples while dosing a gas mixture in the mbar range [285]. The small volume of the XPS cell (ca. 150 mL) allows performing transient experiments with fast gas switches, while the evolution of a spectral line can be followed either in a swept or fixed (snapshot) mode (time resolution down to the second range) [57,278]. In this work, the signals of Pd 3d and Al 2p were acquired

with an excitation energy of 660 eV, to generate Pd 3d photoelectrons having a kinetic energy of 300 eV. A 20 eV kinetic energy window including the Pd 3d signal was acquired in fast scan (swept) mode in approximately 6 s. Linearly polarized light was used throughout the experiments. The spectra were processed and fitted using the IgorPro and XPSPeak41 software. The catalyst pellet was prepared by pressing 5 mg of powder on a tantalum mesh to decrease the surface charging, then fixed to the sample holder using metal clips. The temperature was monitored with a Pt 100 sensor, and the sample was heated using a tunable power IR laser (976 nm, maximum power 25 W) projected on the backside of the sample holder. In the geometry adopted during the experiments, photoelectrons were detected at an angle of 30° with respect to the direction of the surface normal.

The gas mixing setup was composed of two mass flow controllers, each connected to a solenoid valve (Series 9, Parker) enabling fast changes in gas phase composition. The valves were situated directly at the end of the gas line, right before the experimental cell. The experiment was performed at 300 °C. Periodic switches between pure O_2 and pure CO occurred at 300 °C every 5 min over a period of 6 h while acquiring the Pd 3d core level, and for 1 h while acquiring the Al 2p core level. The pelletized catalyst was heated in oxygen (1 mbar) to 300 °C before starting the experiment, to remove surface carbon contaminations and avoid any structural changes during measurement. In total 36 full cycles were performed. The gas composition in the cell was followed using a quadrupole mass spectrometer located in the second differential pumping stage of the analyser.
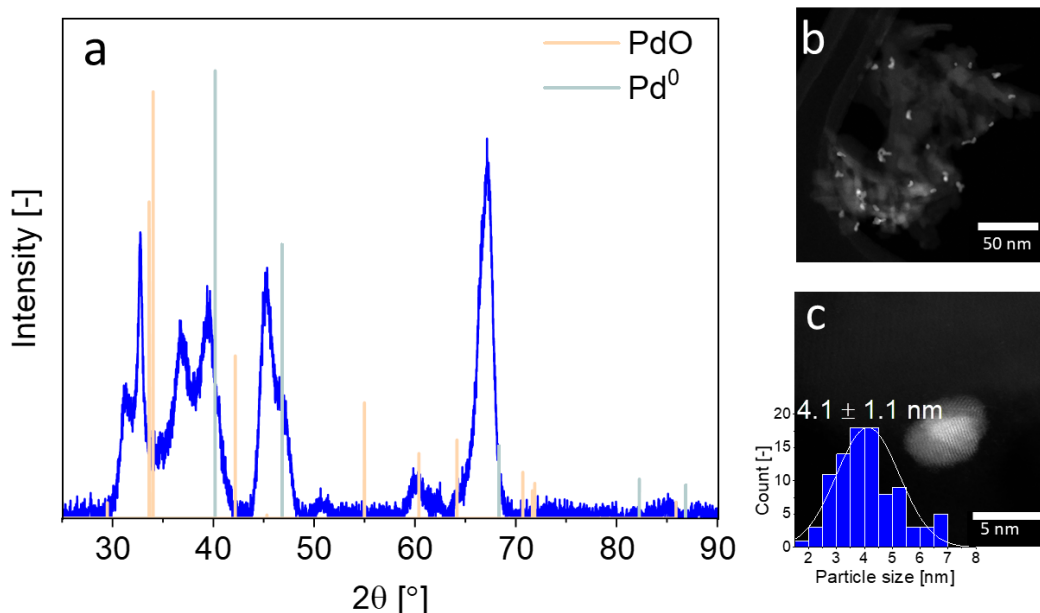
7.3 Results and discussion

Figure 7.1. (a) Powder X-ray diffraction and (b-c) dark-field HAADF-STEM image and particle size distribution of pre-reduced 5 wt% Pd/Al$_2$O$_3$ catalyst.

The electron count of an X-ray photoemission spectrum of a real catalyst (supported nanoparticles) is considerably lower when measurements are carried out at near ambient pressure compared to high vacuum due to the presence of gases in the experimental chamber. As a consequence, the quality (signal-to-noise (S/N) ratio) of a single Pd 3d core level spectrum of the 5 wt% Pd/Al$_2$O$_3$ catalyst is low as shown in Figure 7.2a. To distinguish the main features of the Pd 3d core level, thus getting meaningful fittings of the raw data, 5 to 10 spectra have to be averaged, while 15 averaged spectra are required to achieve an acceptable S/N ratio (Figure 7.2). Because the acquisition time of a single spectrum with an energy window of 20 eV was ca. 6.20 s, it took ca. 93 s to measure 15 spectra, which exceeds the time required to follow surface processes occurring in the second/sub-second range. The acquisition time can be decreased either by narrowing the energy window and focusing for example, on the Pd 3d$_{5/2}$ core level only or by using materials with higher Pd loading. Nonetheless, narrow energy windows would not allow for cross-checking the fitting with the spin-orbit-satellite signal.

Moreover, increasing the Pd loading implies working with rather unrealistic materials for industrial applications.
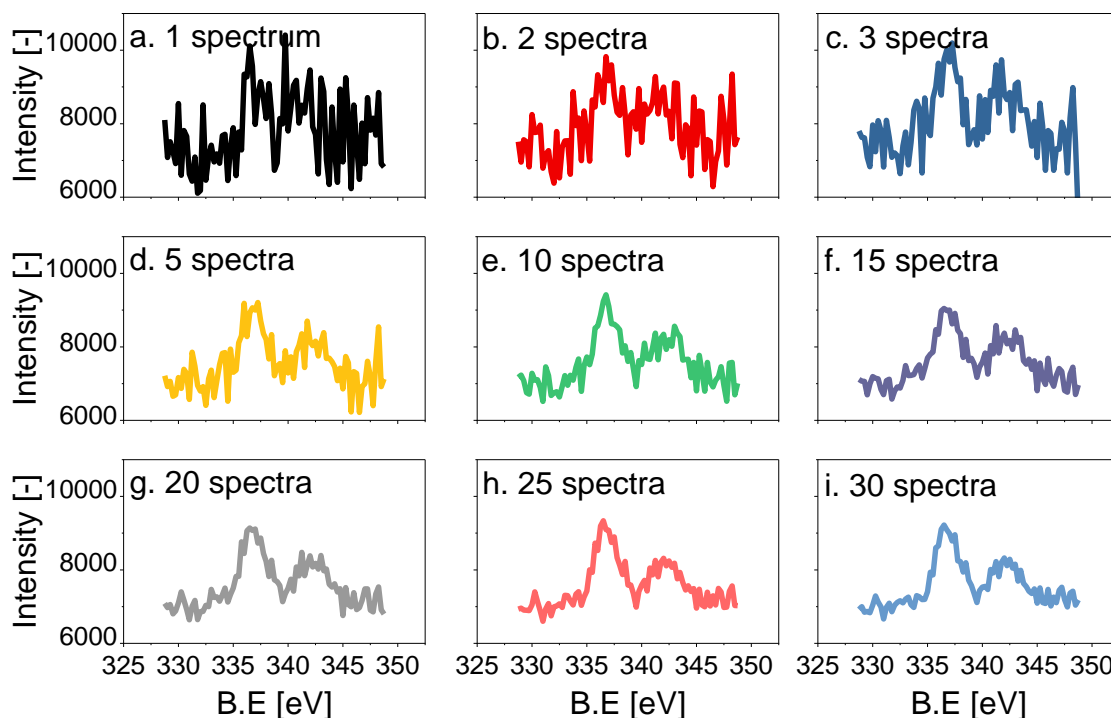

Figure 7.2. X-ray photoelectron acquisition at the Pd 3d core level with a 300 eV kinetic energy over 5 wt% Pd/Al_2O_3, of (a) one spectrum, (b) 2 averaged spectra, (c) 3 averaged spectra, (d) 5 averaged spectra, (e) 10 averaged spectra, (f) 15 averaged spectra, (g) 20 averaged spectra, (h) 25 averaged spectra, and (i) 30 averaged spectra.

7.3.1   Modulation excitation spectroscopy

In order to simultaneously improve the S/N ratio and the time resolution of the NAP-XPS experiment, the modulation excitation spectroscopy method was applied [202]. In this work, the perturbation consisting in changing the gas composition between pure O_2 and pure CO every 5 min over a period of 6 h while measuring at the Pd core level, induced a temporary pressure increase in the experimental cell from 1 up to 1.8 mbar (Figure 7.3). This pressure change translated into a shift of the peak position of ca. 4 eV, as shown at the Al 2p core level (Figure E1). The position of the Al 2p peak only stabilized once the pressure in the cell went

back to ca. 1 mbar. The change in pressure also led to a change in the gas concentration and resulted in a spike in O_2 and CO signals (Figure 7.3, Figure E2a). When the same pulses were performed in a quartz plug-flow reactor, using the catalyst in its powder form, the shape of the pulses did not display any spikes upon the gas switches (Figure E2b). Thus the change in pressure in the experimental cell is due to the XPS chamber geometry and/or to the intrinsic properties of the gases rather than the operation mode of the sinusoidal valves. If the change in pressure was only caused by the chamber geometry, the shape and intensity of the increase in pressure upon the gas switch would be the same for both CO and O_2. However, the shift was stronger and longer when switching from O_2 to CO since CO sticks more to the vacuum system composed of metallic parts and to the root pump situated downstream, whose efficiency varies with the gas composition. Furthermore, the electronic properties of O_2 and CO affect differently the charging of the sample, since gases in the mbar range help to compensate for surface charging by transferring electrons to holes in the solid [286]. Indeed, once the pressure in the cell was stabilized around ca. 1 mbar, there was a 0.25 eV shift in the energy between the cycles measured in O_2 and CO (Figure E1).
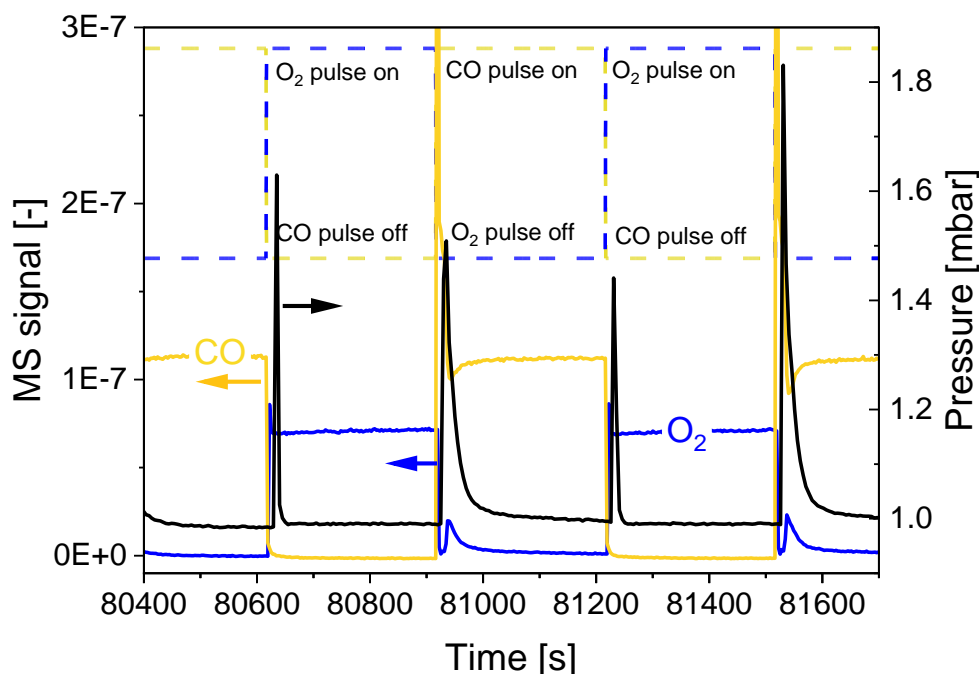

Figure 7.3. CO and O_2 MS signal (—), pressure in the experimental cell (—) as well as pulsing time (---) as a function of time.

In order to correct the shift caused by both, the change of pressure and the charging of the sample, it appears crucial to use a reference signal, whose electronic state is not affected by the reactive environment. Ideally, the reference element is present in the material investigated to avoid any possible errors arising from the change of sample, mounting, etc. In this study, we used the Al 2p core level as an internal reference, since Al is readily available in the catalyst support (Figure 7.4). The first step of the data treatment consisted of aligning each Al 2p spectrum obtained during the experiment (Figure 7.4d-e). This defined the alignment that needed to be applied to Pd at each point in time of the pulsing period. For the connection from the Al data to the Pd data, the acquisition time (time resolution) of the Al and Pd spectrum needs to be the same and the start of the pulses needs to be correctly coordinated with the spectra.
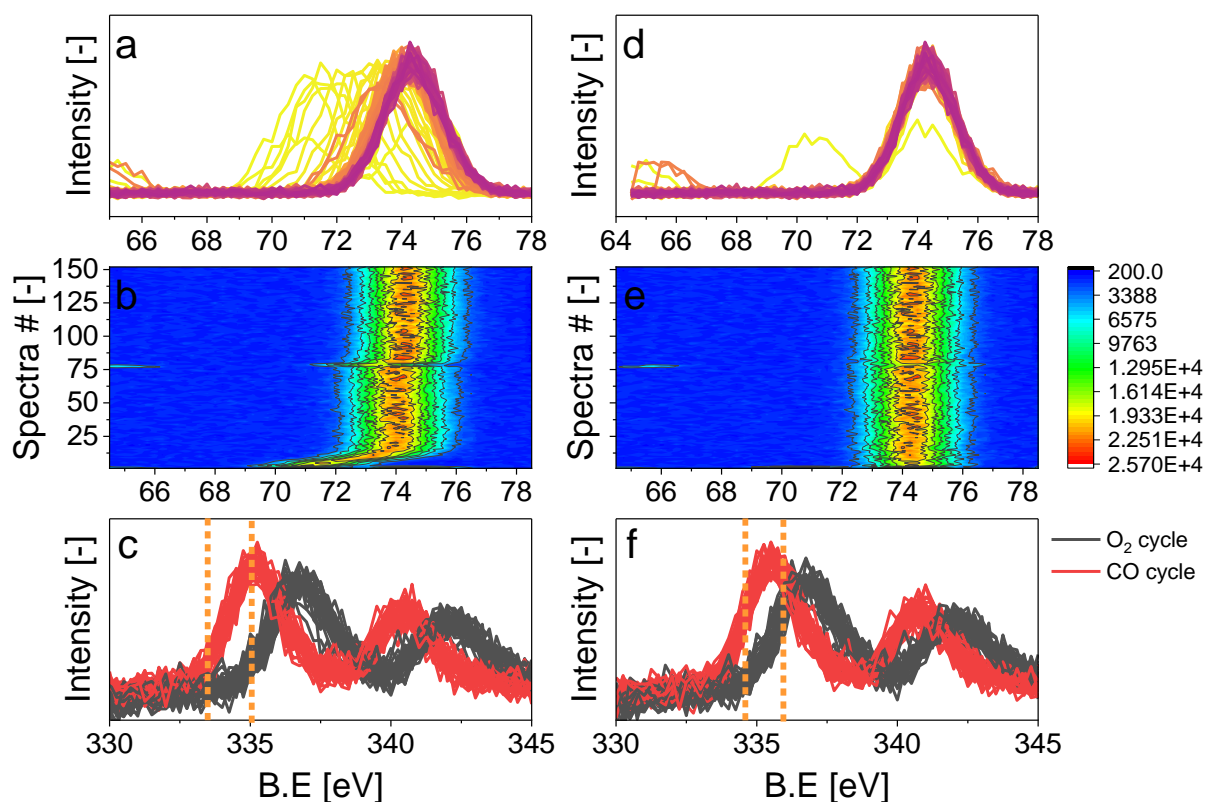

Figure 7.4. X-ray photoelectron spectra of 5 wt% Pd/Al$_2$O$_3$ at (a-b, d-e) the Al 2p core level with a 660 eV kinetic energy and (c, f) the Pd 3d core level with a 300 eV kinetic energy. (a-c) non-aligned spectra, (d-f) aligned spectra. (b, e) Heat map of all spectra acquired during the 6 h measurement.

The second step of the data treatment consisted of applying the shifts evaluated for each Al spectrum to the Pd spectrum making sure that the time and the half-period considered are the same. When comparing the data measured at the Pd 3d core level, before and after alignment (Figure 7.4), while it is difficult to observe the effect of alignment in the heat maps (Figure E3), the difference is mainly observed in the averaged spectra over a half cycle during O_2 or CO pulse (Figure 7.4c, f). Indeed, when not aligned, the difference in binding energy between the two half-cycles is larger (i.e. $\Delta B.E = 1.75$ before alignment and 1.5 after alignment), and the results would be erroneous.

Furthermore, the cycle averaging has to be performed based on a defined event that corresponds either to the gas switching event, or structural modifications of the catalyst surface. We used the gas switching event since our gas switches were well defined, and the delay between the switching time of the valves and the change in gas composition in the experimental cell was short (observed from the MS; Figure 7.3). The delay between the switching time and the time for the gas composition to be exchanged by more than 95 % was ca. 4 s (50 % of gas exchange in ca. 1s) which is a single spectrum acquisition time (6.20 s). The gas switches were fast due to the cell volume (ca. 150 mL), the flow configuration of the cell (described in section 7.2.2), and the short distance between the valves and the cell. The change in gas composition can be further improved by increasing the gas flow used, as the gas exchange speed is dependent on the flow. The pressure measured by the baratron, however, was delayed by ca. 12 s compared to the gas switching event due to the configuration of the analysis cell. The baratron is located on top of the cell whereas, the MS is situated in the second differential pumping stage of the electron analyser [278,285]. Hence, when a gas switch was performed, it took a few seconds for the gases to diffuse to the top of the cell and reach the baratron. Since the inlet gas feed and MS are close to the sample, we assume that the gas composition above the sample is exchanged almost immediately in correspondence with a gas switch. Therefore, with our setup configuration, it is only necessary to synchronize the acquisition of the first spectrum used for the data processing with the time at which the first pulse occurs.
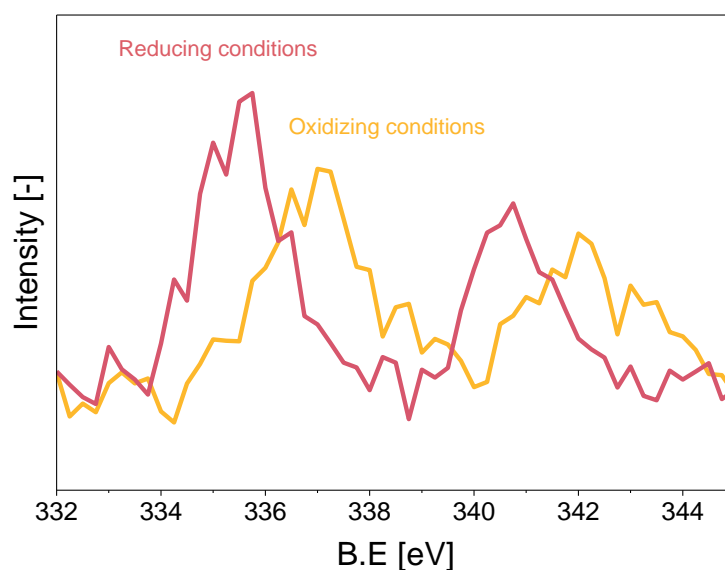
Figure 7.5. Average X-ray photoelectron spectra of 5 wt% Pd/Al$_2$O$_3$ acquired at the Pd 3d core level with a 300 eV kinetic energy, in the reducing and oxidizing pulses at 150 s of the pulses.

Finally, the response of the active species to a periodic stimulation needed several cycles to reach an equilibration around which it oscillated reversibly at the same frequency as that of the stimulation (Figure E4). Thus, it is clear that the first 10 cycles were discarded when applying phase domain detection calculations. Figure 7.5 shows the Pd 3d core level spectra obtained summing 26 iterations, corresponding to the middle of the CO and O$_2$ half-cycles (A(t = 150 s)). Under reducing conditions, the Pd 3d core level signal shifted to lower energies (Figure 7.5) and showed a narrower line shape compared to the spectrum obtained in oxidizing conditions (Figure 7.5), demonstrating that the oxidation state of palladium changed upon the periodic modification of the reaction environment.

7.3.2   Phase-sensitive detection

Figure 7.6 depicts the spectra obtained after phase-sensitive detection was applied to the averaged aligned data collected during the modulation experiment. The resulting features appear to be relatively sudden from one phase angle to another. The spectral resolution (ca. 0.6 eV) is most likely responsible for the sharp oscillating-like features. In addition, one could speculate that the abrupt features are the result of the remaining

noise that was not fully removed after 6 h of modulation. To check if the phase domain spectra obtained still contained high levels of noise, the aligned data were smoothed before performing PSD (binomial smoothing of degrees 1, 2, and 3; Figure E5). The resulting PSD spectra displayed similar intensities and dynamics as the PSD performed on the aligned data, suggesting that the possible remaining noise and the low spectral resolution do not affect the dynamics observed in the phase domain data. However, smoothing the data is not recommended, since it can blur the features of the demodulated data and in turn affect the fitting, especially if the smoothing applied is too relevant (i.e. binomial smoothing 3 in Figure E5).
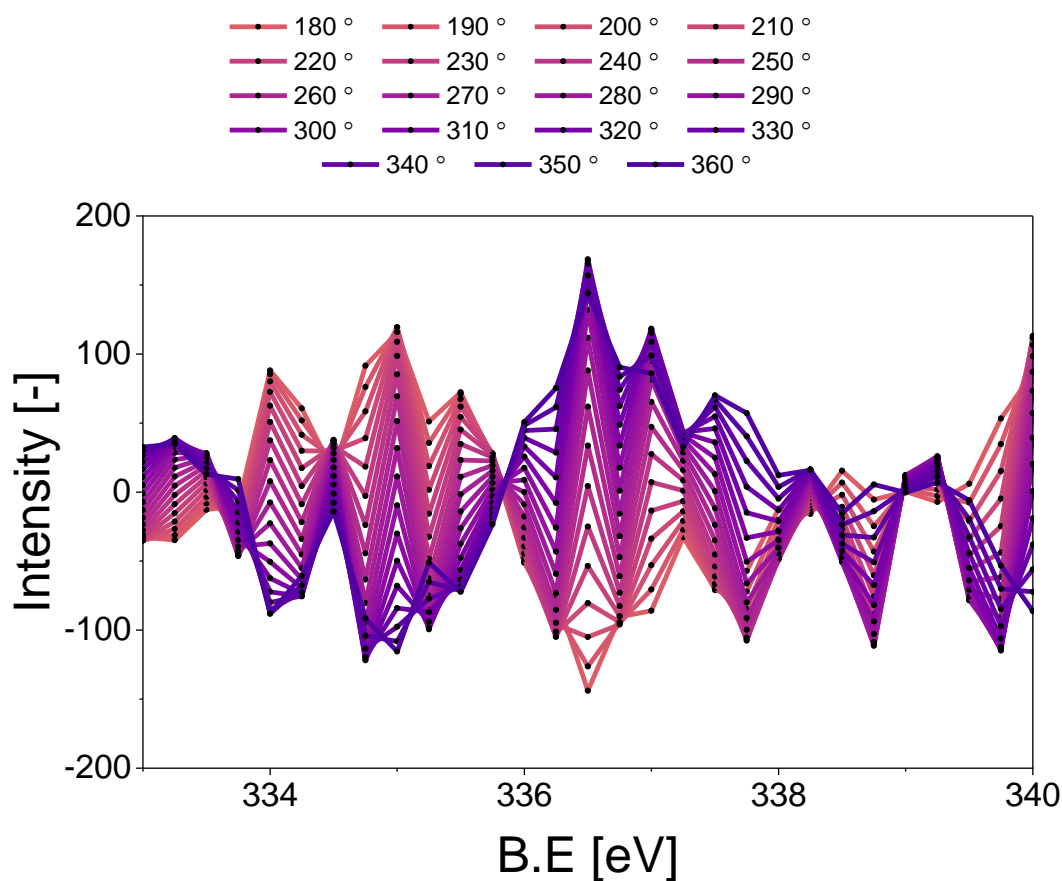

Figure 7.6. Phase domain performed on aligned X-ray photoelectron spectra of 5 wt% Pd/Al$_2$O$_3$ at the Pd 3d core level with a 300 eV kinetic energy obtained when switching between CO and O$_2$ every 5 min.

Fitting of the time and phase domain data

When fitting the time domain spectra it is difficult to evaluate how many Pd species contribute to the signal and it is not trivial to follow their dynamic evolution. By pairing the results of the time and phase domain, it is possible to accurately determine the number of Pd species affected by the perturbation as well as their dynamic evolution. Indeed, our results clearly show that some features were more pronounced in the phase domain while others were more visible in the time domain. The methodology applied in this study consisted of meticulously evaluating and comparing the fits done in the phase and time domain in order to manually cross-adjust each fit in an iterative manner, as shown in Figure 7.7. The spectral range was focused on the main peak, i.e. the Pd $3d_{5/2}$. In this approach, the fitting was performed on the phase domain spectra of the aligned and smoothed (binomial 1) data at selected phase angles (0, 20, and 40 °), using two peaks (Figure 7.7a). The phase angles between 180 and 360 ° are a mirror of the results achieved between 0 and 180 °. The angles between 50 to 130 ° are difficult to fit since the features are not very distinguishable (see Figure E6). Hence, only the angles 0, 20, and 40 ° were considered. Then, the peak features obtained from the phase domain fit (peak position, full width at half maximum) were transferred to fit the time domain spectra. Fitting the time domain with the parameters from the phase domain helps to visualize where a peak might be missing in the initial phase spectra fit. This information was used to iterate the fit in the phase domain spectra including the extra features missing from the time domain. The iterative fit between the phase and time domain started with two peaks (Figure 7.7), and in the end, seven peaks were identified (Figure 7.8, Table 7.1). It should be mentioned that to cross-check the fits, the opposite strategy was also carried out (fitting the time domain and transferring it to the phase domain).

First, the bulk Pd^0 and the surface Pd^0 component were detected at 334.9 eV, and 334.1 eV, respectively [287–289]. The third Pd species centered at 335.6 eV is attributed to CO adsorbed on Pd^0. The CO molecules can adsorb at the hollow, bridge, and on-top sites of the surface Pd^0 but their very close binding energy values (within a 0.7 eV range) do not allow to separate them [287,288,290]. However, under our experimental conditions (1 mbar, 300 °C), we expect CO to adsorb almost quantitatively on bridge sites [289]. The shift of + 0.7 eV compared to Pd^0 is in good agreement with such an adsorption configuration [290].

Table 7.1. Peak features and peak assignment.

	Binding energy [eV]	Full width at half maximum [eV]	Peak assignment
Peak 1	334.1	0.4	Surface Pd^0 [287–289]
Peak 2	334.9	0.9	Bulk Pd^0 [287–289]
Peak 3	335.6	0.9	Adsorbed CO [287–289]
Peak 4	336.55	1	Surface PdO (2-fold) [288,290–297]
Peak 5	337.0	0.9	Surface PdO (4-fold) [288,290–297]
Peak 6	337.6	1	Bulk PdO [287,288]
Peak 7	338.6	0.8	Pd^{n+} (n > 2+) [298–310]

Regarding the cationic Pd species, bulk PdO is found at 337.60 eV [287,290]. In this work, we identified two different Pd oxide species at 336.55 and 337.0 eV, corresponding to a 2-fold Pd and 4-fold surface oxide Pd arising from the two-dimensional Pd_5O_4 surface oxide phase [288,290,291]. In the literature, such species were mainly detected on Pd(111) single crystals [292–294] but were also found on a Pd/Al_2O_3 powder catalyst [295]. These Pd species are defined as sub-stoichiometric $PdO_{x<1}$ which is regarded as an intermediate state between chemisorbed oxygen on Pd metal and PdO bulk [292–295]. The 2-fold Pd surface oxide species are assigned to chemisorbed O species of Pd_5O_4, while the 4-fold Pd surface oxide species are considered to be the subsurface oxide of Pd_5O_4 is regarded as a precursor to the PdO bulk [296,297]. Finally, the assignment of the last component located at high binding energy (338.6 eV) is more complex. Even though palladium species displaying high binding energies have already been observed, their assignment is still unclear [298,299,301,303]. It can be related to cationic Pd species that are: 1) in an oxidation state higher than 2+ [302,304,305], and/or 2) in strong interaction with the alumina support [306–310], and/or 3) diffusing into the metal oxide lattice depending on the support [298,300,301].

Finally, the fit of the averaged photoemission spectrum obtained at 150 s in the O_2 cycle, shows that the main peaks are those assigned to cationic Pd species, while the intensity of Pd^0 and adsorbed CO are low and no contributions from surface Pd^0 is detected (Figure 7.8a; Table 7.2). The fraction of adsorbed CO on Pd^0 is, however, not negligible: 0.11 (Table 7.2), which is thought to be the result of Pd surface poisoning by CO, since the CO-Pd bond is relatively strong. This is further confirmed by the MS data (Figure E2) which clearly shows that CO_2 is formed over the entire O_2 half cycle. Furthermore, the fact that the Pd^0 bulk fraction is higher than the Pd^0 surface under oxidizing conditions suggests that the thickness of the oxide layer formed is smaller than the mean escape depth. This confirms that there is a thin skin of oxide grown on metallic Pd. Under reducing conditions, the fit of the averaged spectrum at 150 s (Figure 7.8b; Table 7.2) shows predominantly the peaks corresponding to metallic Pd species as well as adsorbed CO on surface Pd^0, together with attenuated contributions from cationic Pd and no Pd^{n+}-related component. The contribution from the Pd^0 surface is low: 0.04, which confirms the fact that the Pd surface is mainly covered with adsorbed CO species. The results demonstrate that PSD is very sensitive to the dynamic evolution of the species affected by the perturbations, and allows the detection of small surface changes.
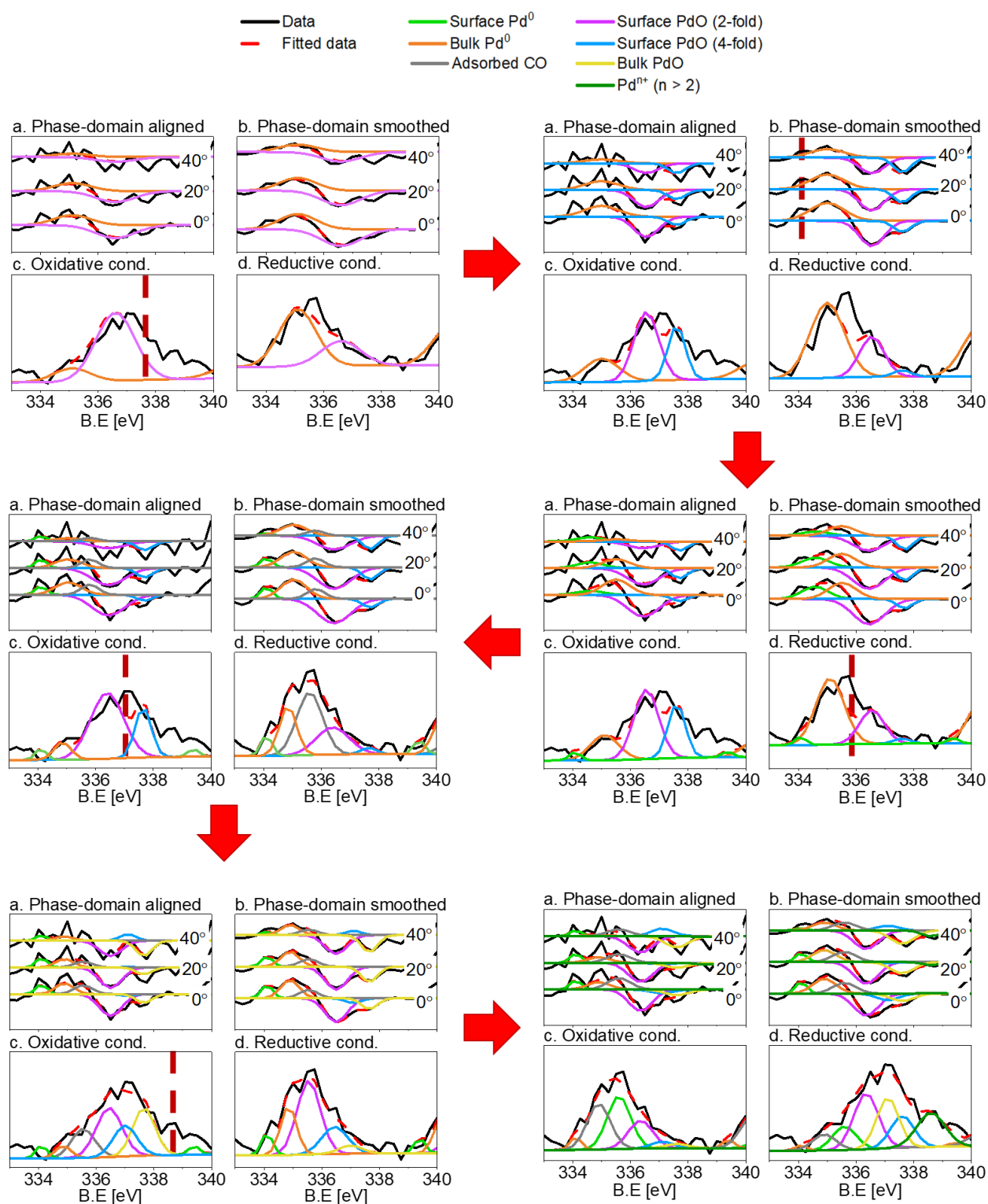
Figure 7.7. Fitting strategy to determine the peak features. (a-b) Phase domain spectra at 0, 20, and 40 °, of (a) raw and

(b) smoothed (binomial 1) data. (c-d) time domain spectra, under (c) oxidative and (d) reductive conditions.
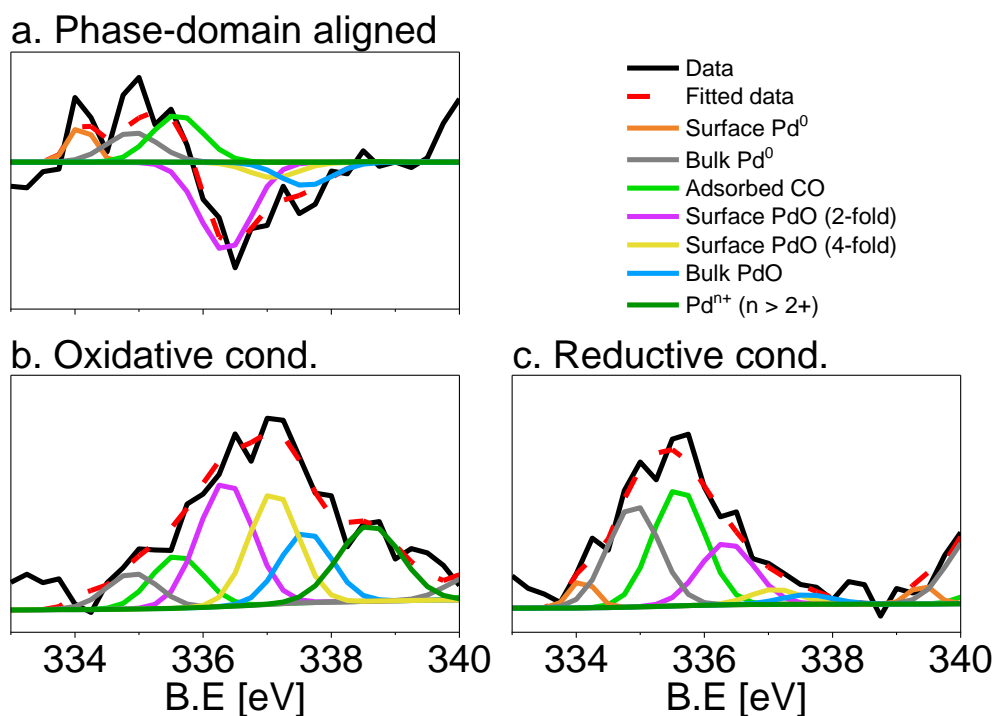
Figure 7.8. Fit of the (a) phase (0 °) and (b-c) time domain X-ray photoelectron spectra of 5 wt% Pd/Al$_2$O$_3$ acquired at the Pd 3d core level with a 300 eV kinetic energy. (b) Average of the spectra in oxidative conditions, (c) average of the spectra in reductive conditions. Peaks are defined in Table 7.1.

Dynamics and mechanism

PSD allowed following the dynamics of the species affected by the perturbation with greater details than in the time domain. In the time domain, no differences in the dynamics of the reduced and oxidized species could be distinguished, because the changes took place quickly (Figure 7.9a-b). In contrast, important information was retrieved from the phase domain data.

The features of reduced and oxidized Pd species exhibited by the phase domain spectra, for the aligned data, are presented in Figure 7.9c and Figure 7.9d, respectively. In the phase domain, a shift to higher angles implies an earlier consumption or reduction of the active specie. Moreover, the kinetic results obtained correspond to the reactivity of the Pd species over the full CO/O$_2$ modulation.

Table 7.2. Peak component fraction of the fit of the averaged time domain X-ray photoelectron spectra of 5 wt% Pd/Al_2O_3 acquired under oxidizing and reducing conditions. Fits are shown in Figure 7.8.

	Binding energy [eV]	Oxidizing cond.	Reducing cond.
Surface Pd^0 [%]	334.1	0.01	0.04
Bulk Pd^0 [%]	334.9	0.07	0.32
Adsorbed CO [%]	335.6	0.11	0.36
Surface PdO (2-fold) [%]	336.35	0.27	0.20
Surface PdO (4-fold) [%]	337.1	0.14	0.04
Bulk PdO [%]	337.6	0.22	0.04
Pd^{n+} (n > 2+) [%]	338.6	0.19	0

The results obtained from the analysis of the phase domain of the aligned data suggest that bulk Pd^0 reacts before surface Pd^0 and CO adsorption on Pd^0 surfaces (Figure 7.9c). The results achieved from the smoothed (binomial 1) data, displayed in Figure 7.9c, suggest that all three reduced components evolve at the same time. The discrepancy in the phase evolution between the aligned and smoothed data shows that the results achieved when smoothing the data need to be evaluated with caution. In contrast to the reduced species, significant differences are visible in the behaviour of the oxidized Pd species. The Pd species represented by the binding energy at 338.6 eV respond faster than the others to the O_2/CO modulation. The second species to react is the 2-fold surface PdO species, followed by the 4-fold surface PdO and the bulk PdO species.

From literature, it is found that PdO reduction by CO proceeds through oxygen diffusion from the bulk to the surface, following the diffusion-controlled reduction model [311,312]. The PSD results suggest that upon reduction bulk Pd^0 grows first and is followed by the formation of surface Pd^0 and surface coverage by adsorbed CO molecules which occur simultaneously. Furthermore, literature states that the reactivity of the Pd^{n+}

species towards CO oxidation is 10 times higher than PdO nanoparticles at room temperature [302], explaining their earlier consumption. The second species to be consumed is supposedly the 2-fold surface PdO species, followed by the 4-fold surface PdO and, the bulk PdO species, in agreement with the observation that the 2-fold coordinated Pd species were more reactive towards CO oxidation than the bulk PdO and 4-fold coordinated Pd species [290,291,296], due to the direct accessibility of the CO binding sites by the surface oxides sites [291,296,297,313].
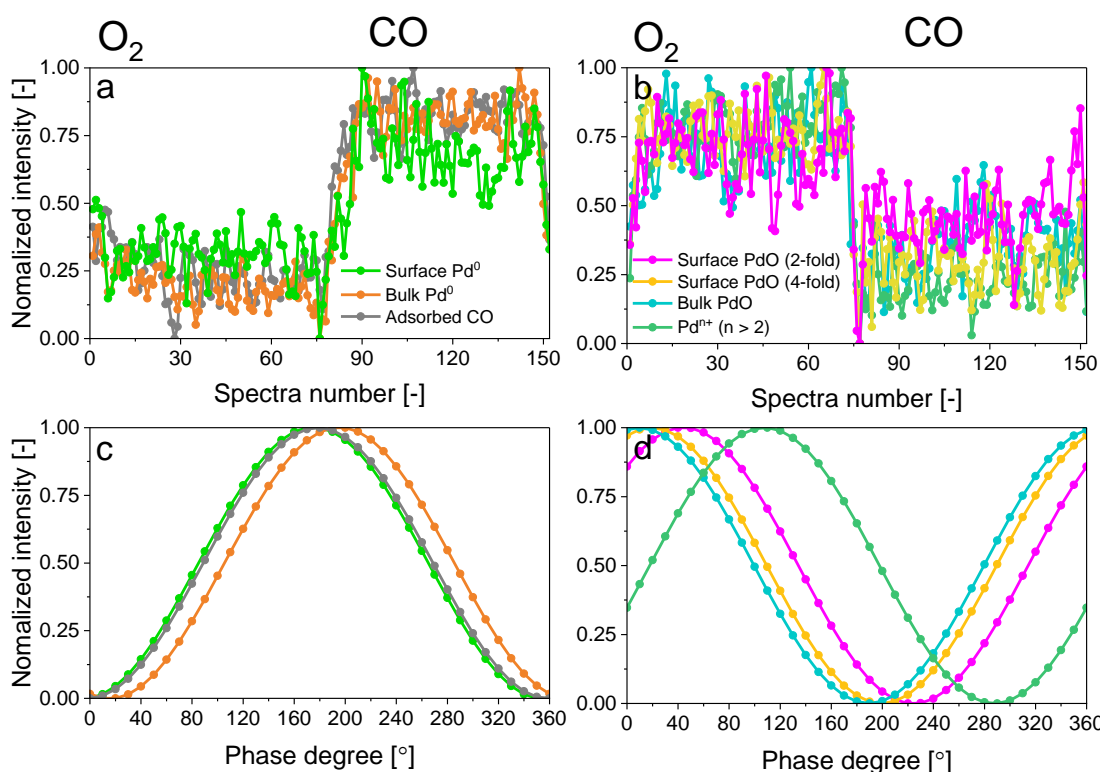
Figure 7.9. (a-b) Normalized time domain and (c-d) normalized phase domain of the (a, c) reduced Pd species, and (b, d) oxidized Pd species from the aligned data set.

On the other hand, Pd oxidation follows the Cabrera-Mott (CM) model [209] until the surface oxide layer reaches 3 nm, and then follows the 3D diffusion model [208]. According to the CM model, a thin oxide film forms upon oxidation, across which electrons tunnel from the metallic core to ionize adsorbed oxygen. The resulting charge separation induces an electric field that is the driving force for ion transport and the growth of the oxide layer. Hence, it is coherent that the Pd surface species (Pd^{n+} and 2-fold surface PdO) are formed

first. Then, the 4-fold surface PdO species are formed before bulk PdO. Indeed, these the 4-fold surface PdO species are known to have a faster initial oxidation rate than bulk PdO, which supports the hypothesis of being the precursors to bulk PdO [296,297,311,314].

Finally, the dynamics of the background/noise were followed to verify that it is not affected by the pulses (Figure E8). The binding energies chosen were 330.5 and 333 eV. The intensity of that spectral line is not affected by the gas switches.

The results shown in this paragraph demonstrate that PSD offers the unique possibility to extrapolate the kinetics of species formation/consumption from in situ time-resolved photoelectron spectroscopy acquired on an actual catalyst.

7.4 Conclusion

Time-resolved in situ X-ray photoelectron measurements were performed on a powder Pd/Al_2O_3 catalyst, while repeatedly switching between oxidative (O_2) and reducing (CO) environment, following the ME approach. All the suitable modulation periods were averaged into one period based on the gas switching events since the setup used allowed for rapid gas switches without significant delays between the pulsing event and the change in gas composition in the experimental cell. By averaging the ME cycles both, the signal-to-noise ratio of a photoemission spectrum and the time resolution of the measurement, which was now only limited to the acquisition time of one spectrum, were improved. By comparative fitting of phase and time domain spectra, a total of seven Pd species were detected to evolve during the gas switches: three reduced Pd species (bulk and surface Pd^0, and adsorbed CO on Pd^0), and four oxidized species (bulk and surface PdO (2- and 4-fold), as well as Pd^{n+} species). The phase domain data obtained from the PSD algorithm allowed following the dynamic evolution of these species in great detail. It was found that the most active species towards CO oxidation were the Pd^{n+} species and the 2-fold surface PdO species. The work presented here paves the way for important advances in the field of time-resolved near ambient pressure X-ray photoemission spectroscopy applied on

powder catalysts with low metal loadings, especially since the method proposed is fairly simple and can be used to process data acquired at different facilities. However, for the study of more complex or new systems, it is crucial to acquire the XPS spectra with a higher spectral resolution and to perform more sets of ME experiments.

Chapter 8 Conclusions and outlooks

8.1 Conclusions

The work presented in this thesis contributes to advancing the knowledge of enhanced methane removal from the exhaust of natural gas engines operated under periodic conditions.

This thesis work aimed at combining catalytic and spectroscopic measurements to gain knowledge on the catalytic structure/activity relationship of Pd-based catalysts which can then be used to enhance CH_4 removal from the exhaust feed of natural gas engines. In general, the catalytic abatement of CH_4 can be improved either by optimization of the operating conditions or by modifying the material formulation. These two strategies are complementary since not all the catalytic properties (i.e. redox properties, selectivity, reaction pathways, etc.) can be improved using only one of the two approaches. We decided to start by studying the effect of repeated O_2 pulses on a simple Pd/Al_2O_3 catalyst, and then increase the material complexity based on the knowledge acquired, and the remaining requirements that need to be fulfilled.

In this work, we demonstrated that repeated O_2 pulses enhanced the catalytic activity and stability toward CH_4 oxidation, due to the periodic formation and regeneration of the relevant Pd species. Indeed, under wet lean CH_4 oxidation conditions (1 vol% CH_4, 4 vol% O_2, 10 vol% H_2O), the presence of highly active PdO_x species formed upon repeated O_2 cut-offs, maintains and sustains high isothermal activity and stability, while isothermal deactivation of the catalyst is observed under static conditions due to the presence of less active PdO species. Under stoichiometric natural gas engine conditions (1500 ppm CH_4, 1600 ppm NO, 7000 ppm CO, 5700 ppm O_2, 5 vol% H_2O) simultaneous high conversion of all pollutants was only achieved over fully reduced Pd species. CH_4 steam reforming reaction appeared as a valuable indication for enhanced pollutant removal since this reaction pathway was only induced when the Pd species were fully reduced. Under these conditions, NO conversion dropped as soon as the catalyst was oxidized, and CH_4 oxidation was limited when

the Pd nanoparticles were only surface oxidized. To maintain the catalyst in a highly reduced state, O_2 pulses of small amplitude and high frequency were required. Such valuable knowledge on the catalytic structure/activity relationship of Pd/Al_2O_3 allowed anticipating the effect of periodic O_2 oscillations on the activity and reaction pathways involved during CH_4 oxidation from the exhaust feed of stoichiometric natural gas engines.

The Pd redox properties in Pd/Al_2O_3 were seen to be strongly affected by the O_2 concentration present in the exhaust feed, which led to important oscillations of the activity between the rich and lean phases of the O_2 pulses. As a consequence, only a narrow number of optimal operating conditions (cf. pulsing amplitude and frequency) induced high conversions over the entire pulsing sequence. Hence, modification of the material formulation (i.e. bimetallic systems) was required to control and improve the catalyst redox properties. Rh was added to the Pd/Al_2O_3 catalyst ($Pd-Rh/Al_2O_3$). It was observed that once reduced, the Rh species were only mildly affected by the O_2 concentration present in the feed, and were very active toward the steam reforming reaction. Moreover, since the presence of metallic Rh maintained CH_4-SR, the hydrogen produced from this reaction sustained the metallic Pd species. Hence, the presence of Rh maintained the catalyst in a reduced state (c.f. high conversion of all pollutants) over a broad range of O_2 concentration and therefore allowed maintaining high activity over a broader range of dithering conditions compared to Pd/Al_2O_3.

Because it is essential to follow the catalyst redox behaviour during periodic operation, spectroscopic techniques need to meet the requirements that arise from measuring in transient mode. The time resolution of a spectrum needs to be within the second to sub-second range, while the signal intensity and spectral resolution have to be high enough to distinguish between the spectral features originating from the active species, the spectator species, and the noise. Depending on the technique, noise can be high because only small spectral variations are expected from short pulses. Moreover, the equipment needs to match the experimental conditions. For example, cells with small dead volumes and withstanding high temperatures need to be used. In this work, synchrotron-based X-ray absorption spectroscopy (XAS) was the technique of choice to follow the Pd oxidation state under realistic working conditions and periodic operation. Nonetheless, XAS provides information on the bulk, while it would also be insightful to study the response of the surface Pd species which are

in direct contact with the gas molecules. This can be is achieved with near ambient pressure X-ray photoemission spectroscopy (NAP-XPS). However, NAPS-XPS measurements have low time resolution and signal-to-noise ratio, which limits the applicability of this method for realistic working conditions (i.e. low metal loading, diluted gas compositions, etc.). Hence, in this work, we demonstrate that the time resolution and signal-to-noise ratio of NAP-XPS measurements can be significantly improved by combining the modulation excitation method with phase-sensitive detection.

8.2 Outlook

Outlook for periodic operation

In this thesis work, it was shown that in order to maximize the effect of the O_2 pulses on the activity and to propose optimal pulsing protocols it is important to inspect, for each material, how the relevant parameters affect the catalyst redox properties and catalytic activity. However, since catalysts used in NGVs are expected to operate for extended mileage, the catalyst state will evolve with time (i.e. sintering, phase segregation, poisoning, etc.), and the optimal pulsing conditions will most certainly differ with the mileage. Hence, pulsing studies on used catalysts will allow proposing pulsing protocols that can be adapted as a function of aging/poisoning.

Improving the material formulation is essential to further enhance the beneficial effect of periodic operation. Two main approaches can be applied: refining the composition of Pd-based catalysts used specifically for periodic operation or exploring new catalysts that were previously discarded because of inefficient performance under static conditions but that may exhibit satisfactory activity under transient operation. In the latter case, catalysts based on transition elements could play an important role. Either way, when considering catalysts used for periodic operation, special attention should be placed on mitigating the formation of undesired by-products (i.e. NH_3, N_2O) as well as on refining the redox behaviour of the active species. Indeed, this thesis

work demonstrated that when high conversion levels were achieved upon periodic operation, it came together with important NH_3 slips, which emissions are stringently regulated by the European emissions standards. Also, tuning the redox properties of the active metals to answer specific requirements will allow broadening the range of applicability of the O_2 pulses. For example, for stoichiometric NG engine applications, the most relevant species for achieving high conversion levels are Pd^0, hence, adding Rh to a Pd/Al_2O_3 catalyst could maintain the catalyst in its reduced state over a wider range of pulsing conditions (amplitude and frequency). In view of these results and considering the high price of Rh, future studies should focus on evaluating the optimal Pd:Rh ratio under pulsing conditions that allows minimizing the amount of precious metal while preserving the beneficial effects of Rh during periodic operation. Moreover, the support can also be modified. Oxygen storage components such as CeO_2 are typically present in industrial catalysts and can be of interest as they modify the Pd redox behaviour and, can actively participate in SR and water gas shift reactions. Irreducible supports can be valuable for NG lean-burn applications since these materials are less affected by the presence of water than reducible supports. Finally, it would be very interesting to dedicate efforts to searching for new materials (i.e. transition metals). Indeed, there is plenty of room for discovery since not much research has been devoted to the assessment of the catalytic activity of new materials for CH_4 and NO removal from the exhaust of NGVs, under periodic operation. Among the few studies reported, NO reduction was shown to be enhanced only under transient conditions on a Cu-based perovskite-type TWC ($CuO/La_{0.5}Sr_{0.5}CoO_3$) as reduction of $La_{0.5}Sr_{0.5}CoO_3$ and CuO to more active brownmillerite and metallic Cu was not possible under static operation [315]. Furthermore, improved NO reduction was also achieved on a Cu/CeO_2 catalyst when operated under periodic conditions due to the emergence of a synergistic redox effect between Cu and Ce [316].

Outlook for operando spectroscopy research methodology

Finally, in this thesis work, we demonstrated the importance of following the redox response of the catalyst during periodic operation, since the catalyst oxidation state defines the catalytic activity. Hence, the operando spectroscopic techniques used need to have sub-second time resolution and high signal-to-noise ratio, to pre-

cisely follow the dynamic working structure of the catalyst during transient operation. To fulfil these requirements, synchrotron-based spectroscopic measurements are usually necessary when working with realistic gas compositions (cf. diluted conditions), materials (cf. low active metals loadings), and conditions (cf. high frequencies, low amplitudes).

In this thesis, the method of choice was synchrotron-based X-ray absorption spectroscopy since it provides qualitative and quantitative information on the oxidation state and local environment of a specific element of the catalyst. This is especially relevant when working with complex material compositions. Nonetheless, not all synchrotron-based spectroscopy methods allow working under realistic conditions and follow fast dynamics taking place within the sub-second range. For example, near ambient pressure X-ray photoemission spectroscopy requires working with pure gas mixtures to avoid expanding the pressure gap, while the low signal-to-noise ratio of a spectrum necessitates long acquisition times. Moreover, synchrotron-based techniques are not easily accessible, are difficult to set up and the data processing is usually challenging.

Hence, it would be very valuable to spread the use of lab-scale operando spectroscopic measurements in order to follow the redox dynamics of systems such as supported noble metals under periodic operation. Indeed, taking IR and UV-vis spectroscopies as an example, these methods have good time resolution, high signal-to-noise ratio, are easily accessible (lab scale instrument), and have simple data processing, which makes these techniques appealing alternatives to synchrotron measurements for operando studies. Nonetheless, one of the main drawbacks is that the signal acquired by IR and UV-vis is usually measured in diffuse reflectance mode (DRIFT, DRUV) and therefore the spectra acquired are the result of overlapping effects (i.e. plasmonic effect, reflectivity, scattering, etc.) making the interpretation of the results difficult. Therefore, future development of experimental cells and protocols are needed to allow dissociation of the various concurrent effects taking place. This is especially important when conducting operando spectroscopic measurements. Another difficulty that arises with these two techniques, is that the changes in the oxidation state of supported Pd nanoparticles result in the variation of the overall spectra intensity (cf. broad features) rather than the change of a specific peak position, width, or intensity, which complicates the results reading. Hence, even if these

methods can provide qualitative information on the reduction/oxidation state of the material, they are not element specific. Nonetheless, breaking down the complexity of the materials (i.e. Pd/Al$_2$O$_3$) will help gain information on the redox dynamics of the individual components, and bring essential knowledge to understand and optimize the system. Therefore, protocols explaining how to deconvolute the contribution of the different

References

[1] H. Engerer, M. Horn, *Energy Policy* **2010**, *38*, 1017–1029.

[2] S. Chu, A. Majumdar, *Nature* **2012**, *488*, 294–303.

[3] G. T. Chala, A. R. A. Aziz, F. Y. Hagos, *Energies* **2018**, *11*, 2934.

[4] F. Ahmad, E. L. Silva, M. B. A. Varesche, *Renew. Sustain. Energy Rev.* **2018**, *98*, 108–124.

[5] M. Mehrpooya, M. Khalili, M. M. M. Sharifzadeh, *Renew. Sustain. Energy Rev.* **2018**, *91*, 869–887.

[6] H. Li, Z. Yu, S. Wang, X. Long, L. M. Zhang, Z. Zhu, L. Yang, *J. Photochem. Photobiol. B Biol.* **2015**, *142*, 212–219.

[7] S. K. Sansaniwal, M. A. Rosen, S. K. Tyagi, *Renew. Sustain. Energy Rev.* **2017**, *80*, 23–43.

[8] S. N. Naik, V. V. Goud, P. K. Rout, A. K. Dalai, *Renew. Sustain. Energy Rev.* **2010**, *14*, 578–597.

[9] J. S. Luterbacher, M. Froling, F. Vogel, F. Marechal, J. W. Tester, *Environ. Sci. Technol.* **2009**, *43*, 1578–1583.

[10] M. H. Waldner, F. Vogel, *Ind. Eng. Chem. Res.* **2005**, *44*, 4543–4551.

[11] M. Gassner, F. Vogel, G. Heyen, F. Maréchal, *Energy Environ. Sci.* **2011**, *4*, 1742–1758.

[12] A. Kruse, *Biofuels, Bioprod. Biorefining* **2008**, *2*, 415–437.

[13] A. Kruse, T. Henningsen, A. Smag, J. Pfeiffer, *Ind. Eng. Chem. Res.* **2003**, *42*, 3711–3717.

[14] A. Kruse, D. Meier, P. Rimbrecht, M. Schacht, *Ind. Eng. Chem. Res.* **2000**, *39*, 4842–4848.

[15] S. Subramanian, R. J. Kudla, M. S. Chattha, *Ind. Eng. Chem. Res.* **1992**, *31*, 11, 2460–2465.

[16] G. Karavalakis, T. D. Durbin, M. Villela, J. W. Miller, *J. Nat. Gas Sci. Eng.* **2012**, *4*, 8–16.

[17] D. Jiang, K. Khivantsev, Y. Wang, *ACS Catal.* **2020**, *10,* 14304–14314.

[18] C. Huang, W. Shan, Z. Lian, Y. Zhang, H. He, *Catal. Sci. Technol.* **2020**, *10*, 6407–6419.

[19] A. Thiruvengadam, M. Besch, V. Padmanaban, S. Pradhan, B. Demirgok, *Energy Policy* **2018**, *122*, 253–259.

[20] H. M. Cho, B. Q. He, *Energy Convers. Manag.* **2007**, *48*, 608–618.

[21] P. Forzatti, *Catal. Today* **2003**, *83*, 3–18.

[22] M. Lyubovsky, L. L. Smith, M. Castaldi, H. Karim, B. Nentwick, S. Etemad, R. LaPierre, W. C. Pfefferle, *Catal. Today* **2003**, *83*, 71–84.

[23] S. Su, X. Yu, *Energy* **2015**, *79*, 428–438.

[24] Z. R. Ismagilov, N. V. Shikina, S. A. Yashnik, A. N. Zagoruiko, M. A. Kerzhentsev, V. A. Ushakov, V. A. Sazonov, V. N. Parmon, V. M. Zakharov, B. I. Braynin, O. N. Favorski, *Catal. Today* **2010**, *155*, 35–44.

[25] H. Sadamori, *Catal. Today* **1999**, *47*, 325–338.

[26] K. I. Khidr, Y. A. Eldrainy, M. M. EL-Kassaby, *Renew. Sustain. Energy Rev.* **2017**, *67*, 1237–1266.

[27] T. M. Gür, *Prog. Energy Combust. Sci.* **2016**, *54*, 1–64.

[28] Y. S. Seo, S. P. Yu, S. J. Cho, K. S. Song, *Chem. Eng. Sci.* **2003**, *58*, 43–53.

[29] S. Specchia, G. Toniato, *Catal. Today* **2009**, *147*, S99–S106.

[30] S. Jugjai, N. Rungsimuntuchart, *Exp. Therm. Fluid Sci.* **2002**, *26*, 581–592.

[31] S. R. Vaillant, A. S. Gastec, *Catal. Today* **1999**, *47*, 415–420.

[32] A. Gavriilidis, M. Zanfir, *Chem. Eng. Sci.* **2001**, *56*, 2671–2683.

[33] K. Venkataraman, J. M. Redenius, L. D. Schmidt, *Chem. Eng. Sci.* **2002**, *57*, 2335–2343.

[34] M. Van Sint Annaland, H. A. R. Scholts, J. A. M. Kuipers, W. P. M. Van Swaaij, *Chem. Eng. Sci.* **2002**, *57*, 855–872.

[35] Y. Chen, H. Xu, X. Jin, G. Xiong, *Catal. Today* **2006**, *116*, 334–340.

[36] H. Mei, C. Li, S. Ji, H. Liu, *Chem. Eng. Sci.* **2007**, *62*, 4294–4303.

[37] M. R. Rahimpour, M. R. Dehnavi, F. Allahgholipour, D. Iranshahi, S. M. Jokar, *Appl. Energy* **2012**, *99*, 496–512.

[38] E. K. Nam, T. E. Jensen, T. J. Wallington, *Environ. Sci. Technol.* **2004**, *38*, 2005–2010.

[39] International Energy Agency, https://www.iea.org/, accessed in July 2022.

[40] J. Barbier, C. Micheaud, E. Rohart, E. Lafitte, *Catal. by Met.* **1997**, *6,* 133–151.

[41] https://ec.europa.eu/clima/eu-action/european-green-deal/2030-climate-target-plan_en, accessed in September 2022.

[42] https://eur-lex.europa.eu/legal-content/EN/TXT/?uri=CELEX%3A02019R0631-20210301, accessed in September 2022.

[43] G. J. K. Acres, *Stud. Environ. Sci.* **1991**, *44*, 376–396.

[44] J. Brettschneider, *Bosch Tech. Ber.* **1979**, *6*.

[45] B. C. Singer, *Environ. Sci. Technol.* **1998**, *32*, 3241–3248.

[46] J. Davidson, J. M. Norbeck, **2012**, *6,* 133-151.

[47] https://www.epa.gov/clean-air-act-overview/evolution-clean-air-act#caa70, accessed in August 2022.

[48] F. G. Dwyer, *Cata. Reviews,* **1972**, *1,* 6, 261–291.

[49] J. Graham, *Patent,* US3741725A, **1973**.

[50] A. J. Martyr, M A Plint, *Elsevier,* **2012**, *4th edition.*

[51] T. Korakianitis, A. M. Namasivayam, R. J. Crookes, *Prog. Energy Combust. Sci.* **2011**, *37*, 89–112.

[52] K. C. Taylor, *Springer-Verlag* **1984**, *1st Edition.*

[53] H. M. Wiedenmann, L. Raff, R. Noack, *SAE-Paper,* **1984,** 840141**.**

[54] T. Wang, R. E. Soltis, E. M. Logothetis, J. A. Cook, D. R. Hamburg, *SAE Tech. Pap.* **1993**

[55] C. Thompson, J. Mooney, C. Keith, W. Mannion, *Patent,* **1979,** *4* 157, 316.

[56] Z. P. Liu, P. Hu, *J. Am. Chem. Soc.* **2003**, *125*, 1958–1967.

[57] J. Gong, J. Pihl, D. Wang, M. Y. Kim, W. P. Partridge, J. Li, M. Cunningham, K. Kamasamudram, N. Currier, A. Yezerets, *Catal. Today* **2021**, *360*, 294–304.

[58] X. Shi, R. Seiser, J. Y. Chen, R. Dibble, R. Cattolica, *SAE Int. J. Engines* **2015**.

[59] D. Ferri, M. Elsener, O. Kröcher, *Appl. Catal. B Environ.* **2018**, *220*, 67–77.

[60] J. M. Trichard, *Stud. Surf. Sci. Catal.* **2007**, *171*, 211–233.

[61] Q. Liu, C. Bian, S. Ming, L. Guo, S. Zhang, L. Pang, P. Liu, Z. Chen, T. Li, *Appl. Catal. A Gen.* **2020**, *607*, 117865.

[62] S. Mohan, P. Dinesha, S. Kumar, *Chem. Eng. J.* **2020**, *384*, 123253.

[63] R. W. Howarth, *Energy Sci. Eng.* **2014**, *2*, 47–60.

[64] R. J. Farrauto, M. C. Hobson, T. Kennelly, E. M. Waterman, *Appl. Catal. A, Gen.* **1992**, *81*, 227–237.

[65] P. Gélin, M. Primet, *Appl. Catal. B Environ.* **2002**, *39*, 1–37.

[66] V. Marchionni, M. Nachtegaal, A. Petrov, O. Kröcher, D. Ferri, in *J. Phys. Conf. Ser.*, **2016**, *712*.

[67] V. Marchionni, M. Nachtegaal, D. Ferri, *ACS Catal.* **2020**, *10*, 4791–4804.

[68] N. Sadokhina, G. Smedler, U. Nylén, M. Olofsson, L. Olsson, *Appl. Catal. B Environ.* **2017**, *200*, 351–360.

[69] G. S. Herman, C. H. F. Peden, S. J. Schmieg, D. N. Belton, *Catal. Letters* **1999**, *62*, 131–138.

[70] Y. Hu, K. Griffiths, P. R. Norton, *Surf. Sci.* **2009**, *603*, 1740–1750.

[71] C. A. De Wolf, B. E. Nieuwenhuys, *Catal. Today* **2001**, *70*, 287–300.

[72] D. Bounechada, G. Groppi, P. Forzatti, K. Kallinen, T. Kinnunen, *Top. Catal.* **2013**, *56*, 372–377.

[73] C. Chen, Y. H. Yeh, M. Cargnello, C. B. Murray, P. Fornasiero, R. J. Gorte, *ACS Catal.* **2014**, *4*, 3902–3909.

[74] M. Monai, T. Montini, C. Chen, E. Fonda, R. J. Gorte, P. Fornasiero, *ChemCatChem* **2015**, *7*, 2038–2046.

[75] C. Zhou, H. Ma, W. Yuan, F. Qi, *Catal. Commun.* **2021**, *149*, 106185.

[76] G. H. Meguerian, E. H. Hirschberg, F. W. Rakowsky, *Patent*, US4006103A, **1975**.

[77] G. Jones, J. G. Jakobsen, S. S. Shim, J. Kleis, M. P. Andersson, J. Rossmeisl, F. Abild-Pedersen, T. Bligaard, S. Helveg, B. Hinnemann, J. R. Rostrup-Nielsen, I. Chorkendorff, J. Sehested, J. K. Nørskov, *J. Catal.* **2008**, *259*, 147–160.

[78] E. Kikuchi, S. Tanaka, Y. Yamazaki, Y. Morita, *Bull. Japan Pet. Inst.* **1974**, *16*, 95–98.

[79] B. Harrison, A. F. Diwell, C. Hallett, *Platinum Metals Rev.,* **1988,** *32,* 2, 73.

[80] J. Biener, A. Wittstock, T. F. Baumann, J. Weissmüller, M. Bäumer, A. V. Hamza, *Materials* **2009**, *2*, 2404.

[81] Y. Kaneko, H. Kobayashi, R. Komagome, O. Hirako and O. Nakayama, *SAE int.,* **1978**, *87,* 2225-2233.

[82] R. M. Heck, K. S. Patel, J. R. Adomaltis, *SAE Tech. Pap.* **1989**.

[83] H. Muraki, H. Shlnjoh, H. Sobukawa, K. Yokota, Y. Fujitani, *Ind. Eng. Chem. Prod. Res. Dev* **1985**, *24*, 43–49.

[84] R. Gholami, M. Alyani, K. J. Smith, *Catal. 2015, Vol. 5, Pages 561-594* **2015**, *5*, 561–594.

[85] A. Setiawan, J. Friggieri, H. Hosseiniamoli, E. M. Kennedy, B. Z. Dlugogorski, A. A. Adesina, M. Stockenhuber, *Phys.Chem. Chem. Phys.* **2016**, *18*, 10528–10537.

[86] C. Descorme, P. Gélin, C. Lécuyer, M. Primet, *Appl. Catal. B Environ.* **1997**, *13*, 185–195.

[87] H. S. Gandhi, M. Shelef, *Appl. Catal.* **1991**, *77*, 175–186.

[88] H. Arai, M. Machida, *Appl. Catal. A Gen.* **1996**, *138*, 161–176.

[89] P. Burtin, J. P. Brunelle, M. Pijolat, M. Soustelle, *Appl. Catal.* **1987**, *34*, 225–238.

[90] M. Machida, K. Eguchi, H. Arai, *Bull. Chem. Soc. Jpn.* **2006**, *61*, 3659–3665.

[91] B. Beguin, E. Garbowski, M. Primet, *J. Catal.* **1991**, *127*, 595–604.

[92] S. Bernal, J. J. Calvino, M. A. Cauqui, J. M. Gatica, C. López Cartes, J. A. Pérez Omil, J. M. Pintado, *Catal. Today* **2003**, *77*, 385–406.

[93] R. Di Monte, P. Fornasiero, J. Kaspar, M. Graziani, J. M. Gatica, S. Bernal, A. Gomez-Herrero, *Chem. Commun.* **2000**, *0*, 2167–2168.

[94] H. Vidal, J. Kašpar, M. Pijolat, G. Colon, S. Bernal, A. Cordón, V. Perrichon, F. Fally, *Appl. Catal. B Environ.* **2001**, *30*, 75–85.

[95] Z. Han, J. Wang, H. Yan, M. Shen, J. Wang, W. Wang, M. Yang, *Catal. Today* **2010**, *158*, 481–489.

[96] R. W. McCabe, R. K. Usmen, *Stud. Surf. Sci. Catal.* **1996**, *101*, 355–368.

[97] C. H. Bartholomew, *Appl. Catal. A Gen.* **2001**, *212*, 17–60.

[98] M. Shelef, R. W. McCabe, *Catal. Today* **2000**, *62*, 35–50.

[99] J. Kašpar, P. Fornasiero, N. Hickey, *Catal. Today* **2003**, *77*, 419–449.

[100] A. K. Datye, Q. Xu, K. C. Kharas, J. M. McCarty, *Catal. Today* **2006**, *111*, 59–67.

[101] G. W. Graham, A. E. O'Neill, A. E. Chen, *Appl. Catal. A Gen.* **2003**, *252*, 437–445.

[102] J. A. Lupescu, J. W. Schwank, G. B. Fisher, X. Chen, S. L. Peczonczyk, A. R. Drews, *Appl. Catal. B Environ.* **2016**, *185*, 189–202.

[103] R. Di Monte, P. Fornasiero, J. Kašpar, P. Rumori, G. Gubitosa, M. Graziani, *Appl. Catal. B Environ.* **2000**, *24*, 157–167.

[104] A. Martínez-Arias, M. Fernández-García, A. B. Hungría, A. Iglesias-Juez, K. Duncan, R. Smith, J. A. Anderson, J. C. Conesa, J. Soria, *J. Catal.* **2001**, *204*, 238–248.

[105] G. W. Graham, A. N. Shigapov, *Catal. Lett.* **2002**, *81*, 253–257.

[106] L. Kępiński, M. Wołcyrz, J. Okal, *J. Chem. Soc. Faraday Trans.* **1995**, *91*, 507–515.

[107] M. Zhao, M. Shen, J. Wang, W. Wang, *Ind. Eng. Chem. Res.* **2007**, *46*, 7883–7890.

[108] R. J. Gorte, *AIChE J.* **2010**, *56*, 1126–1135.

[109] T. Bunluesin, R. J. Gorte, G. W. Graham, *Appl. Catal. B Environ.* **1998**, *15*, 107–114.

[110] E. Mamontov, T. Egami, R. Brezny, M. Koranne, S. Tyagi, *J. Phys. Chem. B* **2000**, *104*, 11110–11116.

[111] J. Nilsson, P. A. Carlsson, N. M. Martin, P. Velin, D. M. Meira, H. Grönbeck, M. Skoglundh, *Catal. Commun.* **2018**, *109*, 24–27.

[112] M. Cargnello, J. J. Delgado Jaén, J. C. Hernández Garrido, K. Bakhmutsky, T. Montini, J. J. Calvino Gámez, R. J. Gorte, P. Fornasiero, *Science* **2012**, *337*, 713–717.

[113] S. K. Matam, G. L. Chiarello, Y. Lu, A. Weidenkaff, D. Ferri, *Top. Catal.* **2013**, *56*, 239–242.

[114] J. Nilsson, P. A. Carlsson, N. M. Martin, E. C. Adams, G. Agostini, H. Grönbeck, M. Skoglundh, *J. Catal.* **2017**, *356*, 237–245.

[115] M. Zimowska, J. B. Wagner, J. Dziedzic, J. Camra, B. Borzęcka-Prokop, M. Najbar, *Chem. Phys. Lett.* **2006**, *417*, 137–142.

[116] C. H. Li, J. Wu, A. B. Getsoian, G. Cavataio, J. R. Jinschek, *Chem. Mater.* **2022**, *34*, 2123–2132.

[117] P. Velin, M. Ek, M. Skoglundh, A. Schaefer, A. Raj, D. Thompsett, G. Smedler, P. A. Carlsson, *J. Phys. Chem. C* **2019**, *123*, 25724–25737.

[118] X. Li, X. Wang, K. Roy, J. A. Van Bokhoven, L. Artiglia, *ACS Catal.* **2020**, *10*, 5783–5792.

[119] O. Mihai, G. Smedler, U. Nylén, M. Olofsson, L. Olsson, *Catal. Sci. Technol.* **2017**, *7*, 3084–3096.

References

[120] J. J. Willis, A. Gallo, D. Sokaras, H. Aljama, S. H. Nowak, E. D. Goodman, L. Wu, C. J. Tassone, T. F. Jaramillo, F. Abild-Pedersen, M. Cargnello, *ACS Catal.* **2017**, *7*, 7810–7821.

[121] D. Ciuparu, N. Katsikis, L. Pfefferle, *Appl. Catal. A Gen.* **2001**, *216*, 209–215.

[122] W. R. Schwartz, D. Ciuparu, L. D. Pfefferle, *J. Phys. Chem. C* **2012**, *116*, 8587–8593.

[123] D. Ciuparu, E. Perkins, L. Pfefferle, *Appl. Catal. A Gen.* **2004**, *263*, 145–153.

[124] K. I. Fujimoto, F. H. Ribeiro, M. Avalos-Borja, E. Iglesia, *J. Catal.* **1998**, *179*, 431–442.

[125] H. Stotz, L. Maier, A. Boubnov, A. T. Gremminger, J. D. Grunwaldt, O. Deutschmann, *J. Catal.* **2019**, *370*, 152–175.

[126] Y. Q. Su, J. X. Liu, I. A. W. Filot, L. Zhang, E. J. M. Hensen, *ACS Catal.* **2018**, *8*, 6552–6559.

[127] A. Hellman, A. Resta, N. M. Martin, J. Gustafson, A. Trinchero, P. A. Carlsson, O. Balmes, R. Felici, R. Van Rijn, J. W. M. Frenken, J. N. Andersen, E. Lundgren, H. Grönbeck, *J. Phys. Chem. Lett.* **2012**, *3*, 678–682.

[128] A. Toso, S. Colussi, J. Llorca, A. Trovarelli, *Appl. Catal. A Gen.* **2019**, *574*, 79–86.

[129] D. Ciuparu, E. Altman, L. Pfefferle, *J. Catal.* **2001**, *203*, 64–74.

[130] D. Ciuparu, L. Pfefferle, *Catal. Today* **2002**, *77*, 167–179.

[131] D. Ciuparu, F. Bozon-Verduraz, L. Pfefferle, *J. Phys. Chem. B* **2002**, *106*, 3434–3442.

[132] W. R. Schwartz, L. D. Pfefferle, *J. Phys. Chem. C* **2012**, *116*, 8571–8578.

[133] S. Colussi, A. Trovarelli, G. Groppi, J. Llorca, *Catal. Commun.* **2007**, *8*, 1263–1266.

[134] K. Okumura, S. Matsumoto, N. Nishiaki, M. Niwa, *Appl. Catal. B Environ.* **2003**, *40*, 151–159.

[135] K. Okumura, E. Shinohara, M. Niwa, *Catal. Today* **2006**, *117*, 577–583.

[136] H. Maeda, Y. Kinoshita, K. R. Reddy, K. Muto, S. Komai, N. Katada, M. Niwa, *Appl. Catal. A Gen.* **1997**, *163*, 59–69.

[137] A. W. Petrov, D. Ferri, M. Tarik, O. Kröcher, J. A. van Bokhoven, *Top. Catal.* **2017**, *60*, 123–130.

[138] A. W. Petrov, D. Ferri, F. Krumeich, M. Nachtegaal, J. A. Van Bokhoven, O. Kröcher, *Nat. Commun.* **2018**, *9*, 1–8.

[139] W. Barrett, J. Shen, Y. Hu, R. E. Hayes, R. W. J. Scott, N. Semagina, *ChemCatChem* **2020**, *12*, 944–952.

[140] J. Yang, M. Peng, G. Ren, H. Qi, X. Zhou, J. Xu, F. Deng, Z. Chen, J. Zhang, K. Liu, X. Pan, W. Liu, Y. Su, W. Li, B. Qiao, D. Ma, T. Zhang, *Angew. Chemie* **2020**, *132*, 18680–18684.

[141] M. Casapu, A. Fischer, A. M. Gänzler, R. Popescu, M. Crone, D. Gerthsen, M. Türk, J. D. Grunwaldt, *ACS Catal.* **2017**, *7*, 343–355.

[142] H. Yamamoto, H. Uchida, *Catal. Today* **1998**, *45*, 147–151.

[143] K. Persson, A. Ersson, K. Jansson, J. L. G. Fierro, S. G. Järås, *J. Catal.* **2006**, *243*, 14–24.

[144] K. Persson, A. Ersson, A. M. Carrera, J. Jayasuriya, R. Fakhrai, T. Fransson, S. Järås, *Catal. Today* **2005**, *100*, 479–483.

[145] A. Ersson, H. Kušar, R. Carroni, T. Griffin, S. Järås, *Catal. Today* **2003**, *83*, 265–277.

[146] K. Persson, L. D. Pfefferle, W. Schwartz, A. Ersson, S. G. Järås, *Appl. Catal. B Environ.* **2007**, *74*, 242–250.

 [147] G. Lapisardi, L. Urfels, P. Gélin, M. Primet, A. Kaddouri, E. Garbowski, S. Toppi, E. Tena, *Catal. Today* **2006**, *117*, 564–568.

[148] A. H. Habibi, R. E. Hayes, N. Semagina, *Appl. Catal. A Gen.* **2018**, *556*, 129–136.

[149] W. Barrett, J. Shen, Y. Hu, R. E. Hayes, R. W. J. Scott, N. Semagina, *ChemCatChem* **2020**, *12*, 944–952.

[150] P. Silveston, R. R. Hudgins, A. Renken, *Catal. Today* **1995**, *25*, 91–112.

[151] D. Bounechada, G. Groppi, P. Forzatti, K. Kallinen, T. Kinnunen, *Appl. Catal. B Environ.* **2012**, *119–120*, 91–99.

[152] P. A. Carlsson, E. Fridell, M. Skoglundh, *Catal. Letters* **2007**, *115*, 1–7.

[153] K. A. Karinshak, P. Lott, M. P. Harold, O. Deutschmann, *ChemCatChem* **2020**, *12*, 3712–3720.

[154] P. Pospíšl, M. Haumann, J. Dittmer, V. A. Solé, H. Dau, *Biophys. J.* **2003**, *84*, 1370–1386.

[155] R. Desamero, S. Rozovsky, N. Zhadin, A. McDermott, R. Callender, *Biochemistry* **2003**, *42*, 2941–2951.

[156] A. A. Quader, R. F. Majkowski, *SAE Tech. Pap.* **1999**.

[157] R. K. Herz, E. J. Shlnouskls, *Ind. Eng. Chem. Prod. Res. Dev* **1985**, *24*, 385–390.

[158] J. C. Schlatter, P. M. Mitchell, R. M. Slnkevltch, P. J. Mitchell, K. C. Taylor, R. K. Herz, D. R. Monroe, *Ind. Eng. Chem. Prod. Res. Dev* **1983**, *22*, 51–56.

[159] M. Horio, H. Hayashi, K. Morishita, *Ind. Eng. Chem. Res* **1988**, *27*, 30–36.

[160] G. W. M Eng Thesis, B. K. Cho, L. A. West, *J. Appl. Sci. Res. Sect* **1986**, *25*, 1197.

[161] M. Weibel, F. Garin, P. Bernhardt, G. Maire, M. Prigent, *Stud. Surf. Sci. Catal.* **1991**, *71*, 195–205.

[162] E. Rogemond, N. Essayem, R. Fréty, V. Perrichon, M. Primet, M. Chevrier, C. Gauthier, F. Mathis, *J. Catal.* **1987**, *186*, 414–422. [165] K. Yokota, H. Muraki, Y. Fujitani, *SAE Int.* **1985,** *94,* 790-797.

[164] H. C. J Phys, T. C. In Mossbauer Spectroscopy, Y. B. Klnet Katal, W. F. J Catal, R. B. J Phys Chem, van der Kraan, van Dijk, van der Baan, H. S. J Phys Chem, H. Murakl, Y. Fujltani, *Ind. Eng. Chem. Process Des. Dev* **1978**, *20*, 116.

[165] R. K. Herz, J. B. Klela, J. A. Sell, *Ind. Eng. Chem. Prod. Res. Dev* **1983**, *22*, 387–396.

[166] L. L. Hegedus, W. K. Hall, J. C. Schlatter, P. J. Mitchell, *Ind. Eng. Chem. Prod. Res. Dev* **1980**, *19*, 288–293.

[167] M. Wang, P. Dimopoulos Eggenschwiler, T. Franken, D. Ferri, O. Kröcher, *Chem. Eng. J.* **2021**, 129932.

[168] M. Wang, P. Dimopoulos Eggenschwiler, D. Ferri, O. Kröcher, *Chem. Eng. J.* **2022**, *430*, 132848.

[169] A. Marberger, A. W. Petrov, P. Steiger, M. Elsener, O. Kröcher, M. Nachtegaal, D. Ferri, *Nat. Catal.* **2018**, *13*, 221–227.

[170] J. Meyer, S. Yurkovich, S. Midlam-Mohler, *IEEE Trans. Control Syst. Technol.* **2013**, *21*, 636–648.

[171] M. Defoort, D. Olsen, B. Willson, *Int. J. Engine Res.* **2005**, *5*, 115–122.

[172] F. Zeng, J. Finke, D. Olsen, A. White, K. L. Hohn, *Chem. Eng. J.* **2018**, *352*, 389–404.

[173] G. C. Koltsakis, A. M. Stamatelos, *Chem. Eng. Sci.* **1999**, *54*, 4567–4578.

[174] I. Mejía-Centeno, S. Castillo, G. A. Fuentes, *Appl. Catal. B Environ.* **2012**, *119–120*, 234–240.

[175] A. Baylet, P. Marécot, D. Duprez, P. Castellazzi, G. Groppi, P. Forzatti, *Phys. Chem. Chem. Phys.* **2011**, *13*, 4607–4613.

[176] S. C. Su, J. N. Carstens, A. T. Bell, *J. Catal.* **1998**, *176*, 125–135.

[177] J. D. Grunwaldt, N. Van Vegten, A. Baiker, *Chem. Commun.* **2007**, *0*, 4635–4637.

[178] N. M. Kinnunen, J. T. Hirvi, T. Venäläinen, M. Suvanto, T. A. Pakkanen, *Appl. Catal. A Gen.* **2011**, *397*, 54–61.

[179] R. Burch, F. J. Urbano, *Appl. Catal. A, Gen.* **1995**, *124*, 121–138.

[180] S. K. Matam, M. H. Aguirre, A. Weidenkaff, D. Ferri, *J. Phys. Chem. C* **2010**, *114*, 9439–9443.

[181] T. Huai, T. D. Durbin, J. W. Miller, J. T. Pisano, C. G. Sauer, S. H. Rhee, J. M. Norbeck, *Environ. Sci. Technol.* **2003**, *37, 21*, 4841–4847.

[182] Y. H. Chin, C. Buda, M. Neurock, E. Iglesia, *J. Am. Chem. Soc.* **2013**, *135*, 15425–15442.

[183] A. W. Petrov, D. Ferri, O. Kröcher, J. A. van Bokhoven, *ACS Catal.* **2019**, *9*, 2303–2312.

[184] S. Chenevarin, F. Thibault-Starzyk, F. Thibault-Starzyk, S. Chenevarin, *Angew. Chemie* **2004**, *116*, 1175–1178.

[185] G. Onyestyák, J. Valyon, L. V. C. Rees, *Phys. Chem. Chem. Phys.* **2000**, *2*, 3077–3082.

[186] J. Stötzel, D. Lützenkirchen-Hecht, R. Frahm, J. D. Grunwaldt, *J. Phys. Conf. Ser.* **2013**, *430*, 012126.

[187] V. Marchionni, M. A. Newton, A. Kambolis, S. K. Matam, A. Weidenkaff, D. Ferri, *Catal. Today* **2014**, *229*, 80–87.

[188] X. Wang, T. Bürgi, *J. Phys. Chem. C* **2021**, *125*, 25284–25289.

[189] C. J. Baranowski, T. Fovanna, M. Roger, M. Signorile, J. McCaig, A. M. Bahmanpour, D. Ferri, O. Kröcher, *ACS Catal.* **2020**, *10*, 8106–8119.

[190] G. L. Chiarello, Y. Lu, M. Agote-Arán, R. Pellegrini, D. Ferri, *Catal.* **2021**, *11*, 116.

[191] A. G. Greenaway, A. Marberger, A. Thetford, I. Lezcano-González, M. Agote-Arán, M. Nachtegaal, D. Ferri, O. Kröcher, C. R. A. Catlow, A. M. Beale, *Chem. Sci.* **2020**, *11*, 447–455.

[192] S. K. Matam, M. A. Newton, A. Weidenkaff, D. Ferri, *Catal. Today* **2013**, *205*, 3–9.

[193] G. L. Chiarello, D. Ferri, *Phys. Chem. Chem. Phys.* **2015**, *17*, 10579–10591.

[194] D. Ferri, M. A. Newton, M. Nachtegaal, *Top. Catal.* **2011**, *54*, 1070–1078.

[195] J. Knudsen, T. Gallo, V. Boix, M. D. Strømsheim, G. D'Acunto, C. Goodwin, H. Wallander, S. Zhu, M. Soldemo, P. Lömker, F. Cavalca, M. Scardamaglia, D. Degerman, A. Nilsson, P. Amann, A. Shavorskiy, J. Schnadt, *Nat. Commun.* **2021**, *12*, 1–8.

[196] C. Papp, B. Tränkenschuh, R. Streber, T. Fuhrmann, R. Denecke, H. P. Steinrück, *J. Phys. Chem. C* **2007**, *111*, 2177–2184.

[197] E. A. Redekop, N. Johansson, E. Kokkonen, S. Urpelainen, F. Lopes Da Silva, M. Kaipio, H. E. Nieminen, F. Rehman, V. Miikkulainen, M. Ritala, U. Olsbye, *Rev. Sci. Instrum.* **2021**, *92*, 044101.

[198] O. Höfert, C. Gleichweit, H. P. Steinrück, C. Papp, *Rev. Sci. Instrum.* **2013**, *84*, 093103.

[199] R. Timm, A. R. Head, S. Yngman, J. V. Knutsson, M. Hjort, S. R. McKibbin, A. Troian, O. Persson, S. Urpelainen, J. Knudsen, J. Schnadt, A. Mikkelsen, *Nat. Commun.* **2018**, *9*, 1–9.

[200] N. E. Richey, C. De Paula, S. F. Bent, *J. Chem. Phys.* **2020**, *152*, 040902.

[201] L. Artiglia, F. Orlando, K. Roy, R. Kopelent, O. Safonova, M. Nachtegaal, T. Huthwelker, J. A. Van Bokhoven, *J. Phys. Chem. Lett.* **2017**, *8*, 102–108.

[202] D. Baurecht, U. P. Fringeli, *Rev. Sci. Instrum.* **2001**, *72*, 3782.

[203] A. Urakawa, T. Bürgi, A. Baiker, *Chem. Eng. Sci.* **2008**, *63*, 4902–4909.

[204] J. Nilsson, P. A. Carlsson, S. Fouladvand, N. M. Martin, J. Gustafson, M. A. Newton, E. Lundgren, H. Grönbeck, M. Skoglundh, *ACS Catal.* **2015**, *5*, 2481–2489.

[205] R. S. Monteiro, D. Zemlyanov, J. M. Storey, F. H. Ribeiro, *J. Catal.* **2001**, *199*, 291–301.

[206] J. C. Van Giezen, F. R. Van Den Berg, J. L. Kleinen, A. J. Van Dillen, J. W. Geus, *Catal. Today* **1999**, *47*, 287–293.

[207] F. H. Ribeiro, M. Chow, R. A. Dalla Betta, *J. Catal.* **1994**, *146*, 537–544.

[208] A. Khawam, D. R. Flanagan, *J. Phys. Chem. B* **2006**, *110*, 17315–17328.

[209] N. Cabrera, N. F. Mott, *Reports Prog. Phys.* **1949**, *12*, 163–184.

[210] J. M. Thomas, *Angew. Chemie Int. Ed.* **2009**, *48*, 3390–3391.

[211] A. H. Clark, J. Imbao, R. Frahm, M. Nachtegaal, *J. Synchrotron Radiat.* **2020**, *27*, 551–557.

[212] B. Ravel, M. Newville, *J. Synchrotron Radiat.* **2005**, *12*, 537–541.

[213] A. Jentys, *Phys. Chem. Chem. Phys.* **1999**, *1*, 4059–4063.

[214] W. S. Epling, G. B. Hoflund, *J. Catal.* **1999**, *182*, 5–12.

[215] D. Ciuparu, M. R. Lyubovsky, E. Altman, L. D. Pfefferle, A. Datye, *Catal. Rev. - Sci. Eng.* **2002**, *44*, 593–649.

[216] T. R. Baldwin, R. Burch, *Appl. Catal.* **1990**, *66*, 337–358.

[217] K. Persson, A. Ersson, S. Colussi, A. Trovarelli, S. G. Järås, *Appl. Catal. B Environ.* **2006**, *66*, 175–185.

[218] A. Gremminger, P. Lott, M. Merts, M. Casapu, J. D. Grunwaldt, O. Deutschmann, *Appl. Catal. B Environ.* **2017**, *218*, 833– 843.

[219] M. Alyani, K. J. Smith, *Ind. Eng. Chem. Res.* **2016**, *55*, 8309–8318.

[220] H. Yoshida, R. Kakei, A. Fujiwara, Y. Uchida, M. Machida, *J. Phys. Chem. C* **2018**, *122*, 28173–28181.

[221] Y. H. C. Chin, M. García-Diéguez, E. Iglesia, *J. Phys. Chem. C* **2016**, *120*, 1446–1460.

[222] V. P. Zhdanov, B. Kasemo, *Chem. Phys. Lett.* **2008**, *452*, 285–288.

[223] A. K. Datye, J. Bravo, T. R. Nelson, P. Atanasova, M. Lyubovsky, L. Pfefferle, *Appl. Catal. A Gen.* **2000**, *198*, 179–196.

[224] J. G. McCarty, *Catal. Today* **1995**, *26*, 283–293.

[225] T. Engel, G. Ertl, *Adv. Catal.* **1979**, *28*, 1–78.

[226] M. Bowker, R. A. Bennett, I. Z. Jones, *Top. Catal.* **2004**, *28*, 25–30.

[227] O. Mihai, G. Smedler, U. Nylén, M. Olofsson, L. Olsson, *Catal. Sci. Technol.* **2017**, *7*, 3084–3096.

[228] D. Ciuparu, L. Pfefferle, *Appl. Catal. A Gen.* **2001**, *209*, 415–428.

[229] D. Ciuparu, L. Pfefferle, *Appl. Catal. A Gen.* **2001**, *218*, 197–209.

[230] P. A. Carlsson, M. Nordström, M. Skoglundh, *Top. Catal.* **2009**, *52*, 1962–1966.

[231] P.-A. Carlsson, P. Thormählen, M. Skoglundh, H. Persson, E. Fridell, E. Jobson, B. Andersson, *Top. Catal. 2001 161* **2001**, *16*, 343–347.

[232] P. Nevalainen, N. M. Kinnunen, A. Kirveslahti, K. Kallinen, T. Maunula, M. Keenan, M. Suvanto, *Appl. Catal. A Gen.* **2018**, *552*, 30–37.

[233] W. Bin Bae, D. Y. Kim, S. W. Byun, M. Hazlett, D. Y. Yoon, C. Jung, C. H. Kim, S. B. Kang, *Chem. Eng. J. Adv.* **2022**, *9*, 100222.

[234] J. H. Sinfelt, D. J. C J Catal, A. E. J Catal, *Phys. Rev. B Solid State* **1987**, *20*, 1361.

[235] J. A. Rodriguez, D. W. Goodman, *J. Phys. Chem.* **1991**, *95*, 4196–4206.

[236] J. A. Rodriguez, D. W. Goodman, *Acc. Chem. Res.* **1995**, *28*, 477–478.

[237] W. M. H. Sachtler, R. A. van Santen, *Adv. Catal.* **1977**, *26*, 69–119.

[238] J. A. Rodriguez, *Surf. Sci. Rep.* **1996**, *24*, 223–287.

[239] V. Ponec, *Adv. Catal.* **1983**, *32*, 149–214.

[240] W. M. H. Sachtler, R. A. van Santen, *Appl. Surf. Sci.* **1979**, *3*, 121–144.

[241] L. Guczi, *Catal. Today* **2005**, *101*, 53–64.

[242] S. Shan, V. Petkov, B. Prasai, J. Wu, P. Joseph, Z. Skeete, E. Kim, D. Mott, O. Malis, J. Luo, C. J. Zhong, *Nanoscale* **2015**, *7*, 18936–18948.

[243] H. Kobayashi, K. Kusada, H. Kitagawa, *Acc. Chem. Res.* **2015**, *48*, 1551–1559.

[244] H. Shang, Y. Wang, Y. Cui, R. Fang, W. Hu, M. Gong, Y. Chen, *Chinese J. Catal.* **2015**, *36*, 290–298.

[245] Y. Hilli, N. M. Kinnunen, M. Suvanto, A. Savimäki, K. Kallinen, T. A. Pakkanen, *Appl. Catal. A Gen.* **2015**, *497*, 85–95.

[246] A. Shipitcyna, N. M. Kinnunen, Y. Hilli, M. Suvanto, T. A. Pakkanen, *Top. Catal.* **2016**, *59*, 1097–1103.

[247] A. A. Vedyagin, A. M. Volodin, R. M. Kenzhin, V. O. Stoyanovskii, Y. V. Shubin, P. E. Plyusnin, I. V. Mishakov, *Catal. Today* **2017**, *293–294*, 73–81.

[248] T. Zheng, B. Lu, G. Harle, D. Yang, C. Wang, Y. Zhao, *Appl. Catal. A Gen.* **2020**, *602*, 117649.

[249] A. A. Vedyagin, A. M. Volodin, V. O. Stoyanovskii, R. M. Kenzhin, E. M. Slavinskaya, I. V. Mishakov, P. E. Plyusnin, Y. V. Shubin, *Catal. Today* **2014**, *238*, 80–86.

[250] F. Tao, M. E. Grass, Y. Zhang, D. R. Butcher, J. R. Renzas, Z. Liu, J. Y. Chung, B. S. Mun, M. Salmeron, G. A. Somorjai, *Science.* **2008**, *322*, 932–934.

[251] H. S. Gandhi, G. W. Graham, R. W. McCabe, in *J. Catal.*, **2003**, *216,* 433–442.

[252] S. Roy, M. S. Hegde, G. Madras, *Appl. Energy* **2009**, *86*, 2283–2297.

[253] T. Maillet, J. Barbier, D. Duprez, P. Gelin, H. Praliaud, *J. Catal.* **2001**, *202*, 367–378.

[254] V. O. Stoyanovskii, A. A. Vedyagin, G. I. Aleshina, A. M. Volodin, A. S. Noskov, *Appl. Catal. B Environ.* **2009**, *90*, 141–146.

[255] H. C. Yao, S. Japar, M. Shelef, *J. Catal.* **1977**, *50*, 407–418.

[256] A. A. Vedyagin, V. O. Stoyanovskii, P. E. Plyusnin, Y. V. Shubin, E. M. Slavinskaya, I. V. Mishakov, *J. Alloys Compd.* **2018**, *749*, 155–162.

[257] H. C. Yao, H. K. Stepien, H. S. Gandhi, *J. Catal.* **1980**, *61*, 547–550.

[258] F. Tao, M. E. Grass, Y. Zhang, D. R. Butcher, F. Aksoy, S. Aloni, V. Altoe, S. Alayoglu, J. R. Renzas, C. K. Tsung, Z. Zhu, Z. Liu, M. Salmeron, G. A. Somorjai, *J. Am. Chem. Soc.* **2010**, *132*, 8697–8703.

[259] F. Bernardi, M. E. Grass, Y. P. Hong, R. Chang, N. Jabeen, C. Zhang, B. W. Eichhorn, B. Seo, S. Alayoglu, Z. Hussain, S. H. Joo, Z. Liu, *Catal. Today* **2016**, *260*, 95–99.

[260] H. Kondoh, R. Toyoshima, N. Shirahata, A. Hoda, M. Yoshida, K. Amemiya, K. Mase, B. S. Mun, *Phys. Chem. Chem. Phys.* **2018**, *20*, 28419–28424.

[261] J. R. Renzas, W. Huang, Y. Zhang, M. E. Grass, G. A. Somorjai, *Catal. Letters* **2011**, *141*, 235–241.

[262] J. Sá, G. D. Arteaga, R. A. Daley, J. Bernardi, J. A. Anderson, *J. Phys. Chem. B* **2006**, *110*, 17090–17095.

[263] E. Groppo, G. Agostini, A. Piovano, N. B. Muddada, G. Leofanti, R. Pellegrini, G. Portale, A. Longo, C. Lamberti, *J. Catal.* **2012**, *287*, 44–54.

[264] G. Goula, G. Botzolaki, A. Osatiashtiani, C. M. A. Parlett, G. Kyriakou, R. M. Lambert, I. V. Yentekakis, *Catal.* **2019**, *9*, 541.

[265] Q. Zheng, R. Farrauto, M. Deeba, I. Valsamakis, *Catal.* **2015**, *5*, 1770–1796.

[266] M. Machida, Y. Uchida, Y. Ishikawa, S. Hinokuma, H. Yoshida, J. Ohyama, Y. Nagao, Y. Endo, K. Iwashina, Y. Nakahara, *J. Phys. Chem. C* **2019**, *123*, 24584–24591.

[267] R. Burch, P. K. Loader, N. A. Cruise, *Appl. Catal. A, Gen.* **1996**, *2*, 375–394.

[268] H. Shinjoh, H. Muraki, Y. Fujitani, *Stud. Surf. Sci. Catal.* **1991**, *71*, 617–628.

[269] M. Shelef, G. W. Graham, *Catal. Reviews* **2006**, *36*, 433–457.

[270] Q. Xu, K. C. Kharas, B. J. Croley, A. K. Datye, *ChemCatChem* **2011**, *3*, 1004–1014.

[271] M. Machida, *Chem. Rec.* **2016**, *16*, 2219–2231.

[272] C. H. Li, J. Wu, A. B. Getsoian, G. Cavataio, J. R. Jinschek, *Chem. Mater.* **2022**, *34*, 2123–2132.

[273] P. A. Crozier, A. K. Datye, *Stud. Surf. Sci. Catal.* **2000**, *130*, 3119–3124.

[274] M. P. Seah, *Surf. Interface Anal.* **1980**, *2*, 222–239.

[275] S. Hagström, C. Nordling, K. Siegbahn, *Zeitschrift für Phys.* **1964**, *178*, 439–444.

[276] A. R. Head, S. Nemšák, B. Eren, Eds. *ACS Symposium series,* **2021**, *1396*.

[277] M. Salmeron, *Top. Catal.* **2018**, *61*, 2044–2051.

[278] K. Roy, L. Artiglia, J. A. van Bokhoven, *ChemCatChem* **2018**, *10*, 666–682.

[279] E. J. Crumlin, Z. Liu, H. Bluhm, W. Yang, J. Guo, Z. Hussain, *J. Electron Spectros. Relat. Phenomena* **2015**, *200*, 264–273.

[280] D. E. Starr, Z. Liu, M. Hävecker, A. Knop-Gericke, H. Bluhm, *Chem. Soc. Rev.* **2013**, *42*, 5833–5857.

[281] J. A. Rodriguez, J. C. Hanson, P. J. Chupas, *Wiley,* **2013.**

[282] F. Aksoy, M. E. Grass, S. H. Joo, N. Jabeen, Y. P. Hong, Z. Hussain, B. S. Mun, Z. Liu, *Nucl. Instruments Methods Phys. Res. Sect. A Accel. Spectrometers, Detect. Assoc. Equip.* **2011**, *645*, 260–265.

[283] H. Bluhm, *J. Electron Spectros. Relat. Phenomena* **2010**, *177*, 71–84.

[284] K. F. Kalz, R. Kraehnert, M. Dvoyashkin, R. Dittmeyer, R. Gläser, U. Krewer, K. Reuter, J. D. Grunwaldt, *ChemCatChem* **2017**, *9*, 17–29.

[285] F. Orlando, A. Waldner, T. Bartels-Rausch, M. Birrer, S. Kato, M. T. Lee, C. Proff, T. Huthwelker, A. Kleibert, J. Van Bokhoven, M. Ammann, *Top. Catal.* **2016**, *59*, 591–604.

[286] A. R. Head, *ACS Symp. Ser.* **2021**, *1396*, 19–37.

[287] H. Kondoh, R. Toyoshima, Y. Monya, M. Yoshida, K. Mase, K. Amemiya, B. S. Mun, *Catal. Today* **2016**, *260*, 14–20.

[288] R. Toyoshima, M. Yoshida, Y. Monya, K. Suzuki, B. S. Mun, K. Amemiya, K. Mase, H. Kondoh, *J. Phys. Chem. Lett.* **2012**, *3*, 3182–3187.

[289] S. Blomberg, U. Hejral, M. Shipilin, S. Albertin, H. Karlsson, C. Hulteberg, P. Lömker, C. Goodwin, D. Degerman, J. Gustafson, C. Schlueter, A. Nilsson, E. Lundgren, P. Amann, *ACS Catal.* **2021**, *11*, 9128–9135.

[290] R. Toyoshima, M. Yoshida, Y. Monya, Y. Kousa, K. Suzuki, H. Abe, B. S. Mun, K. Mase, K. Amemiya, H. Kondoh, *J. Phys. Chem. C* **2012**, *116*, 18691–18697.

[291] R. Westerström, M. E. Messing, S. Blomberg, A. Hellman, H. Grönbeck, J. Gustafson, N. M. Martin, O. Balmes, R. Van Rijn, J. N. Andersen, K. Deppert, H. Bluhm, Z. Liu, M. E. Grass, M. Hävecker, E. Lundgren, *Phys. Rev. B - Condens. Matter Mater. Phys.* **2011**, *83*, 115440.

[292] H. Gabasch, W. Unterberger, K. Hayek, B. Klötzer, G. Kresse, C. Klein, M. Schmid, P. Varga, *Surf. Sci.* **2006**, *600*, 205–218.

[293] E. Lundgren, G. Kresse, C. Klein, M. Borg, J. N. Andersen, M. De Santis, Y. Gauthier, C. Konvicka, M. Schmid, P. Varga, *Phys. Rev. Lett.* **2002**, *88*, 246103.

[294] M. A. Van Spronsen, J. W. M. Frenken, I. M. N. Groot, *Chem. Soc. Rev.* **2017**, *46*, 4347–4374.

[295] K. Zorn, S. Giorgio, E. Halwax, C. R. Henry, H. Grönbeck, G. Rupprechter, *J. Phys. Chem. C* **2011**, *115*, 1103–1111.

[296] H. Gabasch, W. Unterberger, K. Hayek, B. Klötzer, E. Kleimenov, D. Teschner, S. Zafeiratos, M. Hävecker, A. Knop- Gericke, R. Schlögl, J. Han, F. H. Ribeiro, B. Aszalos-Kiss, T. Curtin, D. Zemlyanov, *Surf. Sci.* **2006**, *600*, 2980–2989.

[297] D. Zemlyanov, B. Aszalos-Kiss, E. Kleimenov, D. Teschner, S. Zafeiratos, M. Hävecker, A. Knop-Gericke, R. Schlögl, H. Gabasch, W. Unterberger, K. Hayek, B. Klötzer, *Surf. Sci.* **2006**, *600*, 983–994.

[298] M. M. Khader, M. J. Al-Marri, S. Ali, A. G. Abdelmoneim, *Catal. 2018, Vol. 8, Page 66* **2018**, *8*, 66.

[299] G. Chen, Y. Yang, Z. Guo, D. Gao, W. Zhao, H. Yan, W. W. Wang, C. J. Jia, G. Sun, *Catal. Sci. Technol.* **2018**, *8*, 4413–4419.

[300] A. J. Hill, C. Y. Seo, X. Chen, A. Bhat, G. B. Fisher, A. Lenert, J. W. Schwank, *ACS Catal.* **2020**, *10*, 1731–1741.

[301] S. Fazlikeshteli, X. Vendrell, J. Llorca, *React.* **2021**, *2*, 30–42.

[302] L. S. Kibis, A. I. Stadnichenko, S. V. Koscheev, V. I. Zaikovskii, A. I. Boronin, *J. Phys. Chem. C* **2012**, *116*, 19342–19348.

[303] J. Kappler, N. Bârsan, U. Weimar, A. Dièguez, J. L. Alay, A. Romano-Roclriguez, J. R. Morante, W. Göpel, *Fresenius' J. Anal. Chem.* **1998**, *361*, 110–114.

[304] L. S. Kibis, A. I. Titkov, A. I. Stadnichenko, S. V. Koscheev, A. I. Boronin, *Appl. Surf. Sci.* **2009**, *255*, 9248–9254.

[305] F. Yin, S. Ji, P. Wu, F. Zhao, C. Li, *J. Catal.* **2008**, *257*, 108–116.

[306] A. S. Ivanova, E. M. Slavinskaya, R. V. Gulyaev, V. I. Zaikovskii, O. A. Stonkus, I. G. Danilova, L. M. Plyasova, I. A. Polukhina, A. I. Boronin, *Appl. Catal. B Environ.* **2010**, *97*, 57–71.

[307] A. Aznárez, A. Gil, S. A. Korili, *RSC Adv.* **2015**, *5*, 82296–82309.

[308] B. Ealet, E. Gillet, *Surf. Sci.* **1993**, *281*, 91–101.

[309] B. Ealet, E. Gillet, *Surf. Sci.* **1996**, *367*, 221–230.

[310] K. Sun, J. Liu, N. Nag, N. D. Browning, *Catal. Lett.* **2002**, *84*, 193–199.

[311] G. Ketteler, D. F. Ogletree, H. Bluhm, H. Liu, E. L. D. Hebenstreit, M. Salmeron, *J. Am. Chem. Soc.* **2005**, *127*, 18269–18273.

[312] K. Reuter, M. Scheffler, *Appl. Phys. A* **2004**, *78*, 793–798.

[313] H. Gabasch, A. Knop-Gericke, R. Schlögl, M. Borasio, C. Weilach, G. Rupprechter, S. Penner, B. Jenewein, K. Hayek, B. Klötzer, *Phys. Chem. Chem. Phys.* **2007**, *9*, 533–540.

[314] Z. N. Schmahl and E. Minzl, *Phys. Chem.* **1975**, *47*, 547.

[315] I. Alxneit, A. Garbujo, G. Carollo, D. Ferri, A. Glisenti, *Phys. Chem. Chem. Phys.* **2020**, *22*, 18798–18805.

[316] Y. Nagai, K. Dohmae, Y. F. Nishimura, H. Kato, H. Hirata, N. Takahashi, *Phys. Chem. Chem. Phys.* **2013**, *15*, 8461–8465.

Appendices

Appendix A (Chapter 3)

Experimental section

Results

Material properties

Table A1. Physico-chemical properties of the Pd/Al$_2$O$_3$ catalyst calcined, hydrothermally aged (HT), and thermally aged (T).

Sample	S$_{BET}$ [m^{2}g^{-1}]	d$_{particle}$ (TEM) [nm]	d$_{particle}$ (EXAFS) [nm]
Pd/Al$_2$O$_3$ (calcined)	128	7.6 ± 1.9	9.6
Pd/Al$_2$O$_3$ (HT)	124	10.0 ± 2.9	n.a.
Pd/Al$_2$O$_3$ (T)	112	9.2 ± 2.4	n.a.

Temperature programmed reduction of calcined Pd/Al$_2$O$_3$

Temperature programmed reduction with CH$_4$ (CH4-TPR) was conducted in the same reactor as the catalytic tests. In brief, 50 mg of catalysts (sieve fraction 150 - 200 µm) mixed with 150 mg of cordierite (sieve fraction 100 - 150 µm) were placed in the reactor. CH$_4$-TPR was performed in a flow of 1 vol% CH$_4$ and 10 vol% H$_2$O (balance Ar) at a total WHSV of 120 L·h^{-1}·g^{-1}. The temperature was raised by 5 °Cmin^{-1} while analysing the effluent gases using a mass spectrometer.

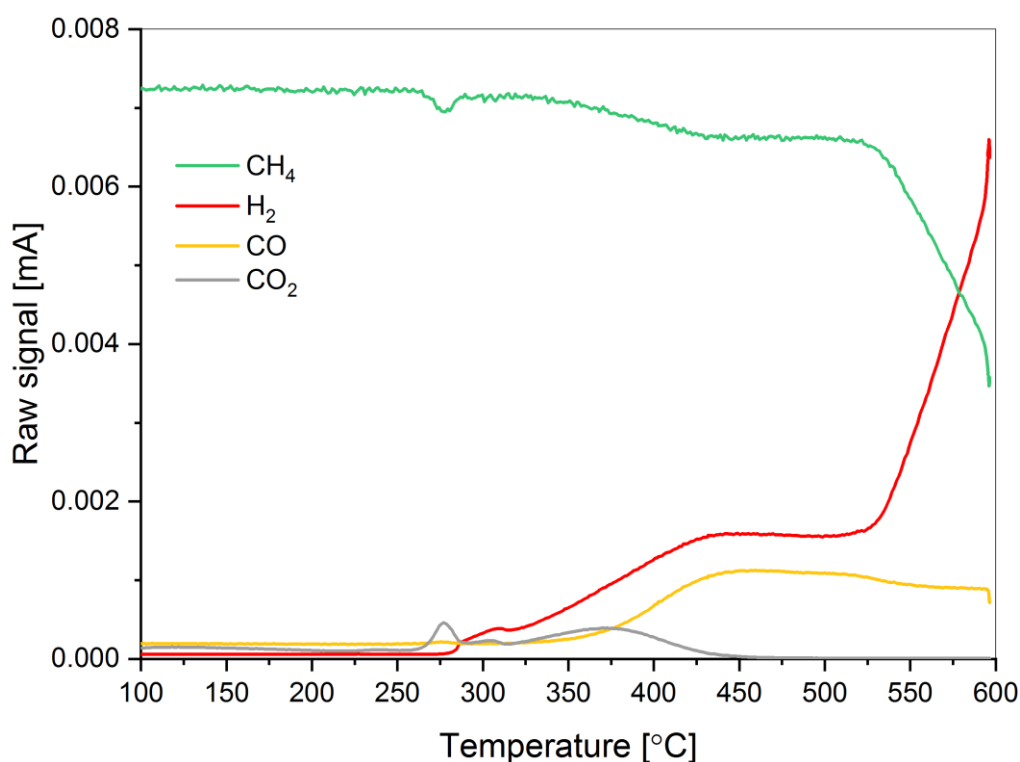

Figure A1. MS data of signals (m/z= 2: H$_2$, 15: CH$_4$, 28: CO, 44: CO$_2$) obtained during temperature-programmed reduction of calcined Pd/Al$_2$O$_3$ with 1 vol% CH$_4$ in the presence of 10 vol% H$_2$O; balance, Ar; WHSV = 120 Lh^{-1}g^{-1}, ΔT = 5 °Cmin^{-1}.
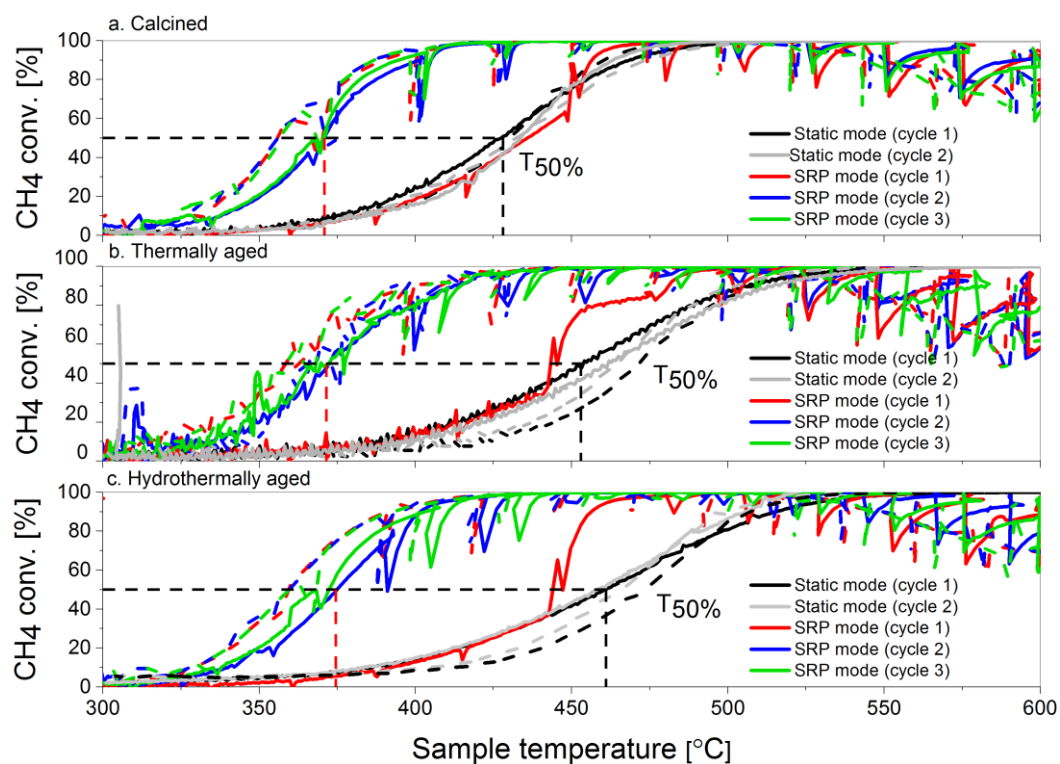
Catalytic activity evaluation

Figure A2. CH$_4$ conversion obtained from ascending (—) and descending (- -) linear temperature ramps under static and SRP wet lean conditions over 2 wt% Pd/Al$_2$O$_3$. a. Calcined, b. thermally aged, and c. hydrothermally aged. The dashed lines represent T$_{50\%}$ in static (black) and SRP (red) mode. Conditions: 1 vol% CH$_4$, 4 vol% O$_2$, 10 vol% H$_2$O; WHSV = 120 Lh^{-1}g^{-1}.
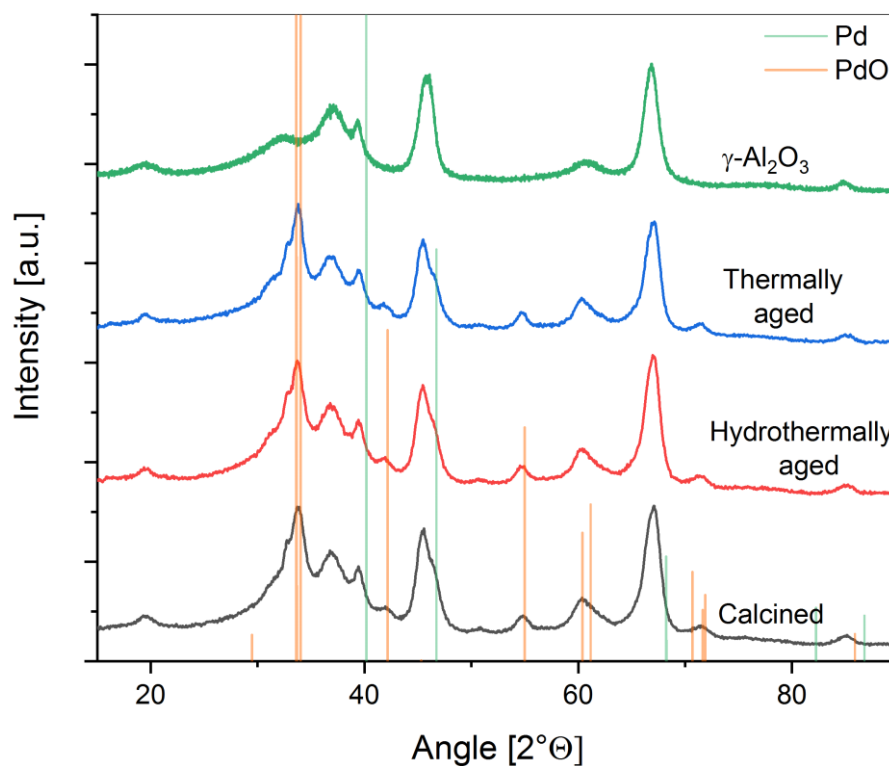
XRD of Pd/Al₂O₃ samples

Figure A3. Powder X-ray diffraction of unused Pd/Al₂O₃ calcined, hydrothermally aged, and thermally aged, as well as the support, γ-Al₂O₃, before impregnation. Pd and PdO reflections are shown in green and orange respectively.
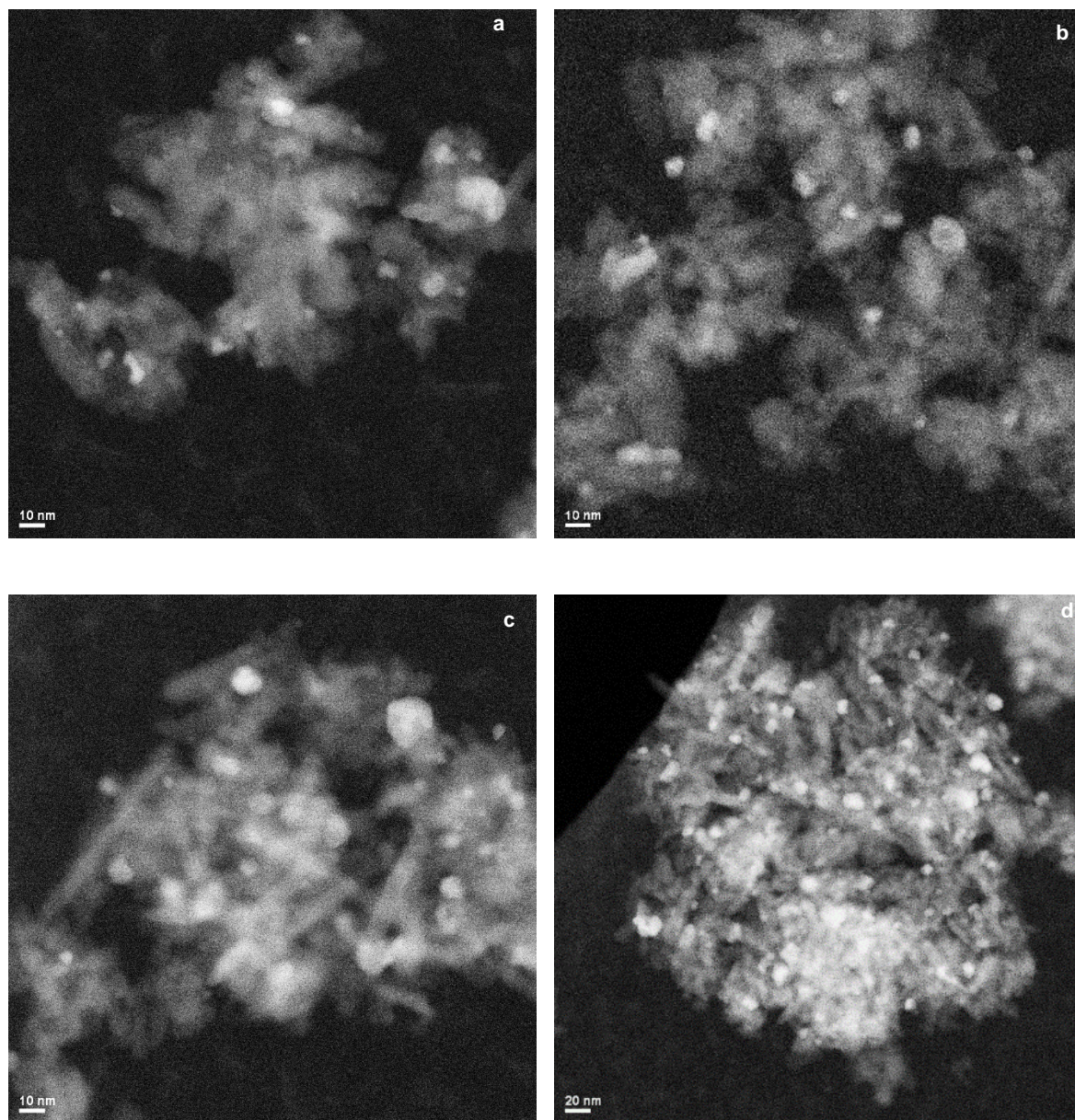
HAADF-STEM of all unused samples

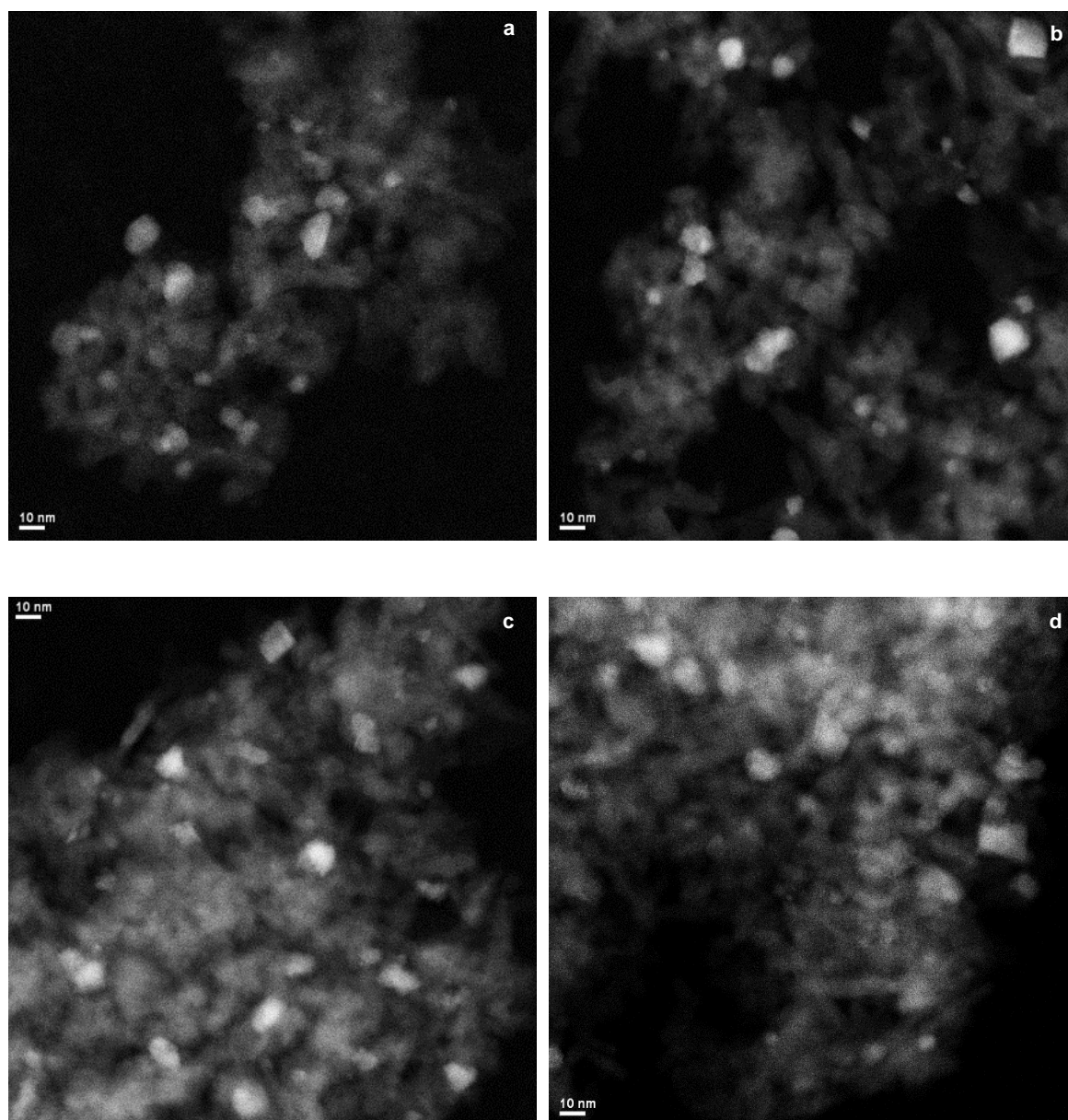Figure A4. Calcined 2 wt% Pd/Al₂O₃ unused.

Figure A5. Hydrothermally treated 2 wt% Pd/Al$_2$O$_3$ unused.
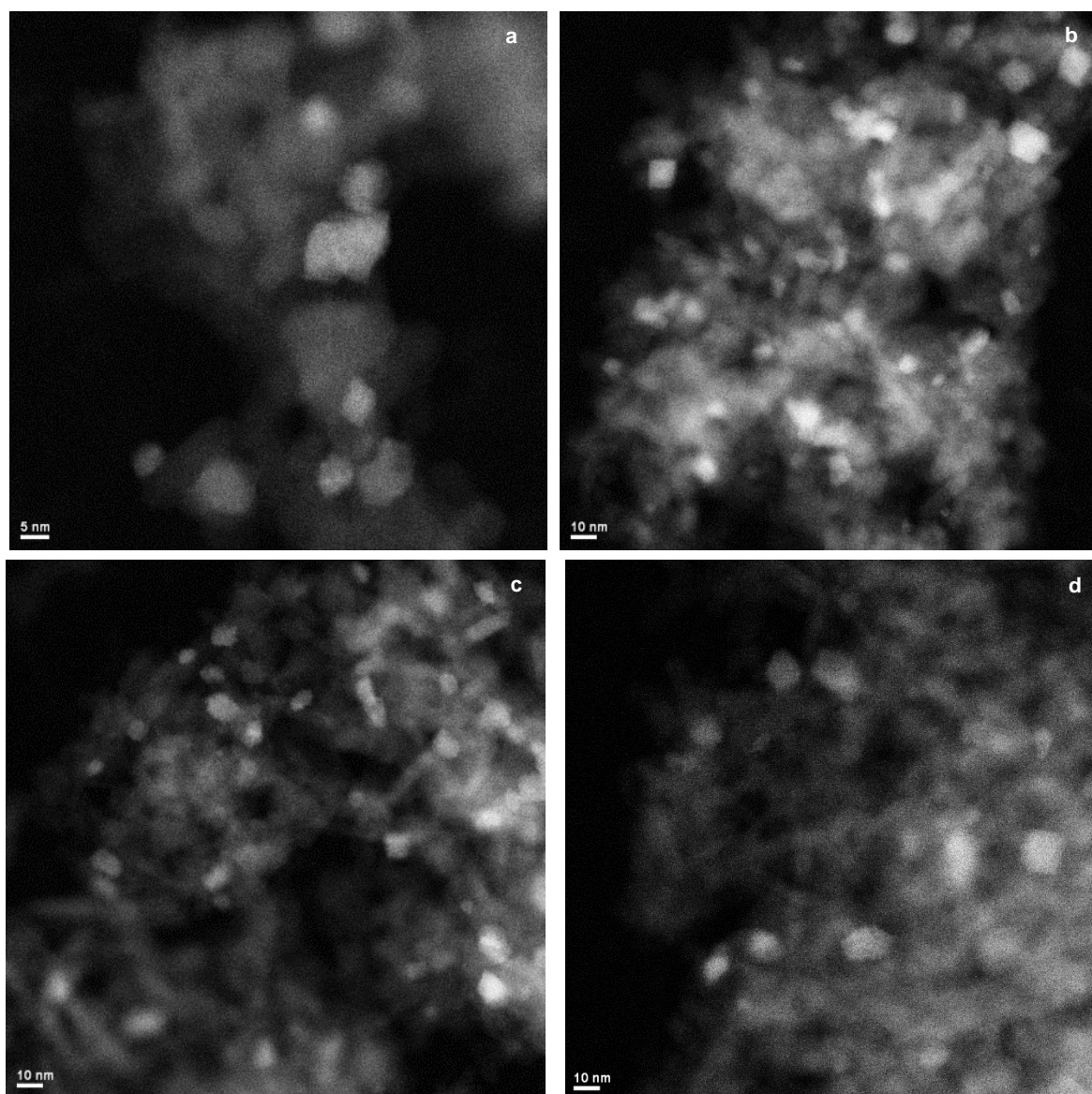
Figure A6. Thermally treated 2 wt% Pd/Al$_2$O$_3$, unused.

Effect of temperature on SRP
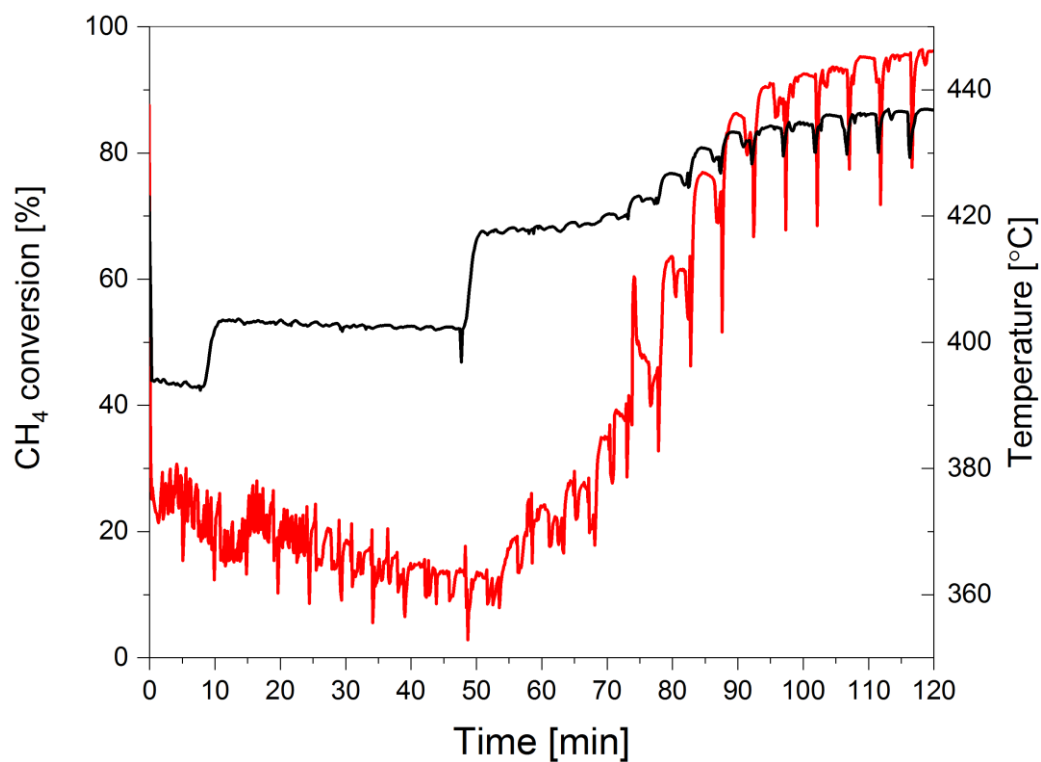
Figure A7. Temperature increase (black) to obtain activation by SRP observed from CH_4 conversion (red) on calcined Pd/Al_2O_3. Conditions: 1 vol% CH_4, 4 vol% O_2, 10 vol% H_2O; WHSV = 120 $Lh^{-1}g^{-1}$.

Effect of SRP at different temperatures
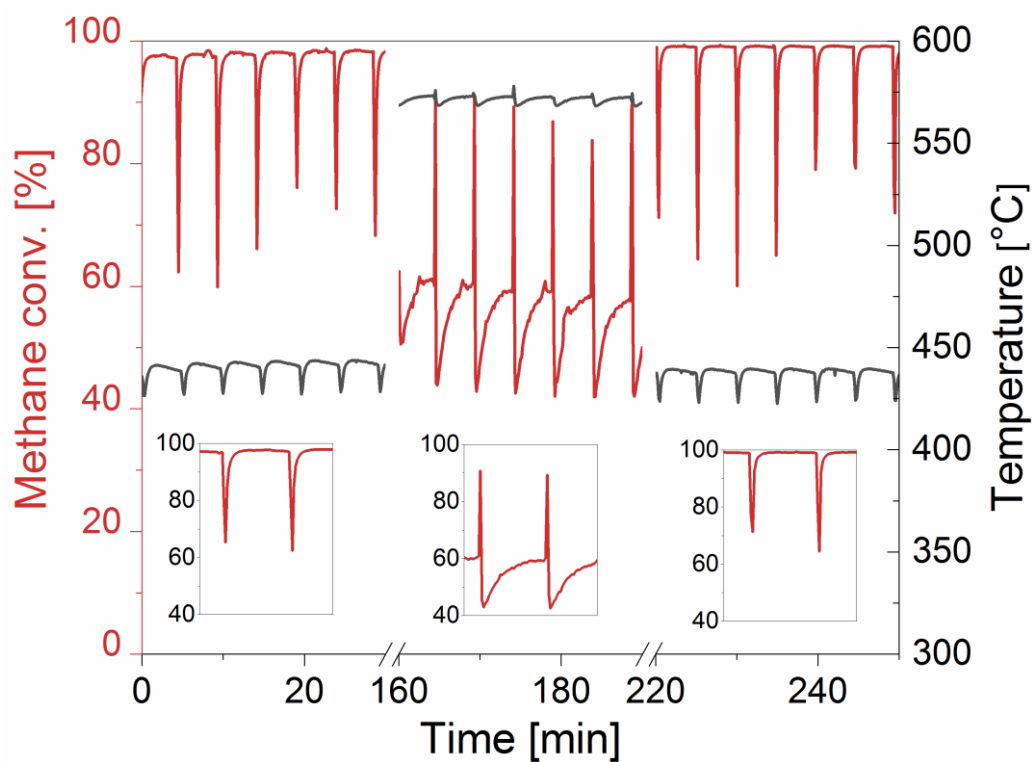

Figure A8. Methane conversion over calcined Pd/Al$_2$O$_3$ in SRP lean operation. Conditions: 1 vol% CH$_4$, 4 vol% O$_2$, 10 vol% H$_2$O; WHSV = 360 Lh^{-1}g^{-1}.

Effect of space velocity
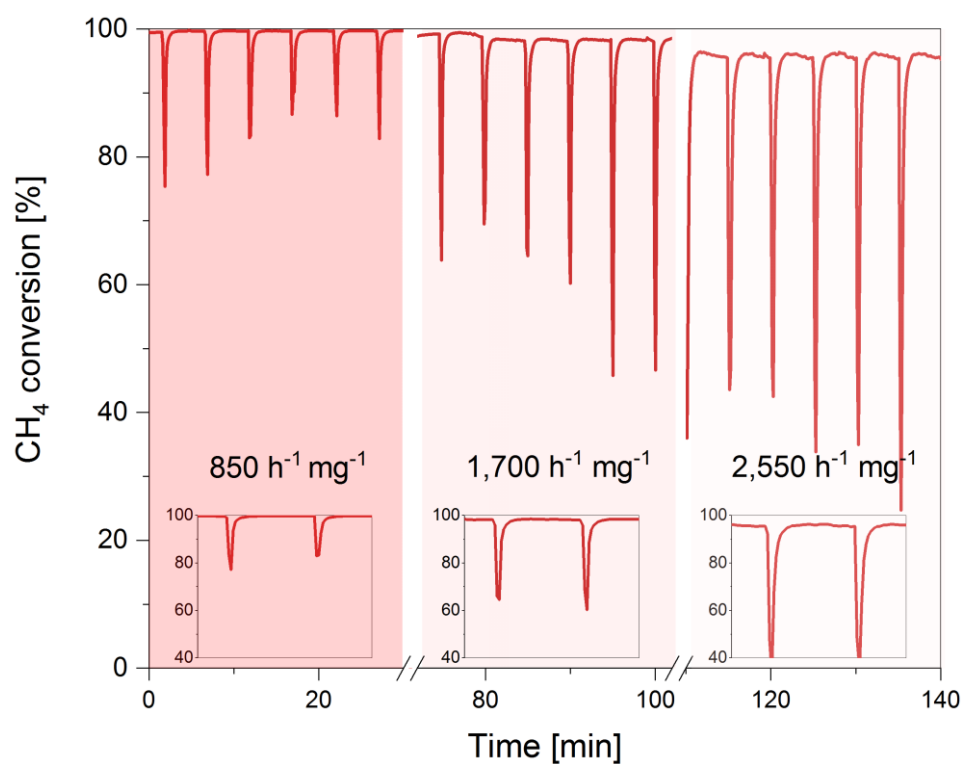
Figure A9. CH₄ conversion obtained at increasing WHSV: 120, 240, and 360 Lh⁻¹g⁻¹ at 435 C over calcined Pd/Al₂O₃ in SRP mode. Conditions: 1 vol% CH₄, 4 vol% O₂, 10 vol% H₂O.

XRD of all samples

XRD of calcined Pd/Al₂O₃

Figure A10. Powder X-ray diffraction of calcined Pd/Al$_2$O$_3$ unused and after use for 16 h at 435 C under static and SRP mode, as well as the support, γ-Al$_2$O$_3$, before impregnation. Pd and PdO reflections are shown in green and orange respectively. Reaction conditions: 1 vol% CH$_4$, 4 vol% O$_2$, 10 vol% H$_2$O; WHSV = 120 Lh^{-1}g^{-1}.

XRD of hydrothermally aged Pd/Al₂O₃
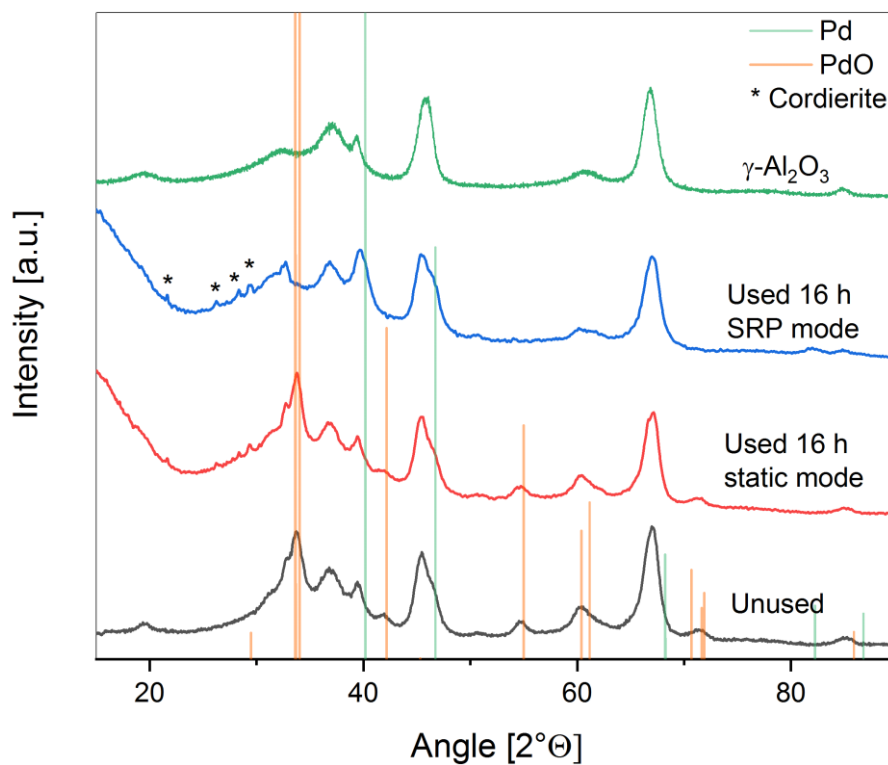
Figure A11. Powder X-ray diffraction of hydrothermally aged Pd/Al$_2$O$_3$ unused and after use for 16 h at 435 C under static and SRP mode, as well as the support, γ-Al$_2$O$_3$, before impregnation. Pd and PdO reflections are shown in green and orange respectively. Reaction conditions: 1 vol% CH$_4$, 4 vol% O$_2$, 10 vol% H$_2$O; WHSV = 120 Lh^{-1}g^{-1}.
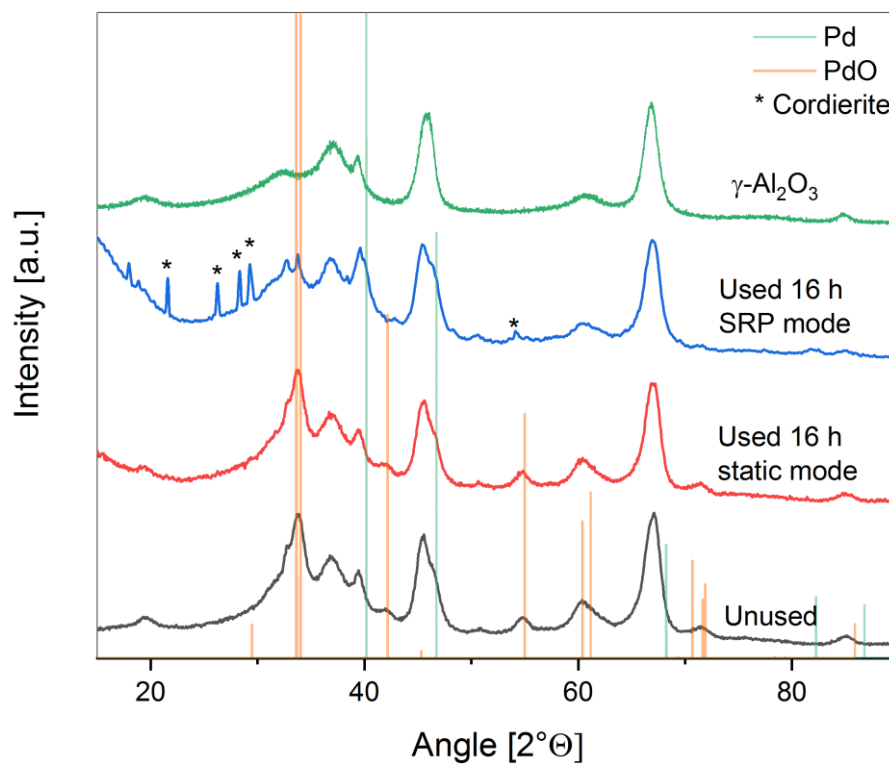
XRD of thermally aged Pd/Al₂O₃
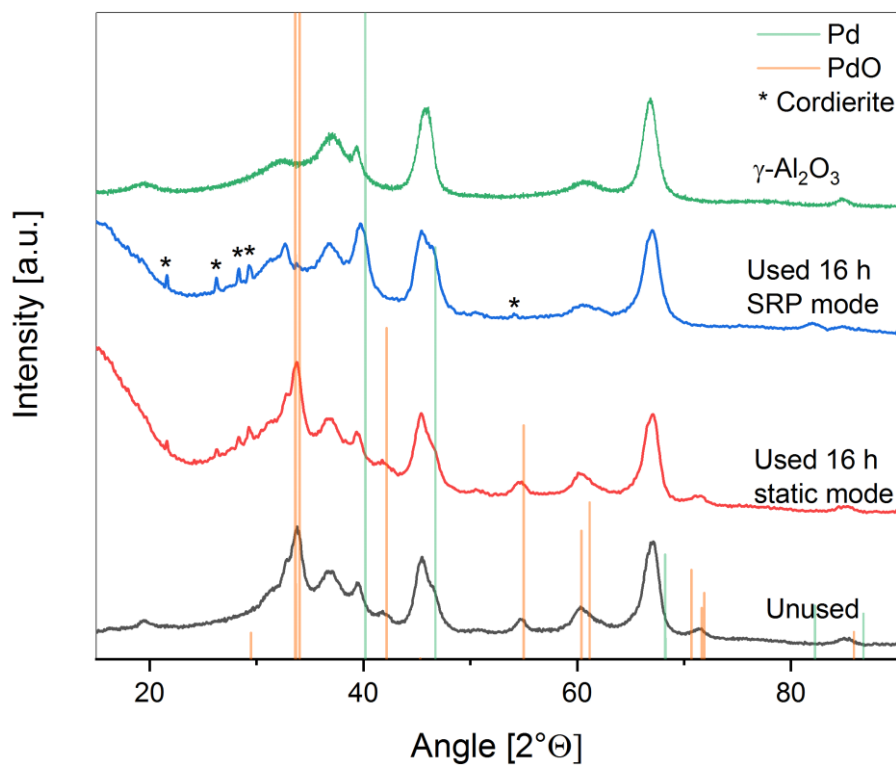
Figure A12. Powder X-ray diffraction of thermally aged Pd/Al$_2$O$_3$ unused and after use for 16 h at 435 C under static and SRP mode, as well as the support, γ-Al$_2$O$_3$, before impregnation. Pd and PdO reflections are shown in green and orange respectively. Reaction conditions: 1 vol% CH$_4$, 4 vol% O$_2$, 10 vol% H$_2$O; WHSV = 120 Lh^{-1}g^{-1}.

HAADF-STEM of all samples after SRP operation
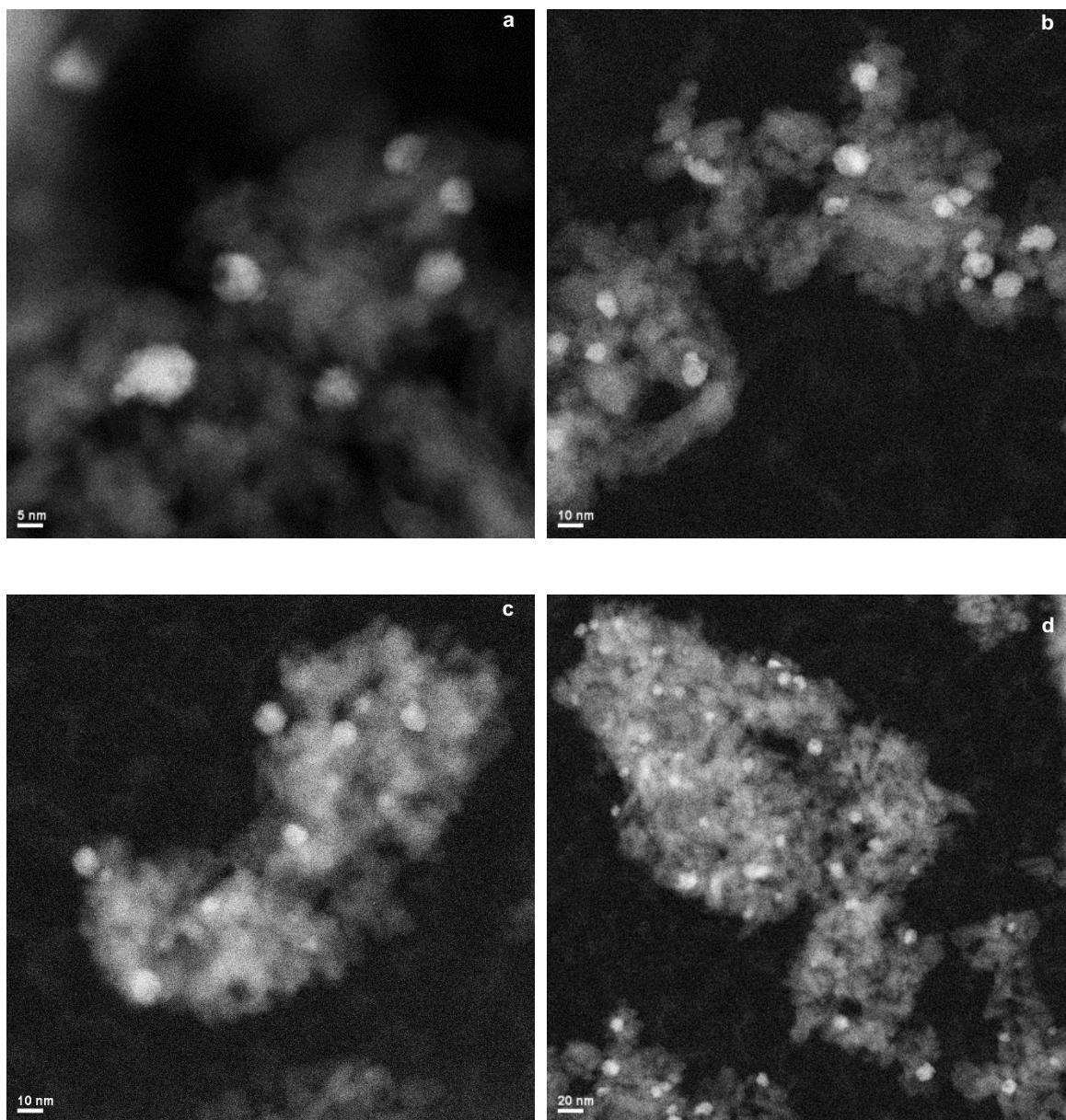
Figure A13. Calcined 2 wt% Pd/Al$_2$O$_3$ after SRP operation.
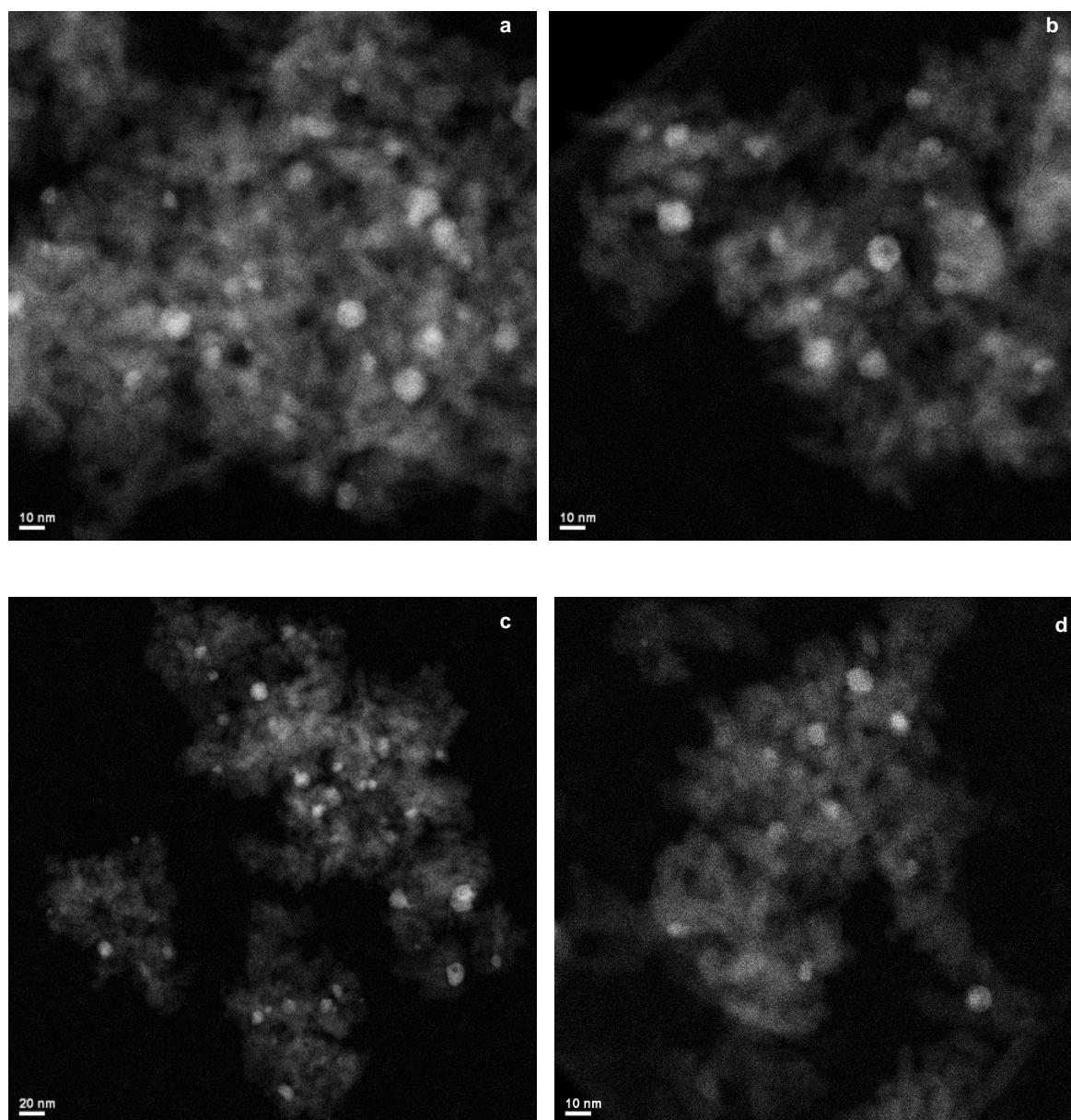
Figure A14. Hydrothermally treated 2 wt% Pd/Al$_2$O$_3$ after SRP operation.
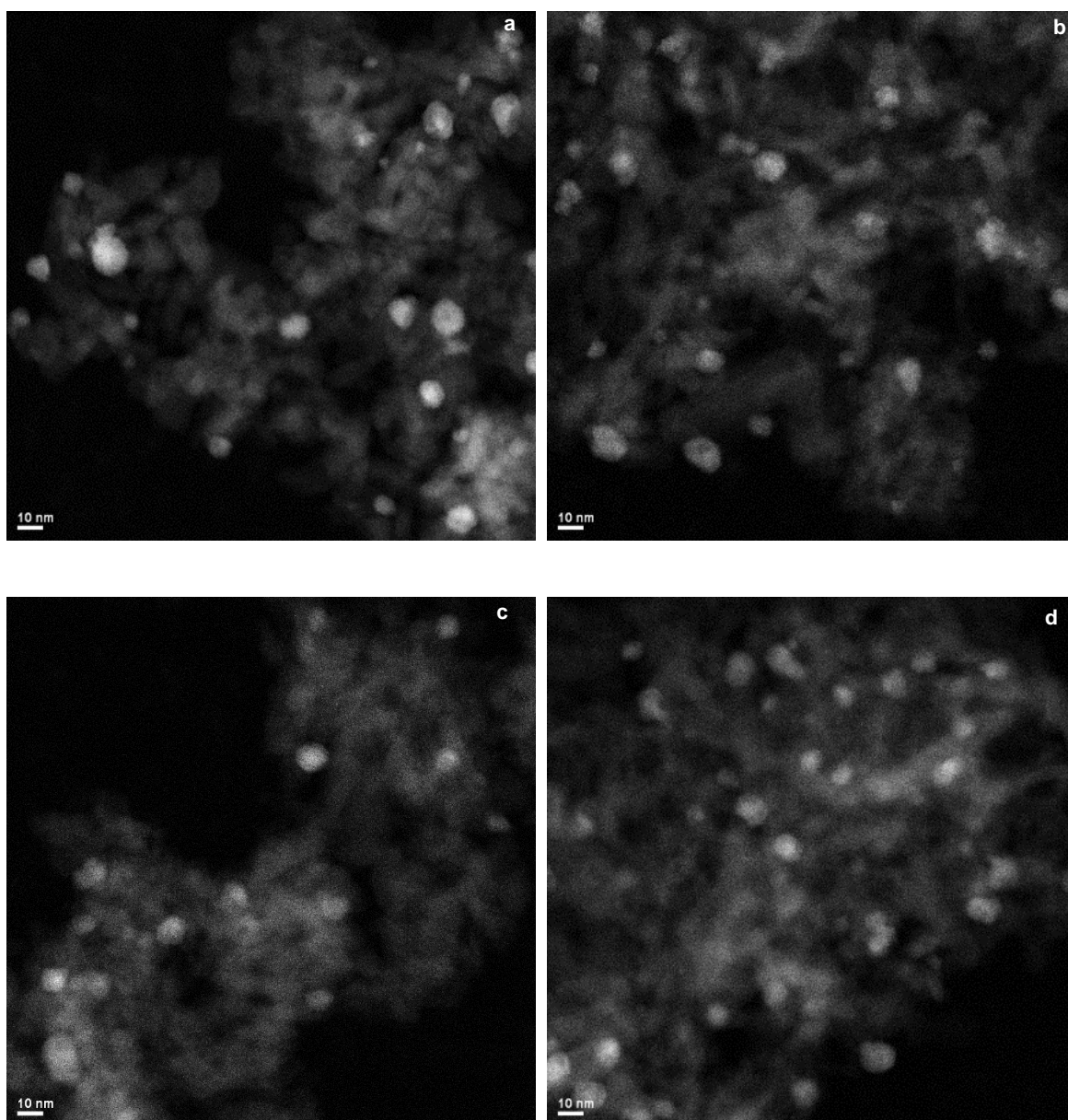
Figure A15. Thermally treated 2 wt% Pd/Al$_2$O$_3$ after SRP operation.

Particle size distribution of all samples after calcination
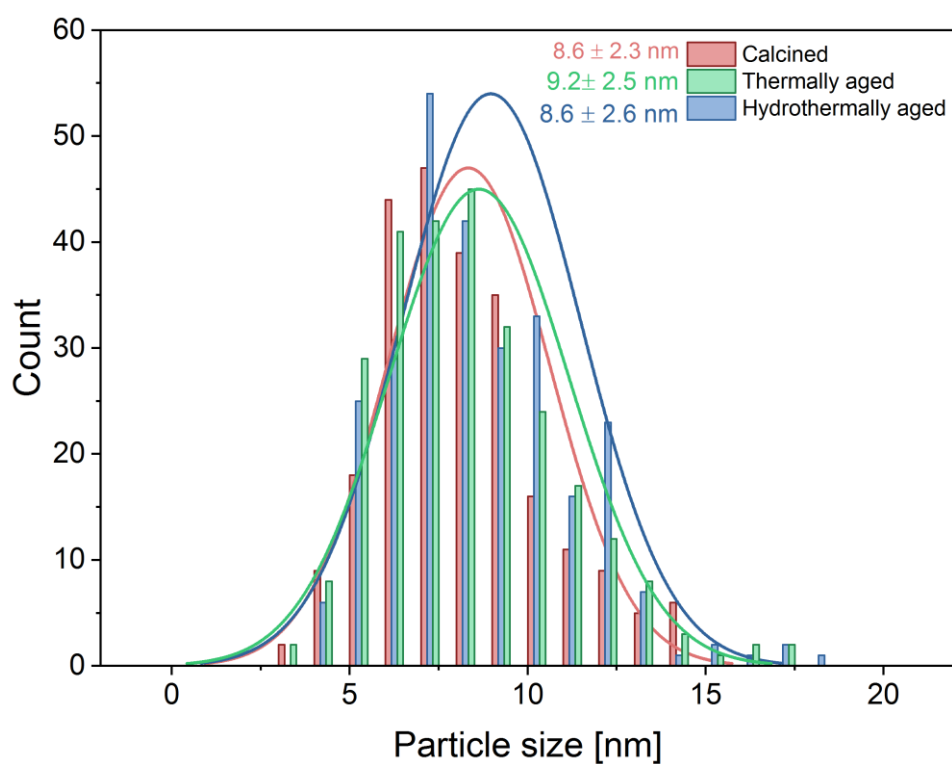
Figure A16. Particle size distribution of all samples after calcination.

Particle size distribution of all samples after SRP operation
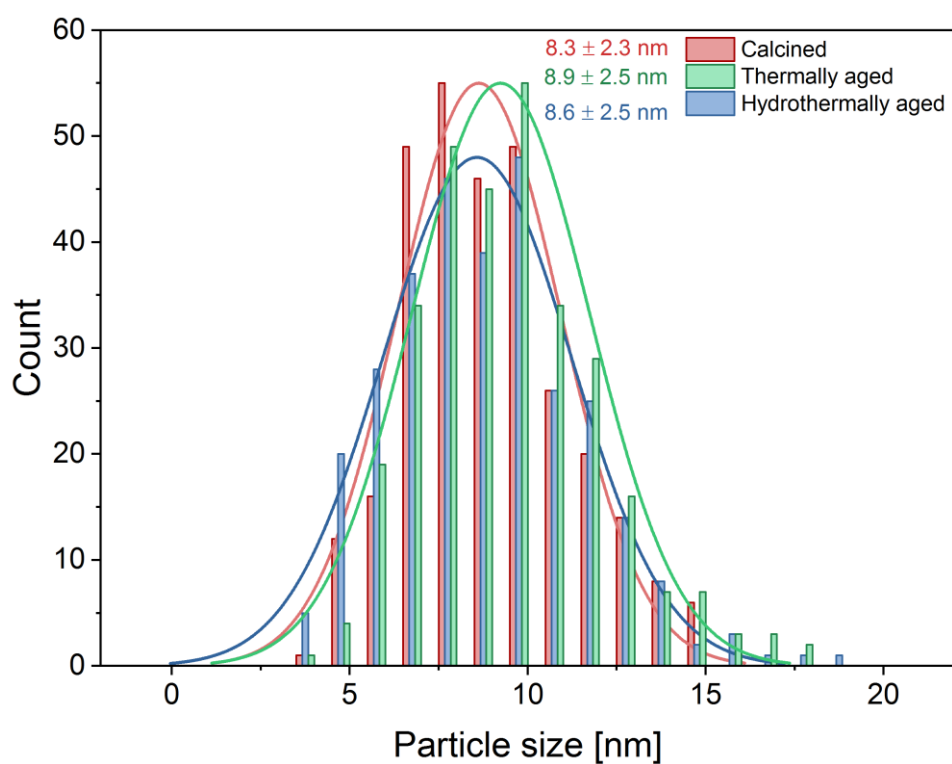
Figure A17. Particle size distribution of all samples after SRP operation.

FT-EXAFS
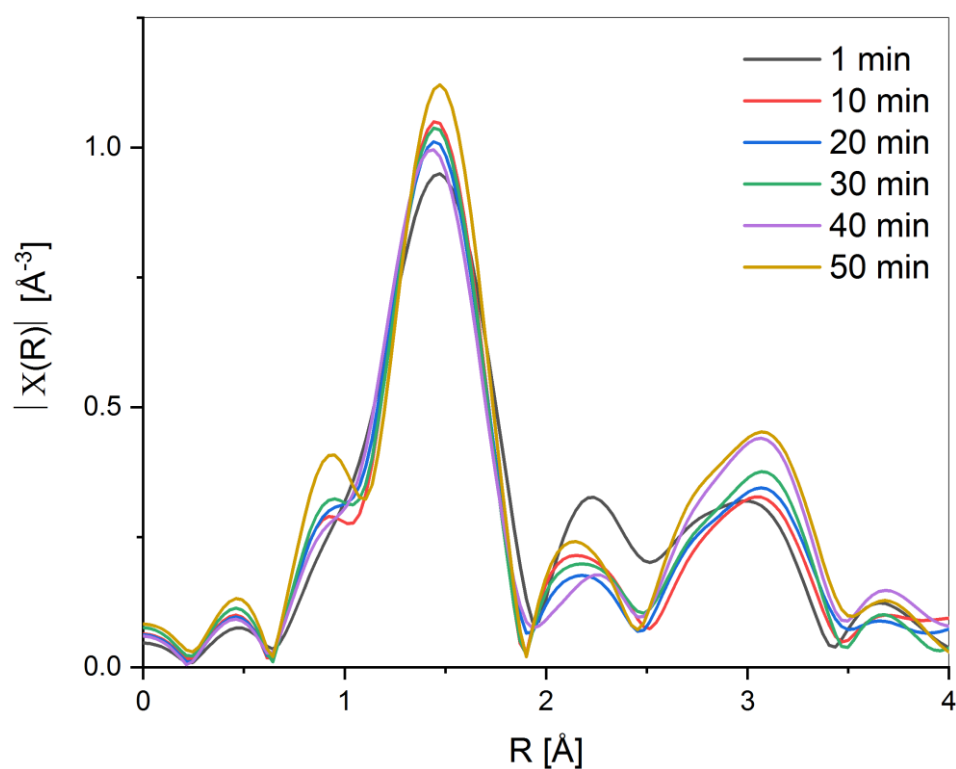
Figure A18. Pd K-edge FT-XAFS (not phase corrected) for calcined Pd/Al_2O_3 illustrating the change of intensities of Pd-Pd and Pd-O scattering path in PdO over time at static reaction conditions at 435°C as a qualitative measure for increasing crystallinity.

Effect of water on activity and Pd oxidation state
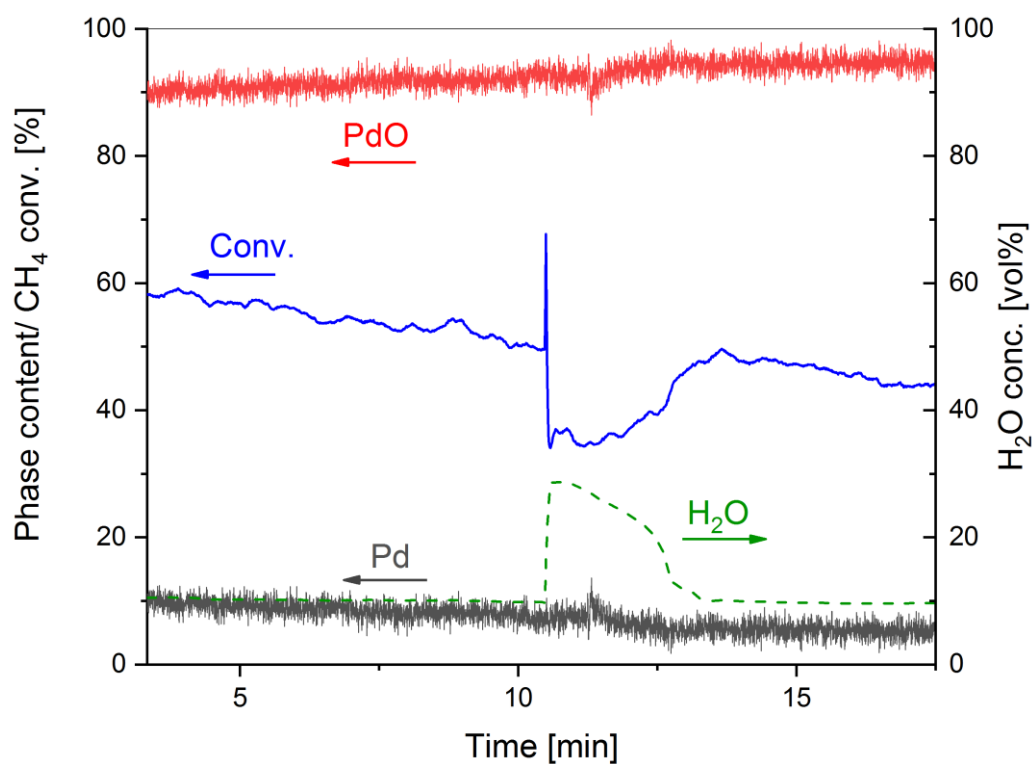
Figure A19. Effect of water concentration on CH_4 conversion (blue) and Pd phase content (PdO (red) / Pd (black)) of calcined Pd/Al_2O_3 under lean static conditions at 435 °C. Conditions: 1 vol% CH_4, 4 vol% O_2, 10 vol% H_2O; WHSV = 360 $Lh^{-1}g^{-1}$.

Fitting of the different kinetic models
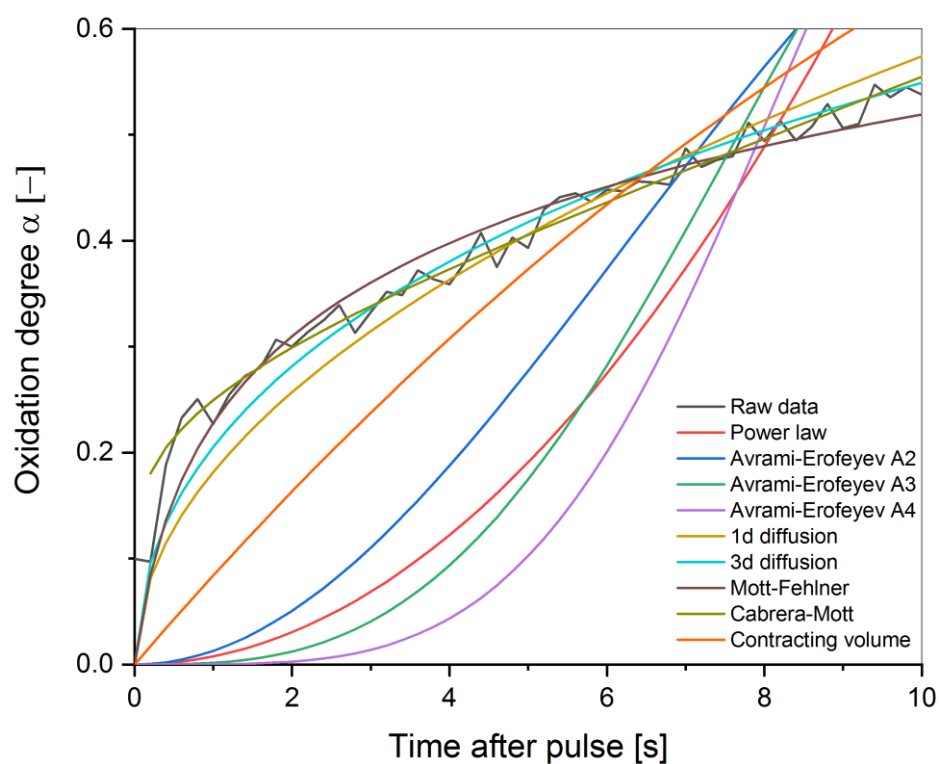
Figure A20. Fitting of the different oxidation mechanisms with the raw data of oxidation degree directly after the SRP obtained from LCF-analysis of the Pd K-edge XAS spectra.

EXAFS fitting

Table A2. Results of Pd K-edge EXAFS fitting of the Pd-Reference foil for determination of the amplitude reduction factor (amp).

Reference	Phase	Path	R-factor	CN	Amp	E_0 [eV]	r [Å]	σ^2
Pd-foil	Pd	Pd-Pd	0.008	12	0.78	-6.06	2.74	0.005
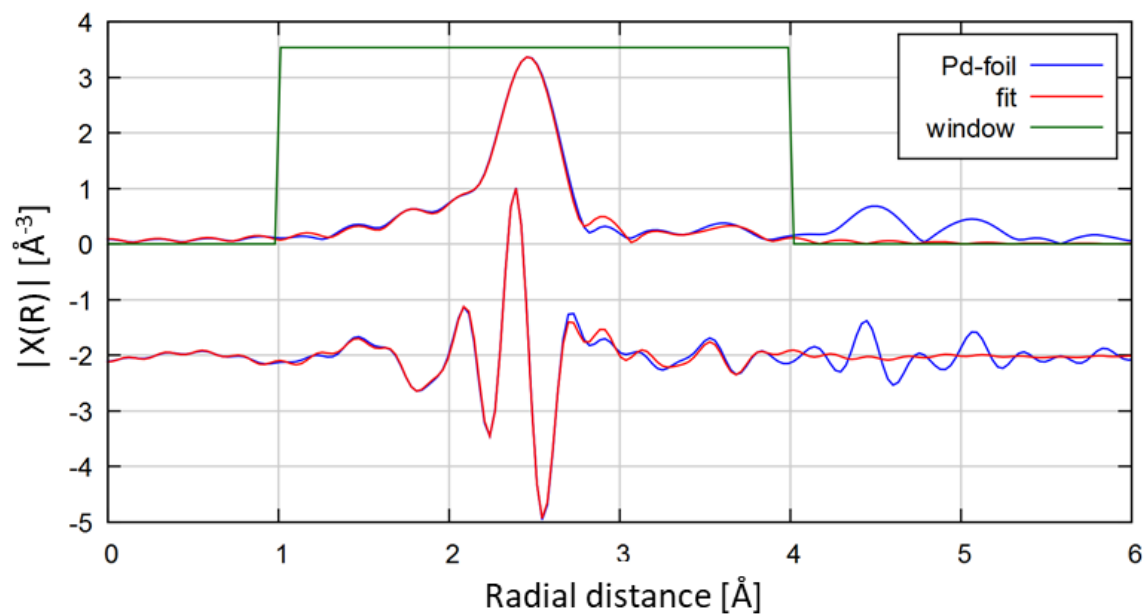
Figure A21. Pd K-edge EXAFS fit of the Pd foil utilized for the determination of the amplitude reduction factor.

Table A3. Pd K-edge EXAFS fitting results of commonly fitted factors in multiple data fitting. The data correspond to those shown in Figure 3.4 of the main text. For each spectrum, individually fitted coordination numbers of the pulsed and static experiments are given in Table C3 and A4 respectively. A k-range of 3-12 Å^{-1} was used in all fits.

Operation mode	T [°C]	Phase	R-factor	Path	Amp	E_0 [eV]	r [Å]	σ^2
Pulsed (Figure 3.4a)	435	PdO	0.03	Pd-O	0.78	-2.56	2.017	0.004
				Pd-Pd(1)			3.05	0.007
				Pd-Pd(2)			3.45	0.011
				Pd(-O-)Pd(1)			3.55	0.016
				Pd(-O-)Pd(2)			3.75	0.019
		Pd		Pd-Pd			2.82	0.018
Static (Figure 3.4b)	435	PdO	0.03	Pd-O	0.78	-2.87	2.02	0.004
				Pd-Pd(1)			3.06	0.006
				Pd-Pd(2)			3.44	0.008
				Pd(-O-)Pd(1)			3.56	0.014
		Pd		Pd-Pd			2.83	0.019

Table A4. Pd K-edge EXAFS fitting results of individually fitted factors in multiple data fitting of the first pulsed activation experiment at 435 °C corresponding to the data of Figure 3.4a of the main text.

Operation Mode	T [°C]	Phase	Path	Cycle	CN	ΔCN
Pulsed	435	PdO	Pd-O	1	4.40	0.31
				2	4.41	0.27
				3	4.40	0.28
				4	4.35	0.28
				5	4.19	0.28
				6	4.33	0.29
				7	4.01	0.23
				8	3.87	0.31
				9	3.54	0.23
				10	3.60	0.22
				11	3.52	0.22
				12	3.32	0.27
		Pd	Pd-Pd	1	0.39	1.11
				2	0.35	0.67
				3	0.30	1.14
				4	0.44	1.40
				5	0.67	1.38
				6	1.25	1.46
				7	2.22	1.32
				8	1.03	1.57
				9	2.84	1.37
				10	2.49	1.26
				11	3.04	1.36
				12	4.05	1.81
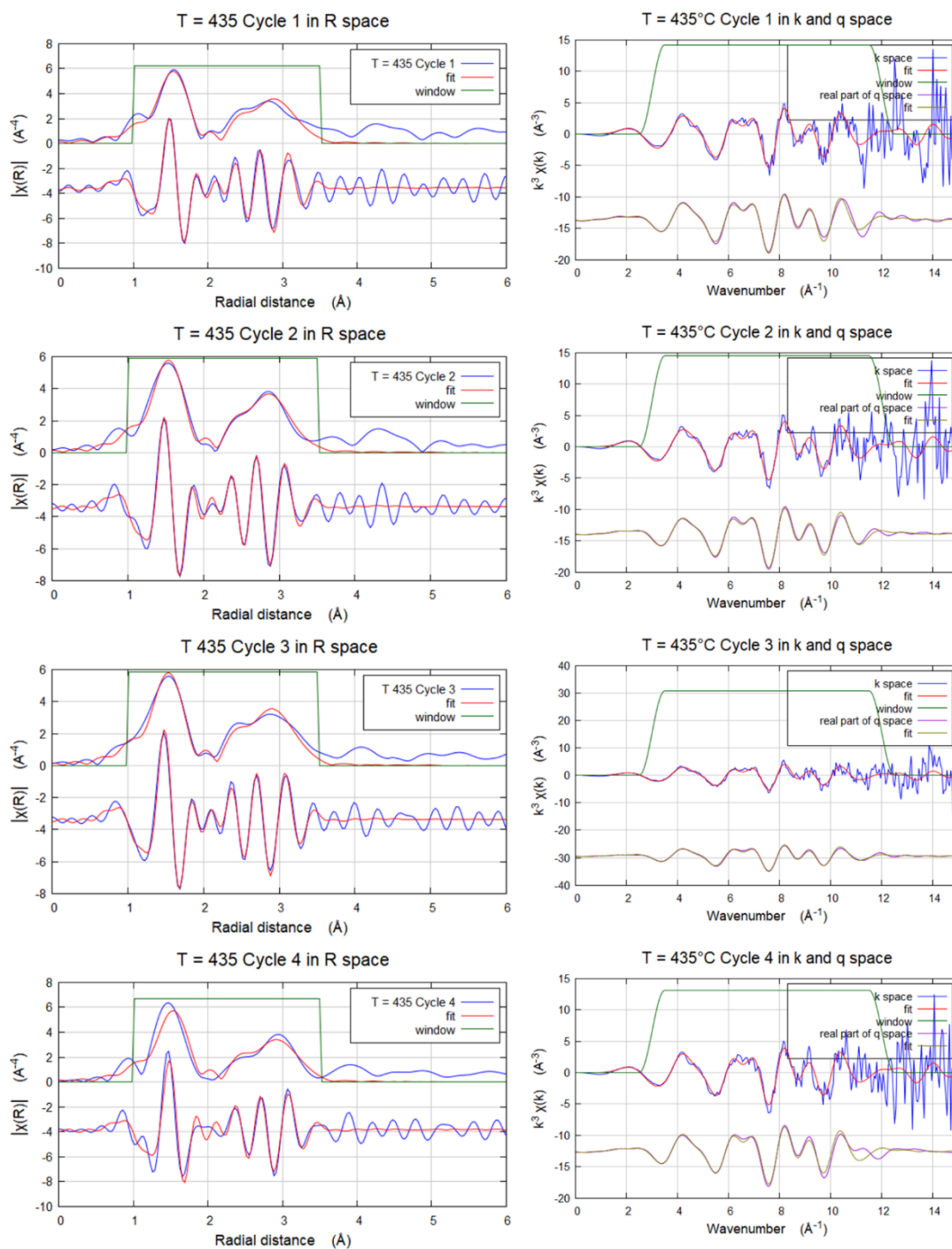
Figure A22. R and k plots for the fit of pulsing cycles 1 to 4 at 435°C, 3 min after the SRP and obtained under lean CH_4 oxidation conditions. The data correspond to those shown in Figure 3.4a of the main text.
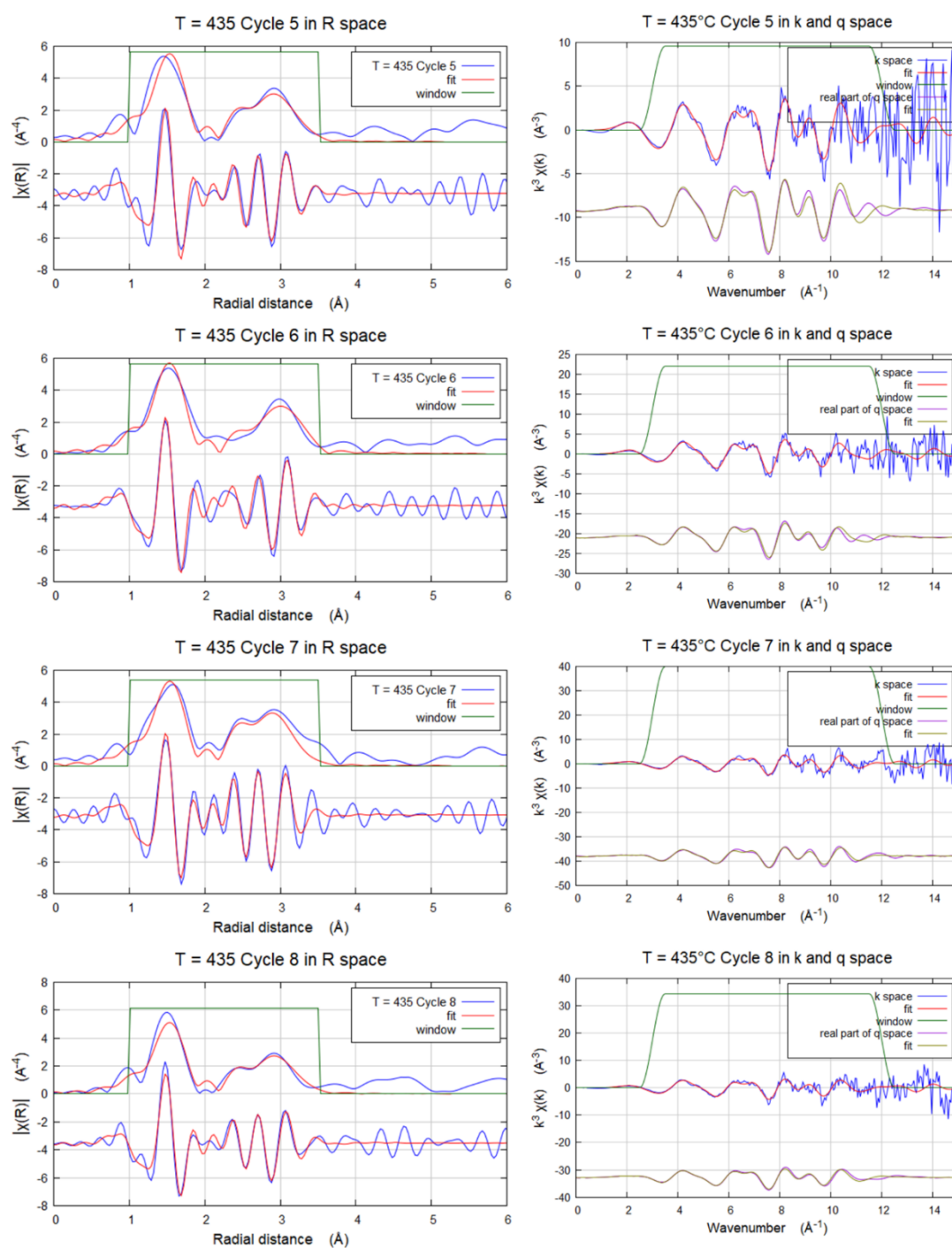
Figure A23. R and k plots for the fit of pulsing cycles 5 to 8 at 435°C, 3 min after the SRP, and obtained under lean CH_4 oxidation conditions. The data correspond to those shown in Figure 3.4a of the main text.
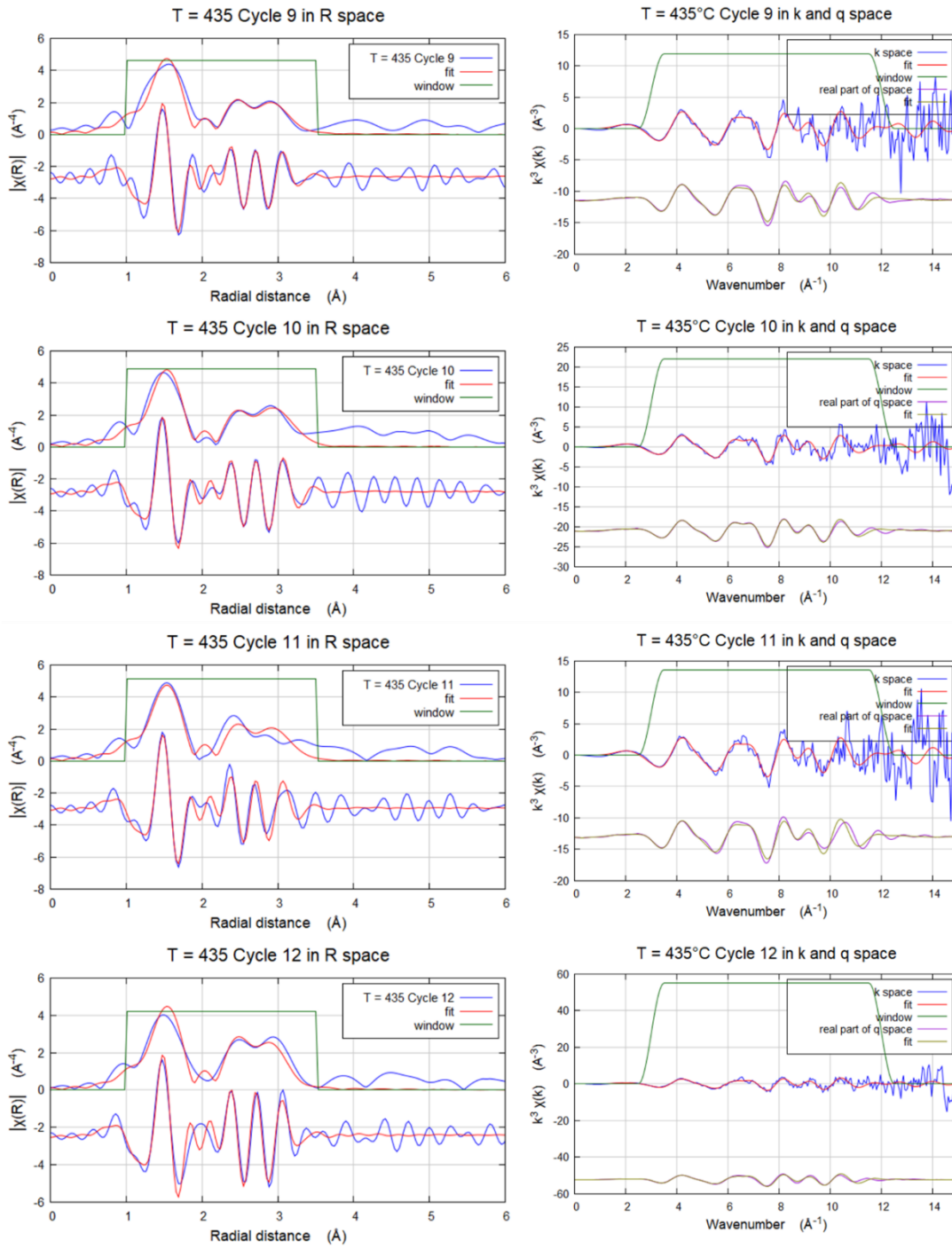
Figure A24. R and k plots for the fit of pulsing cycles 9 to 12 at 435°C, 3 min after the SRP, and obtained under lean CH_4 oxidation conditions. The data correspond to those shown in Figure 3.4a of the main text.

Table A5. Pd K-edge EXAFS fitting results of individually fitted factors in multiple data fitting of the static experiment at 435°C. The data correspond to those shown in Figure 3.4b of the main text. A k-range of 3-12 Å^{-1} was used in all fits.

Operation Mode	T [°C]	Phase	Path	Time [min]	CN	ΔCN
Static	435	PdO	Pd-O	0	4.08	0.30
				1	3.92	0.33
				5	4.08	0.28
				10	4.08	0.28
				15	4.15	0.21
				20	4.08	0.26
				25	3.94	0.27
				30	4.27	0.28
				40	4.36	0.26
				50	4.31	0.26
		Pd	Pd-Pd	0	0.83	1.46
				1	0.94	1.64
				5	0.47	1.30
				10	Including this path in the fit leads to negative σ^2-values	
				15		
				20		
				25		
				30		
				40		

Figure A25. R plots for the fit of the time-resolved data collected under static conditions at 435 °C under lean CH_4 oxidation at 0, 1, 5, 10, and 15 min. The data correspond to those shown in Figure 3.4b of the main text.
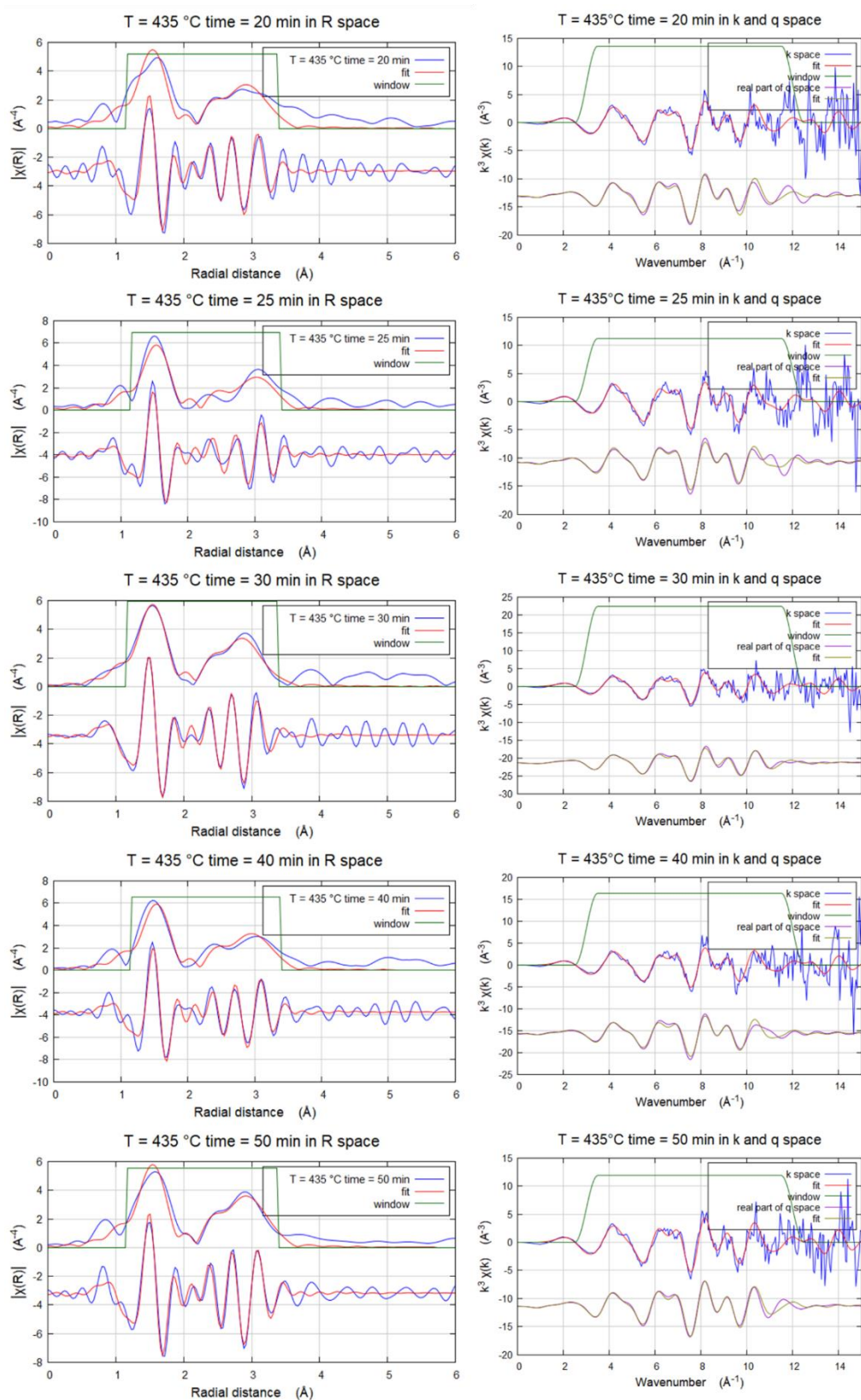
Figure A26. R plots for the fit of the time-resolved data collected under static conditions at 435 °C under lean CH_4 oxidation at 20, 25, 30, 40, and 50 min. The data correspond to those shown in Figure 3.4b of the main text.

Appendix B (Chapter 4)
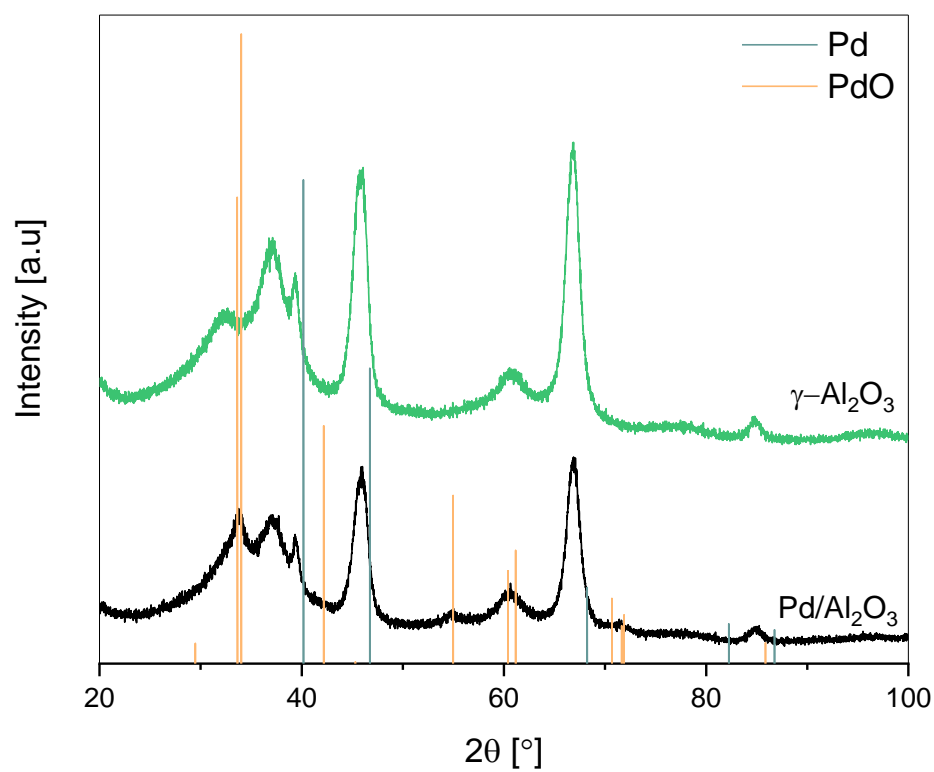
Figure B1. Powder X-ray diffraction of unused Pd/Al$_2$O$_3$ as well as the support, γ-Al$_2$O$_3$, before impregnation.
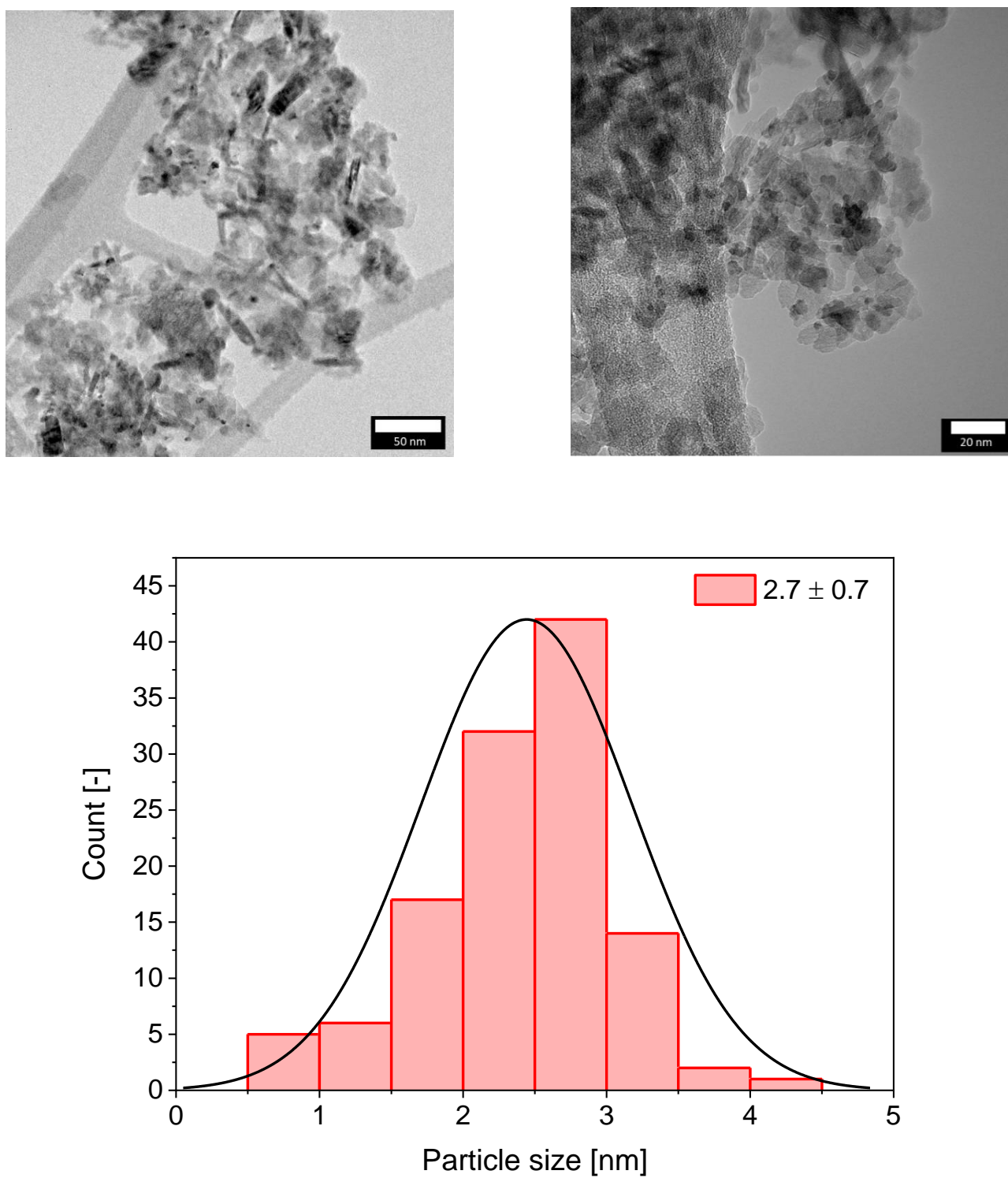
Figure B2. Dark-field STEM images and particle size distribution of catalyst (Pd/Al$_2$O$_3$).
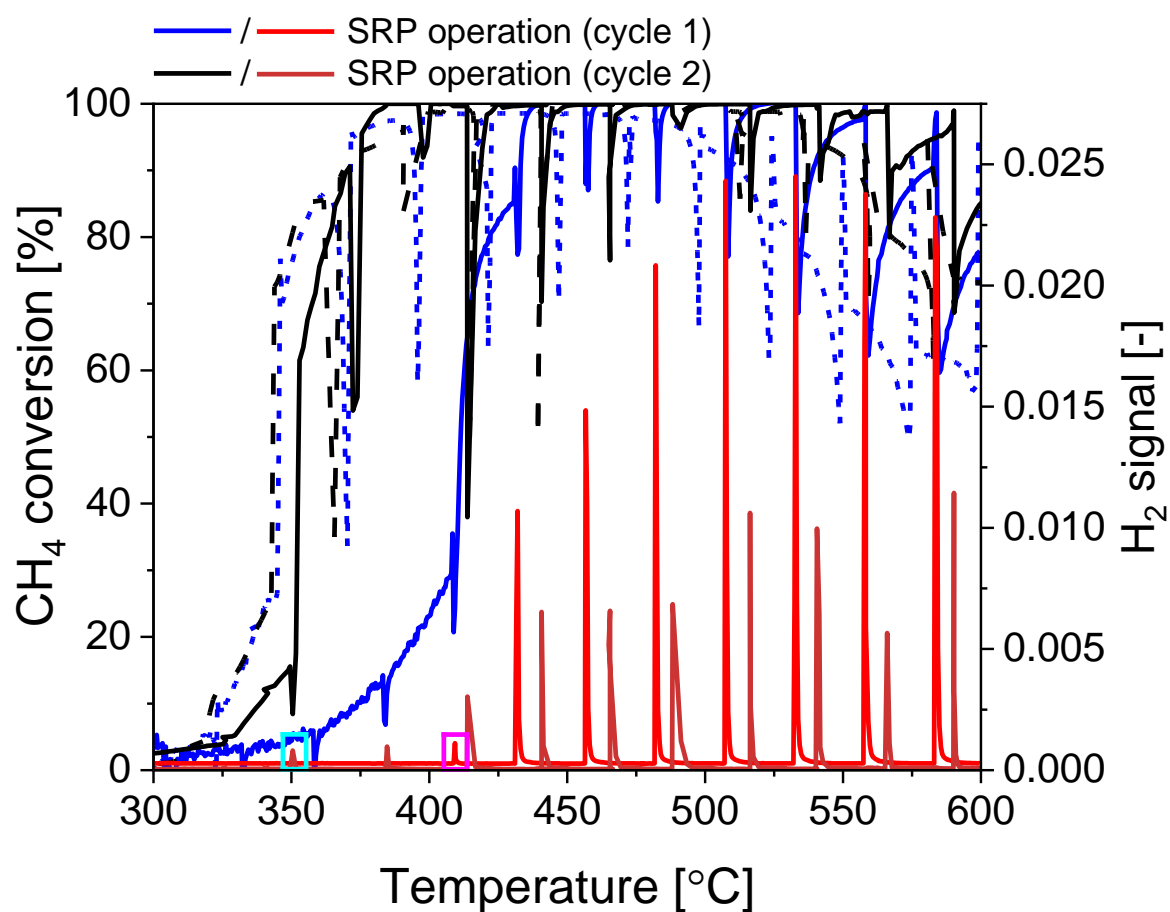
Figure B3.CH$_4$ conversion over two consecutive cycles during heating (—) and cooling (---), under SRP wet lean concentrated conditions in the presence of CH$_4$/H$_2$O. The pink and blue rectangles highlight the first H$_2$ appearance during the heating ramp of the 1st and 2nd cycle, respectively. Conditions: 1 vol% CH$_4$, 4 vol% O$_2$, 5 vol% H$_2$O; WHSV = 240 Lh^{-1}g^{-1}.

Table B1. Pd K-edge FT-XAFS (not phase corrected) illustrating the change in intensities of Pd-Pd and Pd-O scattering path during and 294 s after a pulse at 435 °C and 575 °C under SRP wet lean methane oxidation (concentrated conditions). Conditions: 1 vol% CH_4, 4 vol% O_2, 5 vol% H_2O; WHSV = 240 $Lh^{-1}g^{-1}$.

			CN	R	σ^2
435 °C	During a pulse	Pd-Pd	9.67 ± 0.95	2.72 ± 0.0076	0.013 ± 0.001
		Pd-O	0.93 ± 1.01	2.02 ± 0.15	0.0058 (set)
	294 s after a pulse	Pd-Pd	3.35 ± 0.84	2.73 ± 0.023	0.011 ±0.0024
		Pd-O	2.88 ± 0.46	1.99 ± 0.0022	0.006 ± 0.0022
575 °C	During a pulse	Pd-Pd	10.73 ± 1.2	2.71 ± 0.011	0.016 ± 0.0016
		Pd-O	-	-	-
	294 s after a pulse	Pd-Pd	10.64 ± 1.32	2.71 ± 0.014	0.018 ± 0.0019
		Pd-O	0.25 ± 0.17	1.97 ± 0.052	0.0012 (set)
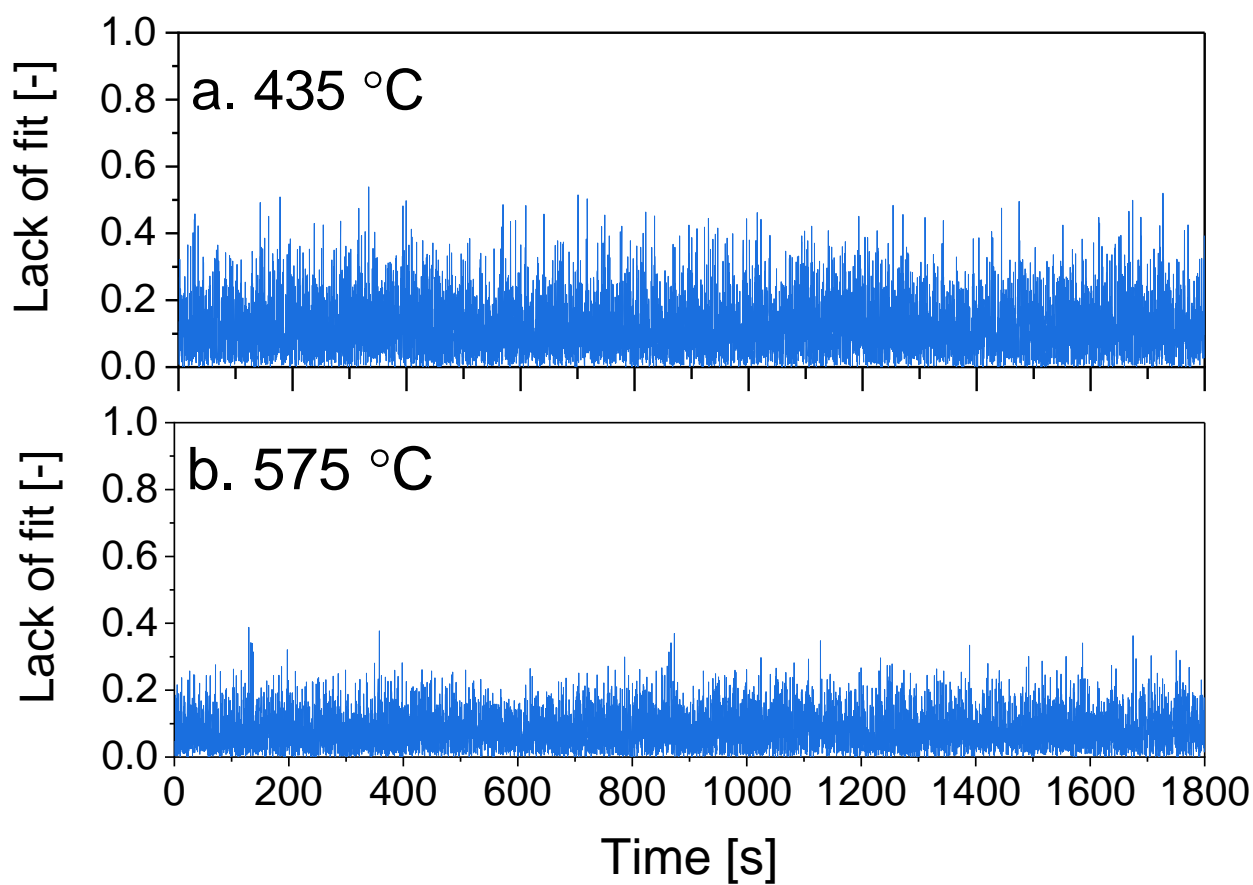
Figure B4. Lack of fit of the LCF analysis performed from the XANES region of the XAS spectra measured at the Pd K-edge, under SRP wet lean concentrated conditions in the presence of CH_4/H_2O, at (a) 435 °C and (b) 575 °C. Conditions: 1 vol% CH_4, 4 vol% O_2, 5 vol% H_2O; WHSV = 240 $Lh^{-1}g^{-1}$.
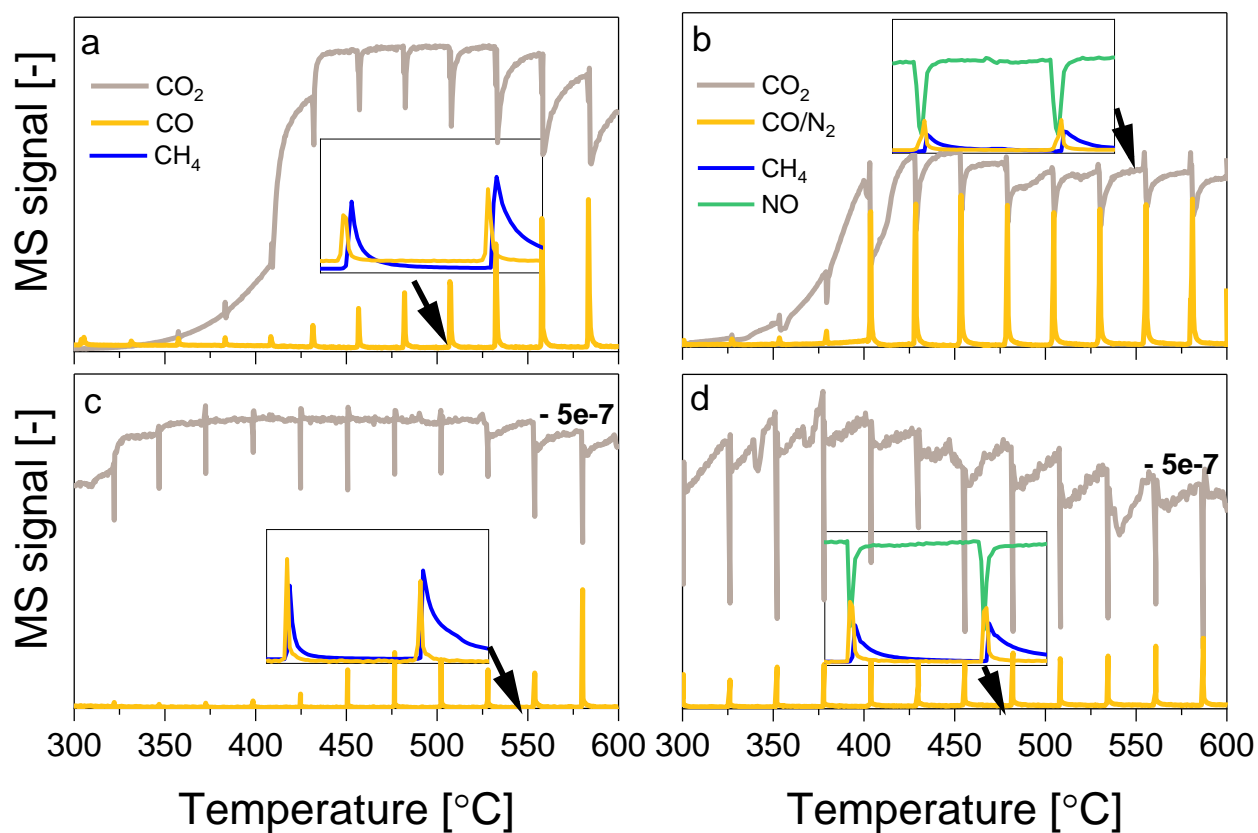
Figure B5. MS signals of CH_4, CO/N_2, CO_2, and NO during heating ramps under SRP wet lean concentrated conditions in the presence of (a) CH_4/H_2O, (b) $CH_4/NO/H_2O$, (c) $CH_4/CO/H_2O$ and, (d) $CH_4/NO/CO/H_2O$. Conditions: (a) 1 vol% CH_4, 4 vol% O_2, 5 vol% H_2O; (b) 1 vol% CH_4, 1 vol% NO, 3 vol% O_2, 5 vol% H_2O; (c) 1 vol% CH_4, 4.6 vol% CO, 8.6 vol% O_2, 5 vol% H_2O; (d) 1 vol% CH_4, 1 vol% NO, 4.6 vol% CO, 7.6 vol% O_2, 5 vol% H_2O; WHSV = 240 $Lh^{-1}g^{-1}$.
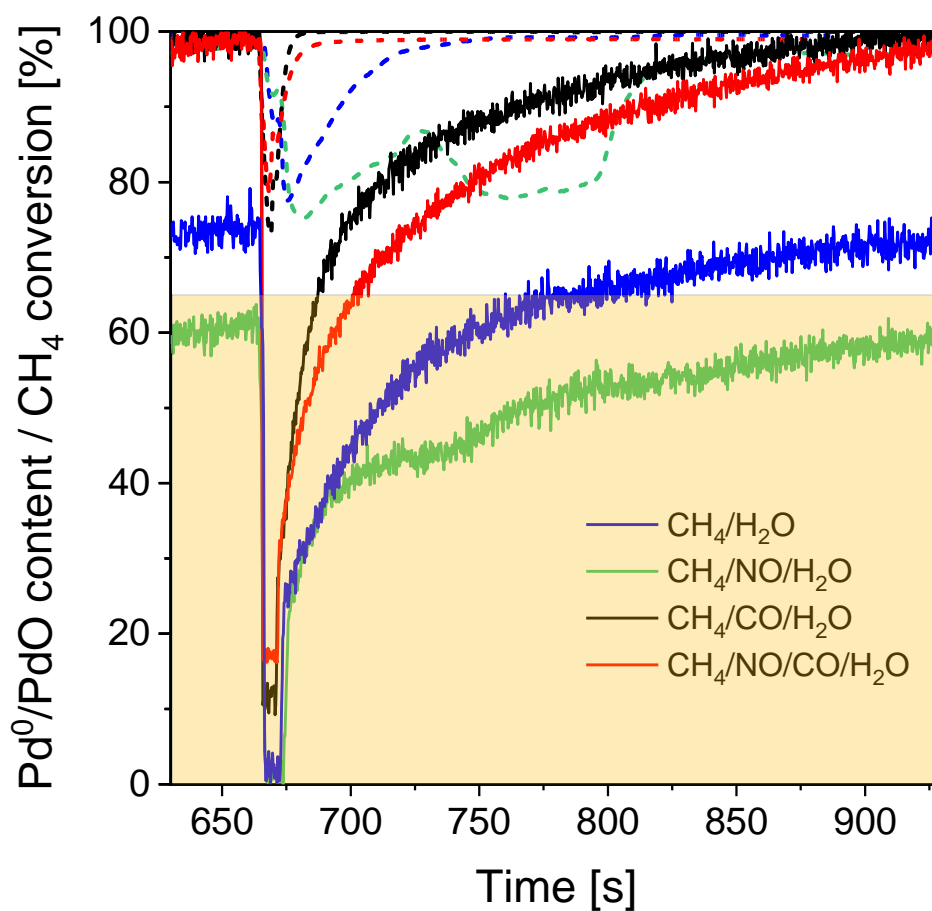
Figure B6. CH$_4$ and NO conversions, Pd phase content (PdO / Pd), and H$_2$ MS signals at 435 °C, under SRP wet lean concentrated conditions in the presence of CH$_4$/H$_2$O, CH$_4$/NO/H$_2$O, CH$_4$/CO/H$_2$O, CH$_4$/CO/NO/H$_2$O. Conditions: (blue) 1 vol% CH$_4$, 4 vol% O$_2$, 5 vol% H$_2$O; (green) 1 vol% CH$_4$, 1 vol% NO, 3 vol% O$_2$, 5 vol% H$_2$O; (black) 1 vol% CH$_4$, 4.6 vol% CO, 8.6 vol% O$_2$, 5 vol% H$_2$O; (red) 1 vol% CH$_4$, 1 vol% NO, 4.6 vol% CO, 7.6 vol% O$_2$, 5 vol% H$_2$O; WHSV = 240 Lh^{-1}g^{-1}.
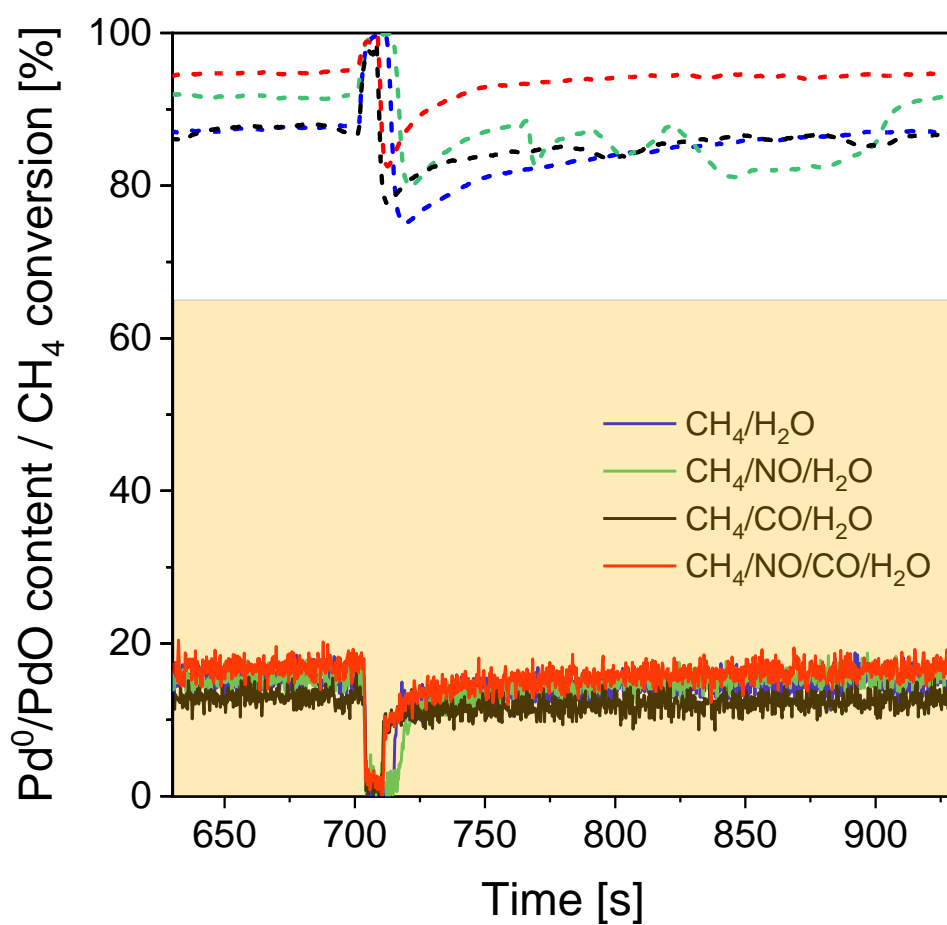
Figure B7. CH_4 and NO conversions, Pd phase content (PdO / Pd), and H_2 MS signals at 575 °C, under SRP wet lean concentrated conditions in the presence of CH_4/H_2O, $CH_4/NO/H_2O$, $CH_4/CO/H_2O$, $CH_4/CO/NO/H_2O$. Conditions: (blue) 1 vol% CH_4, 4 vol% O_2, 5 vol% H_2O; (green) 1 vol% CH_4, 1 vol% NO, 3 vol% O_2, 5 vol% H_2O; (black) 1 vol% CH_4, 4.6 vol% CO, 8.6 vol% O_2, 5 vol% H_2O; (red) 1 vol% CH_4, 1 vol% NO, 4.6 vol% CO, 7.6 vol% O_2, 5 vol% H_2O; WHSV = 240 $Lh^{-1}g^{-1}$.
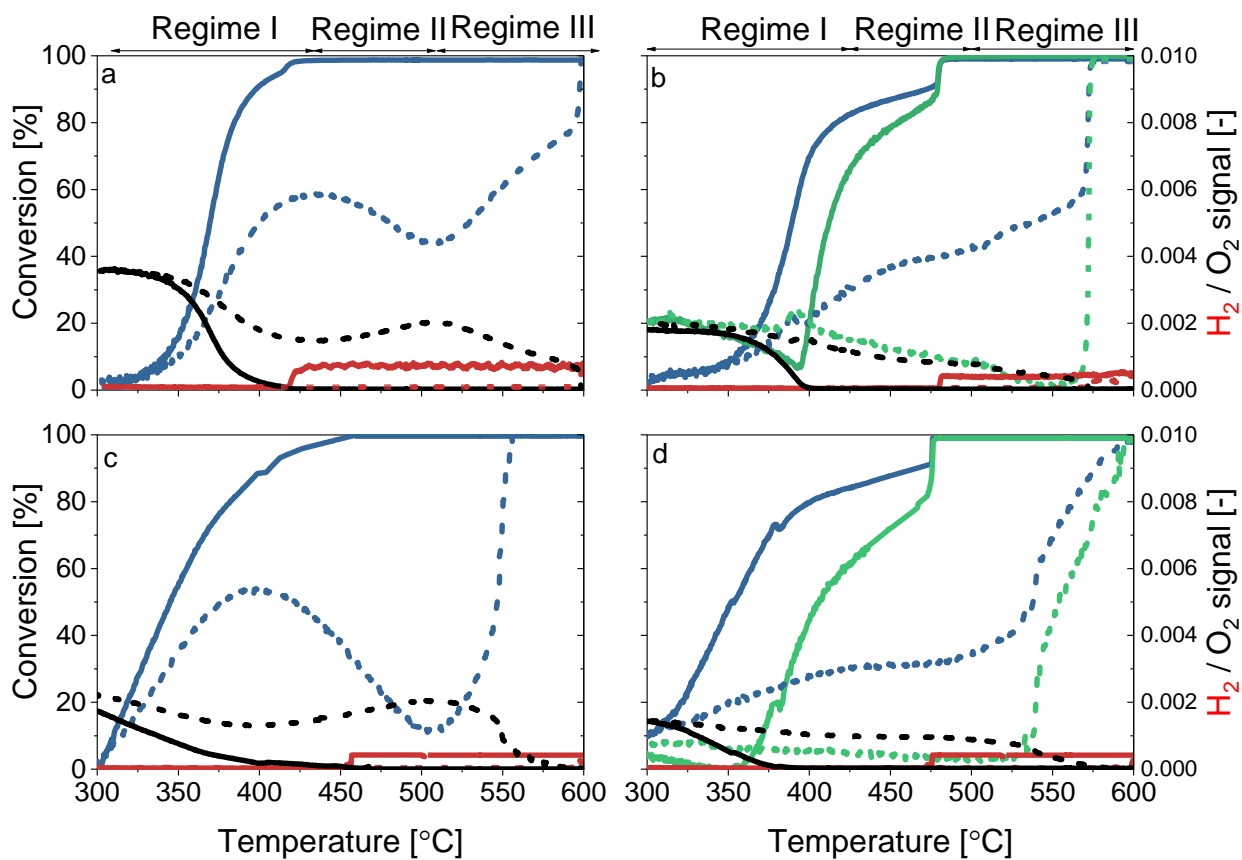
Figure B8. CH_4 and NO conversions and H_2 (red) and O_2 (black) MS signals under static wet stoichiometric concentrated conditions in the presence of (a) $CH_4//H_2O$, (b) $CH_4/NO/H_2O$, (c) $CH_4/CO/H_2O$, and (d) $CH_4/CO/NO/H_2O$. Conditions: (a) 1 vol% CH_4, 2 vol% O_2, 5 vol% H_2O; (b) 1 vol% CH_4, 1 vol% NO, 1.5 vol% O_2, 5 vol% H_2O; (c) 1 vol% CH_4, 4.6 vol% CO, 4.3 vol% O_2, 5 vol% H_2O; (d) 1 vol% CH_4, 1 vol% NO, 4.6 vol% CO, 3.8 vol% O_2, 5 vol% H_2O; WHSV = 240 $Lh^{-1}g^{-1}$.

Figure B9. CH_4 (blue) and NO (green) conversion, as well as H_2 (red) and O_2 (black) MS signals during heating (—) and cooling (- - -) ramps, under SRP wet stoichiometric concentrated conditions, in the presence of (a) CH_4/H_2O, (b) $CH_4/CO/H_2O$ and (c'-c'') $CH_4/NO/H_2O$. Conditions: (a) 1 vol% CH_4, 2 vol% O_2, 5 vol% H_2O; (b) 1 vol% CH_4, 4.6 vol% CO, 4.3 vol% O_2, 5 vol% H_2O; (c'-c'') 1 vol% CH_4, 1 vol% NO, 1.5 vol% O_2, 5 vol% H_2O; WHSV = 240 $Lh^{-1}g^{-1}$.
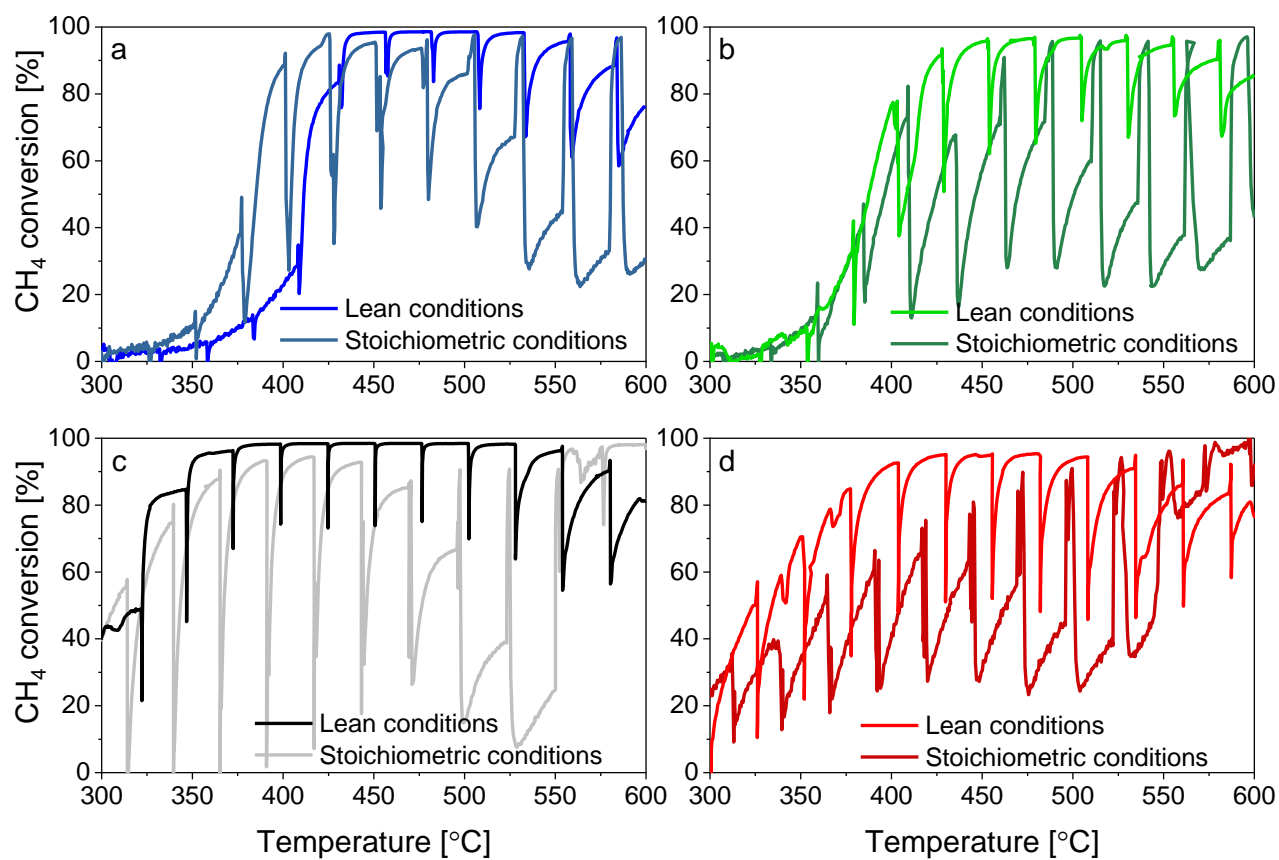
Figure B10 CH$_4$ conversion during heating ramp under SRP wet lean and stoichiometric concentrated conditions, in the presence of (a) CH$_4$/H$_2$O, (b) CH$_4$/NO/H$_2$O, (c) CH$_4$/CO/H$_2$O, and (d) CH$_4$/CO/NO/H$_2$O.
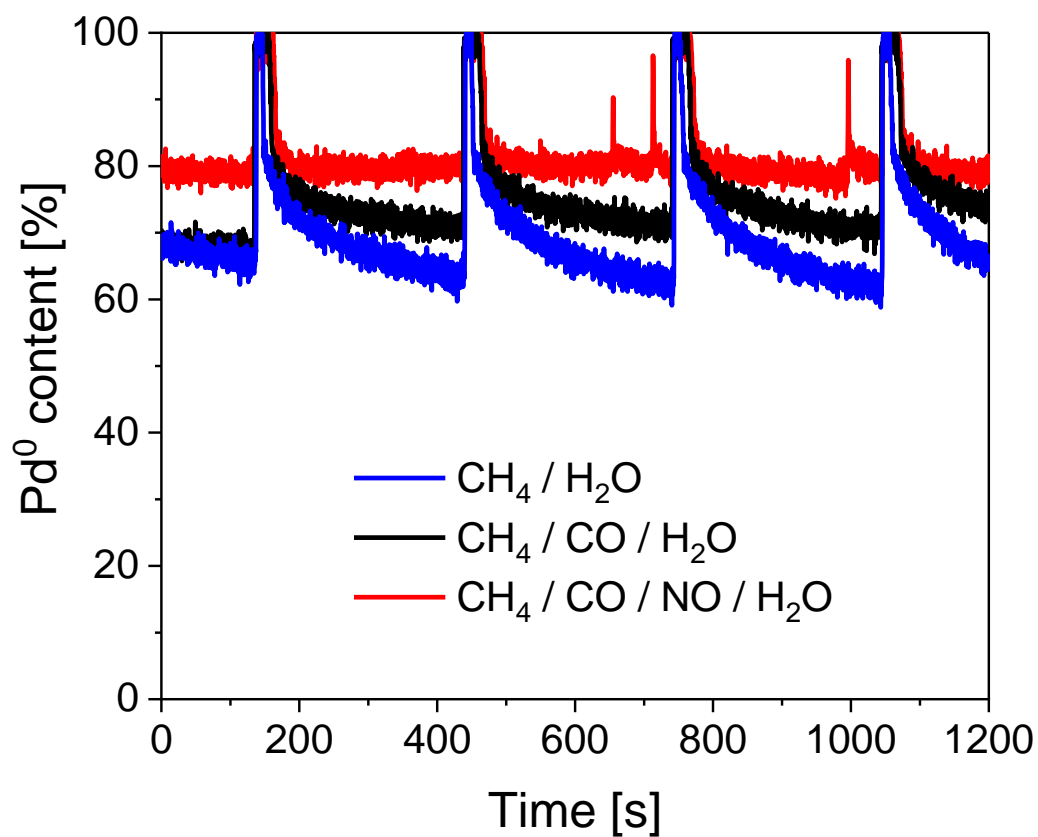
Figure B11. Pd^0 content under SRP wet stoichiometric concentrated conditions in the presence of (blue) CH_4/H_2O, (black) $CH_4/CO/H_2O$, and (red) $CH_4/CO/NO/H_2O$. Conditions: (blue) 1 vol% CH_4, 2 vol% O_2, 5 vol% H_2O; (black) 1 vol% CH_4, 4.6 vol% CO, 4.3 vol% O_2, 5 vol% H_2O; (red) 1 vol% CH_4, 4.6 vol% CO, 1 vol% NO, 3.8 vol% O_2, 5 vol% H_2O; WHSV = 240 $Lh^{-1}g^{-1}$.
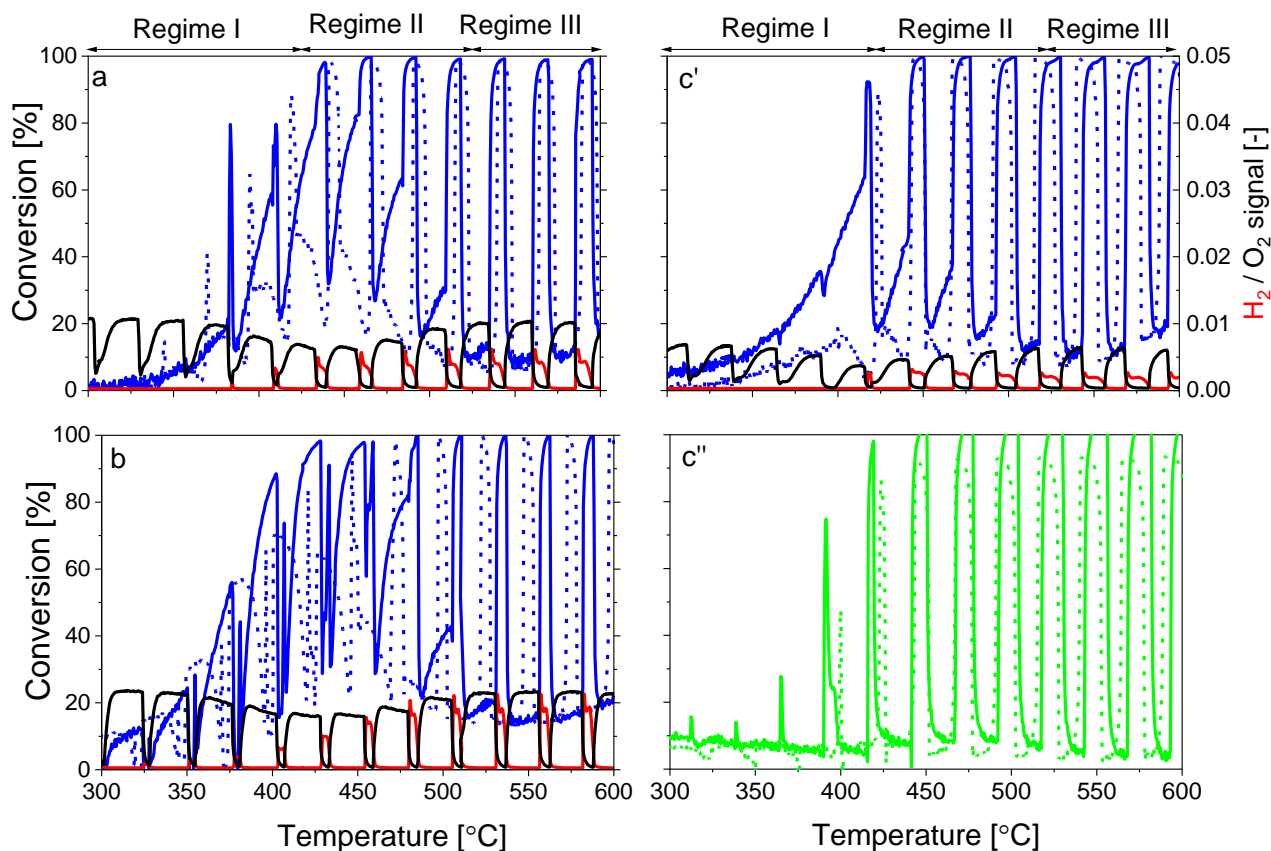
Figure B12. CH_4 and NO conversions as well as H_2 (red) and O_2 (black) MS signals under SRP wet lean diluted conditions in the presence of (a) CH_4/H_2O, (b) $CH_4/CO/H_2O$, and (c'-c'') $CH_4/NO/H_2O$. Conditions: (a) 0.15 vol% CH_4, 0.6 vol% O_2, 5 vol% H_2O, (b) 0.15 vol% CH_4, 0.7 vol% CO, 1.3 vol% O_2, 5 vol% H_2O; (c'-c'') 0.15 vol% CH_4, 0.16 vol% NO, 0.44 vol% O_2, 5 vol% H_2O; WHSV = 240 $Lh^{-1}g^{-1}$.
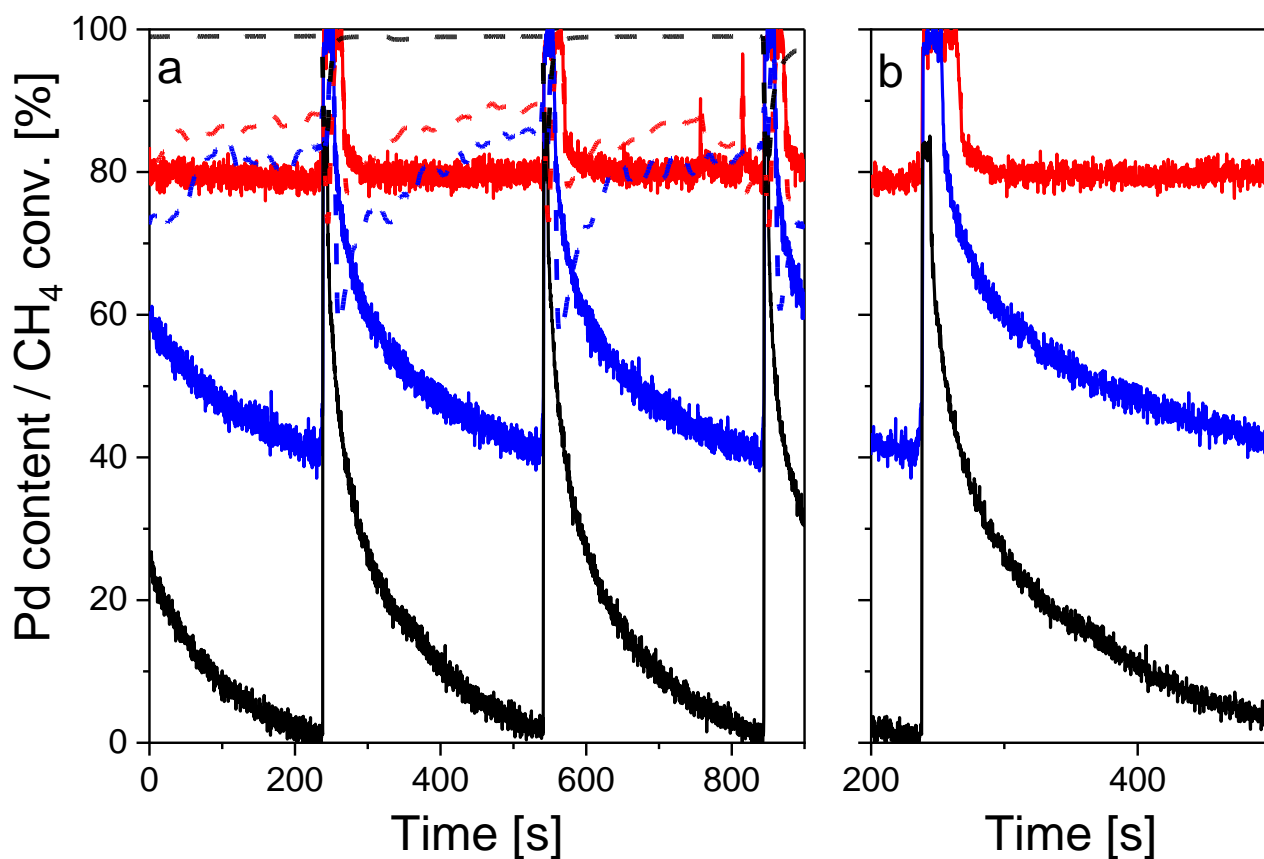
Figure B13. Pd content (—) and CH_4 conversion (---) in the presence of $CH_4/CO/NO/H_2O$ under SRP (black) lean concentrated, (red) stoichiometric concentrated, and (blue) lean diluted conditions over (a) three pulses and (b) one pulse. Conditions: (black) 1 vol% CH_4, 1 vol% NO, 4.6 vol% CO, 7.6 vol% O_2, 5 vol% H_2O; (red) 0.15 vol% CH_4, 0.16 vol% NO, 0.7 vol% CO, 1.14 vol% O_2, 5 vol% H_2O; (blue) 1 vol% CH_4, 1 vol% NO, 4.6 vol% CO, 3.8 vol% O_2, 5 vol% H_2O; WHSV = 240 $Lh^{-1}g^{-1}$.
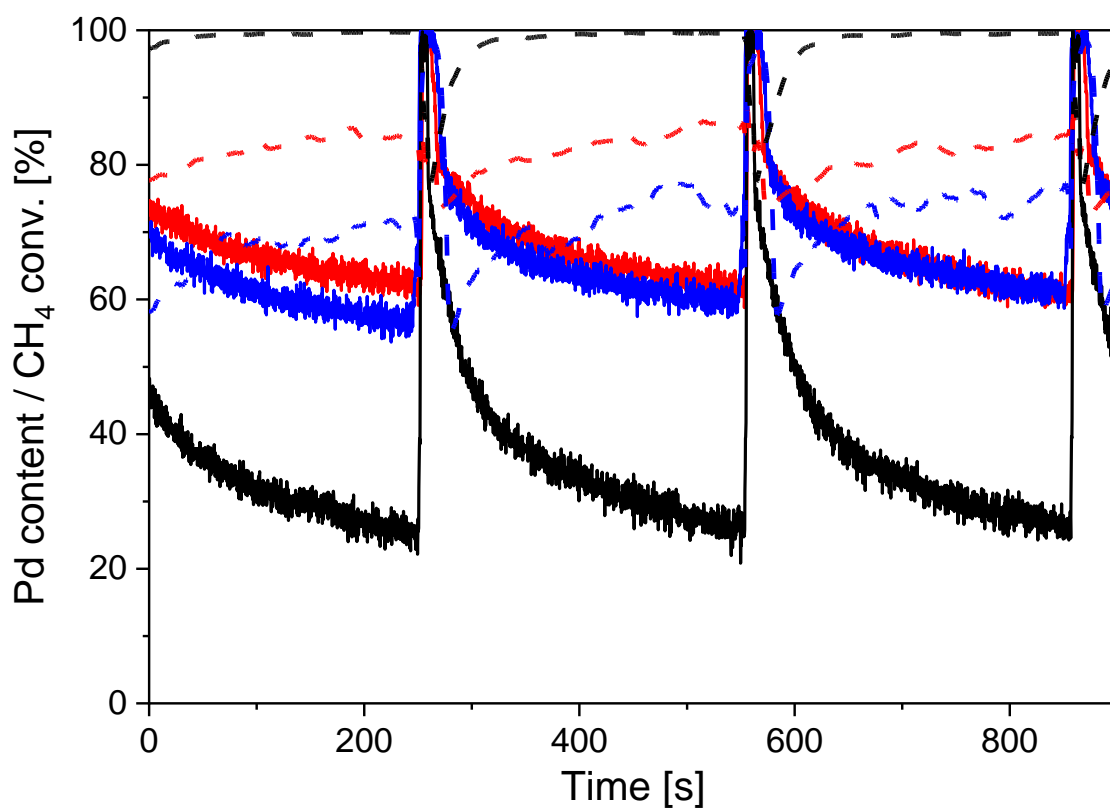
Figure B14. Pd content (—) and CH_4 conversion (---) in the presence of CH_4/H_2O under SRP (black) lean concentrated, (red) stoichiometric concentrated, and (blue) lean diluted conditions. Conditions: (black) 1 vol% CH_4, 4 vol% O_2, 5 vol% H_2O; (red) 1 vol% CH_4, 2 vol% O_2, 5 vol% H_2O; (blue) 0.15 vol% CH_4, 0.6 vol% O_2, 5 vol% H_2O; WHSV = 240 $Lh^{-1}g^{-1}$.
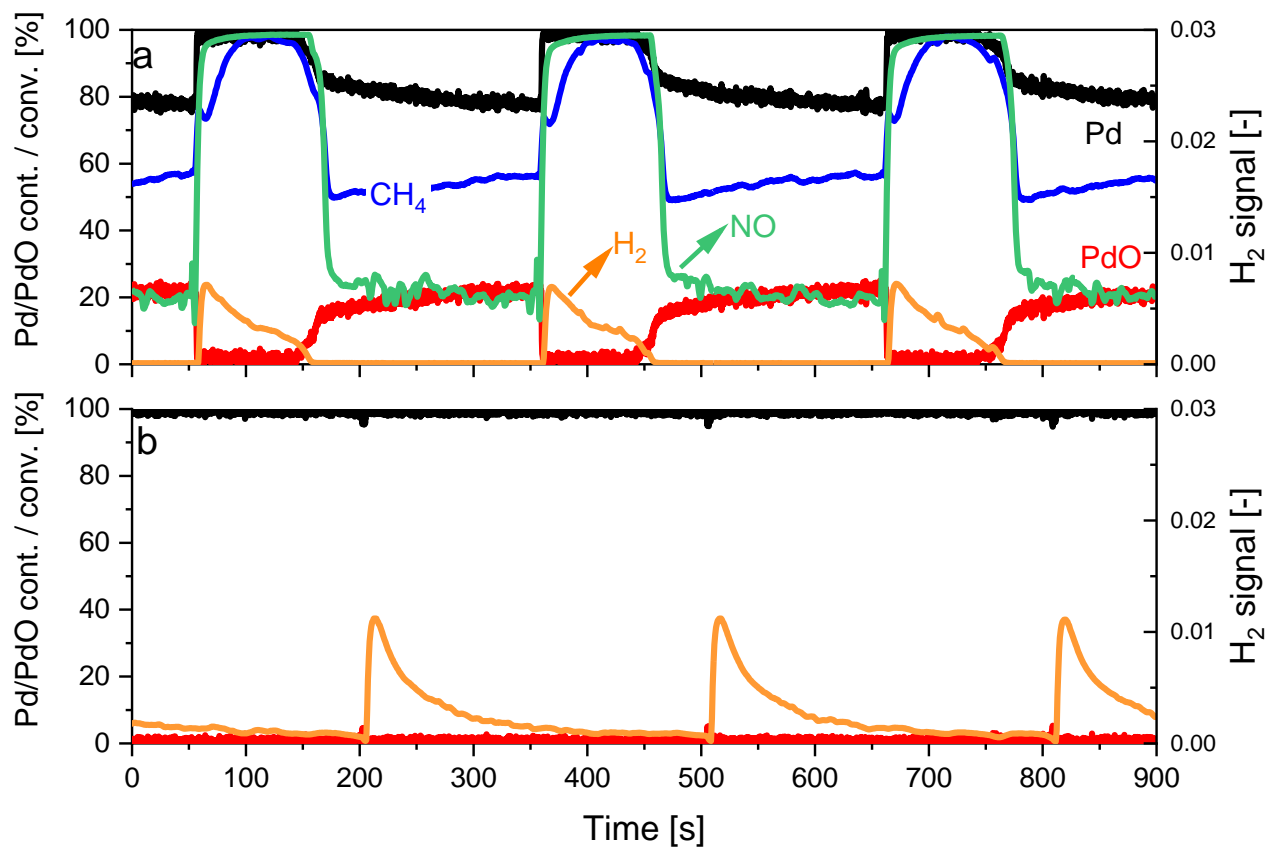
Figure B15. CH$_4$ (blue) and NO (green) conversions, Pd phase content (PdO (red) / Pd (black)) and H$_2$ (orange) MS signals at (a) 435 °C (b) 575 °C under SRP wet stoichiometric diluted conditions in the presence of CH$_4$/NO/CO/H$_2$O/O$_2$. Conditions: 0.15 vol% CH$_4$, 0.16 vol% NO, 0.7 vol% CO, 0.57 vol% O$_2$, 5 vol% H$_2$O; WHSV = 240 Lh^{-1}g^{-1}.
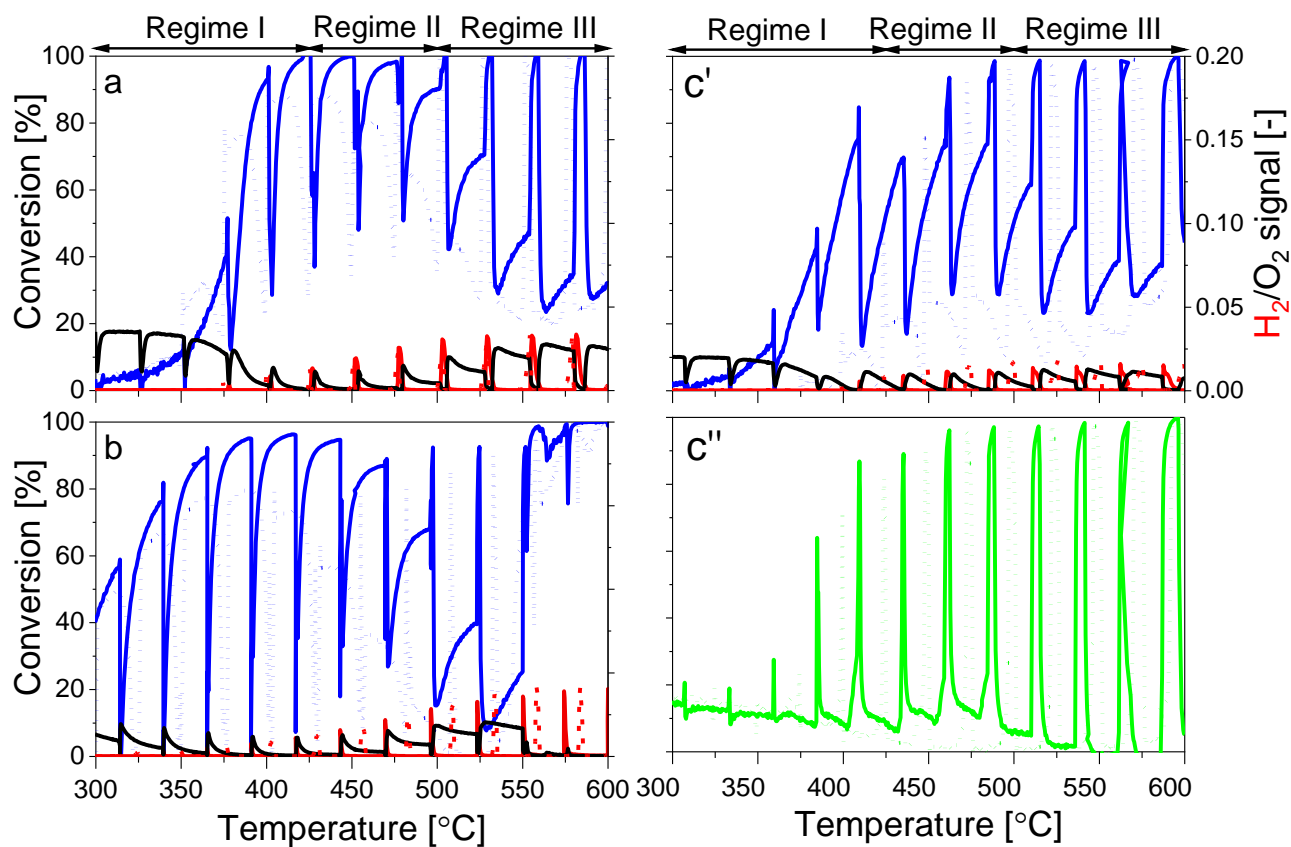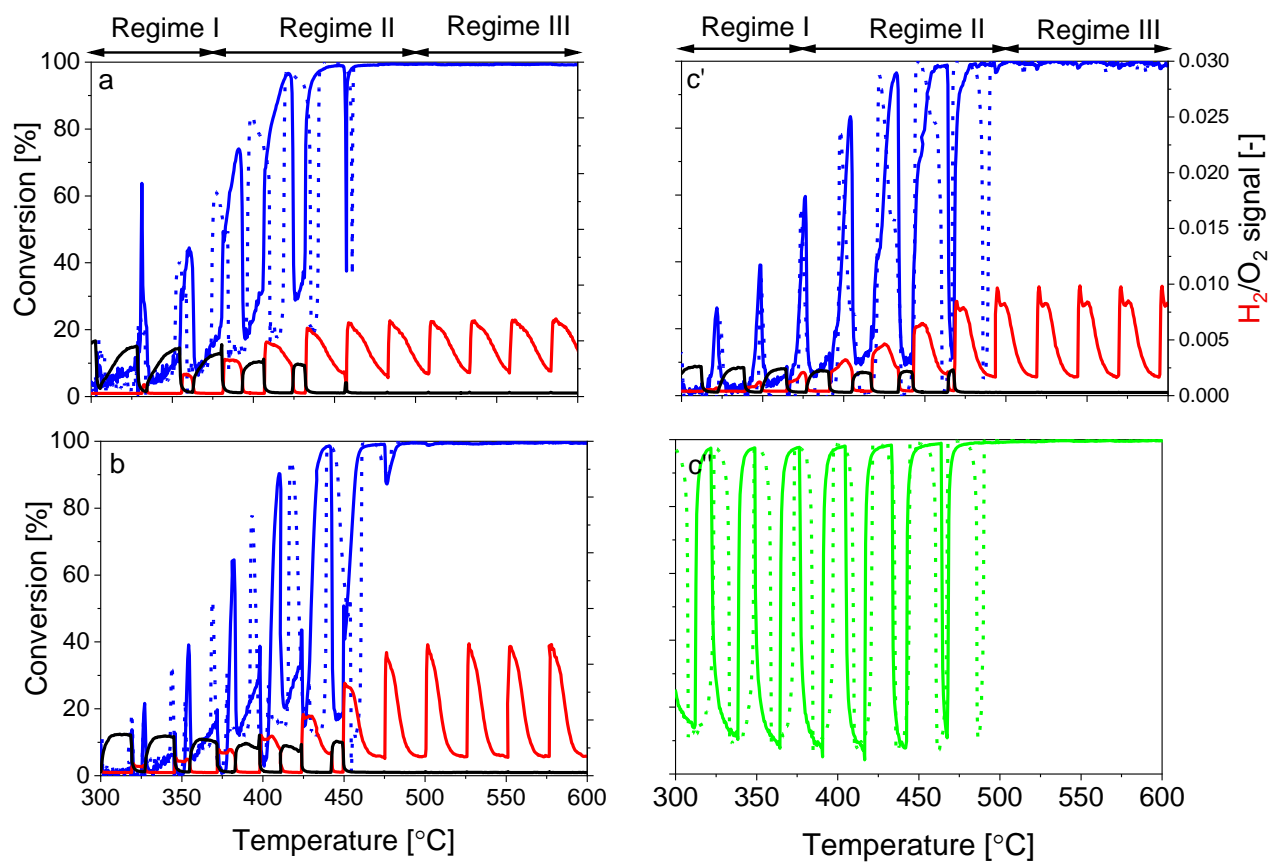
Figure B16. CH_4 (blue) and NO (green) conversion, as well as H_2 (red) and O_2 (black) MS signals during heating (—) and cooling (- - -) ramps, under SRP wet stoichiometric diluted conditions, in the presence of (a) CH_4/H_2O, (b) $CH_4/CO/H_2O$, (c'-c'') $CH_4/NO/H_2O$. Conditions: (a) 0.15 vol% CH_4, 0.3 vol% O_2, 5 vol% H_2O; (b) 0.15 vol% CH_4, 0.7 vol% CO, 0.65 vol% O_2, 5 vol% H_2O; (c'-c'') 0.15 vol% CH_4, 0.16 vol% NO, 0.22 vol% O_2, 5 vol% H_2O; WHSV = 240 $Lh^{-1}g^{-1}$.
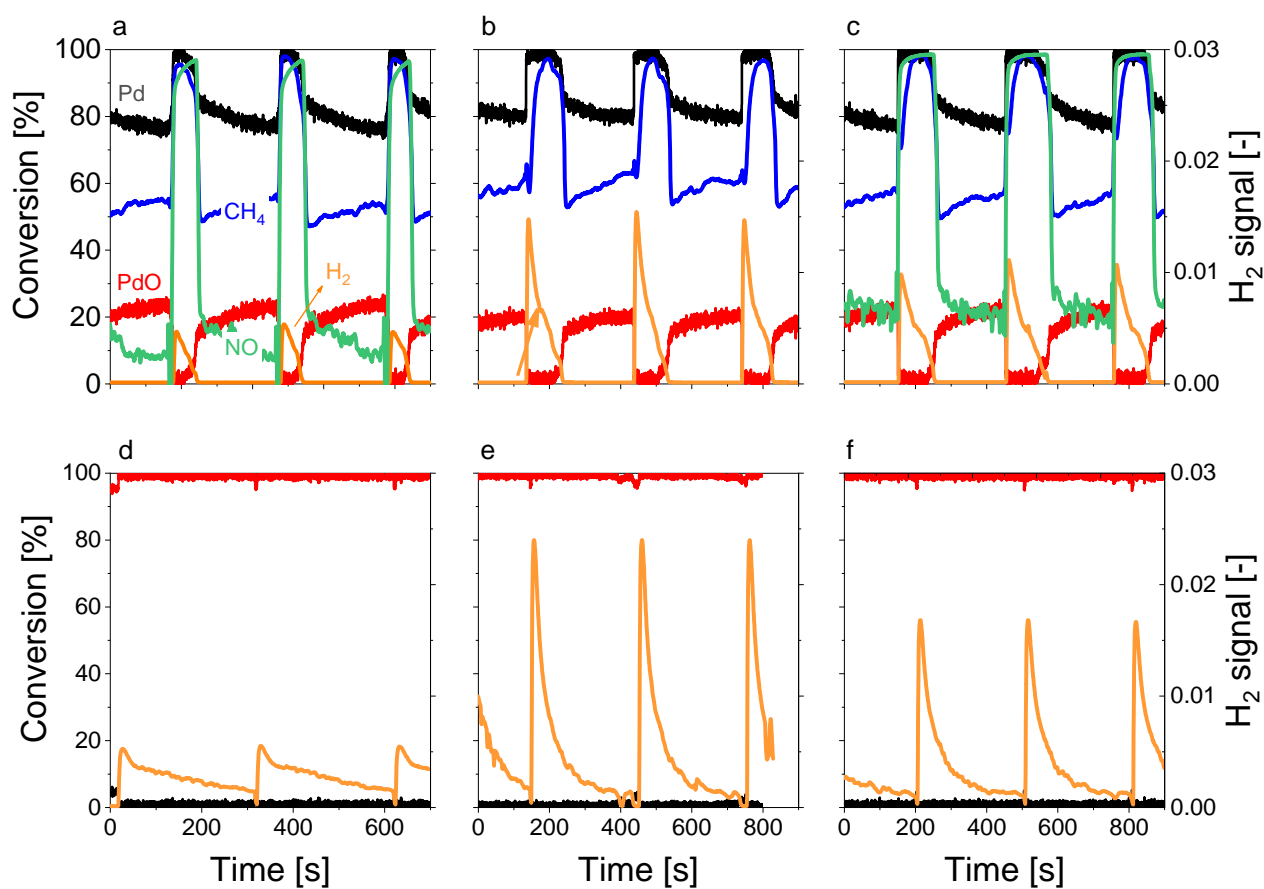
Figure B17. CH_4 and NO conversions, Pd phase content (PdO / Pd), and H_2 MS signals at (a-c) 435 °C (d-h) 575 °C under SRP wet stoichiometric diluted conditions in the presence (a) CH_4/H_2O, (b) $CH_4/CO/H_2O$ and (c) $CH_4/NO/H_2O$. Conditions: (a) 0.15 vol% CH_4, 0.3 vol% O_2, 5 vol% H_2O; (b) 0.15 vol% CH_4, 0.7 vol% CO, 0.65 vol% O_2, 5 vol% H_2O; (c) 0.15 vol% CH_4, 0.16 vol% NO, 0.22 vol% O_2, 5 vol% H_2O; WHSV = 240 $Lh^{-1}g^{-1}$.

Appendix C (Chapter 5)
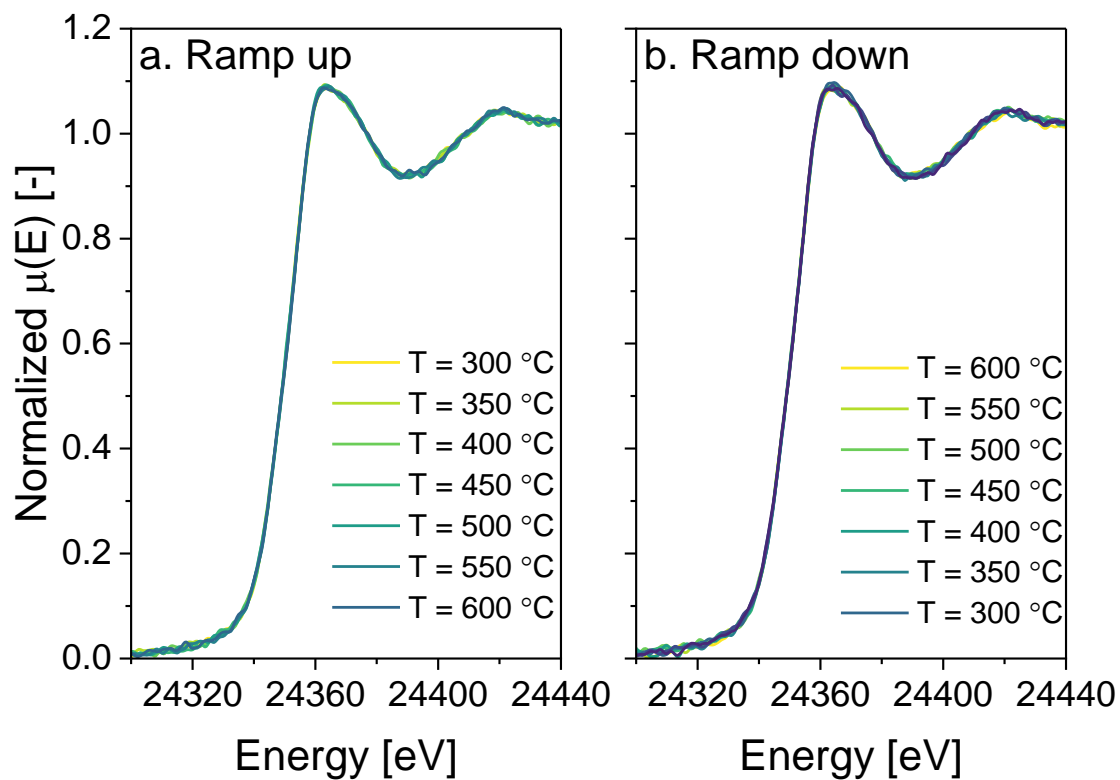
Figure C1. Operando XAS measured at the Pd K-edge, during pre-treatment in CH_4/O_2, under stoichiometric static conditions, during (a) ramp up and (b) ramp down. Conditions: 1500 ppm CH_4, 3000 ppm O_2; WHSV = 240 $Lh^{-1}g^{-1}$.
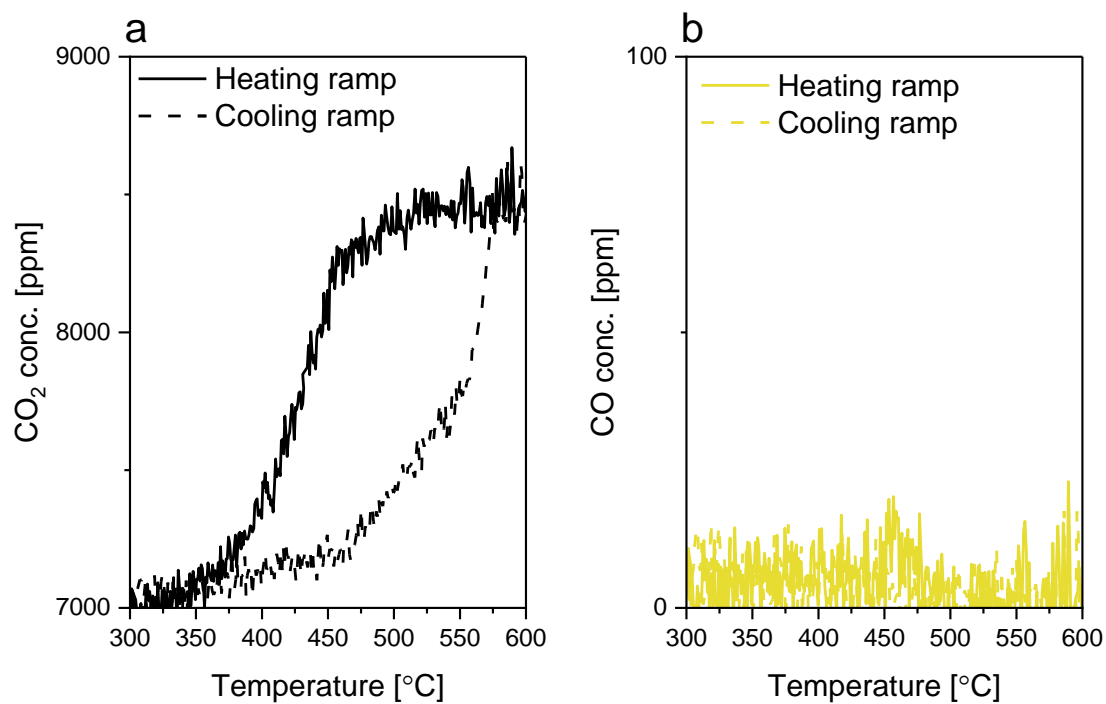
Figure C2. (a) CO_2 and (b) CO concentrations under static lean (5980 ppm O_2; $\lambda = 1.001$) conditions. Conditions: 1500 ppm CH_4, 1600 ppm NO, 7000 ppm CO, 5980 ppm O_2, 5 vol% H_2O; WHSV = 240 $Lh^{-1}g^{-1}$.
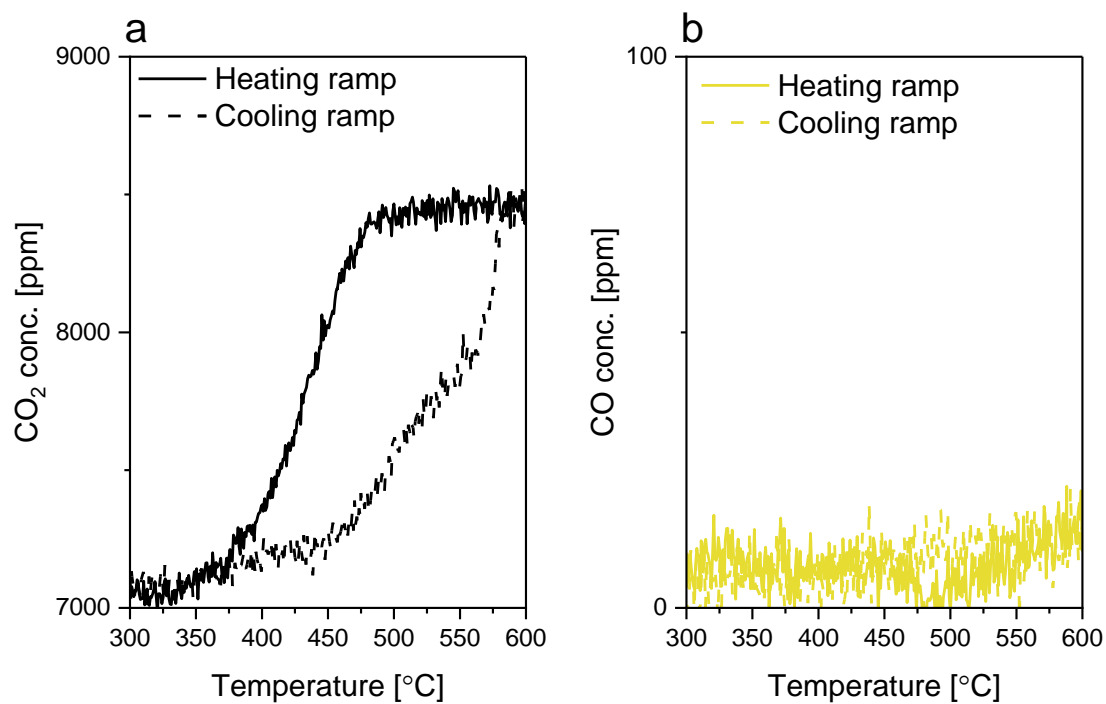
Figure C3. (a) CO_2 and (b) CO concentrations under static stoichiometric (5700 ppm O_2; λ = 1.000) conditions. Conditions: 1500 ppm CH_4, 1600 ppm NO, 7000 ppm CO, 5700 ppm O_2, 5 vol% H_2O; WHSV = 240 $Lh^{-1}g^{-1}$.
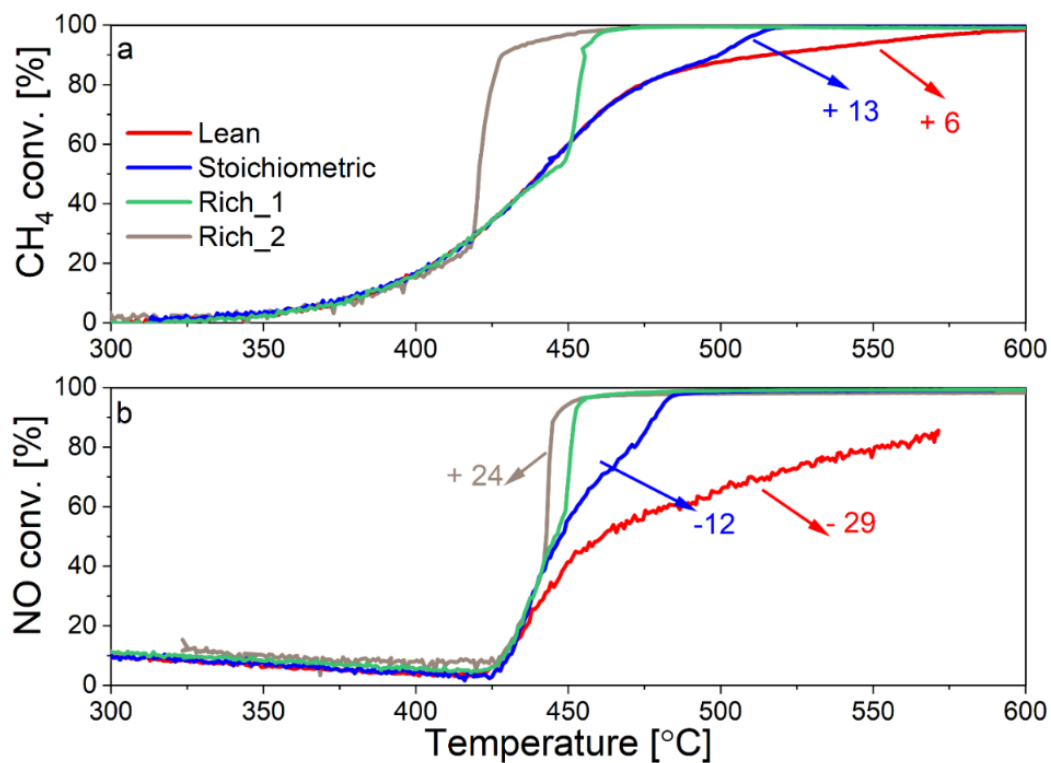
Figure C4. (a) CH$_4$ and (b) NO conversions under static lean (5980 ppm O$_2$; λ = 1.001), stoichiometric (5700 ppm O$_2$; λ = 1.0), rich_1 (4845 ppm O$_2$; λ = 0.996) and rich_2 (4275 ppm O$_2$; λ = 0.993) conditions shifted in order to overlap in the low temperature range. The numerical values indicate the extent of the shift applied. Conditions: 1500 ppm CH$_4$, 1600 ppm NO, 7000 ppm CO, 5 vol% H$_2$O; WHSV = 240 Lh^{-1}g^{-1}.
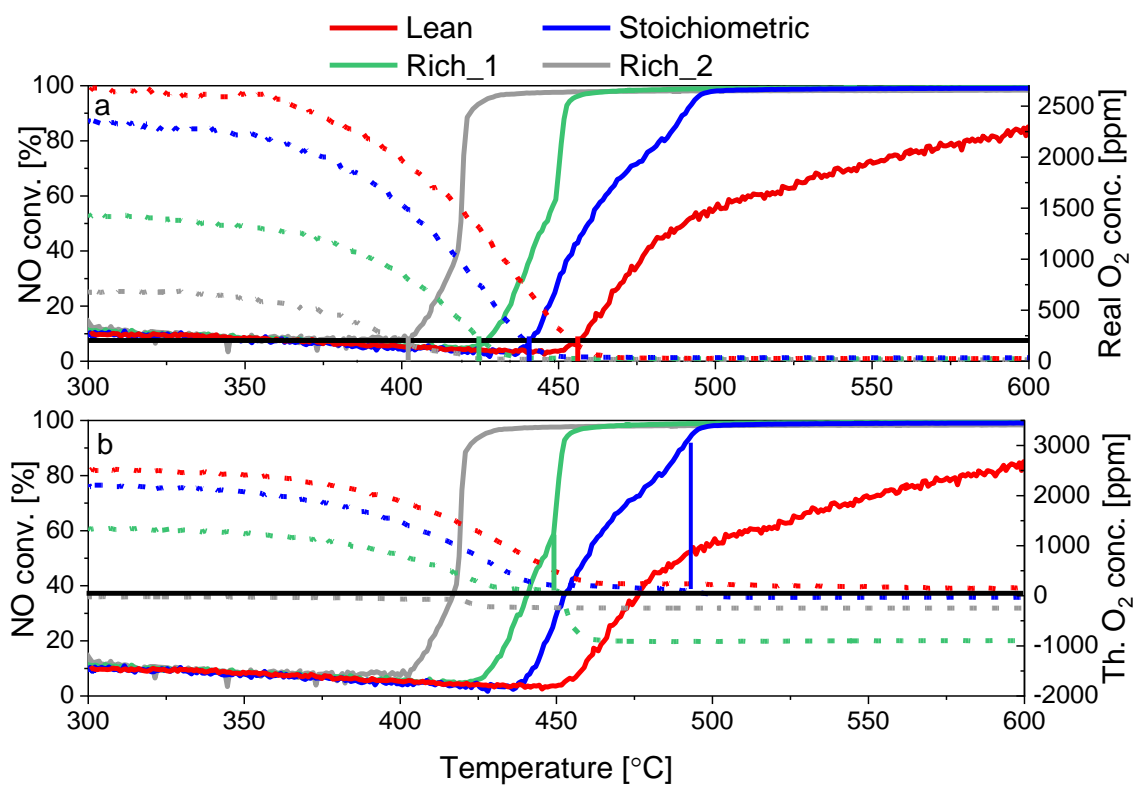
Figure C5. NO conversion under static lean (5980 ppm O_2; $\lambda = 1.001$), stoichiometric (5700 ppm O_2; $\lambda = 1.0$), rich_1 (4845 ppm O_2; $\lambda = 0.996$) and rich_2 (4275 ppm O_2; $\lambda = 0.993$) conditions as well as (a) the real O_2 concentration in the reactive feed (dashed) and (b) the theoretical O_2 concentration (dashed). Conditions: 1500 ppm CH_4, 1600 ppm NO, 7000 ppm CO, 5 vol% H_2O; WHSV = 240 $Lh^{-1}g^{-1}$.
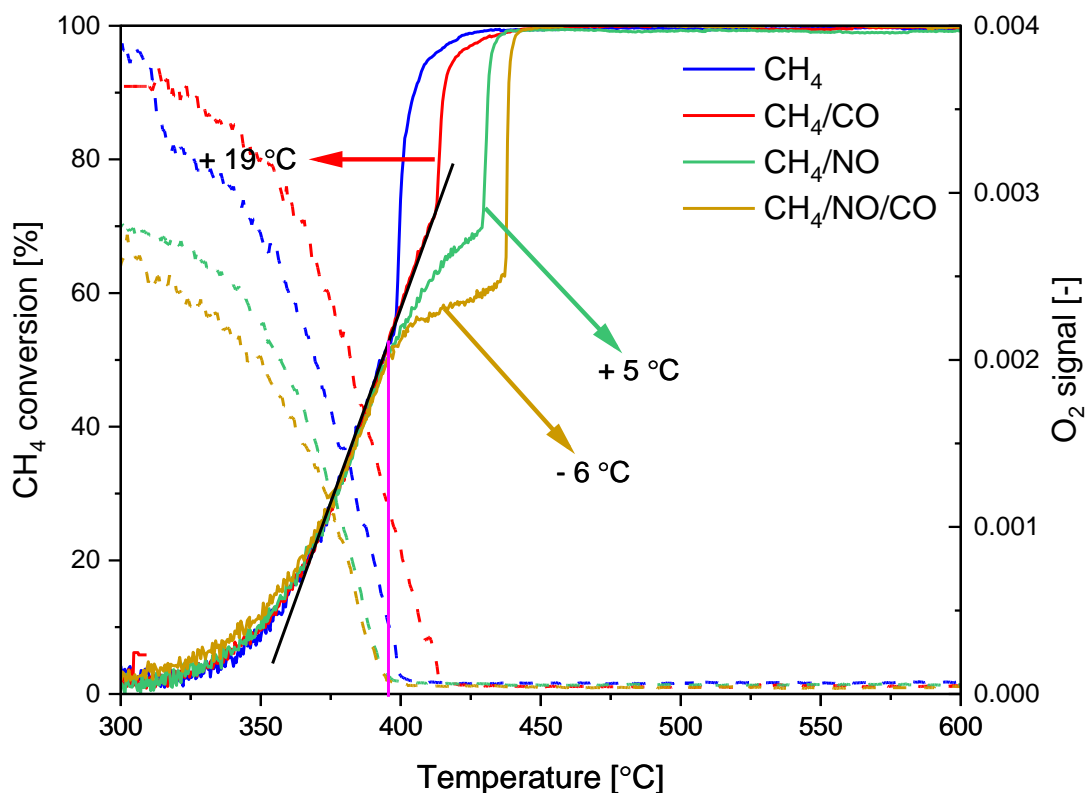
Figure C6. CH$_4$ conversion (—) as well as MS signal of O$_2$ (---) under static stoichiometric conditions in CH$_4$/O$_2$/H$_2$O, CH$_4$/CO/O$_2$/H$_2$O, CH$_4$/NO/O$_2$/H$_2$O and CH$_4$/NO/CO/O$_2$/H$_2$O feeds. The numerical values indicate the extent of the shift applied. The black line indicates the reaction rate of CH$_4$ oxidation at low temperatures. The pink line indicates the moment at which the reaction rate of CH$_4$ oxidation deviates in the presence of NO, which also corresponds to the point of full consumption of O$_2$. Conditions: (blue) 1500 ppm CH$_4$, 3000 ppm O$_2$, 5 vol% H$_2$O, (red) 1500 ppm CH$_4$, 1600 ppm NO, 2200 ppm O$_2$, 5 vol% H$_2$O, (green) 1500 ppm CH$_4$, 7000 ppm CO, 6500 ppm O$_2$, 5 vol% H$_2$O, (brown) 1500 ppm CH$_4$, 1600 ppm NO, 7000 ppm CO, 5700 ppm O$_2$, 5 vol% H$_2$O; WHSV = 240 Lh^{-1}g^{-1}.

Table C1. Dithering efficiency, η_d, obtained when pulsing 1000 ppm O_2/Ar in Ar (WHSV = 240 Lh^{-1}g^{-1}) at room temperature at different amplitudes (A) and frequencies (F). The pulsing flows correspond to the flows needed to reach amplitudes of + 5130, + 4560 + 3990, + 2850, and + 1710 ppm O_2 around stoichiometry (1500 ppm CH$_4$, 1600 ppm NO, 7000 ppm CO, 5 vol% H$_2$O).

A [ppm]	+ 5130		+ 4560		+ 3990		+ 2850		+ 1710	
	η_d [%]		η_d [%]		η_d [%]		η_d [%]		η_d [%]	
F [Hz]	Lean	Rich	Lean	Rich	Lean	Rich	Lean	Rich	Lean	Rich
0.025	95.07	14.87	73.65	9.50	66.49	9.05	66.39	10.57	42.90	8.57
0.033	77.00	14.34	59.49	10.21	53.40	10.30	52.77	11.11	34.55	8.93
0.05	53.49	14.15	41.93	9.46	36.60	9.50	36.11	10.3	21.47	7.60
0.1	24.19	11.02	16.67	8.15	14.69	6.30	13.60	5.37	10.60	2.80
0.2	3.76	3.76	2.77	2.77	2.23	2.23	2.40	2.40	1.90	1.90
0.5	0	0	0	0	0	0	0	0	0	0

Table C2. Real oxygen concentration obtained when pulsing 1000 ppm O_2/Ar in Ar (WHSV = 240 $Lh^{-1}g^{-1}$) at room temperature at different amplitudes (A) and frequencies (F). The pulsing flows correspond to the flows needed to reach amplitudes of + 5130, + 4560 + 3990, + 2850, and + 1710 ppm O_2 around stoichiometry (1500 ppm CH_4, 1600 ppm NO, 7000 ppm CO, 5 vol% H_2O).

A [ppm]	+ 5130		+ 4560		+ 3420		+ 2850		+ 1710	
	$[O_2]_{expected}$ [ppm]		$[O_2]_{expected}$ [ppm]		$[O_2]_{expected}$ [ppm]		$[O_2]_{expected}$ [ppm]		$[O_2]_{expected}$ [ppm]	
Baseline	3135		3420		3990		4275		4845	
Pulsed	5130		4560		3420		2850		1710	
Baseline + Pulsed	8265		7980		7410		7125		6555	
Average	5700		5700		5700		5700		5700	
F [Hz]	$[O_2]_{real}$ [ppm]		$[O_2]_{real}$ [ppm]		$[O_2]_{real}$ [ppm]		$[O_2]_{real}$ [ppm]		$[O_2]_{real}$ [ppm]	
	Lean	Rich	Lean	Rich	Lean	Rich	Lean	Rich	Lean	Rich
	Average		Average		Average		Average		Average	
0.025	7910	3780	6890	3960	6250	4320	6170	4580	5510	4920
	5850		5430		5290		5380		5210	
0.033	6980	3760	6240	4000	5810	4360	5780	4590	5360	4920
	5370		5120		5090		5190		5140	
0.05	5740	3750	5440	3960	5240	4340	5310	4570	5140	4900
	4750		4700		4790		4940		5020	
0.1	4260	3590	4290	3900	4510	4230	4660	4430	4950	4820
	3920		4100		4370		4550		4890	
0.2	3210	3210	3660	3660	4090	4090	4340	4340	4800	4800
	3210		3660		4090		4340		4800	
0.5	3020	3020	3530	3530	4020	4020	4280	4280	4770	4770
	3020		3530		4020		4280		4770	
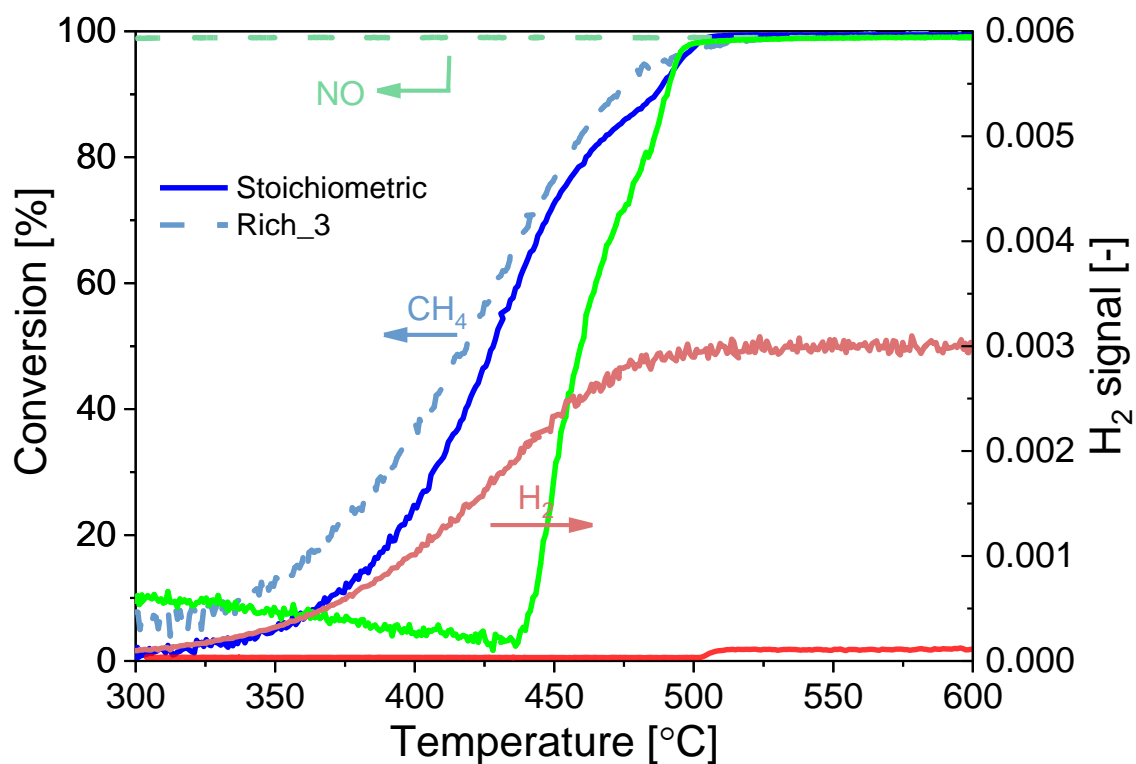
Figure C7. CH$_4$ and NO conversion as well as MS signal of H$_2$ under static stoichiometric (5700 ppm O$_2$; λ = 1.0) and rich_3 (2700 ppm O$_2$; λ = 0.984) conditions. Conditions: 1500 ppm CH$_4$, 1600 ppm NO, 7000 ppm CO, 5 vol% H$_2$O; WHSV = 240 Lh^{-1}g^{-1}.

Table C3. CH_4 and NO conversion in the high conversion regime (oxidation by H_2O) and the corresponding theoretical O_2 concentration in the rich and lean pulses, and the average of both, when performing O_2 dithering (3990 + 3420 ppm O_2 and 0.05 Hz). The initial CH_4 conversion value was taken from the temperature ramp performed in 2700 ppm O_2 ($\lambda = 0.984$) at 400 °C; then, CH_4 conversion was calculated based on the reaction rate increase of 12 $umol_{CH_4}/mol_{Pd}/s$. Conditions: 1500 ppm CH_4, 1600 ppm NO, 7000 ppm CO, 5 vol% H_2O; $\lambda = 1 \pm 0.018$; WHSV = 240 $Lh^{-1}g^{-1}$. The error in the prediction is given in blue. The start of the high conversion regime is indicated in red ($[O_2]_{th} < 84$ ppm). The blue number indicates a calculated value not matching the experimental result.

Temperature [°C]	CH_4 conversion [%]	NO conversion [%]	$[O_2]_{th\_lean}$ [ppm][a,b]	$[O_2]_{th\_rich}$ [ppm][a,b]	$[O_2]_{th\_average}$[a,b] [ppm]
400	37.6	100	1415	508	962
405	42.05	100	1282	375	828
410	46.5	100	1015	241	628
415	50.95	100	1015	108	561
420	55.4	100	881	**-26**	428
425	59.85	100	748	**-159**	294
430	64.3	100	614	**-293**	161
435	68.75	100	481	**-426**	27
440	73.2	100	347	**-560**	**-106**

[a] Considering NO conversion.

[b] Adapting the O_2 concentration seen by the catalyst based on the η_d (Table C1).
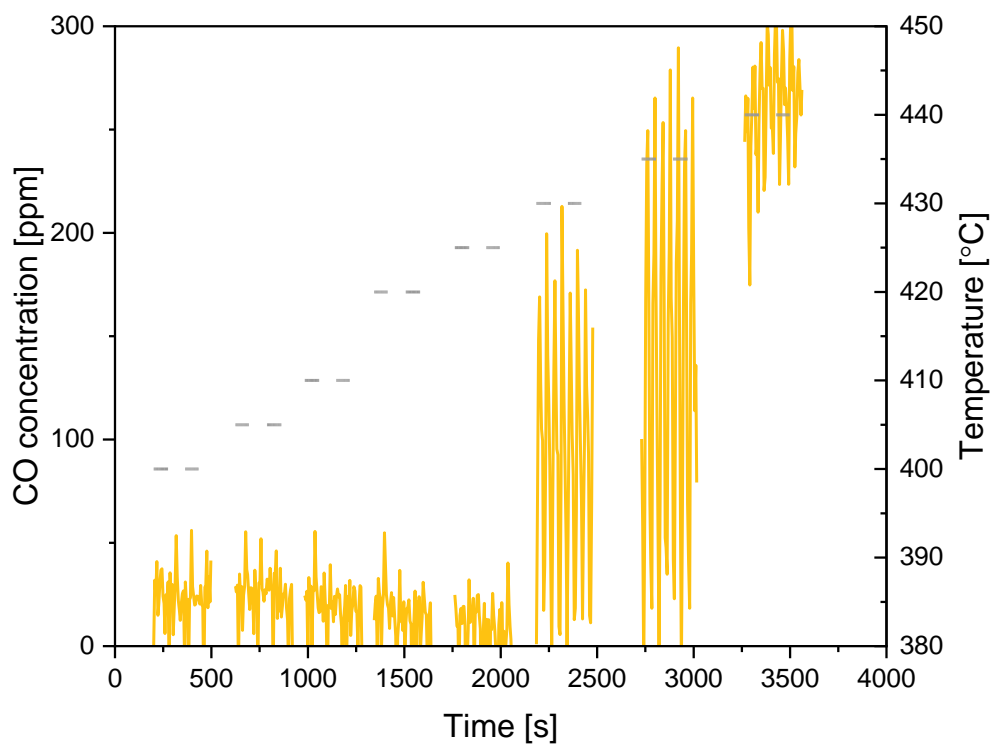
Figure C8. CO concentration at different temperatures (dashed grey) under O_2-dithering conditions (3990 + 3420 ppm O_2 and 0.05 Hz). Conditions: 1500 ppm CH_4, 1600 ppm NO, 7000 ppm CO, 5 vol% H_2O; $\lambda = 1 \pm 0.018$; WHSV = 240 $Lh^{-1}g^{-1}$.
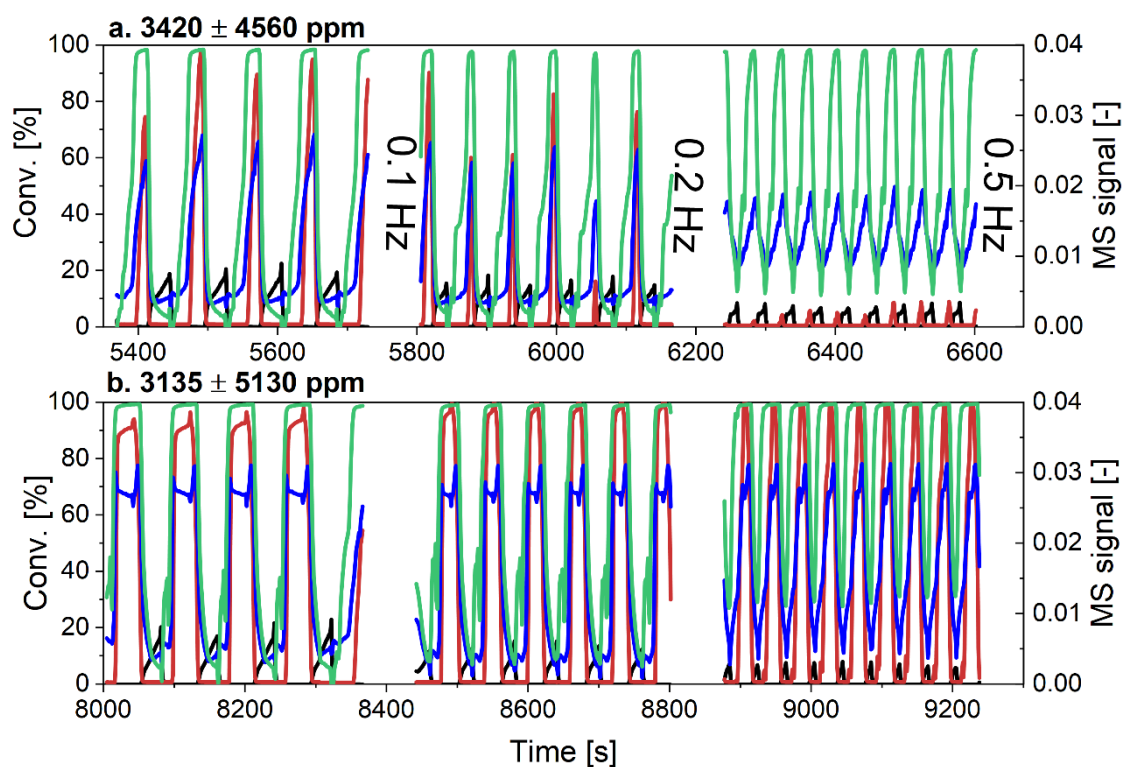
Figure C9. CH_4 (blue) and NO (green) conversion as well as MS signals of H_2 (red) and O_2 (black) under O_2-dithering at 410 °C at frequencies of 0.1, 0.2 and 0.5 Hz and amplitude of (a) 3420 + 4560 ppm O_2, (b) 3135 + 5130 ppm O_2. Conditions: 1500 ppm CH_4, 1600 ppm NO, 7000 ppm CO, 5 vol% H_2O; (a) $\lambda = 1 \pm 0.024$ and (b) $\lambda = 1 \pm 0.027$; WHSV = 240 $Lh^{-1}g^{-1}$.

Table C4. O_2 concentration calculated in the low conversion regime (oxidation by O_2) for amplitudes (A) of 3135 + 5130, 3420 + 4560, 3990 + 3420 and 4275 + 2850 ppm O_2 and frequencies (F) of 0.025, 0.033, 0.05, 0.1, 0.2 and 0.5 Hz at 410 °C. The concentrations were calculated based on the initial O_2 concentrations, the dithering efficiency (Table C1), and CH_4 and NO conversion at 410 °C (retrieved Table 5.1). Conditions: 1500 ppm CH_4, 1600 ppm NO, 7000 ppm CO, 5 vol% H_2O; $\lambda = 1 \pm 0.027$, $\lambda = 1 \pm 0.024$, $\lambda = 1 \pm 0.018$, and $\lambda = 1 \pm 0.015$; WHSV = 240 $Lh^{-1}g^{-1}$. The start of the high conversion regime is indicated in red ($[O_2]_{th} < 84$ ppm).

A [ppm]	+ 5130		+ 4560		+ 3420		+ 2850	
	$[O_2]_{expected}$ [ppm]		$[O_2]_{expected}$ [ppm]		$[O_2]_{expected}$ [ppm]		$[O_2]_{expected}$ [ppm]	
Baseline	3135		3420		3990		4275	
Pulsed	5130		4560		3420		2850	
Baseline + Pulsed	8265		7980		7410		7125	
F [Hz]	$[O_2]_{th}{}^{a}$ [ppm]		$[O_2]_{th}{}^{a}$ [ppm]		$[O_2]_{th}{}^{a}$ [ppm]		$[O_2]_{th}{}^{a}$ [ppm]	
	Lean	Rich	Lean	Rich	Lean	Rich	Lean	Rich
	Average		Average		Average		Average	
0.025	3894	**-229**	2875	**-50**	2238	308	2161	564
	1832		1413		1273		1362	
0.033	2965	**-256**	2230	**-17**	1798	350	1771	580
	1354		1106		1074		1175	
0.05	1628	**-304**	1429	**-52**	1230	323	1295	557
	662		689		776		925	
0.1	250	**-427**	277	**-111**	498	216	651	416
	-88		**83**		356		533	
0.2	**-800**	**-800**	**-357**	**-357**	**79**	**79**	331	331
	-800		**-357**		**79**		330	
0.5	**-993**	**-993**	**-483**	**-483**	**4**	**4**	262	262
	-993		**-483**		**4**		262	

[a] Considering 19.9 % CH_4 conversion and 10.5 % NO conversion (Table 5.1) and η_d (Table C1).

Table C5. O_2 concentration calculated in the high conversion regime (oxidation by H_2O) for amplitudes (A) of 3135 + 5130, 3420 + 4560, 3990 + 3420 and 4275 + 2850 ppm O_2 and frequencies (F) of 0.025, 0.033, 0.05, 0.1, 0.2 and 0.5 Hz at 410 °C. The concentrations were calculated based on the O_2 concentrations initially fed, the dithering efficiency (Table C1), and CH_4 and NO conversion at 410 °C (retrieved from Table C3). Conditions: 1500 ppm CH_4, 1600 ppm NO, 7000 ppm CO, 5 vol% H_2O; $\lambda = 1 \pm 0.027$, $\lambda = 1 \pm 0.024$, $\lambda = 1 \pm 0.018$, and $\lambda = 1 \pm 0.015$; WHSV = 240 $Lh^{-1}g^{-1}$. The start of the high conversion regime is indicated in red ($[O_2]_{th} < 84$ ppm).

A [ppm]	+ 5130		+ 4560		+ 3420		+ 2850	
	$[O_2]_{expected}$ [ppm]		$[O_2]_{expected}$ [ppm]		$[O_2]_{expected}$ [ppm]		$[O_2]_{expected}$ [ppm]	
Baseline	3135		3420		3990		4275	
Pulsed	5130		4560		3420		2850	
Baseline + Pulsed	8265		7980		7410		7125	
F [Hz]	$[O_2]_{th}{}^a$ [ppm]		$[O_2]_{th}{}^a$ [ppm]		$[O_2]_{th}{}^a$ [ppm]		$[O_2]_{th}{}^a$ [ppm]	
	Lean	Rich	Lean	Rich	Lean	Rich	Lean	Rich
	Average		Average		Average		Average	
0.025	3812	**-311**	2793	**-132**	2156	226	2079	482
	1750		1331		1191		1281	
0.033	2883	**-338**	2148	**-99**	1716	268	1689	498
	1272		1024		992		1093	
0.05	1546	**-386**	1347	**-134**	1148	241	1213	475
	580		607		695		844	
0.1	168	**-509**	195	**-193**	416	134	569	334
	-170		**1**		275		451	
0.2	**-882**	**-882**	**-439**	**-439**	**-3**	**-3**	249	249
	-882		**-439**		**-3**		249	
0.5	**-1075**	**-1075**	**-565**	**-565**	**-78**	**-78**	180	180
	-1075		**-565**		**-78**		180	

[a] Considering 49.35 % CH_4 conversion and 100 % NO conversion (Table C3) and η_d (Table C1).

Table C6. O_2 concentration calculated in the low conversion regime (oxidation by O_2) for amplitudes (A) of 3135 + 5130, 3420 + 4560, 3990 + 3420 and 4275 + 2850 ppm O_2 and frequencies (F) of 0.025, 0.033, 0.05, 0.1, 0.2 and 0.5 Hz at 410 °C. The concentrations were calculated only based on the O_2 concentrations initially fed and CH_4 and NO conversions at 410 °C (retrieved from Table 5.1). Conditions: 1500 ppm CH_4, 1600 ppm NO, 7000 ppm CO, 5 vol% H_2O; $\lambda = 1 \pm 0.027$, $\lambda = 1 \pm 0.024$, $\lambda = 1 \pm 0.018$, and $\lambda = 1 \pm 0.015$; WHSV = 240 $Lh^{-1}g^{-1}$. The start of the high conversion regime is indicated in red ($[O_2]_{th} < 84$ ppm).

A [ppm]	+ 5130		+ 4560		+ 3420		+ 2850	
	$[O_2]_{expected}$ [ppm]		$[O_2]_{expected}$ [ppm]		$[O_2]_{expected}$ [ppm]		$[O_2]_{expected}$ [ppm]	
Baseline	3135		3420		3990		4275	
Pulsed	5130		4560		3420		2850	
Baseline + Pulsed	8265		7980		7410		7125	
F [Hz]	$[O_2]_{th}$[a] [ppm]		$[O_2]_{th}$[a] [ppm]		$[O_2]_{th}$[a] [ppm]		$[O_2]_{th}$[a] [ppm]	
	Lean	Rich	Lean	Rich	Lean	Rich	Lean	Rich
	Average		Average		Average		Average	
0.025	4336	**-794**	4051	**-509**	3481	**-61**	3196	346
	1771		1771		1771		1771	
0.033	4336	**-794**	4051	**-509**	3481	**-61**	3196	346
	1771		1771		1771		1771	
0.05	4336	**-794**	4051	**-509**	3481	**-61**	3196	346
	1771		1771		1771		1771	
0.1	4336	**-794**	3481	**-509**	3481	**-61**	3196	346
	1771		1771		1771		1771	
0.2	4336	**-794**	4051	**-509**	3481	**-61**	3196	346
	1771		1771		1771		1771	
0.5	4336	**-794**	4051	**-509**	3481	**-61**	3196	346
	1771		1771		1771		1771	

[a] Considering 19.9 % CH_4 conversion and 10.5 % NO conversion (Table 5.1).

Table C7. O_2 concentration calculated in the low conversion regime (oxidation by O_2) for amplitudes (A) of 3135 + 5130, 3420 + 4560, 3990 + 3420, 4275 + 2850, and 4845 + 1710 ppm O_2 and frequencies (F) of 0.025, 0.033, 0.05, 0.1, 0.2 and 0.5 Hz at 435 °C. The concentrations were calculated based on the O_2 concentrations initially fed, the dithering efficiency (Table C1), and CH_4 and NO conversion at 435 °C, retrieved from Table 5.1). Conditions: 1500 ppm CH_4, 1600 ppm NO, 7000 ppm CO, 5 vol% H_2O; λ = 1 ± 0.027, λ = 1 ± 0.024, λ = 1 ± 0.018, λ = 1 ± 0.015, and λ = 1 ± 0.009; WHSV = 240 $Lh^{-1}g^{-1}$. The error in the prediction is given in blue. The start of the high conversion regime is indicated in red ($[O_2]_{th} < 84$ ppm). The blue number indicates a calculated value not matching the experimental result.

A [ppm]	+ 5130		+ 4560		+ 3420		+ 2850		+ 1710	
	$[O_2]_{expected}$ [ppm]		$[O_2]_{expected}$ [ppm]		$[O_2]_{expected}$ [ppm]		$[O_2]_{expected}$ [ppm]		$[O_2]_{expected}$ [ppm]	
Baseline	3135		3420		3990		4275		4845	
Pulsed	5130		4560		3420		2850		1710	
Baseline + Pulsed	8265		7980		7410		7125		6555	
F [Hz]	$[O_2]_{th}^a$ [ppm]		$[O_2]_{th}^a$ [ppm]		$[O_2]_{th}^a$ [ppm]		$[O_2]_{th}^a$ [ppm]		$[O_2]_{th}^a$ [ppm]	
	Lean	Rich	Lean	Rich	Lean	Rich	Lean	Rich	Lean	Rich
	Average		Average		Average		Average		Average	
0.025	3301	**-821**	2283	**-642**	1645	**-284**	1568	-28	902	312
	1 240		820		681		770		607	
0.033	2372	**-849**	1637	**-610**	1206	**-242**	1179	**-13**	759	318
	762		514		482		582		538	
0.05	1036	**-897**	837	**-644**	638	**-269**	702	**-36**	534	295
	70		96		184		333		414	
0.1	**-342**	**-1019**	**-315**	**-704**	**-95**	**-377**	**58**	**-177**	347	213
	-681		**-510**		**-236**		**-59**		279	
0.2	**-1392**	**-1392**	**-949**	**-949**	**-514**	**-514**	**-262**	**-262**	197	197
	-1392		**-949**		**-514**		**-261**		197	
0.5	**-1586**	**-1586**	**-1076**	**-1076**	**-589**	**-589**	**-331**	**-331**	165	165
	-1586		**-1076**		**-589**		**-331**		165	

[a] Considering 39.65 % CH_4 conversion and 10.5 % NO conversion (Table 5.1) and $η_d$ (Table C1).
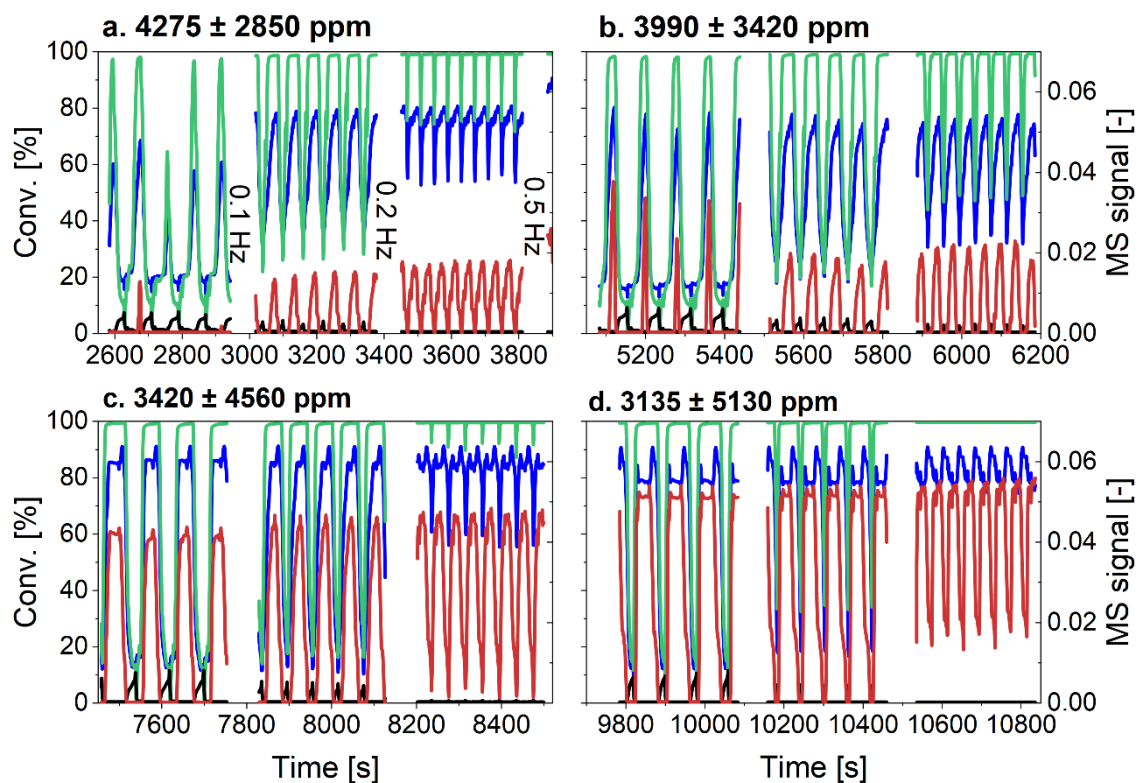
Figure C10. CH_4 (blue) and NO (green) conversions as well as MS signals of H_2 (red) and O_2 (black) under O_2-dithering at 435 °C at frequencies of 0.1, 0.2 and 0.5 Hz and amplitude of (a) 4275 + 2850 ppm O_2, (b) 3990 + 3420 ppm O_2, (c) 3420 + 4560 ppm O_2, (d) 3135 + 5130 ppm O_2. Conditions: 1500 ppm CH_4, 1600 ppm NO, 7000 ppm CO, 5 vol% H_2O; (a) $\lambda = 1 \pm 0.015$, (b) $\lambda = 1 \pm 0.018$, (c) $\lambda = 1 \pm 0.024$ and (d) $\lambda = 1 \pm 0.027$; WHSV = 240 $Lh^{-1}g^{-1}$.

Table C8. O_2 concentration calculated for amplitudes (A) of 3135 + 5130, 3420 + 4560, 3990 + 3420, 4275 + 2850, and 4845 + 1710 ppm O_2 and frequencies (F) of 0.025, 0.033, 0.05, 0.1, 0.2 and 0.5 Hz at 435 °C, in the high conversion regime (oxidation by H_2O). The concentrations were calculated based on the O_2 concentrations initially fed, the dithering efficiency (Table C1), and CH_4 and NO conversions at 435 °C, retrieved from Table C3. Conditions: CH_4: 1500 ppm, NO: 1600 ppm, CO: 7000 ppm, H_2O: 5 vol%; $\lambda = 1 \pm 0.027$, $\lambda = 1 \pm 0.024$, $\lambda = 1 \pm 0.018$, $\lambda = 1 \pm 0.015$, and $\lambda = 1 \pm 0.009$; WHSV = 240 $Lh^{-1}g^{-1}$. The start of the high conversion regime is indicated in red ($[O_2]_{th} < 84$ ppm).

A [ppm]	+ 5130		+ 4560		+ 3420		+ 2850		+ 1710	
	$[O_2]_{expected}$ [ppm]		$[O_2]_{expected}$ [ppm]		$[O_2]_{expected}$ [ppm]		$[O_2]_{expected}$ [ppm]		$[O_2]_{expected}$ [ppm]	
Baseline	3135		3420		3990		4275		4845	
Pulsed	5130		4560		3420		2850		1710	
Baseline + Pulsed	8265		7980		7410		7125		6555	
F [Hz]	$[O_2]_{th}{}^a$ [ppm]		$[O_2]_{th}{}^a$ [ppm]		$[O_2]_{th}{}^a$ [ppm]		$[O_2]_{th}{}^a$ [ppm]		$[O_2]_{th}{}^a$ [ppm]	
	Lean	Rich	Lean	Rich	Lean	Rich	Lean	Rich	Lean	Rich
	Average		Average		Average		Average		Average	
0.025	3144	**-978**	2126	**-799**	1488	**-441**	1411	**-185**	745	155
	1083		663		524		613		450	
0.033	2215	**-1006**	1480	**-767**	1049	**-399**	1022	**-170**	602	161
	605		357		325		426		381	
0.05	879	**-1054**	680	**-801**	481	**-426**	545	**-193**	377	138
	-87		**-61**		27		176		258	
0.1	**-499**	**-1176**	**-472**	**-861**	**-252**	**-534**	**-99**	**-334**	190	56
	-838		**-667**		**-393**		**-216**		1123	
0.2	**-1549**	**-1549**	**-1106**	**-1106**	**-671**	**-671**	**-419**	**-419**	40	40
	-1549		**- 1106**		**-671**		**-419**		40	
0.5	**-1743**	**-1743**	**-1233**	**-1233**	**-746**	**-746**	**-488**	**-488**	7	7
	-1743		**-1233**		**-746**		**-488**		7	

[a] Considering 68.75 % CH_4 conversion and 10.5 % NO conversion (Table C3) and η_d (Table C1).

Table C9. O_2 concentration calculated for dithering conditions: 3990 + 3420 ppm O_2 and 0.05 Hz at 435 °C, in the low and high conversion regimes, for different CH_4 concentrations. The O_2 concentrations were calculated based on the O_2 concentrations initially fed, the dithering efficiency (Table C1), and CH_4 and NO conversions at 435 °C where CH_4 conversion was recalculated as a function of the concentration. Conditions: variable CH_4, 1600 ppm NO, 7000 ppm CO, 5 vol% H_2O; $\lambda = 1 \pm 0.018$; WHSV = 240 $Lh^{-1}g^{-1}$. The start of the high conversion regime is indicated in red ($[O_2]_{th}$ < 84 ppm).

CH$_4$ conc. [ppm]	CH$_4$ conv. [%]		$[O_2]_{expected}$ [ppm]			$[O_2]_{th}$ at 10.5 % NO conv. [ppm]^{a,c}		$[O_2]_{th}$ at 100 % NO conv. [ppm]^{b,c}	
	10.5 % NO	100 % NO	Baseline	Pulsed	Baseline + Pulsed	Lean	Rich	Lean	Rich
						Average		Average	
0	-	-	2000	1585	3585	-1080	-1300	-360	-580
						-1 190		-470	
200	100	100	2260	1840	4100	-1161	-1416	-441	-696
						-1289		-569	
400	100	100	2510	2090	4600	-1261	-1651	-541	-931
						-1456		-736	
600	99.1	100	2760	2350	5110	-1001	-1607	-291	-898
						-1304		-595	
800	74.3	100	3020	2600	5620	-651	-1322	-341	-1 012
						-986		-677	
1000	59.5	100	3260	2186	6120	-317	-1055	-405	-1143
						-686		-774	
1200	49.6	85.9	3510	3110	6620	24	-779	-129	-932
						-378		-531	
1400	42.5	73.7	3770	3370	7140	391	-519	238	-672
						-64		-217	
1500	39.6	68.75	4010	3360	7370	627	-280	474	-433
						173		20	
1600	37.2	64.5	4270	3490	7760	934	-8	781	-161
						463		310	
1700	35.0	60.7	4270	3620	7890	982	-4	829	-149
						493		340	
1800	33.0	57.3	4510	3750	8260	1269	257	1116	104
						763		610	

^{a} Considering CH_4 and NO conversion from Table 5.1

^{b} Considering CH_4 and NO conversion from Table C3

^{c} Considering η_d (Table C1).

Table C10. O_2 concentration calculated for dithering conditions: 3990 + 3420 ppm O_2 and 0.05 Hz at 435 °C, in the low and high conversion regimes, at different CH_4 concentrations. The O_2 concentrations were calculated based on the O_2 concentrations initially fed, the dithering efficiency (Table C1), and CH_4 and NO conversions at 435 °C retrieved from Table 5.1 and Table C4. Conditions: variable CH_4, 1600 ppm NO, 7000 ppm CO, 5 vol% H_2O; $\lambda = 1 \pm 0.018$; WHSV = 240 $Lh^{-1}g^{-1}$. The start of the high conversion regime is indicated in red ($[O_2]_{th} < 84$ ppm).

CH_4 conc. [ppm]	CH$_4$ conv. [%] 10.5 % NO	CH$_4$ conv. [%] 100 % NO	[O$_2$]$_{expected}$ [ppm] Baseline	[O$_2$]$_{expected}$ [ppm] Pulsed	[O$_2$]$_{expected}$ [ppm] Baseline + Pulsed	[O$_2$]$_{th}$ at 10.5 % NO conv. [ppm][a,c] Lean	[O$_2$]$_{th}$ at 10.5 % NO conv. [ppm][a,c] Rich	[O$_2$]$_{th}$ at 100 % NO conv. [ppm][b,c] Lean	[O$_2$]$_{th}$ at 100 % NO conv. [ppm][b,c] Rich
						Average		Average	
0	-	-	2000	1585	3585	**-1080**	**-1300**	**-360**	**-580**
						-1190		**-470**	
200	39.65	68.75	2260	1840	4100	**-924**	**-1179**	**-320**	**-575**
						-1051		**-448**	
400	39.65	68.75	2510	2090	4600	**-778**	**-1169**	**-291**	**-681**
						-974		**-486**	
600	39.65	68.75	2760	2350	5110	**-287**	**-894**	84	**-523**
						-590		**-220**	
800	39.65	68.75	3020	2600	5620	**-96**	**-767**	159	**-512**
						-431		**-177**	
1000	39.65	68.75	3260	2186	6120	**81**	**-658**	219	**-519**
						-289		**-150**	
1200	39.65	68.75	3510	3110	6620	261	**-541**	283	**-520**
						-140		**-118**	
1400	39.65	68.75	3770	3370	7140	470	**-440**	375	**-535**
						15		**-80**	
1500	39.65	68.75	4010	3360	7370	626	**-281**	473	**-435**
						172		19	
1600	39.65	68.75	4270	3490	7760	855	**-87**	644	**-299**
						384		173	
1700	39.65	68.75	4270	3620	7890	823	**-154**	554	**-424**
						334		65	
1800	39.65	68.75	4510	3750	8260	1031	**19**	704	**-309**
						525		197	

[a] Considering CH_4 and NO conversion Table 5.1

[b] Considering CH_4 and NO conversion from Table C3
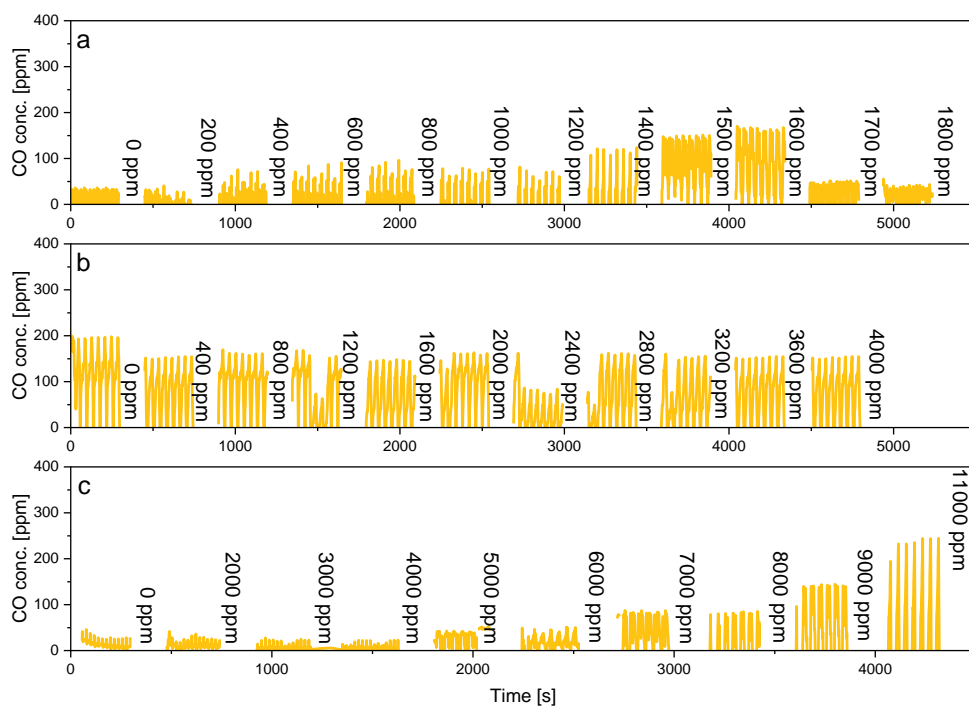
[c] Considering η_d (Table C1).

Figure C11. CO concentration at 435 °C under O_2-dithering conditions: 3990 + 3420 ppm O_2 and 0.05 Hz at 435 °C, while varying (a) CH_4 concentration from 0 to 1800 ppm, (b) NO concentration from 0 to 4000 ppm and (c) CO concentration from 0 to 11000 ppm. Conditions: 1500 ppm CH_4, 1600 ppm NO, 7000 ppm CO, 5 vol% H_2O; $\lambda = 1 \pm 0.018$; WHSV $= 240$ $Lh^{-1}g^{-1}$.

Table C11. O_2 concentration calculated for dithering conditions: 3990 + 3420 ppm O_2 and 0.05 Hz at 435 °C, in the low and high conversion regime, at different NO concentrations. The O_2 concentrations were calculated based on the O_2 concentrations initially fed, the dithering efficiency (Table C1), and CH_4 and NO conversions at 435 °C, retrieved Table 5.1 and Table C4. Conditions: 1500 ppm CH_4, variable NO, 7000 ppm CO, 5 vol% H_2O; $\lambda = 1 \pm 0.018$; WHSV = 240 $Lh^{-1}g^{-1}$. The start of the high conversion regime is indicated in red ($[O_2]_{th} < 84$ ppm).

NO conc. [ppm]	CH4 conv. [%]		[O2]expected [ppm]			[O2]th at 10.5 % NO conv. [ppm][a,c]		[O2]th at 100 % NO conv. [ppm][b,c]	
	10.5 % NO	100 % NO	Baseline	Pulsed	Baseline + Pulsed	Lean	Rich	Lean	Rich
						Average		Average	
0	39.65	68.75	4550	3900	8450	1284	230	534	**-519**
						757		75	
400	39.65	68.75	4520	3870	8390	1263	218	570	**-475**
						740		47	
800	39.65	68.75	4270	3620	7890	941	**-36**	429	**-361**
						453		**-60**	
1200	39.65	68.75	4270	3490	7760	914	**-28**	581	**-396**
						443		110	
1600	39.65	68.75	4020	3360	7380	637	**-270**	484	**-461**
						183		143	
2000	39.65	68.75	3790	3380	7160	432	**-480**	459	**-453**
						-24		3	
2400	39.65	68.75	3790	3120	6900	368	**-482**	575	**-574**
						-57		0.4	
2800	39.65	68.75	3520	3110	6630	105	**-734**	492	**-350**
						-314		73	
3200	39.65	68.75	3520	2990	6510	**70**	**-701**	637	**-134**
						-316		251	
3600	39.65	68.75	3270	2860	6130	**-207**	**-945**	540	**-198**
						-575		171	
4000	39.65	68.75	3270	2860	6130	**-187**	**-924**	740	**0**
						-556		370	
4400	39.65	68.75	3020	2600	5620	**-511**	**-1182**	596	**-75**
						-846		260	

[a] Considering CH_4 and NO conversion Table 5.1

[b] Considering CH_4 and NO conversion from Table C3

[c] Considering η_d (Table C1).

Table C12. O_2 concentration calculated in the low and high conversion regimes for dithering conditions (3990 + 3420 ppm O_2 and 0.05 Hz) at 435 °C at different CO concentrations. The O_2 concentrations were calculated based on the O_2 concentrations initially fed, the dithering efficiency (Table C1), and CH_4 and NO conversion at 435 °C, retrieved from stoichiometric temperature ramp. Conditions: 1500 ppm CH_4, 1600 ppm NO, variable CO, 5 vol% H_2O; $\lambda = 1 \pm 0.018$; WHSV = 240 $Lh^{-1}g^{-1}$. The start of the high conversion regime is indicated in red ([$O_2]_{th} < 84$ ppm).

CO conc. [ppm]	CH₄ conv. [%] 10 % NO	CH₄ conv. [%] 100 % NO	[O₂]expected [ppm] Baseline	[O₂]expected [ppm] Pulsed	[O₂]expected [ppm] Baseline + Pulsed	[O₂]th at 10.5 % NO conv. [ppm][a,c] Lean	[O₂]th at 10.5 % NO conv. [ppm][a,c] Rich	[O₂]th at 100 % NO conv. [ppm][b,c] Lean	[O₂]th at 100 % NO conv. [ppm][b,c] Rich
						Average		Average	
0	39.65	68.75	1510	1330	2840	686	501	533	348
						594		441	
1000	39.65	68.75	2010	1580	3590	739	520	586	367
						630		477	
2000			2260	1970	4230	573	300	420	147
						437		284	
3000	39.65	68.75	2520	2220	4720	387	79	354	46
						233		200	
4000	39.65	68.75	3020	2470	5490	802	165	650	12
						483		330	
5000	39.65	68.75	3270	2860	6130	693	**-45**	540	**-198**
						324		171	
6000	39.65	68.75	3770	3110	6880	795	**-44**	642	**-172**
						375		235	
7000	39.65	68.75	4020	3360	7380	637	**-270**	484	**-396**
						183		43	
8000	39.65	68.75	4280	3750	8030	539	**-473**	386	**-596**
						33		-105	
9000	39.65	68.75	4770	4000	8770	837	**-461**	684	**-614**
						188		35	
11000	39.65	68.75	5330	4640	10170	866	**-640**	2743	**-1513**
						113		614	

[a] Considering CH_4 and NO conversion Table 5.1

[b] Considering CH_4 and NO conversion from Table C3

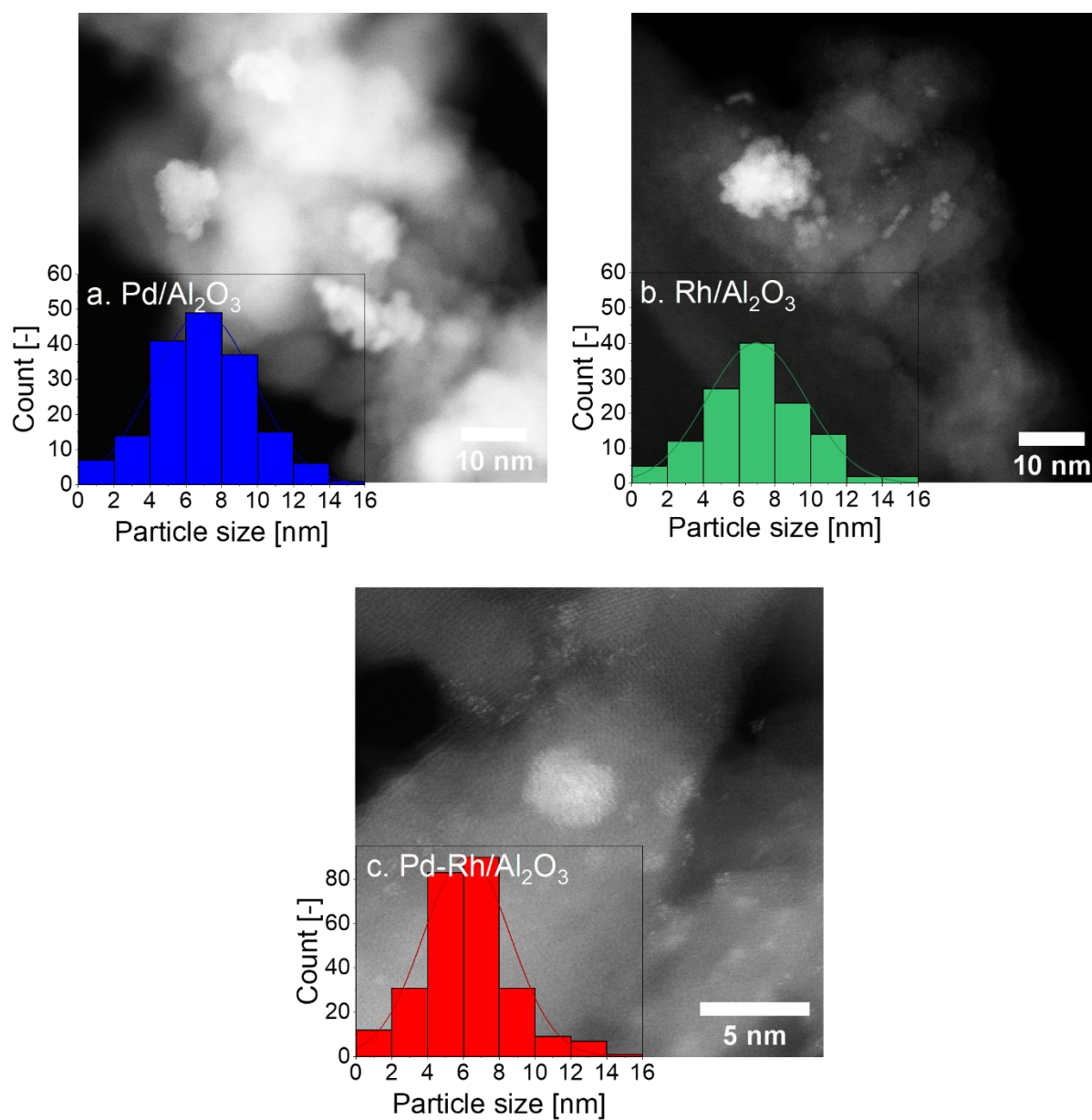[c] Considering η_d (Table C1).

Appendix D (Chapter 6)

Figure D1. Dark-field TEM images (a-c) and particles size distribution (d-f) of (a, d) Pd/Al$_2$O$_3$ (b, e) Rh/Al$_2$O$_3$ and (c, f) Pd-Rh/Al$_2$O$_3$ after calcination.
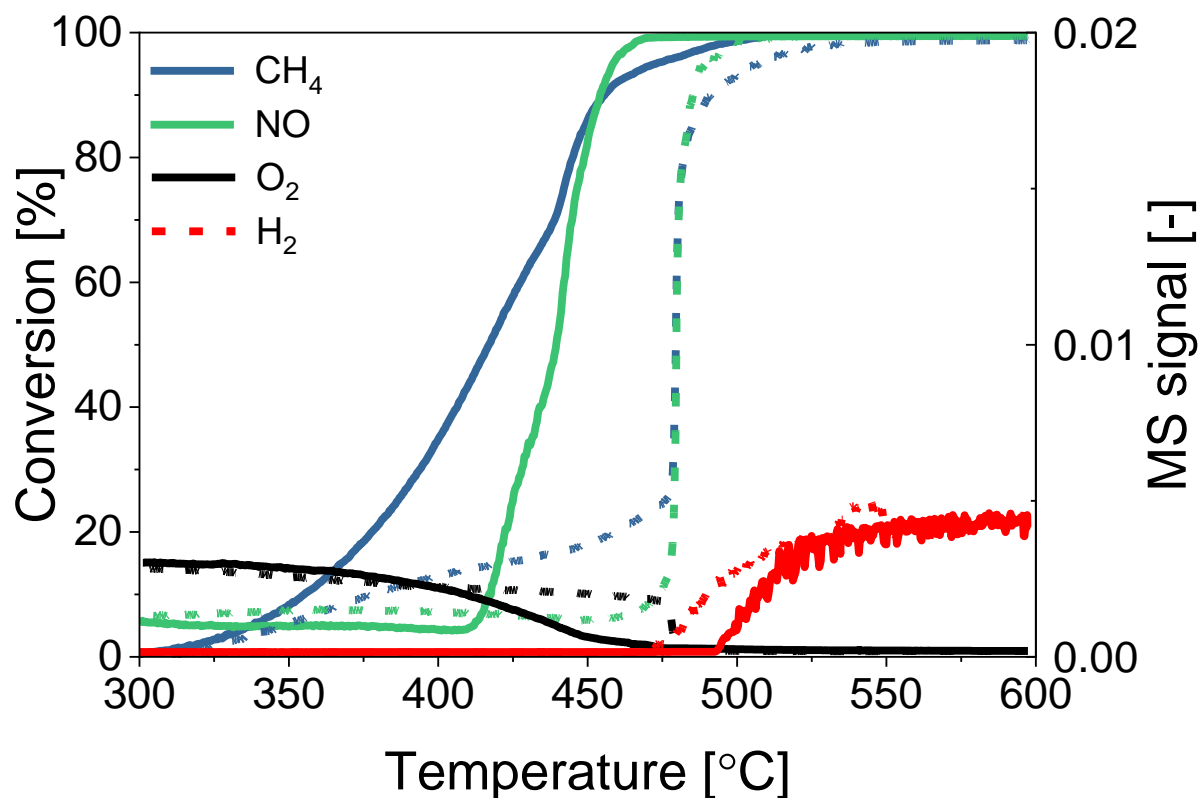
Figure D2. CH$_4$ and NO conversion as well as O$_2$ and H$_2$ MS signal during heating (——) and cooling (- - -) segments performed under static stoichiometric (5700 ppm O$_2$; λ = 1.0) conditions over Pd/Al$_2$O$_3$ (2nd cycle). The catalytic measurements were performed after an oxidative pre-treatment. Conditions: 1500 ppm CH$_4$, 1600 ppm NO, 7000 ppm CO, 5700 ppm O$_2$, 5 vol% H$_2$O; WHSV = 240 Lh^{-1}g^{-1}.
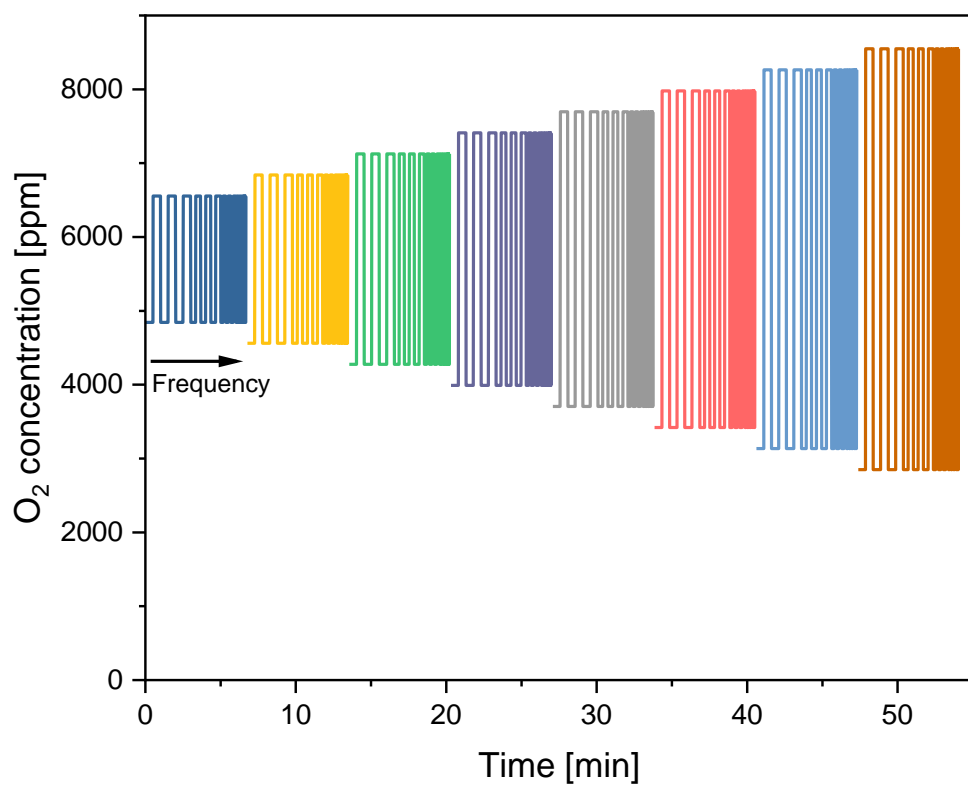
Figure D3. Scheme of the isothermal O_2 pulses experiment.

Table D1. O_2 concentration present in the lean and rich phases of the pulses as well as the average concentration over the full dithering period, at the different amplitudes (A) and frequencies (F) evaluated. The results are analysed for Pd/Al$_2$O$_3$. In red are the values below 4540 ppm O_2, wherein high conversions of CH$_4$ and NO are induced. In blue are the values between 4640 and 4540 ppm O_2, at which high NO conversions are promoted. In purple is the mismatch between calculations and experimental results.

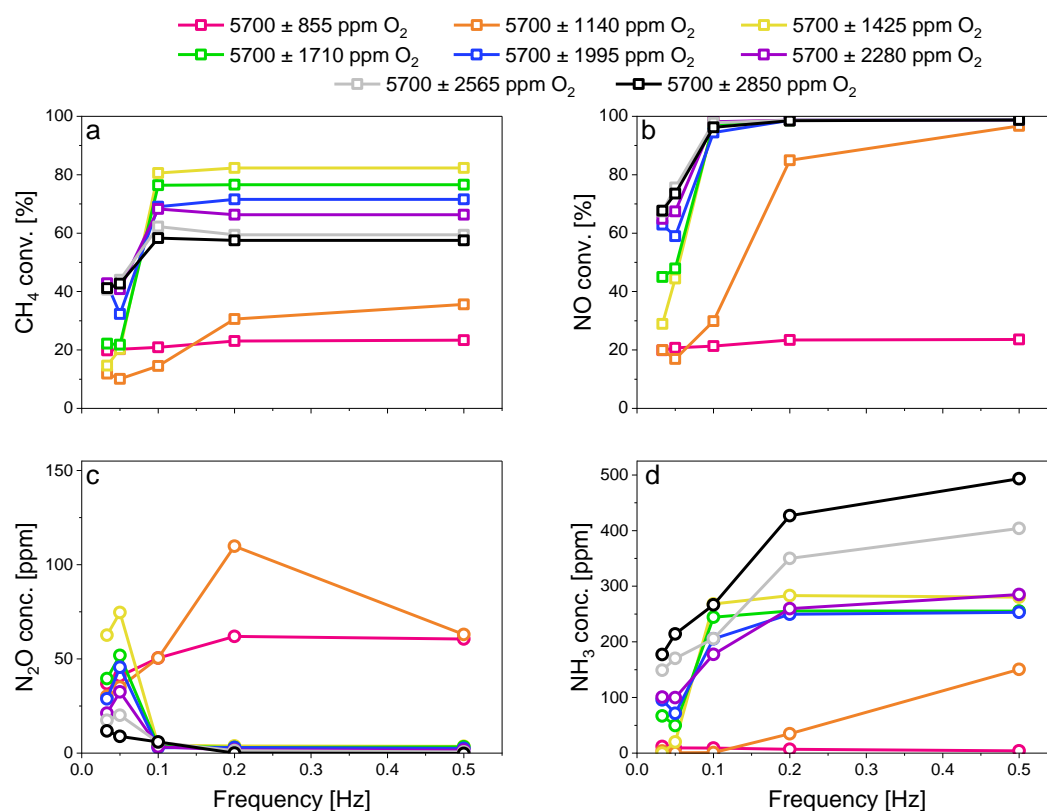| F [Hz]	0.033		0.05		0.1		0.2		0.5	
	[O$_2$] [ppm]		[O$_2$] [ppm]		[O$_2$] [ppm]		[O$_2$] [ppm]		[O$_2$] [ppm]	
A [ppm]	Lean	Rich	Lean	Rich	Lean	Rich	Lean	Rich	Lean	Rich
	Average		Average		Average		Average		Average	
5700 ± 855	4998	5436	4975	5212	4893	5026	4877	4877	4845	4845
	5217		5094		4960		4877		4845	
5700 ± 1140	4788	5555	4764	5216	4653	4836	4609	4609	4560	4560
	5172		4990		4745		4609		4560	
5700 ± 1425	4592	5779	4569	5304	4428	4663	4343	4343	4275	4275
	5185		4936		4545		4343		4275	
5700 ± 1710	4356	5806	4329	5233	4190	4474	4069	4069	3990	3990
	5081		4781		4332		4069		3990	
5700 ± 1995	4116	5836	4084	5165	3956	4291	3794	3794	3705	3705
	4976		4625		4124		3794		3705	
5700 ± 2280	3886	6133	3851	5332	3792	4180	3546	3546	3420	3420
	5009		4592		3986		3546		3420	
5700 ± 2565	3871	7085	3861	5879	3700	4376	3328	3328	3135	3135
	5478		4870		4038		3328		3135	
5700 ± 2850	3667	7239	3657	5899	3478	4229	3064	3064	2850	2850
	5453		4778		3853		3064		2850	

Figure D4. (a) CH_4 and (b) NO conversions as well as (c) N_2O and (d) NH_3 concentration under O_2-dithering conditions at 420 °C over Pd/Al_2O_3 performed at 0.025, 0.033, 0.05, 0.1, 0.2 and 0.5 Hz and amplitude of 5700 ± 855, 5700 ± 1140, 5700 ± 1425, 5700 ± 1710, 5700 ± 1995, 5700 ± 2280, 5700 ± 2565 and 5700 ± 2850 ppm O_2. Conditions: 1500 ppm CH_4, 1600 ppm NO, 7000 ppm CO, 5 vol% H_2O; WHSV = 240 $Lh^{-1}g^{-1}$.
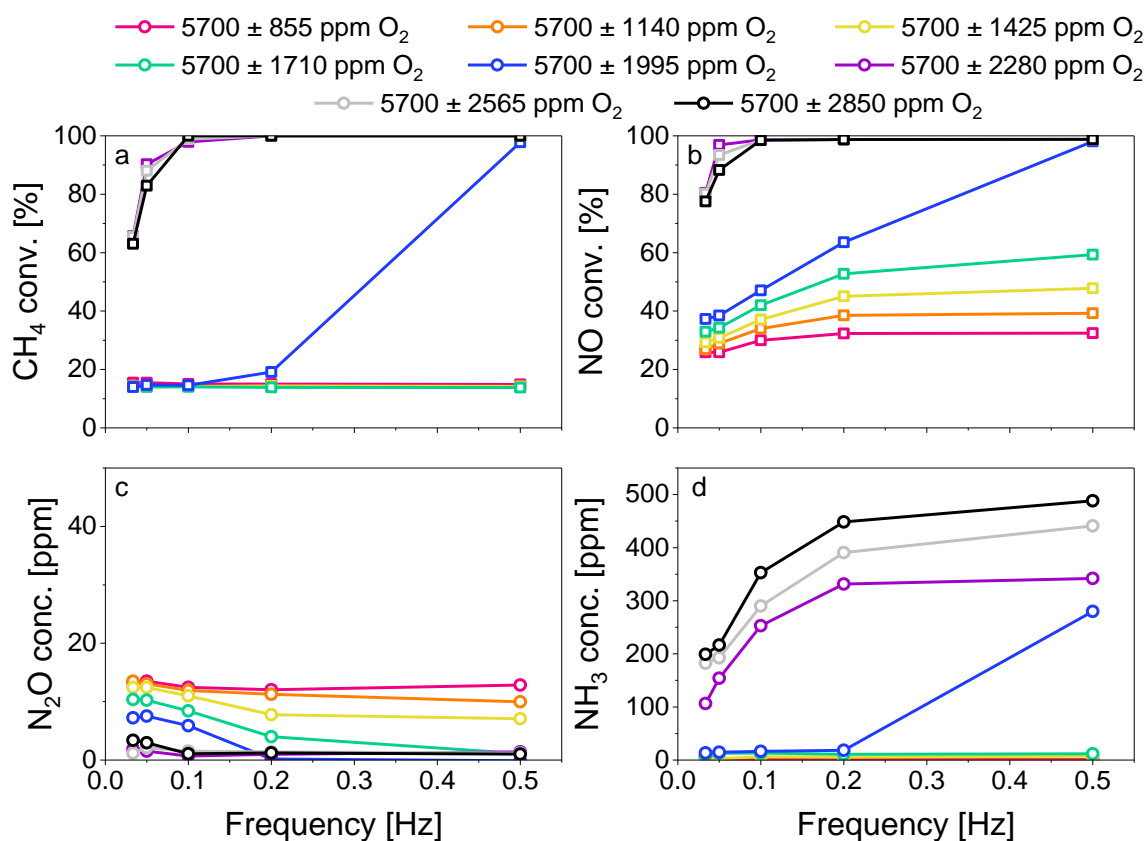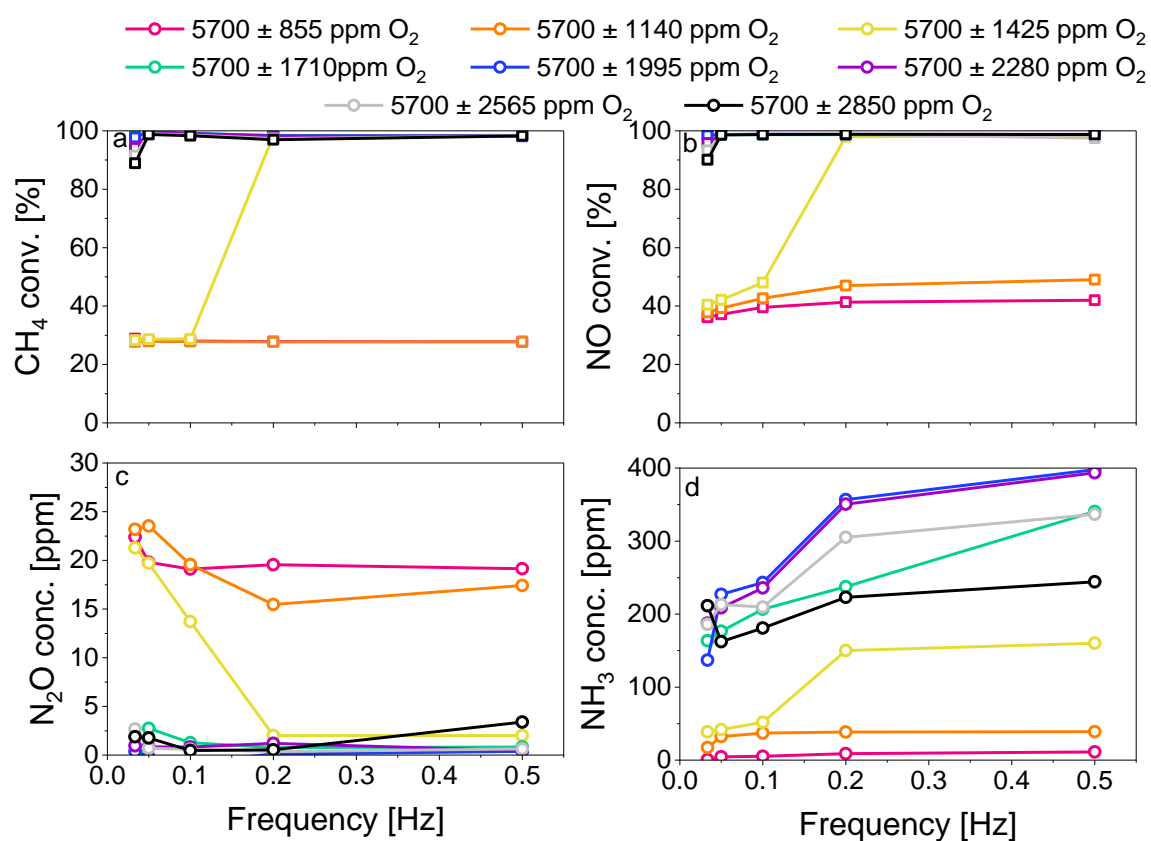
Figure D5. (a) CH$_4$ and (b) NO conversions as well as (c) N$_2$O and (d) NH$_3$ concentration under O$_2$-dithering conditions at 420 °C over Rh/Al$_2$O$_3$ performed at 0.025, 0.033, 0.05, 0.1, 0.2 and 0.5 Hz and amplitude of 5700 ± 855, 5700 ± 1140, 5700 ± 1425, 5700 ± 1710, 5700 ± 1995, 5700 ± 2280, 5700 ± 2565 and 5700 ± 2850 ppm O$_2$. Conditions: 1500 ppm CH$_4$, 1600 ppm NO, 7000 ppm CO, 5 vol% H$_2$O; WHSV = 240 Lh^{-1}g^{-1}.

Figure D6. (a) CH$_4$ and (b) NO conversions as well as (c) N$_2$O and (d) NH$_3$ concentration under O$_2$-dithering conditions at 420 °C over Pd-Rh/Al$_2$O$_3$ performed at 0.025, 0.033, 0.05, 0.1, 0.2 and 0.5 Hz and amplitude of 5700 ± 855, 5700 ± 1140, 5700 ± 1425, 5700 ± 1710, 5700 ± 1995, 5700 ± 2280, 5700 ± 2565 and 5700 ± 2850 ppm O$_2$. Conditions: 1500 ppm CH$_4$, 1600 ppm NO, 7000 ppm CO, 5 vol% H$_2$O; WHSV = 240 Lh^{-1}g^{-1}.

Appendix E (Chapter 7)
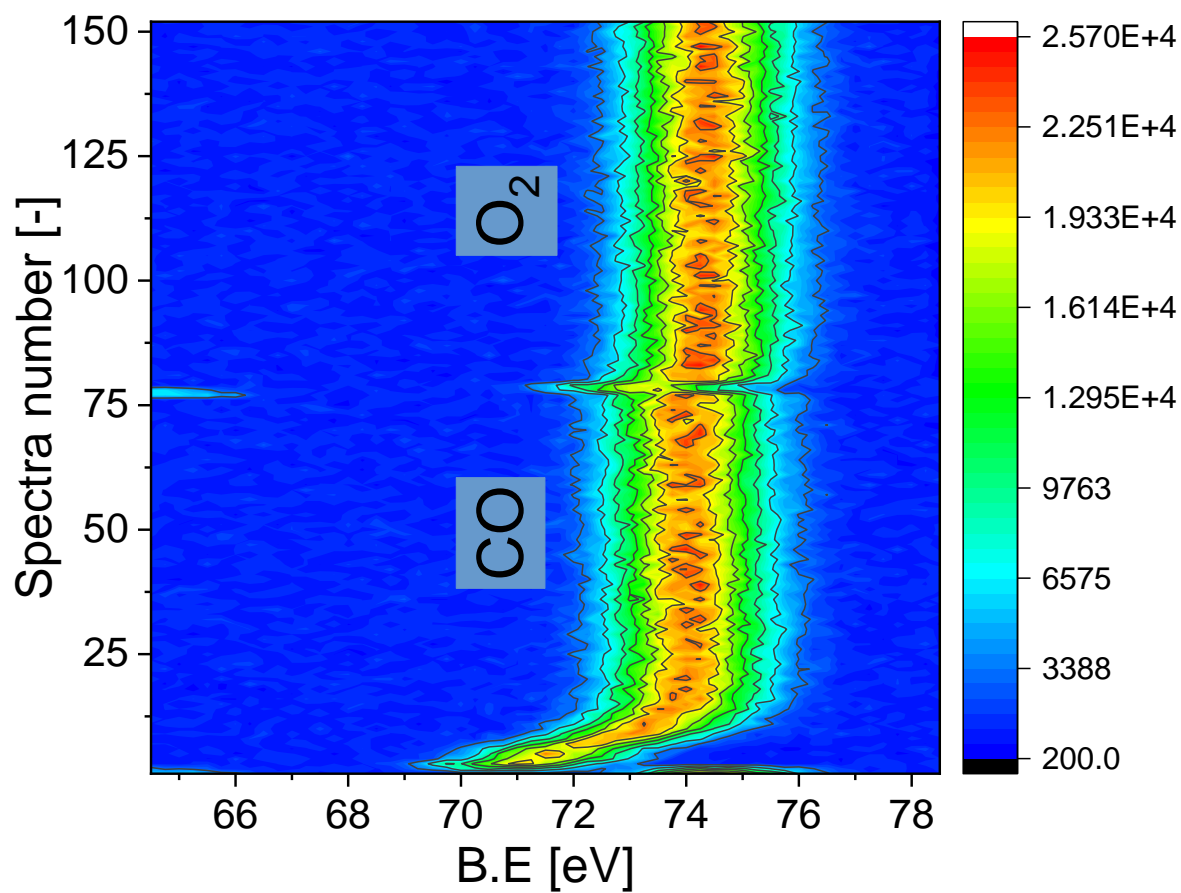
Figure E1. X-ray photoelectron of 5 wt% Pd/Al$_2$O$_3$ at the Al 2p core level acquired with a 660 eV photon energy, measured while pulsing CO and O$_2$.
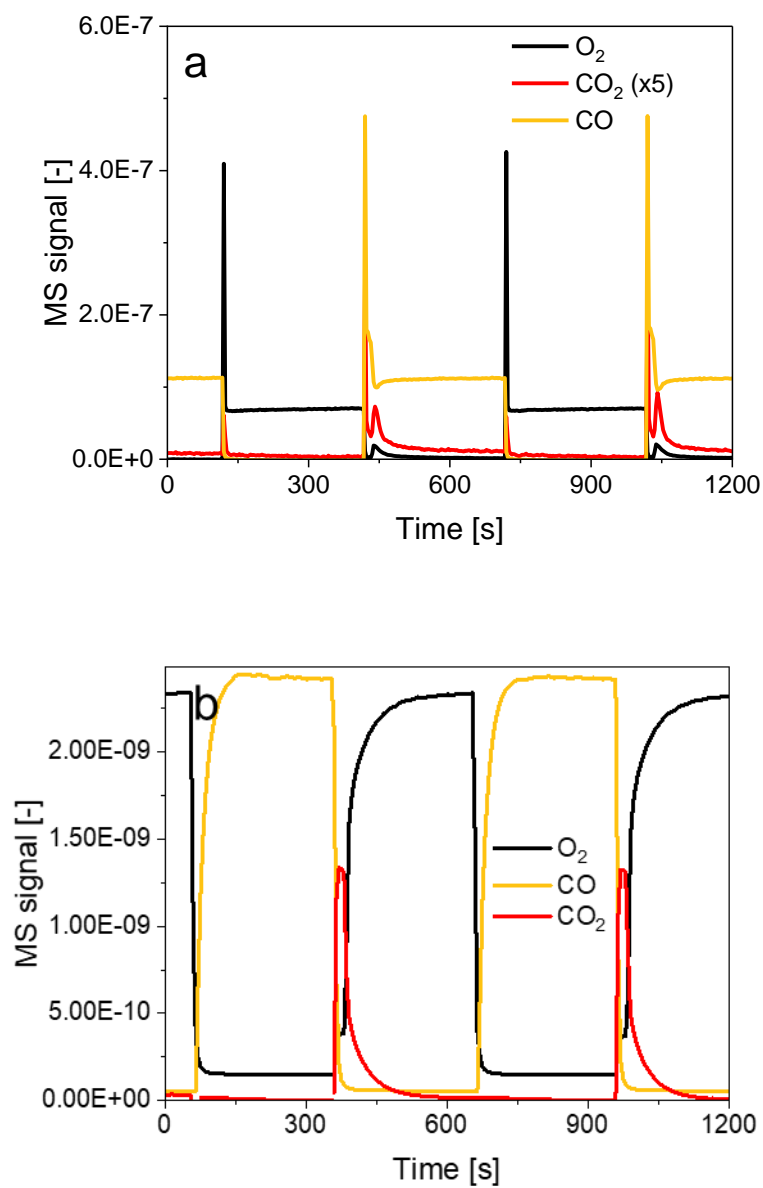
Figure E2. O_2, CO, and CO_2 mass spectrometer signals measured during (a) X-ray photoelectron spectroscopy measurements, and (b) in a quartz plug-flow reactor in the laboratory when performing the O_2 and CO switches every 5 min.
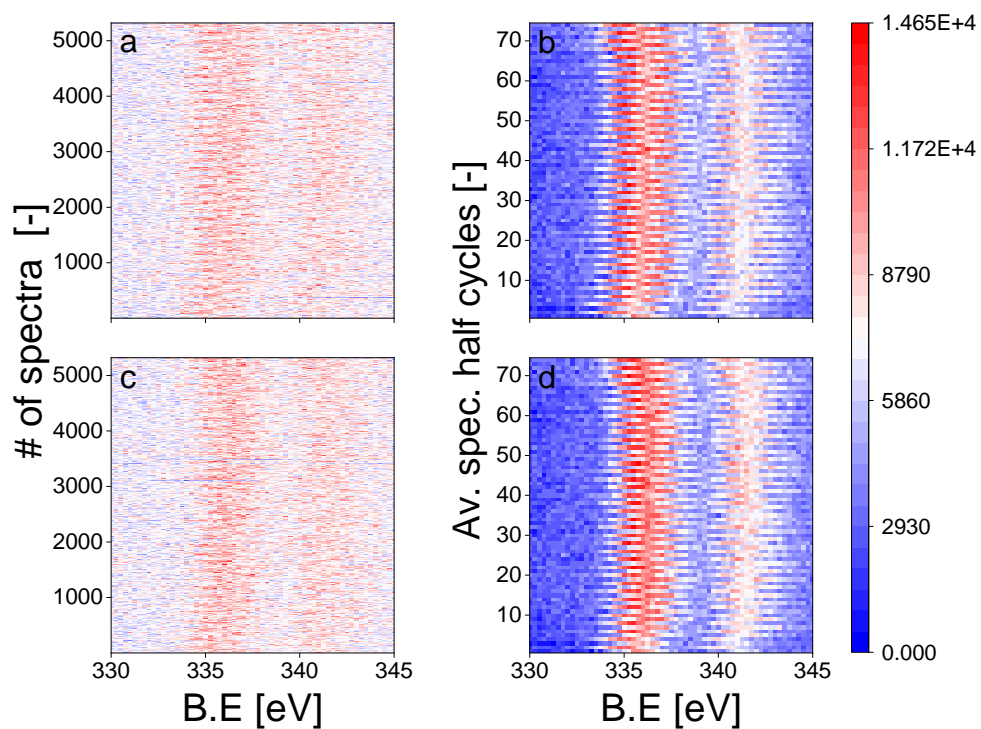
Figure E3. X-ray photoelectron spectra of 5 wt% Pd/Al$_2$O$_3$ at the Pd 3d core level with a 300 eV kinetic energy. (a-b) non-aligned spectra, (c-d) aligned spectra. (a, c) Heat map of all spectra acquired during the 6 h measurement. (b, d) Heat maps of the spectra averaged over each half cycle performed during the 6 h measurement.
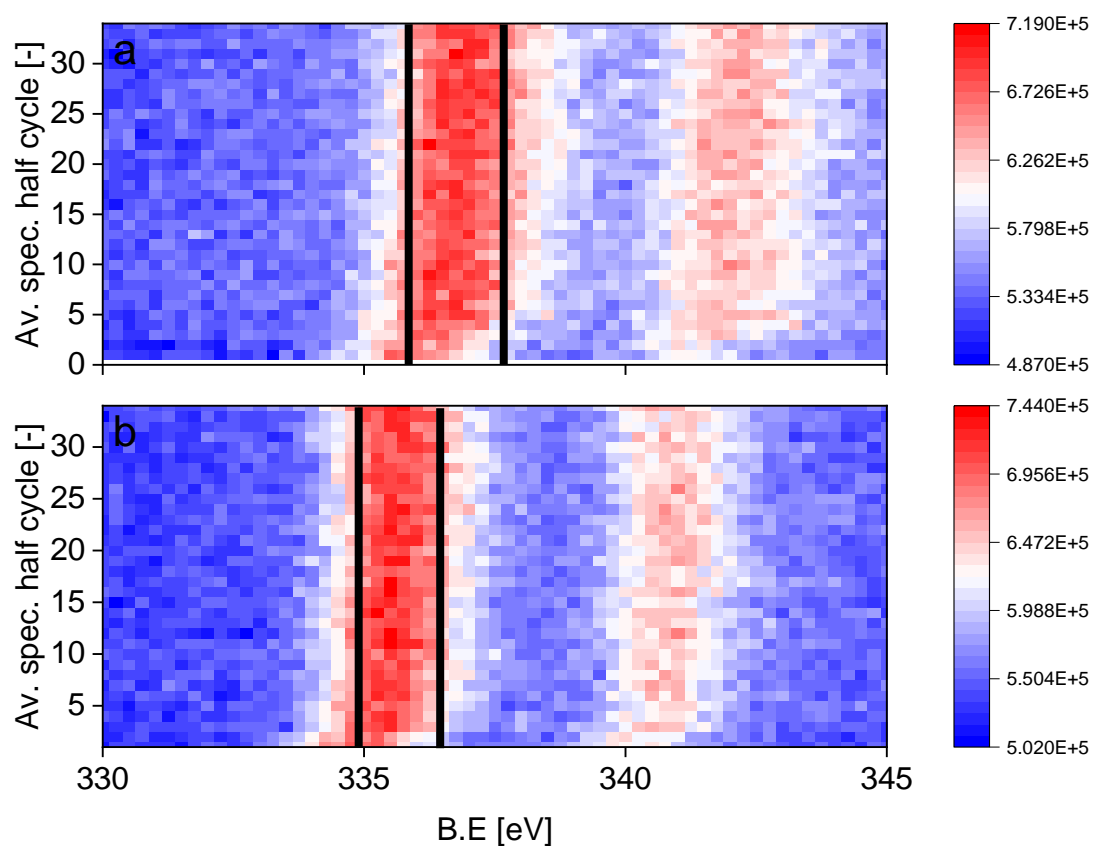
Figure E4. X-ray photoelectron of 5 wt% Pd/Al₂O₃ at the Pd 3d core level with a 300 eV kinetic energy, of the spectra averaged over each half cycle performed during the 6 h measurement, after alignment. (a) Oxidizing conditions. (b) reductive conditions.
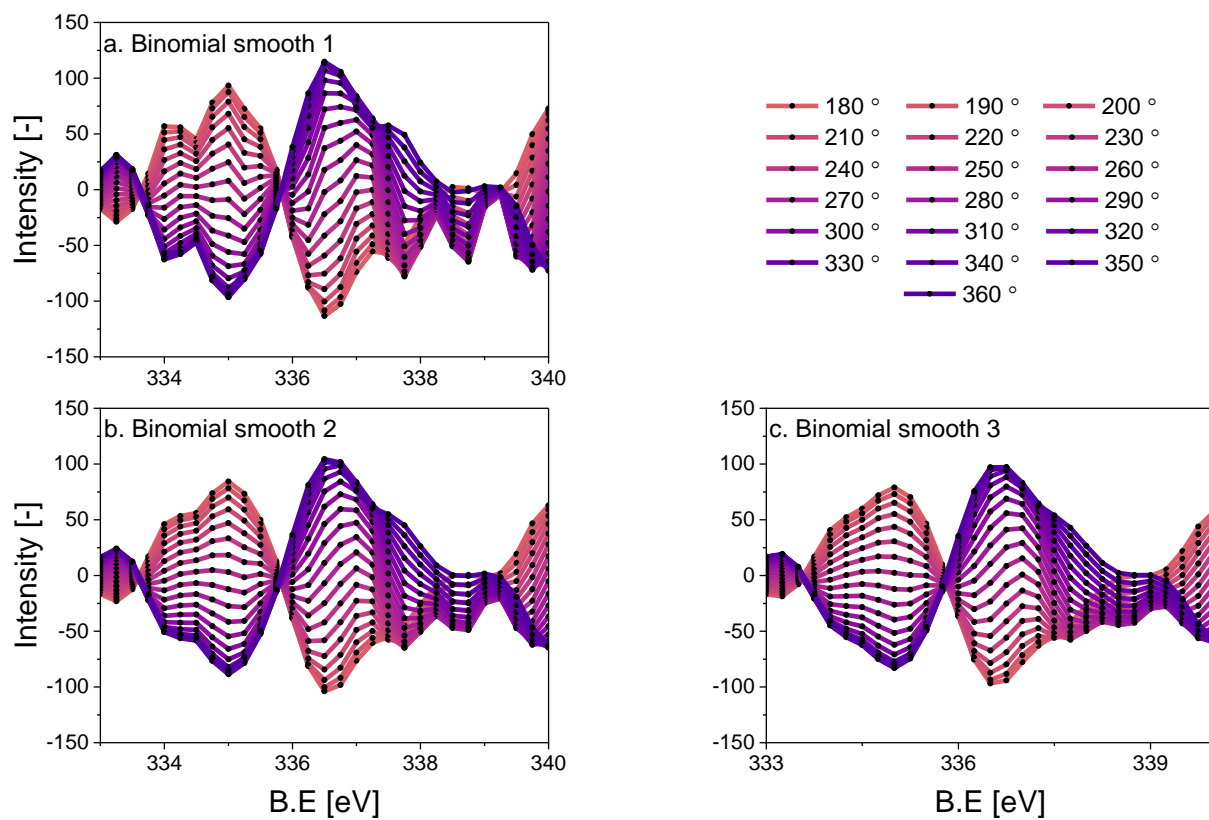
Figure E5. Phase domain performed on (a) binomial smoothed 1, (b) binomial smoothed 2, (c) binomial smoothed 3, X-ray photoelectron spectra acquired at the Pd 3d core level with a 300 eV kinetic energy over 5 wt% Pd/Al_2O_3 obtained when switching between CO and O_2 every 5 min.
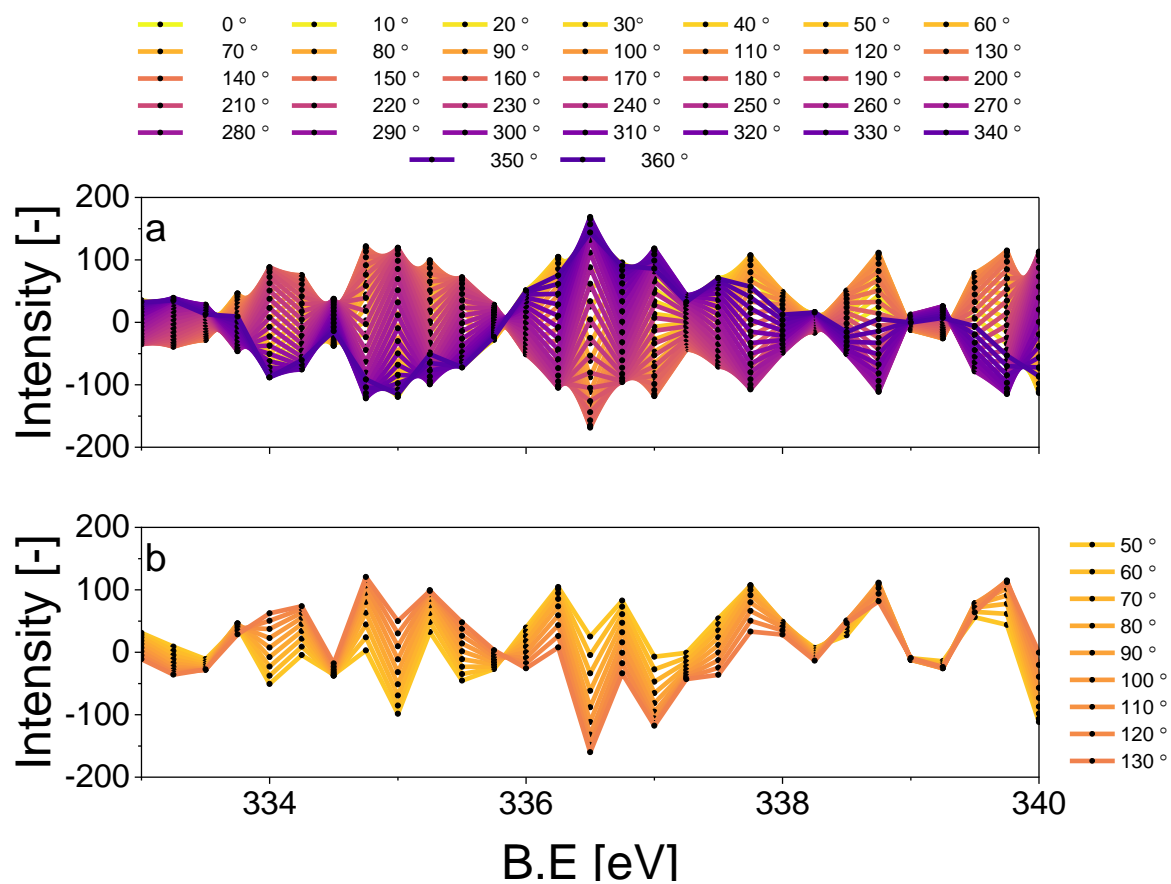
Figure E6. Phase angles 50 to 130 ° of the phase domain results obtained from the raw data set. X-ray photoelectron spectra acquired at the Pd 3d core level with a 300 eV kinetic energy over 5 wt% Pd/Al$_2$O$_3$ obtained when switching between CO and O$_2$ every 5 min.
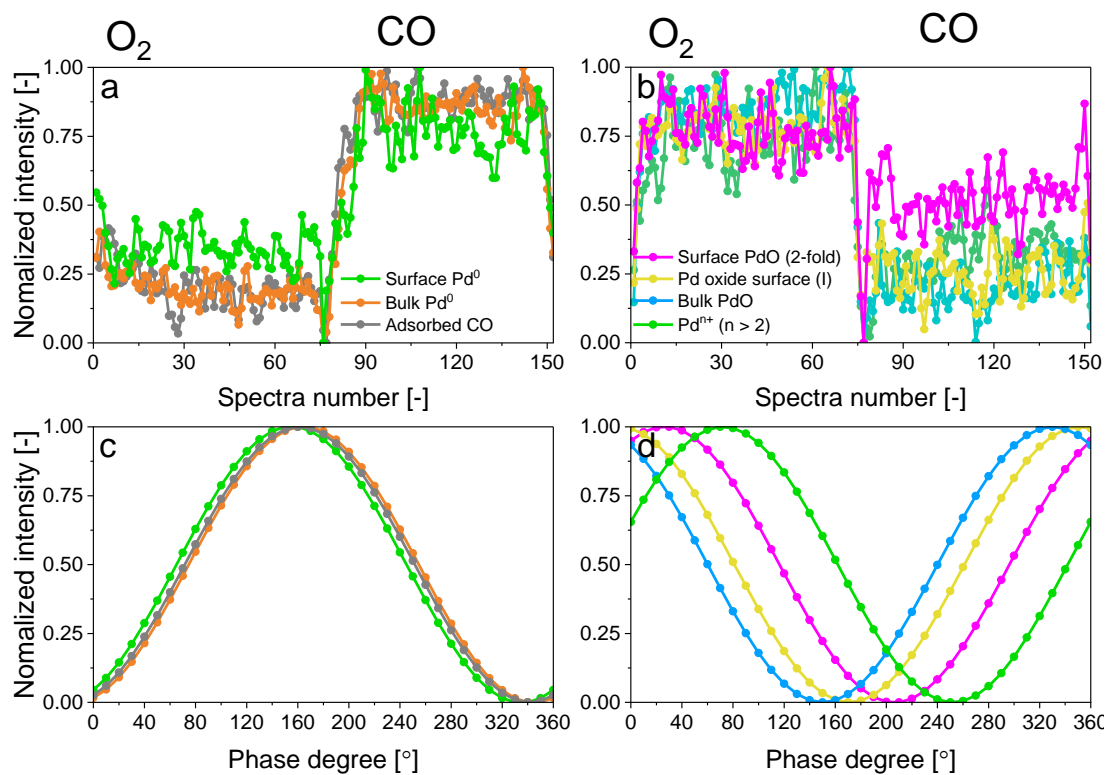
Figure E7. (a-b) Normalized time domain and (c-d) normalized phase domain of the (a, c) reduced Pd species, and (b, d) oxidized Pd species from the aligned and smoothed (binomial 1) data set.
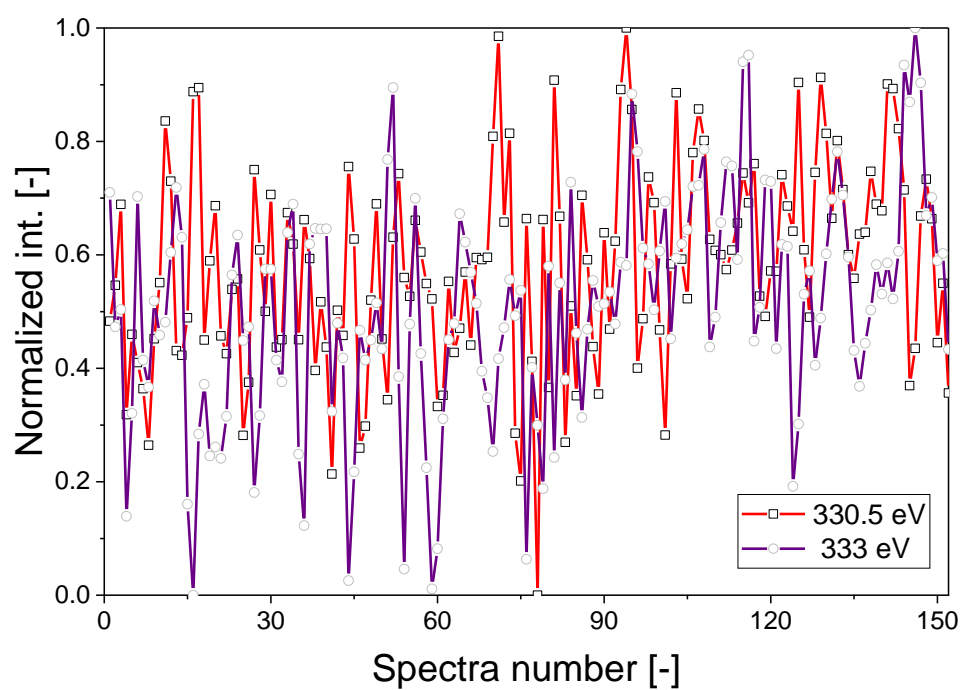
Figure E8. Normalized time domain obtained from the raw data. The X-ray photoelectron spectra was acquired at the Pd 3d core level with a 300 eV kinetic energy over 5 wt% Pd/Al_2O_3 obtained when switching between CO and O_2 every 5 min.

Curriculum Vitae

Name: Maneka Claire Roger

Date of birth: 26.08.1994

Place of birth: Paris, France

Nationality: French

Employment history

Aug. 2017 – Feb. 2018   Earth Space Technical Ecosystem Enterprises (ESTEE),

                               Bussigny, Switzerland – Internship

Professional education

Nov. 2018 – Current   Ph.D. student in the Applied Catalysis and Spectroscopy

                               group the Bioenergy and Catalysis Laboratory and at the Paul

                               Scherrer Institut (PSI; Villigen; Switzerland) under the super-

                               vision of Dr. Davide Ferri, Prof. Dr. Oliver Kröcher

Feb. 2018 – Aug. 2018   MSc thesis group of catalysis for biofuels at the Swiss

                               Federal Institute of Technology Lausanne (EPFL; Lausanne,

                               Switzerland) under the supervision of Dr. Christophe Bar-

                               anowski, Prof. Dr. Oliver Kröcher

Sept. 2016 – Jul. 2018   MSc in Chemical Engineering and Biotechnology at EPFL

Sept. 2013 – Jul. 2016   BSc in Chemistry and Chemical engineering at EPFL